Development of Surface-wave Methods and Its Application to Site Investigations(Dissertation_全文)

AUTHOR(S):

Hayashi, Koichi

Development of the Surface-wave Methods and Its Application to Site Investigations

Koichi Hayashi

Abstract

We have studied surface-wave propagation in two-dimensional space and applied surface-wave methods to near-surface S-wave velocity delineation for civil engineering applications. This dissertation describes fundamental theory of surface-wave propagation, numerical and physical modeling, surface-wave data acquisition and analysis methods that we have developed and application examples of the methods as well.

We have proposed a new analysis method “CMP cross-correlation” that can greatly improve horizontal resolution of the surface-wave method. The CMP cross-correlation gathers of the multi-channel and multi-shot surface waves give accurate phase-velocity curves and enable us to reconstruct two-dimensional velocity structures with high resolutions. Data acquisition for the CMP cross-correlation analysis is similar to a 2D seismic reflection survey. Data processing seems similar to the CDP analysis of the 2D seismic reflection survey but it differs in the point that the cross-correlation of original waveform is calculated before making CMP gathers. Data processing of the CMP cross-correlation analysis consists of following four steps: First, cross-correlations are calculated for every pairs of two traces in each shot gather. Second, correlation traces having common mid-point are gathered and the traces that have equal spacing are stacked in a time domain. Resultant cross-correlation gathers resembles to shot gathers and named as CMP cross-correlation gathers. Third, a multi-channel analysis of surface waves is applied to the CMP cross-correlation gathers for calculating phase-velocities. Finally, 2D S-wave velocity profile is reconstructed through non-linear least square inversion. Analyses of waveform data from numerical modeling and field observations indicated that the new method could greatly improve the accuracy and resolution of underground S-velocity structure, compared to the conventional surface wave methods.

We have performed numerical and physical modeling of surface waves in order to evaluate the applicability of the method. A finite-difference method is used in the numerical modeling and a Laser Doppler Vibrometer is used in the physical modeling. Both numerical and physical modeling has revealed that the surface-waves can be used

for imaging two-dimensional velocity models. The modeling also clearly shows the applicability of the new method. The new method was applied to the real seismic data too. The data acquisition was similar to the shallow P-wave seismic reflection methods. The CMP cross-correlation analysis calculates dispersion curves from shot gathers. A non-linear least square inversion was applied to each dispersion curve in order to obtain one-dimensional S-wave velocity models. The velocity models down to depth of ten meters obtained through the CMP cross-correlation analysis agreed with known geological information very well.

We have modified a passive surface-wave method, so called a micro-tremors array measurement, and applied it to near-surface investigation in civil engineering purposes. We have developed irregular arrays methods, such as L-shape array or linear array, for the micro-tremors array measurement and evaluated the applicability of them in comparison with isotropic array. These results lead to the conclusion that irregular arrays can be used for small-scale passive surface-wave method in which relatively high-frequency (1 to 10Hz) micro-tremors are used.

Our new surface-wave methods have been applied to several different purposes in civil engineering, such as housing site investigations, earthquake disaster mitigation, levee inspections, and environmental issues. All these application examples prove that the surface-wave methods are very effective tool for estimating subsurface S-wave velocity model. The most important character of the surface-wave methods is that the method can estimate subsurface rigidity non-destructively from ground surface in soil engineering applications. Traditional geophysical methods in engineering field, such as a seismic refraction survey and a resistivity survey, are mainly used in rock mechanics field. No geophysical method has been widely used in soil engineering except loggings. The surface-wave methods can be first non-destructive investigation in soil engineering and it implies that the method will be used very widely. We believe that the surface-wave methods must become one of the standard methods in civil engineering investigations.

Acknowledgements

I wish to thank all those people who contributed to my successful stay at Kyoto University. First, I would like to thank my advisor, Professor Toshifumi Matsuoka, for his guidance, the time that he dedicated to me, suggesting new ideas, solving problems related with this work, and reviewing the dissertation, encouragement and friendship during my stay at the Kyoto University. Also lots of thanks to Emeritus Professor Yuzuru Ashida and Professor Hitoshi Mikata for their support and help.

Thanks to all the people of OYO Corporation for giving me this opportunity and supporting me and my work at Kyoto University. A very special thanks to the late Dr. Satoru Ohya for his support and encouragement over the years. I deeply regret not being able to show the dissertation to him. Many thanks to Dr. Hideki Saito and Dr. Yasunori Ohtsuka for their support, encouragement and making arrangement for my stay at Kyoto University. Also many thanks to Dr. Masanori Saito for suggesting new ideas, solving problems related with this work, providing calculation code for dispersion curves, and reviewing a lot of manuscript. A special thanks to Dr. Kazuhito Hikima, Mr. Haruhiko Suzuki, Dr. Hirohito Takahashi and Mr. Chisato Konishi for their support, discussion, friendship and encouragement.

I would like to thank the late Dr. Masahito Tamura of Building Research Institute for his support to field work and the development of the surface-wave methods, discussion, friendship, encouragement and the permission to publish the data. I deeply regret not being able to show the dissertation to him.

I wish to express my gratitude to Dr. Tomio Inazaki of Public Works Research Institute for his support to field work and the development of surface-wave methods, providing me the idea of the land streamer, discussion and encouragement. Many thanks to Dr. Osamu Nishizawa and Dr. Katsumi Kimura of Advanced Industrial Science and Technology for their assistance in physical model experiments and field experiments. Also many thanks to Dr. Toshiaki Yokoi and Dr. Tsutomu Hirade of Building Research Institute for their support to the development of the surface-wave methods and valuable discussion. Also many thanks to Dr. Yoichi Watabe, Dr. Masanori Tanaka and Dr. Shinji Sassa of Port and Airport Research Institute for their support to field work and the

permission to publish the data. Also many thanks to Professor Satoru Shibuya of Kobe University for his support to the field experiment at the leaning tower of Pisa.

I wish to thank all those people who contributed to the development of the surface-wave methods. A very special thanks to Mr. Toru Suzuki of Mony Exploration Corporation for his support to fieldwork, friendship and encouragement over the years. I have acquired most of surface-wave data in the dissertation with him. This research owes much to his various efforts in data acquisition at field. Also many thanks to Mr. Yoshinobu Murata of Network for the Action against Geo-hazards for his support and various efforts to the development of the surface-wave methods, discussion, friendship and encouragement. I would like to Mr. Yasuaki Kikuchi of Polus R&D Center of Life-Style Incorporation for his support to the development of the surface-wave methods. Also many thanks to Mr. Rob Huggins, Mr. Craig Lippus and Ms. Deb Underwood of Geometrics Corporation for their support to the development of the surface-wave methods.

I would like to thank Dr. Choon B. Park and Dr. Jianghai Xia of Kansas Geological Survey for providing the idea of the surface-wave methods to me. They have originally developed the multi-channel analysis of surface-waves and their research has inspired me to start the development of the surface-wave method. Also many thanks to Dr. Robert Kayen of United States Geological Survey for his support to the field experiments in U.S..

I would like to thank Obihiro Development and Construction Department of Hokkaido Regional Development Bureau, Japan Institute of Construction Engineering and Nara National Research Institute for Cultural Properties for their support for fieldwork and the permission to publish the data.

Finally, I would like to thank my father and mother, and my parents-in-law for helping me and my wife Hiroko, and taking very good care of our children. Many thanks to our children, Mari, Daichi and Taiyo for their patience and encouragement. And finally I am grateful to my wife Hiroko for long support and encouragement over the years.

Contents

Chapter 1

Introduction

1.1 Motivation and Objectives

Japan is located at active plate boundary and there are many active volcanoes and earthquakes. Such active and young geological condition makes Japanese ground relatively unstable and danger. For example, land slides associated with earthquakes or heavy rain falls cause the lost of life and wealth almost every year. In order to prevent such ground disaster, subsurface information is needed. Therefore, accurate geotechnical investigation methods are very important for constructing safe and sustainable society that consists of buildings, railways and highways based on civil engineering technology. There are so many geotechnical investigation methods for civil engineering. The most widely used method is a boring and a standard penetrating test (SPT). The boring and the SPT are applied to almost all civil engineering investigations. Recently, there are increasing demands for developing more convenience investigation methods instead of the boring and the SPT.

Geophysical methods have been also applied to civil engineering investigations for many years. Big advantage of the geophysical methods is that the methods are non-destructive and can be performed quickly and cheaply. However, traditional geophysical methods in engineering field, such as a seismic refraction survey and a resistivity survey, are mainly used in rock mechanic engineering, such as tunnels and dams. No geophysical method has been widely used in soil engineering, such as reclaimed land, liquefaction and levees, except logging methods. Most of geotechnical investigations in soil engineering fields are boring and in-situ tests using borehole. Considering the geophysical methods are widely used in rock mechanics in order to obtain geotechnical properties of rocks, the methods can be also used in soil engineering field too.

Theoretical study and the evolution of computer have driven the recent advance of geophysical methods. Most of the in-situ measurements, such as SPT, provide subsurface geotechnical information directly from observed data. The geophysical methods, however, need mathematical analysis based on the physical theory in order to obtain subsurface information from observed data. Therefore, continuous development of computational ability implies the possibility of further development of geophysical methods. Advanced geophysical methods will be able to provide accurate subsurface information much quickly and cheaply. Accurate subsurface information contributes for constructing safe and sustainable society. Therefore, we have started the development of new geophysical methods mainly for soil engineering investigations.

1.2 Seismic Exploration Methods in Civil Engineering Investigations

Seismic exploration methods have played important role in Japanese civil engineering investigations for many years. For example, a P-wave refraction method is one of the most popular geotechnical investigation methods in Japan. The refraction method has been applied to most of tunnels in Japan in order to estimate rock classification along tunnel route in the beginning stage of construction. The refraction method has been also applied to most of dam construction as well. Recently, digital data acquisition and tomographic inversion have been introduced to the refraction method and applicability and reliability are greatly improved (Hayashi and Saito, 1998; Hayashi and Takahashi, 2001). Such new techniques have developed the new applications of the method. However, most of the refraction applications are related to rock mechanics field and not soil engineering. In the rock mechanics field, P-wave velocity can be used for estimating rigidity of rocks. P-wave velocity, however, is not related to soil rigidity in soil mechanics field because the P-wave velocity just indicates water velocity below ground water table. Therefore, S-wave velocity is much useful in soil engineering field for evaluating soil rigidity and the P-wave refraction method is not useful in soil engineering field except ground water survey.

An S-wave refraction method is one of the candidates for estimating the rigidity in the soil engineering field. However, the method has not been widely used in the soil engineering. One reason is the character of S-wave velocity in unconsolidated soil layers. In the unconsolidated soil ground, S-wave velocity contrast is generally small and reversed layers or top high velocity layers sometimes exist. These characters make the refraction analysis to be difficult. Another reason is data acquisition difficulty. In the S-wave refraction method, SH seismic motion must be used. P-waves and Love waves, however, are sometimes included and they complicate first arrival picking.

An S-wave reflection method is another candidate. However, the method has not been widely used in the soil engineering. The most important problem in the method is the inclusion of direct waves, refracted waves and surface-waves (Love waves). All these waves contaminate the reflected waves and complicate reflection analysis. Therefore, it is difficult to obtain not only layered structure but also S-wave velocity through the reflection method in the unconsolidated soil ground.

Only PS-logging has been widely used in the soil engineering in order to obtain

S-wave velocity of the ground. However, the PS-logging needs a borehole and can only provide one-dimensional structure. A cross-hole tomography can provide two-dimensional structure of the ground. An S-wave velocity tomography is still in experimental phase and method has not been widely used in the civil engineering investigations.

Non-destructive methods that can provide two-dimensional S-wave velocity model of the ground have been eagerly waited for many years in soil engineering. It is well known that the phase-velocity of surface-waves reflects the S-wave velocity of the ground. Over the past few decades, a considerable numbers of studies have been made of the development of seismic methods using surface-waves. The first researcher to give much attention to the high frequency surface-waves is Aki. He investigated the micro-tremors as surface-waves and proposed theory of Spatial Auto Correlation (Aki, 1957). A micro-tremor array measurements mainly based on the Spatial Auto Correlation has been developed by Okada in order to estimate deep S-wave velocity structures. Okada (2003) summarizes the detailed theory of the microtremor-array measurements and the example of actual field data. Tokimatsu studied the development of seismic methods using active surface-waves. Tokimatsu (1997) summarizes his enormous effort at the development of active surface-wave methods. The Kansas Geological Survey has developed the Tokimatsu's active surface-wave method further and proposed the multi-channel analysis of the surface-waves (Park et al.,1999a,; 1999b). The multi-channel approach has greatly improved accuracy and reliability of the surface-wave methods. They have also proposed two-dimensional survey using surface-waves (Xia et al., 1999). Their enormous effort at the surface-wave methods has inspired many researchers to start the development of surface-wave methods. The most important theory in the surface-wave methods is the calculation of phase-velocity for layered velocity models. Saito (1979) and Saito and Kabasawa (1993) studied the problem of phase-velocity calculation.

All those development of the surface-wave methods implies that the methods may be used in soil engineering for estimating S-wave velocity model nondestructively. What seems to be lacking, however, is that the data acquisition and analysis for two dimensional surveys and the use of the surface-wave methods to real engineering problems. Most of the surface-wave methods have been one-dimensional survey and stayed at research stage. Therefore, we have started the development of two-dimensional surface-wave methods and the application the methods to real engineering problems.

1.3 Outline of the Dissertation

This dissertation describes fundamental theory of surface-wave propagation, numerical and physical modeling, surface-wave data acquisition and analysis methods that we have developed and application examples of the methods as well. The outline of the dissertation can be summarized as follows and shown in Figure 1.3.1.

In the Chapter 2, we will describe fundamental theory behind our surface-wave methods. At first, fundamental theory of elastic waves and surface-waves will be derived. In order to study surface-wave propagation in two- and three-dimensional medium, we have developed three-dimensional viscoelastic finite-difference code and performed the numerical modeling of surface-waves. Fundamental theory of surface-wave analysis, such as phase-velocity calculation, micro-tremor analysis, and non-linear least square inversion are also introduced in the Chapter.

In the Chapter 3, we will describe our surface-wave method using active sources. We have proposed a new analysis method “CMP cross-correlation” that can greatly improve horizontal resolution of the surface-wave method. Theory, numerical and physical modeling and field example will be described in the Chapter. In the numerical modeling, the finite-difference code that described in the Chapter 2 is employed. In the physical modeling, a Laser Doppler Vibrometer (LDV) is used as a receiver.

In the Chapter 4, we will describe small scale passive surface-wave method. The passive surface-wave method, so called a micro-tremors array measurement is widely used in earth science in order to delineate deep basin structure. We have modified the method and applied it to near-surface investigation in civil engineering purpose. One of the difficulties in passive surface-wave method for civil engineering is the method prefers two-dimensional isotropic arrays, such as equilateral triangle or circle, on ground surface. In the civil engineering applications, it is difficult to set such isotropic array because of the restriction of survey area. Therefore, we have developed irregular arrays methods, such as L-shape array or linear array, and evaluated the applicability of

them in comparison with isotropic array.

In the Chapter 5, we will show the application example of active and passive surface-wave methods to actual civil engineering investigations. The methods have applied several different purposes in civil engineering, such as housing site investigations, earthquake disaster mitigation, levee inspections, and environmental issues. In data acquisition, we have developed a receiver towing tool, so called “land streamer”, in order to move receiver array quickly on paved road. The land streamer has greatly shortened data acquisition time in long survey line, such as levee inspections. The land streamer has also enabled us to apply the surface-wave method on difficult surface condition, such as tidal flat surface. In data processing, we have introduced a joint analysis in which not only phase-velocity but also other geophysical or geotechnical information is used for estimating subsurface structures. For housing site investigations, initial velocity models for non-linear least square inversion are constructed based on N-value obtained through the Swedish Weighted Sounding Tests. We have also developed a joint analysis of the surface-wave and gravity data in order to estimate not only S-wave velocity model but also density model as well.

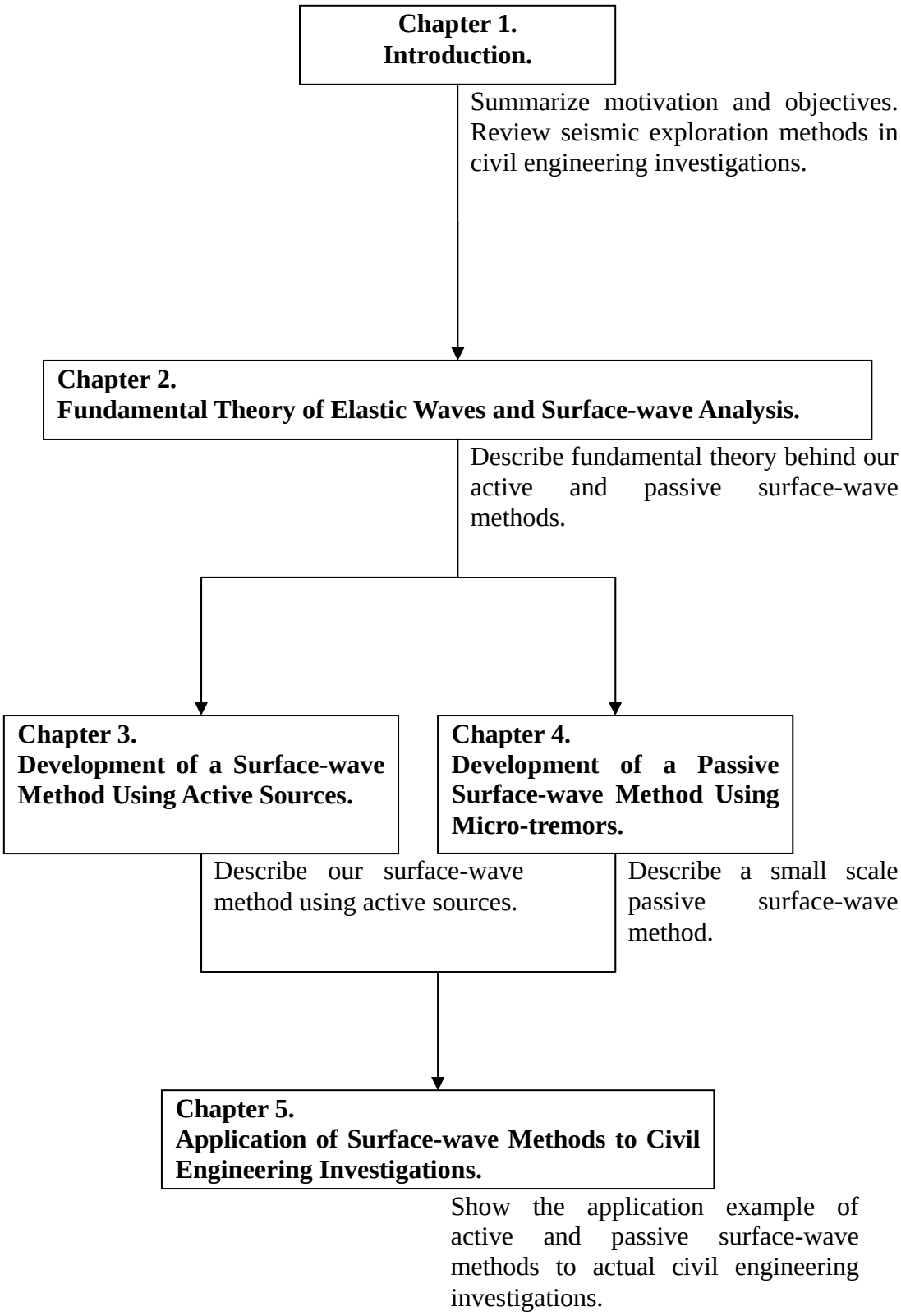

Figure 1.3.1 Outline of the dissertation

References

Aki, K., 1957, Space and time spectra of stationary stochastic waves, with special reference to microtremors, Bull. Earthq. Res. Ins., 35, 415-456.

Hayashi, K. and Saito, H., 1998, High resolution seismic refraction method –Development and applications-, Butsuri-tansa, 51, 471-491, (in Japanese).

Hayashi, K. and Takahashi, T., 2001, High resolution seismic refraction method using surface and borehole data for site characterization of rocks, International Journal of Rock Mechanics and Mining Sciences, 38, 807-813.

Okada, H., 2003, The microtremor survey method, Society of Exploration Geophysicist, Tulsa.

Park, C. B., Miller, R. D., and Xia, J., 1999a, Multimodal analysis of high frequency surface waves, Proceedings of the symposium on the application of geophysics to engineering and environmental problems '99, 115-121.

Park, C. B., Miller, R. D., and Xia, J., 1999b, Multichannel analysis of surface waves, Geophysics, 64, 800-808.

Saito, M., 1979, Computation of reflectivity and surface wave dispersion curves for layered media 1. Sound wave and and SH wave, Butsuri-tanko, 32, 15-26, (in Japanese) .

Saito, M. and Kabasawa, H., 1993, Computation of reflectivity and surface wave dispersion curves for layered media 2. Rayleigh wave calculations, Butsuri-tansa, 46, 283-298, (in Japanese).

Tokimatsu, K., 1997, Geotechnical site-characterization using surface-waves, Earthquake geotechnical engineering, Ishihara (ed.), Balkema, Rotterdam, 1333-1368.

Xia, j., Miller, R. D. and Park, C. B., 1999, Configuration of near-surface shear-wave velocity by inverting surface wave, Proceedings of the symposium on the application of geophysics to engineering and environmental problems '99, 95-104.

Chapter 2

Fundamental Theory of Elastic Waves and Surface-wave Analysis

2.1 Introduction

Conventional seismic methods, such as refraction, reflection, PS-logging and traveltime tomography, can be fundamentally understood by ray theory. Although the reflection method is based on wave equation, the analysis of the reflection method is mainly based on acoustic wave equation at least in civil engineering applications. These conventional methods analyze the waveform data mainly in time-domain. Although some data processings, such as band-pass filter, deconvolution and migration, are performed in frequency domain. Use of frequency domain is mostly due to mathematical convenience and not the physical requirement.

Unlike these conventional methods, surface-wave methods are based on full wave equation (elastic wave equation) and these analyses are completely performed in frequency domain. In order to understand the basic theory behind the surface-wave methods, we will describe fundamental elastic wave equation and derive analytical solution of surface-waves in one-dimensional layered medium.

The analytical solution of the surface-waves can be obtained only for one-dimensional medium so far. However, the real earth has always three-dimensional structures. Effect of three-dimensional structure on surface-wave propagation had not been understood and it had protected the evolution of the surface-wave methods. In order to understand the surface-wave propagation in two-dimensional and three-dimensional medium, we have developed 2D and 3D viscoelastic finite-difference code and applied them to the numerical simulations of the surface-waves. Fundamental theory of our finite-difference code and the result of numerical simulations will be shown in the Chapter 2.4 and 2.5.

The most important part in the surface-wave analysis is the phase-velocity calculation for waveform data. We will describe the fundamental theory of phase-velocity calculation for both active and passive surface-wave data in this chapter. A non-linear least square method for the inversion of dispersion curves is also described in the chapter briefly.

2.2 Elastic Waves

In this section, we derive velocity-stress elastic wave equations at first. Then, we extend it to the viscoelastic case.

2.2.1 Elastic waves

1) Introduction

The derivation of the velocity-stress elastic wave equations gives the fundamental idea and mathematical foundation of the wave equation. The relationship between forces and deformation in infinitesimal strain theory is largely empirically based and given by a constitutive law called Hook's law. The deformation is a function of material properties of the body such as density, rigidity (resistance to shear), and incompressibility (resistance to change in volume). The material properties are known as elastic moduli. When stress varies with time, strain varies similarly, and the balance between stress and strain results in seismic waves. These waves travel at velocities that depend on the elastic moduli and are governed by equations of motion.

2) Stress, strain, Newton's second law and Hooke's law

In the following description of the elastic wave equations, we will employ Cartesian coordinate (x_1, x_2, x_3). At first, we show a general three-dimensional relationships between nine strain components and three displacement components (u_1, u_2, u_3). Normal strain can be defined by

$$\varepsilon_{11} = \frac{\partial u_1}{\partial x_1} \qquad \varepsilon_{22} = \frac{\partial u_2}{\partial x_2} \qquad \varepsilon_{33} = \frac{\partial u_3}{\partial x_3}, \tag{2.2.1}$$

here, x_2, x_2, x_3 are the coordinate axes. The first subscript indicates the orientation of the line segment, and second indicates the direction of length change. Shear strains are defined by

$$\varepsilon_{12} = \frac{1}{2}\left(\frac{\partial u_1}{\partial x_2} + \frac{\partial u_2}{\partial x_1} \right) \qquad \varepsilon_{21} = \frac{1}{2}\left(\frac{\partial u_2}{\partial x_1} + \frac{\partial u_1}{\partial x_2} \right)$$

$$\varepsilon_{13} = \frac{1}{2}\left(\frac{\partial u_1}{\partial x_3} + \frac{\partial u_3}{\partial x_1}\right) \qquad \varepsilon_{31} = \frac{1}{2}\left(\frac{\partial u_3}{\partial x_1} + \frac{\partial u_1}{\partial x_3}\right) \quad . \tag{2.2.2}$$

$$\varepsilon_{23} = \frac{1}{2}\left(\frac{\partial u_2}{\partial x_3} + \frac{\partial u_3}{\partial x_2}\right) \qquad \varepsilon_{32} = \frac{1}{2}\left(\frac{\partial u_3}{\partial x_2} + \frac{\partial u_2}{\partial x_3}\right)$$

These nine terms constitute the infinitesimal strain tensor, a symmetric tensor with six independent quantities that can be ordered as

$$\varepsilon_{ij} = \begin{pmatrix} \dfrac{\partial u_1}{\partial x_1} & \dfrac{1}{2}\left(\dfrac{\partial u_2}{\partial x_1} + \dfrac{\partial u_1}{\partial x_2}\right) & \dfrac{1}{2}\left(\dfrac{\partial u_3}{\partial x_1} + \dfrac{\partial u_1}{\partial x_3}\right) \\ \dfrac{1}{2}\left(\dfrac{\partial u_2}{\partial x_1} + \dfrac{\partial u_1}{\partial x_2}\right) & \dfrac{\partial u_2}{\partial x_2} & \dfrac{1}{2}\left(\dfrac{\partial u_3}{\partial x_2} + \dfrac{\partial u_2}{\partial x_3}\right) \\ \dfrac{1}{2}\left(\dfrac{\partial u_3}{\partial x_1} + \dfrac{\partial u_1}{\partial x_3}\right) & \dfrac{1}{2}\left(\dfrac{\partial u_3}{\partial x_2} + \dfrac{\partial u_2}{\partial x_3}\right) & \dfrac{\partial u_3}{\partial x_3} \end{pmatrix}. \tag{2.2.3}$$

We can represent all nine strain terms of (2.2.3) with compact indicial notation,

$$\varepsilon_{ij} = \frac{1}{2}\left(\frac{\partial u_i}{\partial x_j} + \frac{\partial u_j}{\partial x_i}\right). \tag{2.2.4}$$

The trace of the strain tensor is called the cubic dilatation, θ ,

$$\theta = \varepsilon_{ii} = \frac{\partial u_1}{\partial x_1} + \frac{\partial u_2}{\partial x_2} + \frac{\partial u_3}{\partial x_3} = \nabla \cdot u \,. \tag{2.2.5}$$

Second, we define a stress tensor. Here, we subdivide the area of fictitious plane into area elements with surface area, ΔA. A small force, ΔF, acts on each elements. The stress components acting on the plane (x_1 face) that has a normal in the x_1 direction are defined by

$$\sigma_{11} = \lim_{\Delta A_1 \to 0} \frac{\Delta F_1}{\Delta A_1}$$

$$\sigma_{12} = \lim_{\Delta A_1 \to 0} \frac{\Delta F_2}{\Delta A_1} \quad , \tag{2.2.6}$$

$$\sigma_{13} = \lim_{\Delta A_1 \to 0} \frac{\Delta F_3}{\Delta A_1}$$

The first index of σ_{ij} in (2.2.6) corresponds to the direction of the normal to the plane being acted on by the force, and the second index indicates the direction of the force. For two other planes, we define six additional stress components,

σ_{21}、 σ_{22}、 σ_{23} acting on the x_2 face,

σ_{31}、 σ_{32}、 σ_{33} acting on the x_3 face.

All of these are implicitly functions of space and time. A three dimensional stress tensor is defined as

$$\sigma_{ij} = \begin{pmatrix} \sigma_{11} & \sigma_{12} & \sigma_{13} \\ \sigma_{21} & \sigma_{22} & \sigma_{23} \\ \sigma_{31} & \sigma_{32} & \sigma_{33} \end{pmatrix}. \qquad (2.2.7)$$

The diagonal terms are called normal stresses, and the off-diagonal terms are called shear stresses.

Third, we consider a force balance on a cubic element in a continuum that is under going internal motions. Applying Newton's second law to the medium gives

$$\rho \frac{\partial^2 u_i}{\partial t^2} = f_i + \frac{\partial \sigma_{ij}}{\partial x_j} \quad . \qquad (2.2.8)$$

where f_i represents body forces. This set of three equations is called the equation of motion for a continuum. For example, u_1 (x_1 component of displacement) can be written as

$$\rho \frac{\partial^2 u_1}{\partial t^2} = \frac{\partial \sigma_{11}}{\partial x_1} + \frac{\partial \sigma_{12}}{\partial x_2} + \frac{\partial \sigma_{13}}{\partial x_3} \quad , \qquad (2.2.9)$$

when there are no body forces.

Fourth, we show the relationship between stress and displacement. There are provided by constitutive laws that relate stress to strain. The most general form of constitutive law for linear elasticity is Hooke's law

$$\sigma_{ij} = c_{ijkl} \cdot \varepsilon_{kl} \quad . \qquad (2.2.10)$$

The constants of proportionality, C_{ijkl} are known as elastic moduli and define the material properties of the medium. In its general form, C_{ijkl} is a third-order tensor with 81 terms relating the nine elements of the strain tensor to nine elements of the stress tensor by linear sum. In the case of an isotropic elastic substance, the elastic moduli can reduce to two independent moduli called Lame constants, λ and μ. These are related to C_{ijkl} by

$$C_{ijkl} = \lambda \delta_{ij} \delta_{kl} + \mu \left(\delta_{ik} \delta_{jl} + \delta_{il} \delta_{jk} \right). \qquad (2.2.11)$$

where the Kronecker dekta function is used. Inserting this into (2.2.10) gives,

$$\sigma_{ij} = \left(\lambda\delta_{ij}\delta_{kl} + \mu\left(\delta_{ik}\delta_{jl} + \delta_{il}\delta_{jk}\right)\right)\varepsilon_{kl}, \tag{2.2.12}$$

which reduces to

$$\sigma_{ij} = \lambda\varepsilon_{kk}\delta_{ij} + 2\mu\varepsilon_{ij}. \tag{2.2.13}$$

Using the equation (2.2.5), (2.2.13) can be written as,

$$\sigma_{ij} = \lambda\theta\delta_{ij} + 2\mu\varepsilon_{ij}. \tag{2.2.14}$$

Thus, the stress-strain relationship is written as,

$$\sigma_{ij} = \begin{pmatrix} \lambda\theta+2\mu\varepsilon_{11} & 2\mu\varepsilon_{12} & 2\mu\varepsilon_{13} \\ 2\mu\varepsilon_{21} & \lambda\theta+2\mu\varepsilon_{22} & 2\mu\varepsilon_{23} \\ 2\mu\varepsilon_{31} & 2\mu\varepsilon_{32} & \lambda\theta+2\mu\varepsilon_{33} \end{pmatrix}. \tag{2.2.15}$$

Substituting the equations (2.2.3) and (2.2.5) into (2.2.15), the stress-strain relationship can be expressed as the stress-displacement relationship as follows (only i=1 terms are shown),

$$\begin{aligned} \sigma_{11} &= \lambda\theta+2\mu\varepsilon_{11} = \lambda\left(\frac{\partial u_1}{\partial x_1}+\frac{\partial u_2}{\partial x_2}+\frac{\partial u_3}{\partial x_3}\right)+2\mu\frac{\partial u_1}{\partial x_1} \\ \sigma_{12} &= 2\mu\varepsilon_{12} = \mu\left(\frac{\partial u_1}{\partial x_2}+\frac{\partial u_2}{\partial x_1}\right) \\ \sigma_{13} &= 2\mu\varepsilon_{13} = \mu\left(\frac{\partial u_1}{\partial x_3}+\frac{\partial u_3}{\partial x_1}\right). \end{aligned} \tag{2.2.16}$$

3) Deriving the equation of motion in three-dimensional case

Now, we combine stress-displacement equations into the equation of Newton's second law in order to derive the equation of motion in three-dimensional case. Substituting equations (2.2.16) into (2.2.8) gives us foloowing equations (u_1 componet),

$$\rho\frac{\partial^2 u_1}{\partial t^2} = \lambda\frac{\partial}{\partial x_1}\left(\frac{\partial u_1}{\partial x_1}+\frac{\partial u_2}{\partial x_2}+\frac{\partial u_3}{\partial x_3}\right)+\mu\frac{\partial}{\partial x_1}\left(\frac{\partial u_1}{\partial x_1}+\frac{\partial u_2}{\partial x_2}+\frac{\partial u_3}{\partial x_3}\right)+\mu\left(\frac{\partial^2 u_1}{\partial x_1^2}+\frac{\partial^2 u_1}{\partial x_2^2}+\frac{\partial^2 u_1}{\partial x_3^2}\right). \tag{2.2.17}$$

Using the Laplacian and the equation (2.2.5) we can reduce the equation (2.2.17) to,

$$\rho \frac{\partial^2 u_1}{\partial t^2} = (\lambda + \mu) \frac{\partial}{\partial x_1} \theta + \mu \nabla^2 u_1 . \tag{2.2.18}$$

Other components can be written as,

$$\rho \frac{\partial^2 u_2}{\partial t^2} = (\lambda + \mu) \frac{\partial}{\partial x_2} \theta + \mu \nabla^2 u_2 \tag{2.2.19}$$

$$\rho \frac{\partial^2 u_3}{\partial t^2} = (\lambda + \mu) \frac{\partial}{\partial x_3} \theta + \mu \nabla^2 u_3 . \tag{2.2.20}$$

If we use the notation,

$$U = (u_1, u_2, u_3), \tag{2.2.21}$$

the equations (2.2.18) to (2.2.20) can be written as,

$$\rho \frac{\partial^2 U}{\partial t^2} = (\lambda + \mu) \nabla (\nabla \cdot U) + \mu \nabla^2 U , \tag{2.1.22}$$

which is the three-dimensional homogeneous vector equation of motion for a uniform, isotropic, linear elastic medium.

A common alternate form of this equation employs the vector identity,

$$\nabla^2 U = \nabla (\nabla \cdot U) - (\nabla \times \nabla \times U), \tag{2.2.23}$$

allowing (2.2.22) to be written as,

$$\rho \frac{\partial^2 U}{\partial t^2} = (\lambda + 2\mu) \nabla (\nabla \cdot U) - (\mu \nabla \times \nabla \times U). \tag{2.2.24}$$

4) P-wave and S-wave

We can use the Helmholtz's theorem to the displacements field as,

$$U = \nabla \Phi + \nabla \times \Psi . \tag{2.2.25).}$$

where, Φ is a curl free scalar potential field ($\nabla \times \Phi = 0$) and Ψ is a divergence-less vector potential field ($\nabla \cdot \Psi = 0$). Substituting the equation (2.2.25) into (2.2.24) and using the vector identity ($\nabla \times \nabla \times \Psi = -\nabla^2 \Psi$ for $\nabla \cdot \Psi = 0$), we find,

$$\nabla \left((\lambda + 2\mu) \nabla^2 \Phi - \rho \ddot{\Phi} \right) + \nabla \times \left(\mu \nabla^2 \Psi - \rho \ddot{\Psi} \right) = 0. \tag{2.2.26}$$

We can clearly satisfy this equation if each term in brackets goes to zero independently. We let,

$$\alpha = \sqrt{\frac{\lambda + 2\mu}{\rho}} \tag{2.2.27}$$

$$\beta = \sqrt{\frac{\mu}{\rho}} \tag{2.2.28}$$

and (2.1.26) can be written as,

$$\nabla\left(\alpha^2\nabla^2\Phi - \ddot{\Phi}\right) + \nabla \times \left(\beta^2\nabla^2\Psi - \ddot{\Psi}\right) = 0 \tag{2.2.29}$$

.

This will be solved if,

$$\nabla^2\Phi - \frac{1}{\alpha^2}\ddot{\Phi} = 0 \tag{2.2.30}$$

$$\nabla^2\Psi - \frac{1}{\beta^2}\ddot{\Psi} = 0 \tag{2.2.31}$$

where (2.2.30) and (2.2.31) are scalar wave equation for Φ and vector wave equation for Ψ. α is the velocity of wave, Φ, and is called the P-wave velocity, and β is the S-wave velocity corresponding to solutions Ψ.

5) P-SV and SH waves

Waves propagating in elastic medium can be written as wave equations implies that the equation can be solved in terms of plane-waves. We will focus on plane wave solutions. We use the *x, y, z* coordinate system in which *x, y* and *z* means x_1 ,x_2 and x_3 axis respectively. If we take a *y* axis in plane waves as,

$$\frac{\partial}{\partial y} = 0, \tag{2.2.32}$$

the equation of motions (2.2.17) can be written as,

$$\rho\frac{\partial^2 u_x}{\partial t^2} = (\lambda + \mu)\frac{\partial}{\partial x}\left(\frac{\partial u_x}{\partial x} + \frac{\partial u_z}{\partial z}\right) + \mu\left(\frac{\partial^2 u_x}{\partial x^2} + \frac{\partial^2 u_x}{\partial z^2}\right) \tag{2.2.33}$$

$$\rho\frac{\partial^2 u_y}{\partial t^2} = \mu\left(\frac{\partial^2 u_y}{\partial x^2} + \frac{\partial^2 u_y}{\partial z^2}\right) \tag{2.2.34}$$

$$\rho\frac{\partial^2 u_z}{\partial t^2} = (\lambda + \mu)\frac{\partial}{\partial z}\left(\frac{\partial u_x}{\partial x} + \frac{\partial u_z}{\partial z}\right) + \mu\left(\frac{\partial^2 u_z}{\partial x^2} + \frac{\partial^2 u_z}{\partial z^2}\right). \tag{2.2.35}$$

We can clearly understand that the displacement of y direction u_y, and the displacement of x and z direction u_x, u_z are completely independent. If we take the z axis as vertical, u_y corresponds to horizontal displacement, and u_x and u_z corresponds to displacements in vertical (x-z) plane. Seismic wave corresponding to the displacement u_y propagates with S-wave velocity β and it is called as SH wave. Waves corresponding to the displacements u_x and u_z are called as P-SV waves.

6) Deriving velocity-stress relationship in a two-dimensional P-SV case.

Now, we derive velocity-stress relationship in a two-dimensional P-SV case for the sake of finite-differential approximation shown later. In a two-dimensional elastic case, the equation (2.2.8) reduces to following two equations.

$$\rho \frac{\partial^2 u_x}{\partial t^2} = \frac{\partial \sigma_{xx}}{\partial x} + \frac{\partial \sigma_{xz}}{\partial z} \tag{2.2.36}$$

$$\rho \frac{\partial^2 u_z}{\partial t^2} = \frac{\partial \sigma_{xz}}{\partial x} + \frac{\partial \sigma_{zz}}{\partial z}$$

And, substituting the equations (2.2.3) and (2.2.5) into (2.2.15) yields the following three equations.

$$\sigma_{xx} = \lambda\theta + 2\mu\varepsilon_{xx} = \lambda\left(\frac{\partial u_x}{\partial x} + \frac{\partial u_z}{\partial z}\right) + 2\mu\frac{\partial u_x}{\partial x} = (\lambda + 2\mu)\frac{\partial u_x}{\partial x} + \lambda\frac{\partial u_z}{\partial z}$$

$$\sigma_{zz} = \lambda\theta + 2\mu\varepsilon_{zz} = \lambda\left(\frac{\partial u_x}{\partial x} + \frac{\partial u_z}{\partial z}\right) + 2\mu\frac{\partial u_z}{\partial z} = (\lambda + 2\mu)\frac{\partial u_z}{\partial z} + \lambda\frac{\partial u_x}{\partial x}. \tag{2.2.37}$$

$$\sigma_{xz} = 2\mu\varepsilon_{xz} = \mu\left(\frac{\partial u_x}{\partial z} + \frac{\partial u_z}{\partial x}\right)$$

The equations (2.2.36) and (2.2.37) can be transformed into the following first order hyperbolic system,

$$\frac{\partial \upsilon_x}{\partial t} = b\left(\frac{\partial \sigma_{xx}}{\partial x} + \frac{\partial \sigma_{xz}}{\partial z}\right)$$

$$\frac{\partial \upsilon_z}{\partial t} = b\left(\frac{\partial \sigma_{xz}}{\partial x} + \frac{\partial \sigma_{zz}}{\partial z}\right)$$

$$\frac{\partial \sigma_{xx}}{\partial t} = (\lambda + 2\mu)\frac{\partial \upsilon_x}{\partial x} + \lambda \frac{\partial \upsilon_z}{\partial z} \quad , \tag{2.2.38}$$

$$\frac{\partial \sigma_{zz}}{\partial t} = (\lambda + 2\mu)\frac{\partial \upsilon_z}{\partial z} + \lambda \frac{\partial \upsilon_x}{\partial x}$$

$$\frac{\partial \sigma_{xz}}{\partial t} = \mu\left(\frac{\partial \upsilon_x}{\partial z} + \frac{\partial \upsilon_z}{\partial x_x}\right)$$

where, $b = 1/\rho$, ρ is a density, υ_x and υ_z are particle velocities, σ_{xx} and σ_{zz} are normal stresses, σ_{xz} is a shear stress, and λ and μ are Lame's constants. This system is a fundamental equations for a velocity-stress staggered grid finite difference method that is widely used in exploration seismology and that our finite-difference method is based on.

2.2.2 Viscoelastic Waves

1) Viscoelastic Formulation Using Standard Linear Solid

In the previous section, I was concerned with an elastic case. The real Earth is, however, not perfectly elastic and propagating waves attenuate with time due to various energy-loss mechanisms. The objective of this study is the application of finite-difference modeling to near surface seismic methods. The effect of attenuation on wave propagation is generally very large in a near surface region. The attenuation should be considered in a study about near surface wave propagation. For this reason, the following discussion of the free surface condition and the variable grid method will be concerned with the viscoelastic case. The anelastic behavior can be described by a viscoelastic model. Blanch et al. (1995) presented efficient viscoelastic modeling based on the Standard Linear Solids (SLS) in which a spring and dashpot in series, in parallel with a spring. In this method, the stress and strain relaxation times can be calculated by the least square method. Robertsson et al. (1994) presented a finite-difference scheme based on the second-order accurate time, fourth-order accurate space, O(2,4), velocity-stress staggered grid (Levander, 1988) for viscoelastic modeling. We employ this method because the additional computer memory requirement is small compared with elastic case.

2)Viscoelastic Modeling Using τ

In this section, we describe a theoretical anelastic model based on viscoelastic theory, a phenomenological way to describe combined elastic and viscous behavior of materials. The basic hypothesis is that the current value of the stress tensor depends on the history of the strain tensor. The viscoelastic hypothesis can be described as

$$\sigma_{ij} = G_{ijkl} * \dot{\varepsilon}_{kl} = \dot{G}_{ijkl} * \varepsilon_{kl}, \tag{2.2.39}$$

(Christensen, 1982) where * denotes time convolution, and dot denotes derivative in time. The convolution transform each strain history, $\varepsilon_{ij}(t)$, into a corresponding stress history, $\sigma_{ij}(t)$. G is a fourth-order tensor-valued function called the relaxation function. The relaxation function G determines the behavior of a material. For one-dimensional or in the special case of a simple shear in an isotropic homogeneous material, the equation (2.2.39) reduces to

$$\sigma = G * \dot{\varepsilon} = \dot{G} * \varepsilon. \tag{2.2.40}$$

The Standard Linear Solid (SLS) has been shown to be a general mechanical viscoelastic model. An array of SLS has the stress relaxation function,

$$G(t) = M_R \left(1 - \sum_{l=1}^{L} \left(1 - \frac{\tau_{\varepsilon l}}{\tau_{\sigma l}} \right) e^{\frac{-t}{\tau_{\sigma l}}} \right) \theta(t) \tag{2.2.41}$$

(Blanch et al., 1993) where, θ (t) is the Heaviside function, M_R is the relaxed stress modulus corresponding to G(t), and $\tau_{\sigma l}$ and $\tau_{\varepsilon l}$ are the stress and strain relaxation times for the lth SLS. M_R is related to the elastic modulus M_U (Liu et al.,1976).

$$M_U = M_R \Big/ \left(1 - \sum_{l=1}^{L} \left(\frac{\tau_{\varepsilon l} - \tau_{\sigma l}}{\tau_{\varepsilon l}} \right) \right). \tag{2.2.42}$$

$M_U = \mu$ for transverse waves, and $M_U = \lambda + 2\mu$ for longitudinal waves (Aki and Richards, 1980). The complex stress modulus $M_C(\omega)$ is defined as the Fourier transform of the stress relaxation function. The quality factor Q is defined as

$$Q(\omega) = \frac{\mathrm{Re}\,(Mc\,(\omega))}{\mathrm{Im}\,(Mc\,(\omega))}, \tag{2.2.43}$$

this equation defines Q as the number of wavelengths a pulse may propagate before its amplitude drops by a factor of $e^{-\pi}$. Thus, Q is a function of frequency. For an array of

Standard Linear Solids, the equation (2.2.3) and (2.2.5) yield,

$$Q(\omega) = \frac{1 - L + \sum_{l=1}^{L} \frac{1 + \omega^2 \tau_{\varepsilon l} \tau_{\sigma l}}{1 + \omega^2 \tau_{\sigma l}^2}}{\sum_{l=1}^{L} \frac{\omega(\tau_{\varepsilon l} - \tau_{\sigma l})}{1 + \omega^2 \tau_{\sigma l}^2}} \quad , \tag{2.2.44}$$

Blanch et al. (1995) proposed the τ-method for the viscoelastic modeling. The τ method is based on the simple observation that the level of attenuation caused by a SLS can be determined by a dimensionless (frequency scale independent) variable τ. If we defined τ as,

$$\tau = \frac{\tau_{\varepsilon l}}{\tau_{\sigma l}} - 1 = \frac{\tau_{\varepsilon l} - \tau_{\sigma l}}{\tau_{\sigma l}}, \tag{2.2.45}$$

the inverse of Q and the velocity c(ω) for one SLS can be written as,

$$Q^{-1} = \frac{\omega \tau_{\varepsilon l} \tau}{1 + \omega^2 \tau_{\sigma l}^2 (1 + \tau)}, \tag{2.2.46}$$

$$(c(\omega))^2 = \frac{M_U}{\rho} \left(1 + \left(\frac{M_U}{M_R} - 1 \right) \frac{1}{1 + \omega^2 \tau_{\varepsilon l}^2} \right)^{-1} . \tag{2.2.47}$$

Using the parameter τ to tune an array of SLSs, and assuming that τ is small (i.e. $1 + \tau \approx 1$), equation (2.2.44) yields

$$Q^{-1} = \sum_{l=1}^{L} \frac{\omega \tau_{\varepsilon l} \tau}{1 + \omega^2 \tau_{\sigma l}^2} . \tag{2.2.48}$$

In this expression Q^{-1} is linear in τ. Therefore, we can easily find the best approximation in the least square sense over a predefined frequency range to any Q_0 by minimizing over τ the expression,

$$J = \int_{\omega_a}^{\omega_b} \left(Q^{-1}(\omega, \tau, \tau_l) - Q_0^{-1} \right)^2 d\omega \ , \tag{2.2.49}$$

to zero and solve for τ. To find the minimum, we set the derivative of J with respect to τ to zero and solve for τ.

$$\frac{dJ}{d\tau} = 2 \int_{\omega_a}^{\omega_b} \left(Q^{-1}(\omega, \tau, \tau_l) - Q_0^{-1} \right) \times \frac{dQ^{-1}(\omega, \tau_{\sigma l}, \tau)}{d\tau} d\omega = 0 . \tag{2.2.50}$$

The final formula for τ is

$$\tau = \frac{1}{Q_0} \cdot \frac{\sum_{l=1}^{L} I_{0l}}{\sum_{l=1}^{L} I_{1l} + 2\sum_{l=1}^{L-1} \sum_{k=l+1}^{L} I_{2kl}} \tag{2.2.51}$$

where,

$$I_{0l} = \frac{1}{2\tau_{\sigma l}} \left[\log \left(1 + \omega^2 \tau_{\sigma l}^2\right) \right]_{\omega_a}^{\omega_b} \tag{2.2.52}$$

$$I_{1l} = \frac{1}{2\tau_{\sigma l}} \left[\arctan \left(\omega \tau_{\sigma l}\right) - \frac{\omega \tau_{\sigma l}}{1 + \omega^2 \tau_{\sigma l}^2} \right]_{\omega_a}^{\omega_b} \tag{2.2.53}$$

$$I_{2lk} = \frac{\tau_{\sigma l} \tau_{\sigma k}}{\tau_{\sigma k}^2 - \tau_{\sigma l}^2} \left[\frac{\arctan \left(\omega \tau_{\sigma l}\right)}{\tau_{\sigma l}} - \frac{\arctan \left(\omega \tau_{\sigma k}\right)}{\tau_{\sigma k}} \right]_{\omega_a}^{\omega_b} \tag{2.2.54}$$

$$\tau_{\sigma l} = \frac{1}{\omega_l}, \tag{2.2.55}$$

where, ω_l is the frequency of interest.

2.3 Surface-wave Propagating with 1D Layered Medium

2.3.1 SH wave and Love wave propagating with 1D layered medium

1) SH wave

Wave equation for SH waves in two-dimensional medium can be written as follows (from equation (2.1.34)).

$$\frac{1}{\beta^2}\frac{\partial^2 u}{\partial t^2} = \frac{\partial^2 u}{\partial x^2} + \frac{\partial^2 u}{\partial z^2} \tag{2.3.1}$$

where, u is y component of displacement, β is S-wave velocity.
We assume that the solution for equation (2.3.1) is

$$u = e^{-i\omega(t-px-\eta z)}. \tag{2.3.2}$$

$$p = \frac{\sin\varphi}{\beta}, \quad \eta = \frac{\cos\varphi}{\beta} \tag{2.3.3}$$

where, φ is angle of wave propagation. Substituting the equation (2.3.2) to (2.3.1) yields,

$$\eta^2 = \frac{1}{\beta^2} - p^2. \tag{2.3.4}$$

2) Love wave propagating with two-layer medium

In two layers model shown in Figure 2.3.1, a general solution in top layer is written as,

$$u_1(z) = \cos\omega\eta_1(z-H) \qquad 0 < z < H \tag{2.3.5}$$

$$\eta_1 = \sqrt{\frac{1}{\beta^2} - p^2}, \qquad p = \frac{1}{c}$$

where, c is phase-velocity in x direction and common term $exp(-i\omega(t-px))$ is neglected. Above solution satisfy free surface-condition and amplitude at the surface is assumed to be 1.

A general solution in bottom layer is,

$$u_2(z) = A_2 e^{\omega\hat{\eta}_2 z} + B_2 e^{-\omega\hat{\eta}_2 z} \tag{2.3.6}$$

Generally, imaginary part of η^2 is chosen positive in SH wave propagation so that reflection or refraction wave can not be diverged. If we use the condition,

$$\mathrm{Im}(\eta^2) > 0 \qquad (\omega>0) \tag{2.3.7}$$

first term of equation (2.3.6) diverges and second term goes to zero when z goes to negative infinite. Therefore, we can write Love wave solution in bottom layer as,

$$u_2(z) = B_2 e^{-\omega\hat{\eta}_2 z} = B_2 e^{\omega\hat{\eta}_2 z} \quad . \tag{2.3.8}$$

$$\hat{\eta}_2 = \sqrt{p^2 - \frac{1}{\beta_2^{\,2}}}$$

where, B_2 is a constant. A boundary condition between top and bottom layer is,

$$u_1 = u_2, \quad \mu_1 \frac{\partial u_1}{\partial z} = \mu_2 \frac{\partial u_2}{\partial z}, \quad z=0. \tag{2.3.9}$$
$$\mu_1 = \rho_1\beta_1^2, \quad \mu_2 = \rho_2\beta_2^2$$

where, μ_1 and μ_2 are share modulus of each layer. The equation (2.3.9) means displacement and shear stress must be continuous at the boundary. The equations (2.3.5), (2.3.8) and (2.3.9) yield,

$$\cos\omega\eta_1 H = B_2, \quad \omega\mu_1\eta_1 \sin\omega\eta_1 H = \omega\mu_2\hat{\eta}_2 B_2 . \tag{2.3.10}$$

In order to remove B2, we substitute first equation to second one.

$$F_L(c,\omega) = \omega\mu_2\hat{\eta}_2 B_2 \cos\omega\eta_1 H - \omega\mu_1\eta_1 \sin\omega\eta_1 H = 0 \tag{2.3.11}$$

Or, we can write as,

$$\tan\omega\eta_1 H = \frac{\mu_2\hat{\eta}_2}{\mu_1\eta_1} \tag{2.3.12}$$

The equations (2.3.11) and (2.3.12) are characteristic equations for the Love wave. In

order to calculate a dispersion curve, we generally fix angular frequency ω and search phase-velocity c that makes characteristic equation (2.3.11) as zero. Figure 2.3.3 shows the example of dispersion curve for a two layer model shown in Figure 2.3.2. The Love wave propagating with more than 3 layers is described in the Appendix A.

2.3.2 P-SV wave and Rayleigh wave propagating with 1D layered medium

1)General solution

Wave equation for P-SV waves in two-dimensional medium can be written as follows (from equations (2.2.33) and (2.2.35)).

$$\rho\frac{\partial^2 u}{\partial t^2}=(\lambda+\mu)\frac{\partial}{\partial x}\left(\frac{\partial u}{\partial x}+\frac{\partial w}{\partial z}\right)+\mu\left(\frac{\partial^2 u}{\partial x^2}+\frac{\partial^2 u}{\partial z^2}\right)$$

$$\rho\frac{\partial^2 w}{\partial t^2}=(\lambda+\mu)\frac{\partial}{\partial z}\left(\frac{\partial u}{\partial x}+\frac{\partial w}{\partial z}\right)+\mu\left(\frac{\partial^2 w}{\partial x^2}+\frac{\partial^2 w}{\partial z^2}\right) \tag{2.3.13}$$

where, u and w are x and z component of displacement respectively.

We assume that the solutions for equation (2.3.13) are

$$u=\varepsilon e^{-i\omega(t-px-\gamma z)}.$$

$$w=e^{-i\omega(t-px-\gamma z)}. \tag{2.3.14}$$

Substituting the equation (2.3.14) and (2.3.13) yields,

$$\begin{aligned}\rho\varepsilon&=\left[(\lambda+2\mu)p^2+\mu\gamma^2\right]\varepsilon+(\lambda+\mu)p\gamma\\ \rho&=(\lambda+\mu)p\gamma\varepsilon+\mu p^2+(\lambda+2\mu)\gamma^2.\end{aligned} \tag{2.3.15}$$

Therefore, following relationship must be existed.

$$\varepsilon=\frac{(\lambda+\mu)p\gamma}{\rho-(\lambda+2\mu)p^2-\mu\gamma^2}=\frac{\rho-\mu p^2-(\lambda+2\mu)\gamma^2}{(\lambda+\mu)p\gamma} \tag{2.3.16}$$

The equation (2.3.16) can be written as,

$$\left[(\lambda+2\mu)(\gamma^2+p^2)-\rho\right]\left[\mu(\gamma^2+p^2)-\rho\right]=0\,. \tag{2.3.17}$$

Therefore, γ is given by,

$$\gamma^2=\frac{1}{\alpha^2}-p^2,\quad \gamma^2=\frac{1}{\beta^2}-p^2\,. \tag{2.3.18}$$

2) P-wave

A solution for the root of first term of the equation (2.3.18),

$$\gamma=\pm\sqrt{\frac{1}{\alpha^2}-p^2}=\pm\xi$$

$$\varepsilon=\pm\frac{p}{\xi} \tag{2.3.19}$$

is wave propagating with P-wave velocity α.

$$\alpha=\sqrt{\frac{\lambda+2\mu}{\rho}} \tag{2.3.20}$$

Displacement can be calculated using the equation (2.3.14) as follows.

$$u=\pm\frac{p}{\xi}e^{-i\omega(t-px\mp\xi z)}$$

$$w=e^{-i\omega(t-px\mp\xi z)}\,. \tag{2.3.21}$$

General solution for these roots are written using constants A and B,

$$u=p\left(Ae^{i\omega\xi}-Be^{-i\omega\xi}\right)e^{-i\omega(t-px)}$$
$$w=\xi\left(Ae^{i\omega\xi}+Be^{-i\omega\xi}\right)e^{-i\omega(t-px)}\,. \tag{2.3.22}$$

3) SV-wave

A solution for the root of second term of the equation (2.3.18),

$$\gamma=\pm\sqrt{\frac{1}{\beta^2}-p^2}=\pm\eta$$

$$\varepsilon = \mp \frac{\eta}{p} \tag{2.3.23}$$

is wave propagating with S-wave velocity β.

$$\beta = \sqrt{\frac{\mu}{\rho}} \tag{2.3.24}$$

General solution for these roots are written using constants C and D,

$$u = \eta\left(-Ce^{i\omega\eta z} + De^{-i\omega\eta z}\right)e^{-i\omega(t-px)}$$
$$w = p\left(Ce^{i\omega\eta z} + De^{-i\omega\eta z}\right)e^{-i\omega(t-px)}. \tag{2.3.25}$$

P-SV wave propagation can be expressed as the summation of the equation (2.3.22) and (2.3.25).

$$u(z) = p\left(Ae^{i\omega\xi z} - Be^{-i\omega\xi z}\right) + \eta\left(Ce^{i\omega\eta z} - De^{-i\omega\eta z}\right)$$
$$w(z) = \xi\left(Ae^{i\omega\xi z} + Be^{-i\omega\xi z}\right) + p\left(Ce^{i\omega\eta z} + De^{-i\omega\eta z}\right) \tag{2.3.26}$$

where, common term *exp(-iω(t-px))* is neglected. Substituting equations (2.3.26) into equations (2.2.37) yields following equations for stresses.

$$\sigma_{xz}(z) = 2i\omega\mu p\xi\left(Ae^{i\omega\xi z} - Be^{-i\omega\xi z}\right) - i\omega\mu\left(\eta^2 - p^2\right)\left(Ce^{i\omega\eta z} - De^{-i\omega\eta z}\right)$$
$$\sigma_{zz}(z) = i\omega\mu\left(\eta^2 - p^2\right)\left(Ae^{i\omega\xi z} - Be^{-i\omega\xi z}\right) + 2i\omega\mu p\eta\left(Ce^{i\omega\eta z} - De^{-i\omega\eta z}\right) \tag{2.3.27}$$

4) Rayleigh wave propagating with homogeneous half space

Rayleigh wave is a surface-wave propagating along the surface and its amplitude is decreasing exponentially with depth. There is a homogeneous half space z < 0. From the solution of P-SV wave (equation (2.3.26)), ξ and η must be imaginary so that the amplitude is 0 when z is infinity. We define,

$$\xi = i\hat{\xi},\ \ \hat{\xi} = \sqrt{p^2 - \frac{1}{\alpha^2}} > 0,\ \ \eta = i\hat{\eta},\ \ \hat{\eta} = \sqrt{p^2 - \frac{1}{\beta^2}} > 0 \tag{2.3.28}$$

The first and third terms of the equation (2.3.26) must be 0. Therefore, general solution

for x and z component of displacement are;

$$u(z) = ipBe^{\omega\hat{\xi}z} + i\hat{\eta}De^{\omega\hat{\eta}z}$$

$$w(z) = \hat{\xi}Be^{\omega\hat{\xi}z} + pDe^{\omega\hat{\eta}z} \quad . \tag{2.3.29}$$

Using the equation (2.3.27), stresses can be calculated as follows.

$$\sigma_{zx}(z) = 2i\omega\rho\beta^2 p\hat{\xi}Be^{\omega\hat{\xi}z} - i\omega\rho(1-\gamma)De^{\omega\hat{\eta}z}$$

$$\sigma_{zz}(z) = -\omega\rho(1-\gamma)Be^{\omega\hat{\xi}z} + 2\omega\rho\beta^2 p\hat{\eta}De^{\omega\hat{\eta}z}$$

$$\gamma = 2\beta^2 p^2 \tag{2.3.30}$$

At the surface ($z=0$), share stress (σ_{zx}) and normal stress (σ_{zz}) must be 0. Therefore, the equation (2.3.30) yields;

$$\begin{aligned} &2\beta^2 p\hat{\xi}B - (1-\gamma)D = 0 \\ &-(1-\gamma)B + 2\beta^2 p\hat{\eta}D = 0\,. \end{aligned} \tag{2.3.31}$$

The equation (2.3.31) can be expressed as a matrix form;

$$\begin{bmatrix} 2\beta^2 p\hat{\xi} & -(1-\gamma) \\ -(1-\gamma) & 2\beta^2 p\hat{\eta} \end{bmatrix} \begin{bmatrix} B \\ D \end{bmatrix} = 0 \tag{2.3.32}$$

In order to solve the equation, determinant must be 0.

$$F_R(p) = (1-\gamma)^2 - 2\beta^2\gamma\hat{\xi}\hat{\eta} = 0 \tag{2.3.33}$$

The equation (2.3.33) is called a characteristic equation for the Rayleigh wave in homogeneous half space. Figure 2.3.4 shows the example of calculation of characteristic equation for the Rayleigh wave. We can see that the Rayleigh waves propagate with phase-velocity that is about 90 to 95% of S-wave velocity.

5) Boundary condition of P-SV wave between two layers

Before solving two-layer problem, we are going to review boundary condition of P-SV wave between two layers. Let us think about a plane wave propagating from layer two to layer one. There are 6 constants (A_1 to D_1 and B_1, D_1)as shown in Figure 2.3.4. Snell's low can be written as,

$$p = \frac{\sin\theta_1}{\alpha_1} = \frac{\sin\varphi_1}{\beta_1} = \frac{\sin\theta_2}{\alpha_2} = \frac{\sin\varphi_2}{\alpha_2}. \tag{2.3.34}$$

At the boundary $z=0$, two displacements ($u(0)$, $w(0)$) and two stresses ($\sigma_{zx}(0)$, $\sigma_{zz}(0)$) must be continuous. Such condition can be derived using equations (2.3.26) and (2.3.27),

$$\begin{aligned}
&p(A_1 - B_1) + \eta_1(-C_1 + D_1) = pA_2 - \eta_2 C_2 \\
&\xi(A_1 + B_1) + p(-C_1 + D_1) = \xi_2 A_2 + pC_2 \\
&2\mu_1 p\xi_1(A_1 + B_1) - \rho_1(1-\gamma_1)(C_1 + D_1) = 2\mu_2 p\xi_2 A_2 - \rho_2(1-\gamma_2)C_2 \\
&\rho_1(1-\gamma_1)(A_1 - B_1) + 2\mu_1 p\eta_1(C_1 - D_1) = \rho_2(1-\gamma_2)A_2 + 2\mu_2 p\eta_2 C_2
\end{aligned} \tag{2.3.35}$$

where,

$$\xi_i^2 = \frac{1}{\alpha_i^2},\quad \eta_i^2 = \frac{1}{\beta_i^2} - p^2,\quad \gamma_i = 2\beta_i^2 p^2 \qquad i=1,2 \qquad . \tag{2.3.36}$$

Following relationship is used to derive equation (2.3.35).

$$\mu_i(\eta_i^2 - p^2) = \rho_i(1-\gamma_i) \tag{2.3.37}$$

In the equation (2.3.35), first and second equations are continuous condition for displacements and third and fourth equations are continuous condition for stresses. Equation (2.3.35) can be written as follows using $A_1 \pm B_1$ and $C_1 \pm D_1$.

$$\begin{aligned}
&\rho_1(A_1 - B_1) = aA_2 + 2(\mu_2 - \mu_1)p\eta_2 C_2 \\
&\rho_1\eta_1(C_1 - D_1) = pdA_2 + b\eta_2 C_2 \\
&\rho_1\xi_1(A_1 + B_1) = \xi_2 bA_2 - pdC_2 \\
&\rho_1(C_1 + D_1) = -2(\mu_2 - \mu_1)p\xi_2 A_2 + aC_2
\end{aligned} \tag{2.3.38}$$

where,

$$
\begin{aligned}
a &= \rho_1\gamma_1 + \rho_2(1-\gamma_2) = \rho_2 - 2(\mu_2 - \mu_1)p^2 \\
b &= \rho_2\gamma_2 + \rho_1(1-\gamma_1) = \rho_2 + 2(\mu_2 - \mu_1)p^2 \\
d &= \rho_2(1-\gamma_2) - \rho_1(1-\gamma_1) = \rho_2 - \rho_1 - 2(\mu_2 - \mu_1)p^2
\end{aligned} \tag{2.3.39}
$$

6) Rayleigh wave propagating with two-layer medium

Let us tale z axis with downward as shown in Figure 2.3.5. At the boundary $z=0$, two displacements and two stresses must be continuous as equations (2.3.35) and (2.3.38). At free surface ($z=-H$), stresses must be zero. This condition can be written as follows using equations 2.3.27.

$$
\begin{aligned}
&2\mu_1 p\xi_1\left(A_1 e^{-i\omega\xi_1 H} + B_1 e^{i\omega\xi_1 H}\right) - \rho_1(1-\gamma_1)\left(C_1 e^{-i\omega\eta_1 H} + D_1 e^{i\omega\eta_1 H}\right) = 0 \\
&\rho_1(1-\gamma_1)\left(A_1 e^{-i\omega\xi_1 H} - B_1 e^{i\omega\xi_1 H}\right) - 2\mu_1 p\eta_1\left(C_1 e^{-i\omega\eta_1 H} - D_1 e^{i\omega\eta_1 H}\right) = 0
\end{aligned} \tag{2.3.40}
$$

Using trigonometric functions, equations (2.3.40) can be written as,

$$
\begin{aligned}
&2\mu_1 p\xi_1\left[(A_1 + B_1)\cos\omega\xi_1 H - i(A_1 - B_1)\sin\omega\xi_1 H\right] \\
&\qquad - \rho_1(1-\gamma_1)\left[(C_1 + D_1)\cos\omega\eta_1 H - i(C_1 - D_1)\sin\omega\eta_1 H\right] = 0 \\
&\rho_1(1-\gamma_1)\left[(A_1 - B_1)\cos\omega\xi_1 H - i(A_1 + B_1)\sin\omega\xi_1 H\right] \\
&\qquad + 2\mu_1 p\eta_1\left[(C_1 - D_1)\cos\omega\eta_1 H - i(C_1 + D_1)\sin\omega\eta_1 H\right] = 0 .
\end{aligned} \tag{2.3.41}
$$

Number of unknown constants are six (A_1 to D_1 and A_2, D_2) and number of equations are six (equations (2.3.38) and (2.3.41)). Amplitude of Rayleigh waves must be zero as z goes to infinite. This condition leads following relationship,

$$
\xi_2 = i\hat{\xi}_2, \quad \hat{\xi}_2 = \sqrt{p^2 - \frac{1}{\alpha_2^2}} > 0, \quad \eta_2 = i\eta_2, \quad \hat{\eta}_2 = \sqrt{p^2 - \frac{1}{\beta_2^2}} > 0 \tag{2.3.42}
$$

Substituting equations (2.3.38) into A_1+B_1 or A_1-B_1 etc. in equations (2.3.41) and using equations (2.3.42) yield equations that contain only A_2 and C_2 as unknown constants.

$$\begin{aligned}
&(X_1 + Y_1)pA_2 + (X_2 + Y_2)iC_2 = 0 \\
&(X_3 + Y_3)pA_2 + (X_4 + Y_4)iC_2 = 0
\end{aligned} \tag{2.3.43}$$

where,

$$\begin{aligned}
X_1 &= 2\beta_1^2\left(b\hat{\xi}C_\alpha - a\xi_1^2 S_\alpha\right) & Y_1 &= (1-\gamma_1)p^2\left[dS_\beta - 2(\mu_2-\mu_1)\hat{\xi}_2 C\beta\right] \\
X_2 &= \gamma_1\left[dC_\alpha - 2(\mu_2-\mu_1)\xi_1^2\hat{\eta}_2 S_\alpha\right] & Y_2 &= (1-\gamma_1)\left(aC_\beta - b\hat{\eta}_2 S_\beta\right) \\
X_3 &= (1-\gamma_1)\left(aC_\alpha - b\hat{\xi}_2 S_\alpha\right) & Y_3 &= \gamma_1\left[dC_\beta - 2(\mu_2-\mu_1)\hat{\xi}_2\eta_1^2 S_\beta\right] \\
X_4 &= (1-\gamma_1)p^2\left[dS_\alpha - 2(\mu_2-\mu_1)\hat{\eta}_2 C_\alpha\right] & Y_4 &= \gamma_1\left(b\hat{\eta}_2 C_\beta - a\eta_1^2 S_\beta\right)
\end{aligned} \tag{2.3.44}$$

where,

$$C_\alpha = \cos\omega\xi_1 H\,,\quad S_\alpha = \frac{\sin\omega\xi_1 H}{\xi_1}\,,\quad C_\beta = \cos\omega\eta_1 H\,,\quad S_\beta = \frac{\sin\omega\eta_1 H}{\eta_1}$$

$$\begin{aligned}
a &= \rho_1\gamma_1 + \rho_2(1-\gamma_2) = \rho_2 - 2(\mu_2-\mu_1)p^2 \\
b &= \rho_2\gamma_1 + \rho_1(1-\gamma_1) = \rho_1 + 2(\mu_2-\mu_1)p^2 \\
d &= \rho_2(1-\gamma_2) - \rho_1(1-\gamma_1) = \rho_2 - \rho_1 - 2(\mu_2-\mu_1)p^2
\end{aligned} \tag{2.3.45}$$

Characteristic equation of Rayleigh waves can be written,

$$F_R(p,\omega) = (X_1 + Y_1)(X_4 + Y_4) - (X_2 + Y_2)(X_3 + Y_3) = 0\,. \tag{2.3.46}$$

The Rayleigh wave propagating with more than 3 layers is described in the Appendix B.

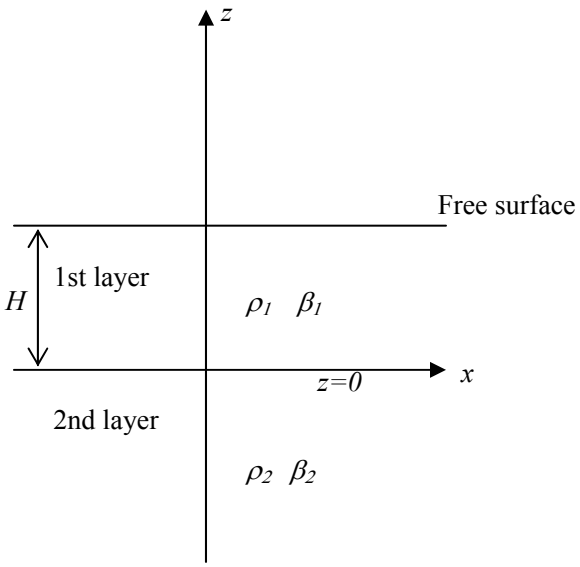

Figure 2.3.1 Two layer model for Love waves. ρ and β are density and S-wave velocity respectively.

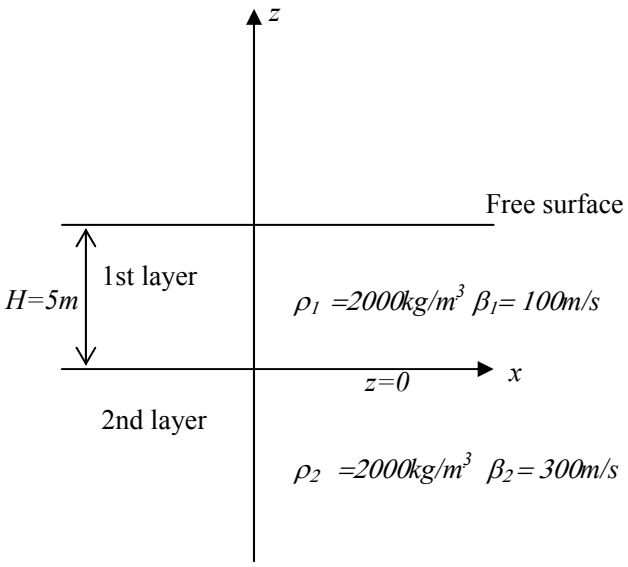

Figure 2.3.2 Example of two layer model for Love waves. ρ and β are density and S-wave velocity respectively.

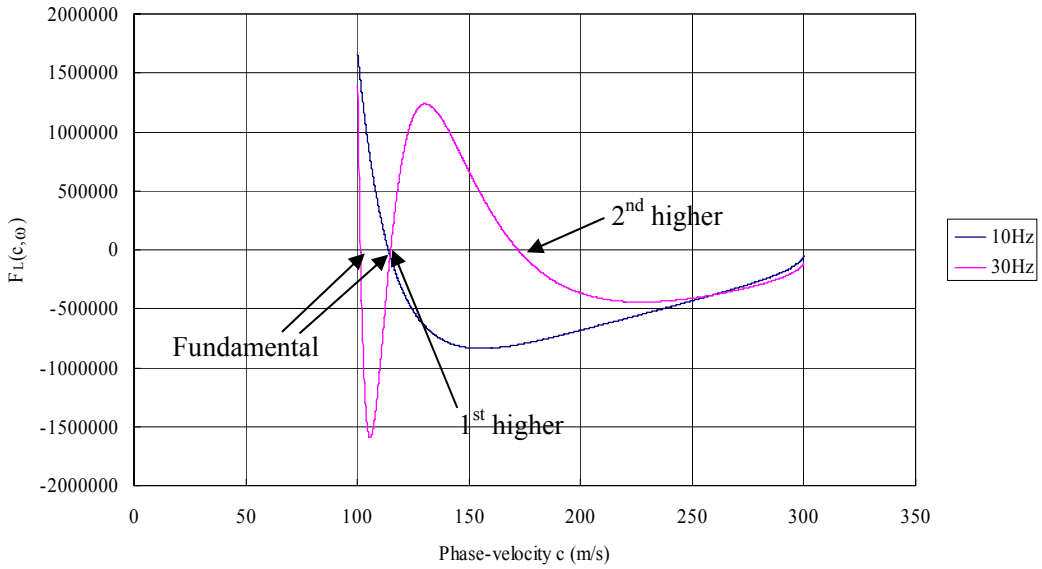

1) Example of calculation of characteristic equation.

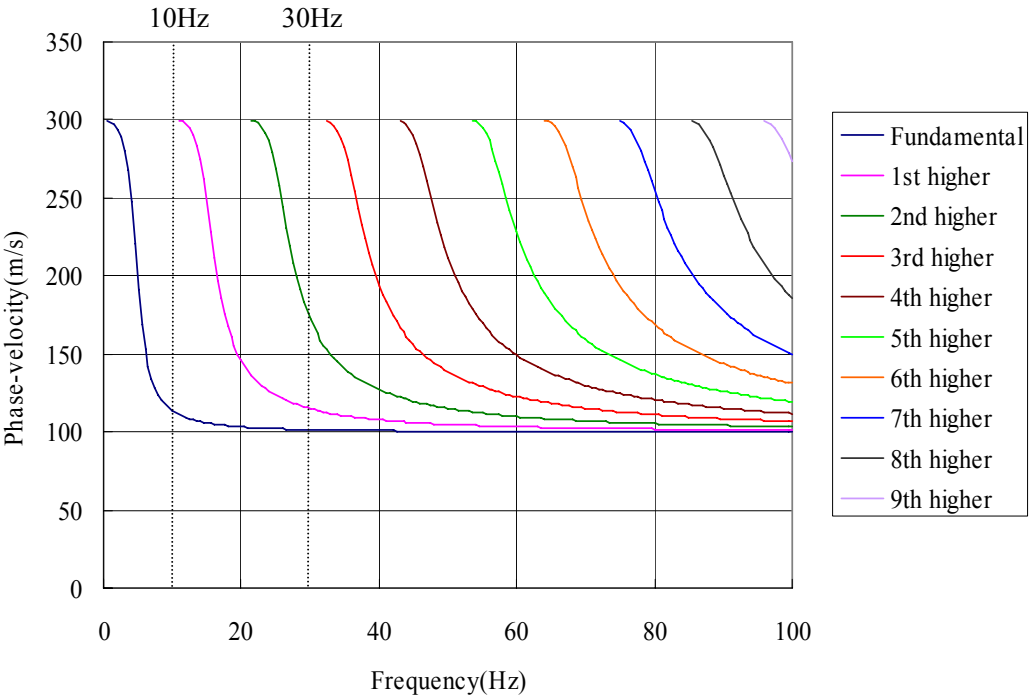

2) Example of dispersion curve.

Figure 2.3.3 example of dispersion curve for a two layer model shown in Figure 2.3.2.

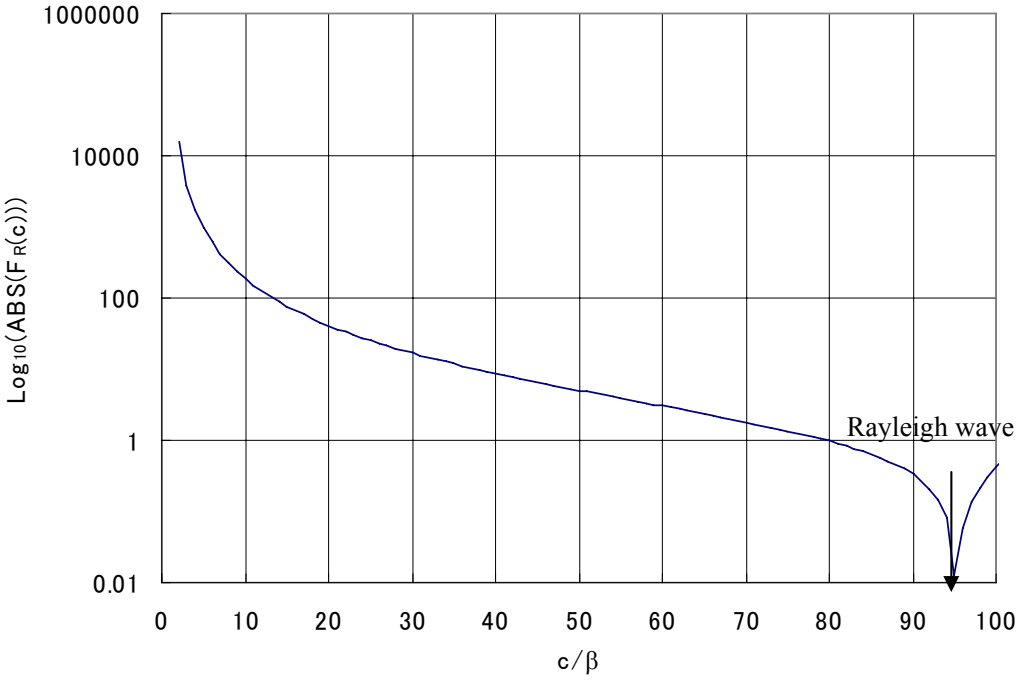

1) Example of calculation of characteristic equation for Rayleigh waves (α=1000m/s, β=500m/s, ρ=1895kg/m^3).

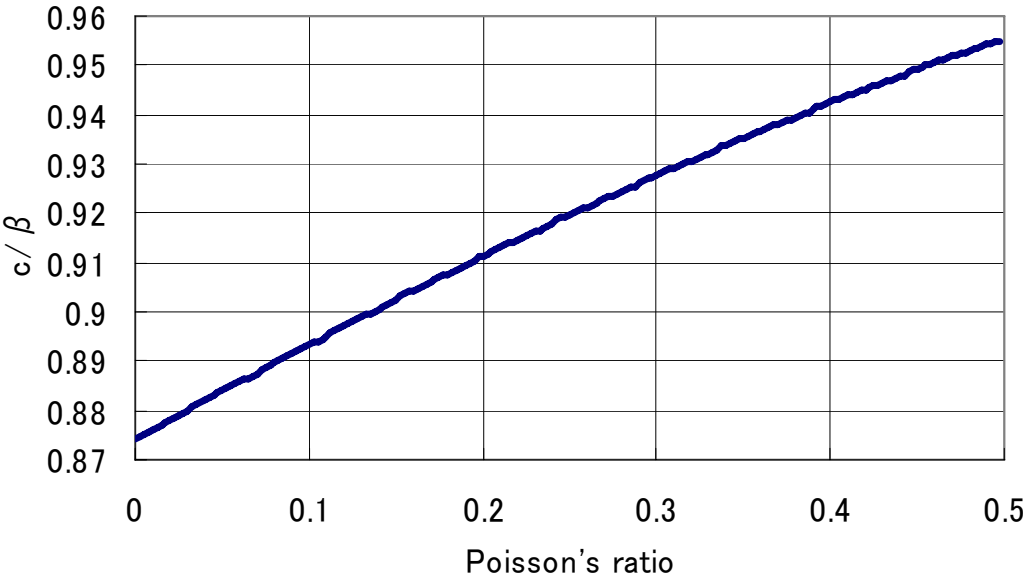

2) Change of Rayleigh wave phase-velocity against Poisson's ratio.

Figure 2.3.4 Example of calculation of Rayleigh wave phase-velocity.

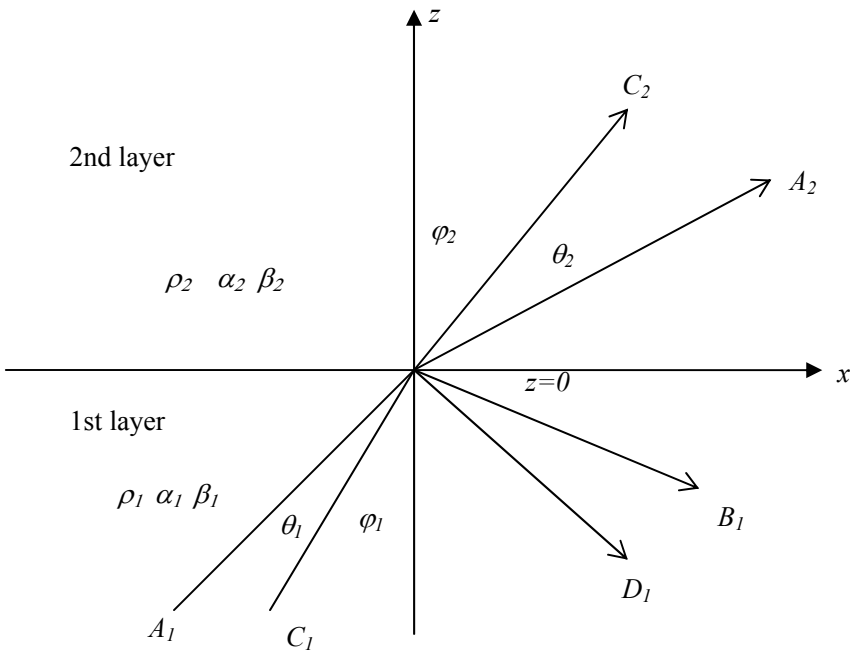

Figure 2.3.5 Boundary condition of P-SV wave between two layers.

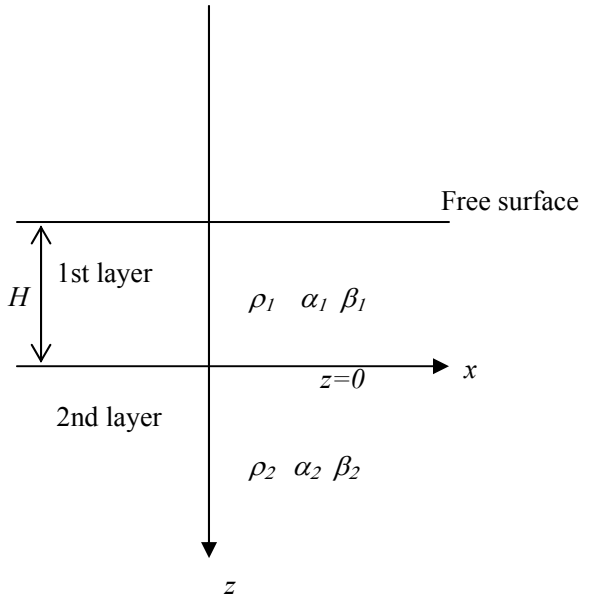

Figure 2.3.6 Two layer model for Rayleigh waves. ρ, α and β are density, P-wave velocity and S-wave velocity respectively..

2.4 Numerical Simulation of Elastic Waves Using Finite-difference Method

2.4.1 Introduction

Finite-difference seismic modeling methods are widely used in various fields, such as seismic exploration and simulation of natural earthquakes. The simulation of wave propagation in seismic exploration is useful for developing new seismic methods in petroleum, engineering, and environmental problems. The strong ground motion simulation of earthquakes is important for predicting earthquake disaster. Realistic seismic modeling for such problems requires several important issues. The inclusion of viscoelastic attenuation and the handling of large velocity contrast are two factors that are particularly important in modeling.

The real earth is not perfectly elastic, and propagating waves attenuate with time due to various energy-loss. The effect of attenuation on wave propagation is generally very large in near surface, and therefore should be considered in the studies of near surface wave propagation. Anelastic attenuation can be described using a viscoelastic model. Numerical modeling of linear viscoelastic seismic responses in the time domain has recently become practical through algorithms based on the superposition of relaxation mechanisms. The standard linear solid (SLS) is a simple viscoelastic model consisting of a spring in parallel with a dashpot in series (Pipkin, 1986). Day and Minster (1984) described a method to connect several SLSs in parallel to yield an excellent approximation to a constant Q in a predefined frequency band, and proposed memory variables to eliminate the convolution terms of viscoelastic equations. Similar approaches were given in Emmerich and Korn (1987) and in Carcione (1993). Day (1998) introduced a method in which the memory variables are coarse grained in order to reduce computational storage requirements. Blanch et al. (1995) showed that several SLSs connected in parallel could be tuned through a single parameter to yield a constant Q approximation. Robertsson et al. (1994), and Xu and McMechan (1998) presented 3-D viscoelastic finite-difference method based on the staggered-grid scheme.

These algorithms enable us to calculate attenuation efficiently.

The velocity contrast is generally very large problem for both seismic exploration and strong ground motion. In the simulation of seismic exploration, minimum S-wave velocity can be 100m/sec and maximum S-wave velocity can be 3000m/sec. In the strong ground motion simulation, minimum S-wave velocity can be 500m/sec and maximum S-wave velocity can be 4500m/sec. A uniformly spaced grid adopted to model such large velocity contrast requires large portions of the model to be over-sampled. The resulting memory requirements would severely limit the size of the models. An efficient solution to this problem is to use a finer grid spacing in the vicinity of the low-velocity near surface compared to the deeper parts of the model. The method is called a multi-grid, variable grid, discontinuous or nonuniform grid method. The nonuniform grid approach allows us to vary the discretization of the model and the wavefield as required by the velocity structure.

Compared to a standard uniform finite-difference grid approach, this method saves a considerable amount of memory and computations. Therefore, we use the nonuniform grid method for the calculation of large velocity contrast. Several seismological studies describing the nonuniform grid approach have been reported (Moczo, 1989; Jastram and Behle, 1992; Jastram and Tessmer, 1994; Moczo et al.,1996). De Lilla (1997) proposed a variable grid finite-difference method that can handle any integer number for a grid spacing ratio. Pitarka (1999) applied a nonuniform grid spacing to seismic wave simulations using a 3-D elastic velocity-stress finite-difference method. Aoi and Fujiwara (1999) applied a discontinuous grid method to 3-D finite-difference modeling. Robertsson and Holliger (1997) and Hayashi et al, (2001) applied the discontinuous grid method to rough topography. We have introduced the nonuniform grid spacing proposed by Pitarka (1999) in which grid spacing of depth direction is varied with respect to velocity model.

For further reduction of computation time and memory requirement, we have also introduced parallel computing using PC-cluster. Recently, parallel computers are commonly used in the analysis of 3D reflection method. Linux and Windows enable us to built huge PC-cluster inexpensively.

In this section, we will show the finite-difference implementation of viscoelastic wave equation at first. Then, we show some fundamental benchmark tests

to demonstrate the accuracy and the reliability of a finite-difference code that we developed.

2.4.2 Two-dimensional Finite-difference modeling

Robertsson et al. (1994) proposed the viscoelastic finite-difference modeling based on the τ method described in the previous chapter. For simplicity, we will derive the equations for a one-dimensional case, where the viscoelastic equations are the same as the viscoacoustic. From the definition of pressure and dilatation,

$$\sigma = -p \quad , \tag{2.4.1}$$

and

$$-\dot{\varepsilon} = \upsilon_x \, , \tag{2.4.2}$$

where v is the particle velocity, and subscript x means spatial derivative. Taking the time derivative of equation (2.2.40) and using equations (2.4.1) and (2.4.2) leads to,

$$-\dot{p} = \dot{G} * \upsilon_x \, . \tag{2.4.3}$$

Substituting equation (2.2.41) into (2.4.3) yields,

$$-\dot{p} = M_R\left(1 - \sum_{l=1}^{L}\left(1 - \frac{\tau_{\varepsilon l}}{\tau_{\sigma l}}\right)\right)\upsilon_x + M_R\left(\sum_{l=1}^{L}\frac{1}{\tau_{\sigma l}}\left(1 - \frac{\tau_{\varepsilon l}}{\tau_{\sigma l}}\right)e^{\frac{-t}{\tau_{\sigma l}}}\right)\theta(t) * \upsilon_x \, . \tag{2.4.4}$$

The convolution terms in the equation (2.4.4) can be eliminated by introducing so-called memory variables, which will be denoted r_l (Carcione et al., 1988). Then, equation (2.4.4) reduces to,

$$-\dot{p} = M_R\left(1 - \sum_{l=1}^{L}\left(1 - \frac{\tau_{\varepsilon l}}{\tau_{\sigma l}}\right)\right)\upsilon_x + \sum_{l=1}^{L} r_l \, , \tag{2.4.5}$$

where

$$r_l = M_R\left(\frac{1}{\tau_{\sigma l}}\left(1 - \frac{\tau_{\varepsilon l}}{\tau_{\sigma l}}\right)e^{\frac{-t}{\tau_{\sigma l}}}\right)\theta(t) * \upsilon_x \, . \qquad 1 \le l \le L \, . \tag{2.4.6}$$

From the equation (2.4.6), we see that r_l is governed by convolutions of v_x with exponential functions. A set of first-order linear differential equations can be obtained instead of the convolution as follows. First, by taking the time derivative of equation

(2.4.6), we obtain,

$$\dot{r}_l = -\frac{1}{\tau_{\sigma l}} M_R \left(\frac{1}{\tau_{\sigma l}} \left(1 - \frac{\tau_{\varepsilon l}}{\tau_{\sigma l}} \right) e^{\frac{-t}{\tau_{\sigma l}}} \right) \theta(t) * \upsilon_x + M_R \left(\frac{1}{\tau_{\sigma l}} \left(1 - \frac{\tau_{\varepsilon l}}{\tau_{\sigma l}} \right) e^{\frac{-t}{\tau_{\sigma l}}} \right) \delta(t) * \upsilon_x \cdot$$

$$1 \le l \le L \tag{2.4.7}$$

From equation (2.4.6) we notice that equation (2.4.7) reduces to

$$\dot{r}_l = -\frac{1}{\tau_{\sigma l}} r_l + M_R \left(\frac{1}{\tau_{\sigma l}} \left(1 - \frac{\tau_{\varepsilon l}}{\tau_{\sigma l}} \right) e^{\frac{-t}{\tau_{\sigma l}}} \right) \upsilon_x , \quad 1 \le l \le L . \tag{2.4.8}$$

We have derived a set of first-order linear differential equations for the memory variables. Newton's second law completes the full description of wave propagation in a viscoelastic medium. That is,

$$\rho \dot{\upsilon} = -p_x , \tag{2.4.9}$$

where ρ is the density. From equations (2.4.5), (2.4.8) and (2.4.9), we can derive staggered grid finite-difference equations (second-order accurate in time, fourth-order accurate in space) as follows,

$$p_j^{n+1/2} = p_j^{n-1/2} - M_R \frac{\tau_{\varepsilon l}}{\tau_{\sigma l}} \frac{\Delta t}{\Delta h} \left(c_1 \left(\upsilon_{j+3/2}^n - \upsilon_{j-3/2}^n \right) + c_2 \left(\upsilon_{j+1/2}^n - \upsilon_{j-1/2}^n \right) \right)$$

$$- \frac{\Delta t}{2} \left(r_j^{n+1/2} + r_j^{n-1/2} \right) \tag{2.4.10}$$

$$r_j^{n+1/2} = \frac{1}{1 + \frac{\Delta t}{2\tau_{\sigma l}}} \left(r_j^{n-1/2} \left(1 - \frac{\Delta t}{2\tau_{\sigma l}} \right) - M_R \frac{1}{\tau_{\sigma l}} \left(\frac{\tau_{\varepsilon l}}{\tau_{\sigma l}} - 1 \right) \right.$$

$$\left. \times \frac{\Delta t}{\Delta h} \left(c_1 \left(\upsilon_{j+3/2}^n - \upsilon_{j-3/2}^n \right) + c_2 \left(\upsilon_{j+1/2}^n - \upsilon_{j-1/2}^n \right) \right) \right) \tag{2.4.11}$$

$$\upsilon_j^{n+1/2} = \upsilon_j^{n-1/2} - \frac{\Delta t}{\Delta h \rho} \left(c_1 \left(p_{j+3/2}^n - p_{j-3/2}^n \right) + c_2 \left(p_{j+1/2}^n - p_{j-1/2}^n \right) \right) \tag{2.4.12}$$

$$c_1 = -\frac{1}{24} 、 \quad c_2 = \frac{9}{8} \tag{2.4.13}$$

where Δt is the time step and Δh is the spatial step. Indices n and j correspond to time and space coordinates respectively ($p_j^n = p(n\Delta t, j\Delta h)$). In the equation (2.4.11), Crank-Nicolson scheme (Strang, 1986) is employed to ensure a stable solution. Figure

2.4.1 shows the one-dimensional staggered finite-difference grid.

The results from the one-dimensional case described above are easily generalized to higher dimensions. In two-dimensional viscoelastic staggered grid finite-difference modeling, the following three sets of equations are solved.

Equations governing stress:

$$\frac{\partial \sigma_{xx}}{\partial t} = \pi \frac{\tau_{\varepsilon}^{p}}{\tau_{\sigma}}\left(\frac{\partial \upsilon_x}{\partial x} + \frac{\partial \upsilon_z}{\partial z}\right) - 2\mu \frac{\tau_{\varepsilon}^{s}}{\tau_{\sigma}}\frac{\partial \upsilon_z}{\partial z} + r_{xx} \tag{2.4.14}$$

$$\frac{\partial \sigma_{zz}}{\partial t} = \pi \frac{\tau_{\varepsilon}^{p}}{\tau_{\sigma}}\left(\frac{\partial \upsilon_x}{\partial x} + \frac{\partial \upsilon_z}{\partial z}\right) - 2\mu \frac{\tau_{\varepsilon}^{s}}{\tau_{\sigma}}\frac{\partial \upsilon_x}{\partial x} + r_{zz} \tag{2.4.15}$$

$$\frac{\partial \sigma_{xz}}{\partial t} = \mu \frac{\tau_{\varepsilon}^{s}}{\tau_{\sigma}}\left(\frac{\partial \upsilon_x}{\partial z} + \frac{\partial \upsilon_z}{\partial x}\right) + r_{xz} \tag{2.4.16}$$

Equations governing particle velocities:

$$\frac{\partial \upsilon_x}{\partial t} = \frac{1}{\rho}\left(\frac{\partial \sigma_{xx}}{\partial x} + \frac{\partial \sigma_{xz}}{\partial z}\right) \tag{2.4.17}$$

$$\frac{\partial \upsilon_z}{\partial t} = \frac{1}{\rho}\left(\frac{\partial \sigma_{xz}}{\partial x} + \frac{\partial \sigma_{zz}}{\partial z}\right) \tag{2.4.18}$$

Equations governing memory variables, which are introduced to eliminate the numerically inconvenient convolution arising in the viscoelastic constitutive relation:

$$\frac{\partial r_{xx}}{\partial t} = -\frac{1}{\tau_{\sigma}}\left(r_{xx} + \pi\left(\frac{\tau_{\varepsilon}^{p}}{\tau_{\sigma}} - 1\right)\left(\frac{\partial \upsilon_x}{\partial x} + \frac{\partial \upsilon_z}{\partial z}\right) - 2\mu\left(\frac{\tau_{\varepsilon}^{s}}{\tau_{\sigma}} - 1\right)\frac{\partial \upsilon_z}{\partial z}\right) \tag{2.4.19}$$

$$\frac{\partial r_{zz}}{\partial t} = -\frac{1}{\tau_{\sigma}}\left(r_{zz} + \pi\left(\frac{\tau_{\varepsilon}^{p}}{\tau_{\sigma}} - 1\right)\left(\frac{\partial \upsilon_x}{\partial x} + \frac{\partial \upsilon_z}{\partial z}\right) - 2\mu\left(\frac{\tau_{\varepsilon}^{s}}{\tau_{\sigma}} - 1\right)\frac{\partial \upsilon_x}{\partial x}\right) \tag{2.4.20}$$

$$\frac{\partial r_{xz}}{\partial t} = -\frac{1}{\tau_{\sigma}}\left(r_{xz} + \mu\left(\frac{\tau_{\varepsilon}^{s}}{\tau_{\sigma}} - 1\right)\left(\frac{\partial v_x}{\partial z} + \frac{\partial \upsilon_z}{\partial x}\right)\right) \tag{2.4.21}$$

σ_{ij} : the ijth component of the symmetric stress tensor.

υ_i : the ith component of the particle velocity.

r_{ij} : the memory variables.

τ_{ε}^{p} 、 τ_{ε}^{s} : the viscoelastic strain relaxation times for P- and SV-waves, respectively.

τ_{σ} :the viscoelastic stress relaxation time for both the P- and SV waves.

μ: the relaxation modulus corresponding to SV-waves, which is analogous to Lame constant μ in the elastic case.

π: the relaxation modulus corresponding to P-wave, which is analogous to $\lambda+2\mu$ in the elastic case.

ρ : the density.

Equation (2.4.14) to (2.4.18) corresponds to equations (2.2.38) in the elastic case. In order to calculate equations (2.4.14) to (2.4.21), we employed second-order accurate in time and forth-order accurate in space O(2,4) scheme as we showed for the one-dimensional case. In this implementation, the finite-difference grid is staggered in space as shown in Figures 2.4.2 to 2.4.4.

In the two-dimensional case, the viscoelastic horizontal free-surface satisfies the following conditions:

$$\sigma_{iz} = 0 \qquad \text{i=x,z} \tag{2.4.22}$$

$$r_{iz} = 0 \qquad \text{i=x,z} \tag{2.4.23}$$

these conditions lead the following equations by using equations (2.4.14) to (2.4.16):

$$\frac{\partial \upsilon_x}{\partial z} = -\frac{\partial \upsilon_z}{\partial x} \tag{2.4.24}$$

$$\frac{\partial \upsilon_z}{\partial z} = -\left(1 - 2\frac{\tau_{\varepsilon}^{s}}{\tau_{\varepsilon}^{p}}\frac{\mu}{\pi}\right)\frac{\partial \upsilon_x}{\partial x} \quad . \tag{2.4.25}$$

Vertical free-surface boundary can be implemented in the same way.

The stability criteria for the conditionally stable schemes are similar to elastic schemes (Levander, 1988). The Courant number ($c\,\Delta t/\Delta x$, where c is the velocity) for viscoelastic schemes has to be adjusted to the highest phase velocity, which is found at

infinite frequency c_{max} as follows :

$$c_{\max} = \sqrt{\tau_\varepsilon M_R / \tau_\sigma \rho} \ . \qquad (2.4.26)$$

In order to minimize artificial reflections from the boundaries of a model, Higdon's (1986, 1987, 1990) absorbing boundary condition is adopted in the calculation.

2.4.3 Three-dimensional Finite-difference Modeling

1) Three-dimensional finite-difference approximation

3-D viscoelastic finite-difference method that we have developed employs the second-order accurate in time, forth-order accurate in space (O(2,4)), velocity-stress staggered grid finite-difference scheme (Virieux, 1986; Levander, 1988). Figure 2.4.5 shows a 3-D staggered grid used in the method.

Robertsson et al. (1994) proposed the viscoelastic finite-difference modeling based on the τ method in which the magnitude of quality factor Q is essentially determined by the difference of the stress and strain relaxation times (Liu et al., 1976; Blanch et al., 1993). A constant (frequency independent) Q can be closely approximated by this method (e.g., Emmerich and Korn, 1987; Day and Minster, 1984; Blanch et al., 1993; Carcione, 1993; Day, 1998). We employ the method presented by Robertsson et al. (1994) because the memory variable formulations are optimized and additional computer memory requirement to that of elastic case is small compared with elastic case. Robertsson et al. (1994) showed that even a single relaxation time provides an adequate approximation in narrow-band applications, such as exploration seismology and strong ground motion simulations. In this method, the optimum relaxation times can be determined by a least square method (Blanch et al., 1995).

In the 3-D (i,j,k = x,y,z) finite-difference calculation, the following equations are solved (in the case of single relaxation mechanism). For the diagonal components of stress tensor (i = j),

$$\frac{\partial \sigma_{ij}}{\partial t} = \left(\pi \frac{\tau_{\varepsilon}^{p}}{\tau_{\sigma}} - 2\mu \frac{\tau_{\varepsilon}^{s}}{\tau_{\sigma}} \right) \frac{\partial \upsilon_{k}}{\partial k} + 2\mu \frac{\tau_{\varepsilon}^{s}}{\tau_{\sigma}} \frac{\partial \upsilon_{j}}{\partial i} + r_{ij} \tag{2.4.27}$$

for the off-diagonal components of stress tensor(i $\neq$ j),

$$\frac{\partial \sigma_{ij}}{\partial t} = 2\mu \frac{\tau_{\varepsilon}^{s}}{\tau_{\sigma}} \left(\frac{\partial \upsilon_{j}}{\partial i} + \frac{\partial \upsilon_{i}}{\partial j} \right) + r_{ij} \tag{2.4.28}.$$

Similary, the diagonal components of memory variable,

$$\frac{\partial r_{ij}}{\partial t} = -\frac{1}{\tau_{\sigma}} \left(r_{ij} + \left(\pi \frac{\tau_{\varepsilon}^{p}}{\tau_{\sigma}} - 2\mu \frac{\tau_{\varepsilon}^{s}}{\tau_{\sigma}} \right) \frac{\partial \upsilon_{k}}{\partial k} + 2\mu \frac{\tau_{\varepsilon}^{s}}{\tau_{\sigma}} \frac{\partial \upsilon_{j}}{\partial i} \right) \tag{2.4.29}$$

for the off-diagonal components of memory variables,

$$\frac{\partial r_{ij}}{\partial t} = -\frac{1}{\tau_{\sigma}} \left(r_{ij} + \mu \frac{\tau_{\varepsilon}^{s}}{\tau_{\sigma}} \left(\frac{\partial \upsilon_{j}}{\partial i} + \frac{\partial \upsilon_{i}}{\partial j} \right) \right) \tag{2.4.30}.$$

Finaly, the particle velocities are calculated by Newton's law as following,

$$\frac{\partial \upsilon_{i}}{\partial t} = \frac{1}{\rho} \frac{\partial \sigma_{ij}}{\partial j} \tag{2.4.31}$$

where, σ_{ij} is ij$_{th}$ component of stress tensor, υ_{i} is i$_{th}$ component of particle velocities, r_{ij} is ij$_{th}$ component of memory variables. τ_{ε}^{p} and τ_{ε}^{s} are the strain relaxation times for P- and S-waves respectively. τ_{σ} is the stress relaxation time. μ is the relaxation modulus (M_R) for S-wave, and π is the relaxation modulus (M_R) for P-wave. ρ is the density.

The viscoelastic horizontal free-surface satisfies following conditions:

$$\sigma_{zz} = \sigma_{xz} = \sigma_{yz} = 0\big|_{Z=0} \tag{2.4.32}$$

$$r_{zz} = r_{xz} = r_{yz} = 0\big|_{Z=0} \tag{2.4.33}.$$

We employed a nonreflecting boundary condition (Cerjan, 1985) for other boundaries.

2) Basic Benchmark Tests

Two basic benchmark tests have been performed to confirm the accuracy of the method. The first example is a planar P-wave propagating in 3-D homogeneous model. A 50Hz Ricker wavelet is used as a source wavelet. Relaxation mechanism is optimized so that quality factor Q is equal to 10 around the frequency of 50Hz. P-wave velocity corresponding to the elastic modulus (M_U) is 1000m/s (P-wave velocity corresponding to the relaxation modulus (M_R) is 909.5m/s). The density is 1000kg/m^3. One relaxation mechanism is used for the calculation. Figure 2.4.6 shows the Q and phase-velocity obtained from two traces calculated by the finite-difference method. The separation of two traces is 50m. Analytical solution is also shown in the figures. We can see that the almost exact Q has been obtained around the frequency of 50Hz.

The next example is the Lamb's problem in which both a source and receivers are placed on the free-surface of homogeneous half space. A source is a point exploration placed at the depth of 5m beneath the surface with a 50Hz Ricker wavelet. S-wave velocity corresponding to elastic modulus (M_U) is 577.35m/s, and quality factor Q for S-wave is 10. P-wave velocity, Q for P-wave, and density is identical with the first example. Receivers are placed on the surface at 15m and 35 m apart from the source. One relaxation mechanism is used for the calculation. Figure 2.4.7 shows the vertical component of particle velocities together with waveforms calculated by the discrete wave-number integral method (Bouchon, 1979). We can see that the finite-difference solutions agree with the solutions of the discrete wave-number integral method.

3) Nonuniform Grid Spacing

Several methods for varying grid spacing with respect to velocity model have been proposed. One approach uses squares or cubes and combines fine grids with coarse

grids as Robertsson and Holliger(1997) or Hayashi and Burns(2001). Another approach uses rectangles or rectangular parallelepipeds as Falk et.al.(1995) or Pitarka(1999). We have chosen latter one because of the method is stable for long calculation and easy for coding.

In our method, the grid spacing in depth direction (z direction) is varied with respect to velocity model (Figure 2.4.8). Generally, the seismic-wave velocity in the Earth is increasing with depth. A finer grid spacing is used in near-surface region and a coarser grid spacing is in deeper region. A seismic source is introduced by a body force term in the equation of motion. (Graves, 1996).

The forth-order finite-difference operator for nonuniform-grid velocity-stress finite-difference scheme presented by Pitarka(1999) can be written as follows;

$$D_z g(x,y,z) = c_1 g(x,y,z+\Delta_1) + c_2 g(x,y,z-\Delta_2) + c_3 g(x,y,z+\Delta_3) + c_4 g(x,y,z-\Delta_4) \tag{2.4.34}$$

where, g is particle velocities or stresses, Δ_1 to Δ_4 is the z direction grid spacing as shown in Figure 2.4.9. Coefficients c_1 to c_4 can be calculated from a following equation.

$$\begin{pmatrix} 1 & 1 & 1 & 1 \\ \Delta_1 & -\Delta_2 & \Delta_3 & -\Delta_4 \\ -\Delta_1^2 & -\Delta_2^2 & -\Delta_3^2 & -\Delta_4^2 \\ -\Delta_1^3 & \Delta_2^3 & -\Delta_3^3 & \Delta_4^3 \end{pmatrix} \begin{pmatrix} c_1 \\ c_2 \\ c_3 \\ c_4 \end{pmatrix} = \begin{pmatrix} 0 \\ 1 \\ 0 \\ 1 \end{pmatrix} \tag{2.4.35}$$

In order to confirm the accuracy of the method, a benchmark test similar to the Pitarka (1999) has been performed. The test compared nonuniform-grid computation with uniform one. Figure 2.4.10 shows the model used in the benchmark test. We used an elastic homogeneous half space model with P-wave velocity of 5600m/s, S-wave velocity of 3200m/s and density of 2200kg/m^3. A source is a 10km-long planar vertical fault that extends from a depth of 2 to 10km. A rake angle of slip vector is 45 degrees. We used a bell-shaped slip velocity function and the constant rupture velocity of 2800m/s. In the uniform-grid computation, the interval of point sources and the grid spacing were set to 200 and 100m respectively. In the nonuniform-grid computation, the

grid spacing was set to 100m in the x and y directions and 100, 300 and 600 in the z direction in the depth intervals of 0 to 4.0, 4.0 to 8.0 and 8.0 to 14.0km, respectively. In these depth intervals, the point source spacing in the vertical direction was set to 200, 300 and 600m respectively. The geometry of the fault and receiver array is shown in Figure 2.4.6b.

Figure 2.4.11 shows the vertical components of particle velocities calculated with the uniform- and nonuniform grid spacing. Good agreement between both waveforms shows the validity of the nonuniform finite-difference method at modeling the response of finite fault.

Grid spacing ratio of minimum and maximum grids can be six in the case of the calculation of strong ground motion in which velocity model from bed rock (Vs=500m/s) to upper mantle (Vs > 3000m/s) using the nonuniform grid spacing. Consequently, in the calculation of strong ground motion down to depth of 50 to 100km, the number of grids can be 1/2 to 1/5 in comparison with uniform grid spacing.

4) Parallel Computation Using PC-cluster

Computation time and memory requirement are two important issues in the application of finite-difference method to large-scale 3D seismic modeling. Graves(1996) proposed the so called cascaded time update procedure in which only a subset of the entire model reside in core memory at one time step. The method enable us to compute large-scale model using commonly available workstations or PCs. However, the method cannot speed up the computation. Bohlen and Milkereit(2001) applied parallel computation to the finite-difference method. Parallel computation is much better than the cascaded time update procedure because it can solve the problem of computation time and the memory requirement simultaneously in the large-scale finite-difference seismic modeling. However, traditional parallel computers have been highly expensive and not so many researchers can use such parallel computers. In order to calculate large-scale model with common PCs, we have been built PC-cluster.

Table 2.4.1 summarizes the specification of PC-cluster system we have built. Our system consists of 8 dual CPU PCs connected with 100BASE Ethernet. We can add several PCs if necessary. An ordinal switching HUB is used for connecting all PCs. The

MPI is used as message passing library. Figure 2.4.12 shows the example of computation time using PC-cluster. O(2,4) velocity-stress staggered grid finite-difference method has been performed. The model is a cube with N grids on an edge (the number of grids is N^3). In the case of small model, an increase of speed is small. However, as the number of cells increases, the efficiency of parallel computing increases. The computation speed becomes up to 10 times faster than single CPU in the 500^3 cells with 16CPUs.

Table 2.4.1. Outline of PC-cluster

	Specification	Single	Total
CPU	Pentium3:1GHz	2	16
RAM	DIMM	2GB	16GB
HD	RAID system	30GB	240GB
Network	100BASE-TX/10BASE-T		
OS	Windows2000		

Table 2.4.2 shows the computation time for a strong ground motion simulation. The model size is 220km by 169km by 50km and minimum grid spacing is 400m. In the nonuniform-grid computation, the number of grids is 550*423*50. One hundreds seconds of viscoelastic wave propagation was calculated. The number of time step is 4096. The nonuniform-grid computation with 16CPU PC-cluster was 12 times faster than the uniform-grid computation with 2CPUs.

Table 2.4.2. The computation time of nonuniform-grid and PC-cluster

	The number of grids	Memory requirement	Computation time(hour)
Uniform 2CPU	550*423*125(29.1M)	2.33GB	46.9
Uniform 8CPU	550*423*125(29.1M)	2.33GB	14.9
Nonuniform 8CPU	550*423*50(11.6M)	0.93GB	6.7
Nonuniform 16CPU	550*423*50(11.6M)	0.93GB	3.8

5) Example of Strong Ground Motion Simulation

We will show two examples of strong ground motion simulations. The first one is the Izu-oshima-kinkai earthquake (M=6.5) in 1990. The location of epicenter was about 100km southwest from Tokyo, Japan. We use the velocity, density and Q model from Yamada and Yamanaka(2001) and the fault model from Fukuyama and Mikumo(1999). The strike of fault is zero degree and dip is 90 degrees. The length of the fault is 19km and width is 14km. Uniform- and nonuniform-grid computations have been compared.

In the uniform-grid computation, the grid spacing was set to 400m. In the nonuniform-grid computation, the grid spacing was set to 400m in the x and y directions and 400, 500 and 2500m in the z direction in the depth intervals of 0 to 2.4km, 2.4 to 17.9km and 17.9 to 50km respectively. The fault was located from depth of 3 to 17km. The point source spacing is set to 800m in the uniform grid and 1000m in the nonuniform-grid computations Figure 2.4.13 shows the particle velocities (horizontal, north-south component) from the simulation. We can see that the nonuniform-grid computation agrees with the uniform one.

The next example is the simulation of a large earthquake (M > 7.5). The model size is 240km by 370km by 73km and minimum grid spacing is set to 200m. Nonuniform-grid spacing was employed and the number of grids was 1200 by 185 by 93. Minimum velocity of the model is 500m/s. Consequently periods down to two seconds of waveforms can be calculated. Computation time was about 7 days for 200 seconds of viscoelastic wave propagation.

Figure 2.4.14 shows the example of snapshots and waveforms from the simulation. Horizontal (North-south) component of particle velocities collected at the ground surface were plotted in snapshots. Horizontal (North-south) and vertical component of particle velocities collected at the ground surface were plotted in waveforms. A large tectonic basin is located at the northeast portion of the model and we can see that clear surface waves were generated at there. Table 2.4.3 summarizes the model size and computation time for strong ground motion simulations we have done.

Table 2.4.3 Example of strong ground motion simulation

Model size (km)	# of CPUs	# of grids (M)	Memory requirement (GB)	Minimum grid spacing (m)	Maximum frequency (Hz)	Computation time for one step (sec)	Computation time for 100seconds (hour)
100*100*50	8	3.13	0.25	400	0.25	1.3	1.4
220*169*50	16	11.6	0.93	400	0.25	3.3	3.8
240*370*73	20	206	16.5	200	0.5	46	102

6) Summary

We have introduced nonuniform-grid spacing method and parallel computation with PC-cluster into a finite-difference seismic modeling for strong ground motion simulations. The comparison of the nonuniform-grid computation with the uniform one has shown the validity of the nonuniform finite-difference method in the simulation of earthquakes. Parallel computation with 16 CPUs PC-cluster is 10 times faster than single CPU computation. The method enables us to calculate large-scale simulations for large magnitude earthquakes at periods down to two seconds in several days.

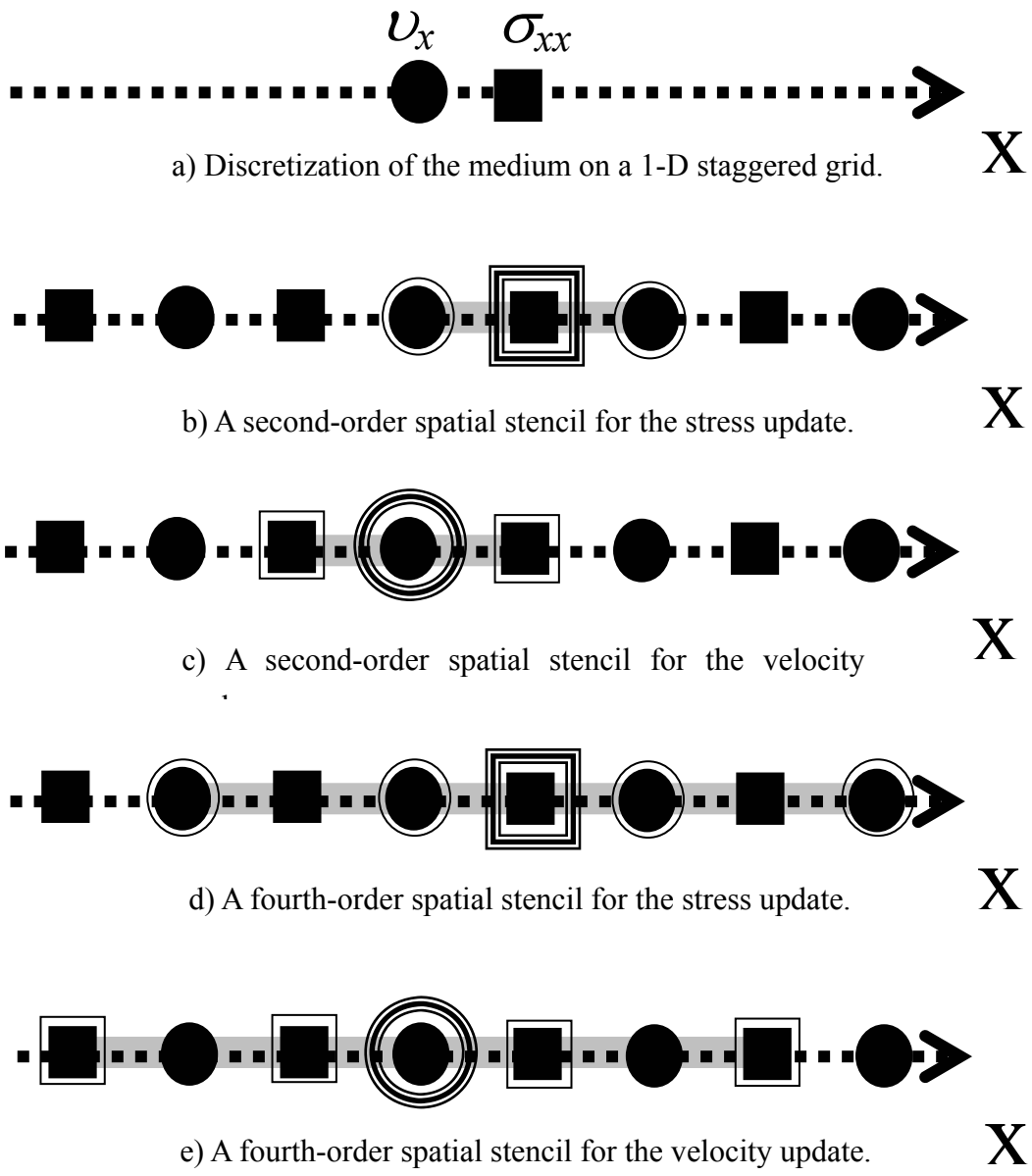

Figure 2.4.1. The one dimensional staggered finite-difference grid.σ_{xx} is a normal stress, and υ_x is a velocity in x-direction.

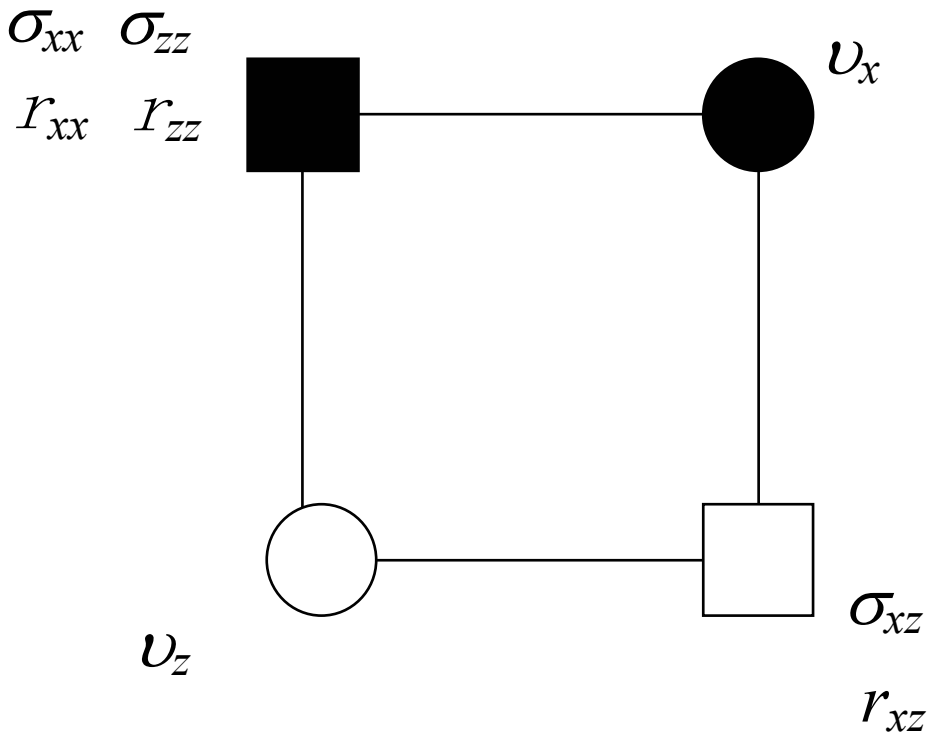

Figure 2.4.2. The two dimensional staggered finite-difference grid. σ_{xx} and σ_{zz} are normal stresses, υ_x and υ_z are particle velocities. r_{xx}, r_{zz} and r_{xz} are memory variables.

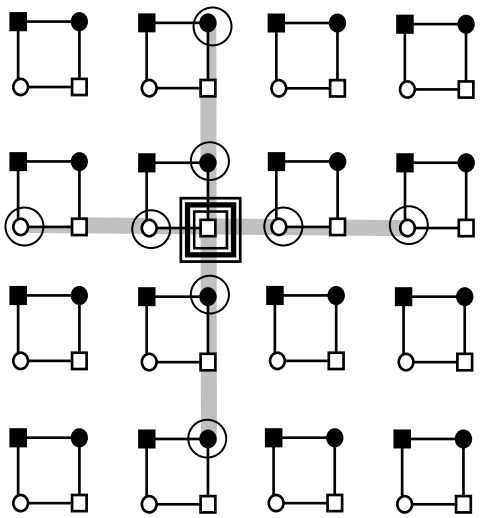

a) A stencil for a shear stress, σ_{xz} , and a memory variable r_{xz}.

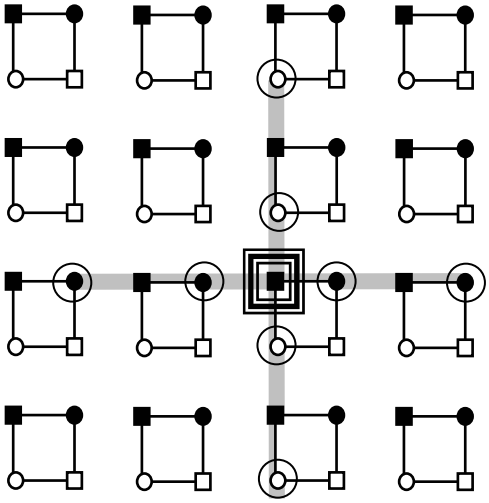

b) A stencil for normal stresses, σ_{xx} and σ_{zz}, and memory variables r_{xx} and r_{zz}.

Figure 2.4.3. Fourth-order spatial stencils for stress update. Within the grid-cells, the solid squares represent the σ_{xx}, σ_{zz}, r_{xx}, r_{zz}, components, the light squares the σ_{xz}, r_{xz} components, the solid circles the υ_x components, the light circles represent the υ_z components(σ: stress, r: memory variable, υ: velocity).

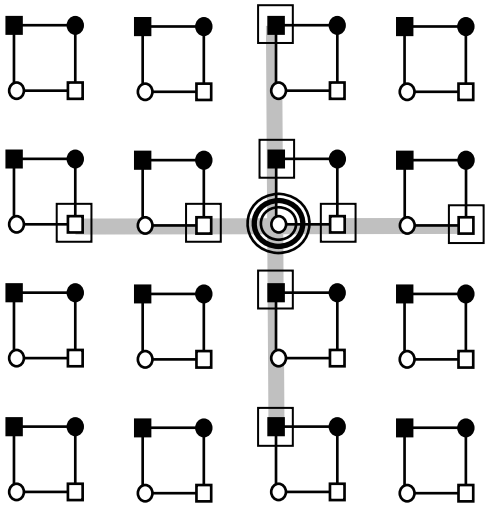

a) A stencil for a particle velocity, υ_z.

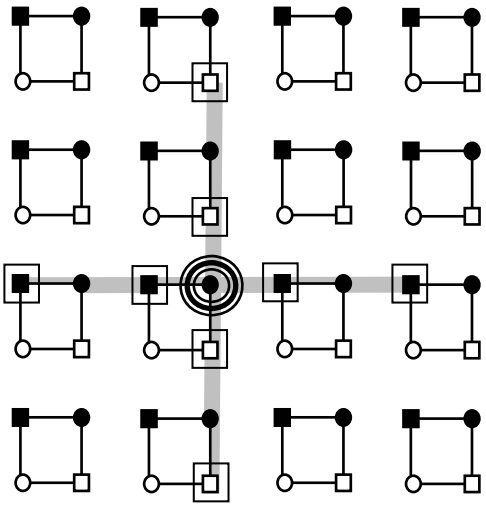

b) A stencil for a particle velocity, υ_x.

Figure 2.4.4. Fourth-order spatial stencils for velocity update. Within the grid-cells, the solid squares represent the σ_{xx}, σ_{zz}, r_{xx}, r_{zz}, components, the light squares the σ_{xz}, r_{xz} components, the solid circles the υ_x components, the light circles represent the υ_z components(σ: stress, r: memory variable, υ : velocity).

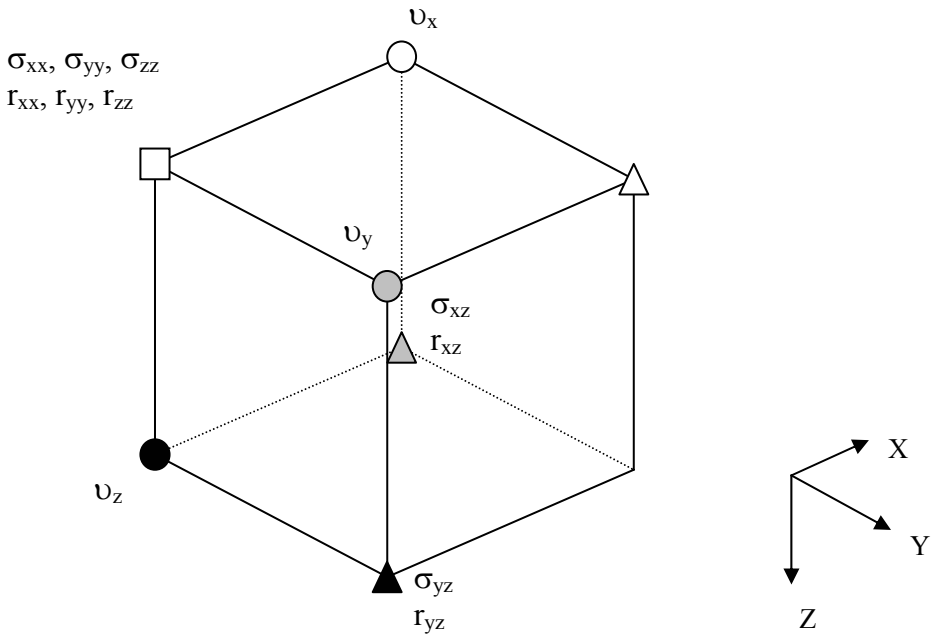

Figure 2.4.5. 3D velocity-stress staggered grid. σ_{ij} is ij_{th} component of stress tensor, υ_i is i_{th} component of particle velocities, r_{ii} is ij_{th} component of memory variables.

a)

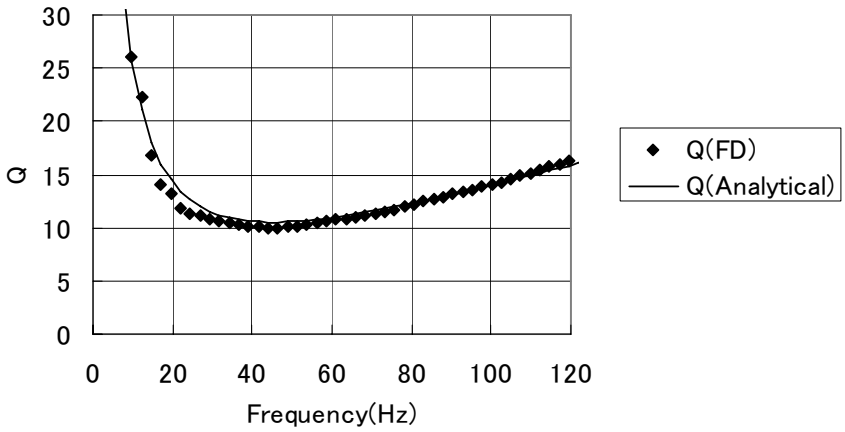

b)

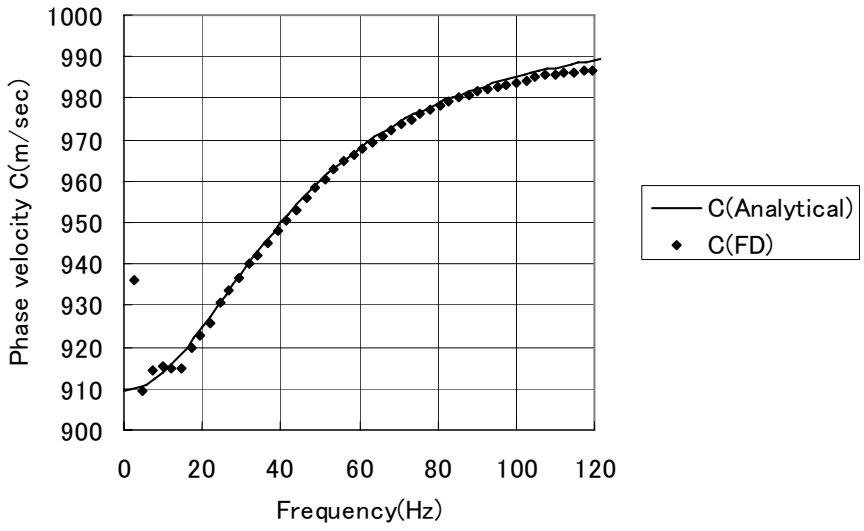

Figure 2.4.6. Comparison of quality factor Q(ω) and phase velocity C(ω) obtained from finite-difference method with analytical solutions. Dots indicate finite-difference solutions and solid lines indicate analytical solutions.

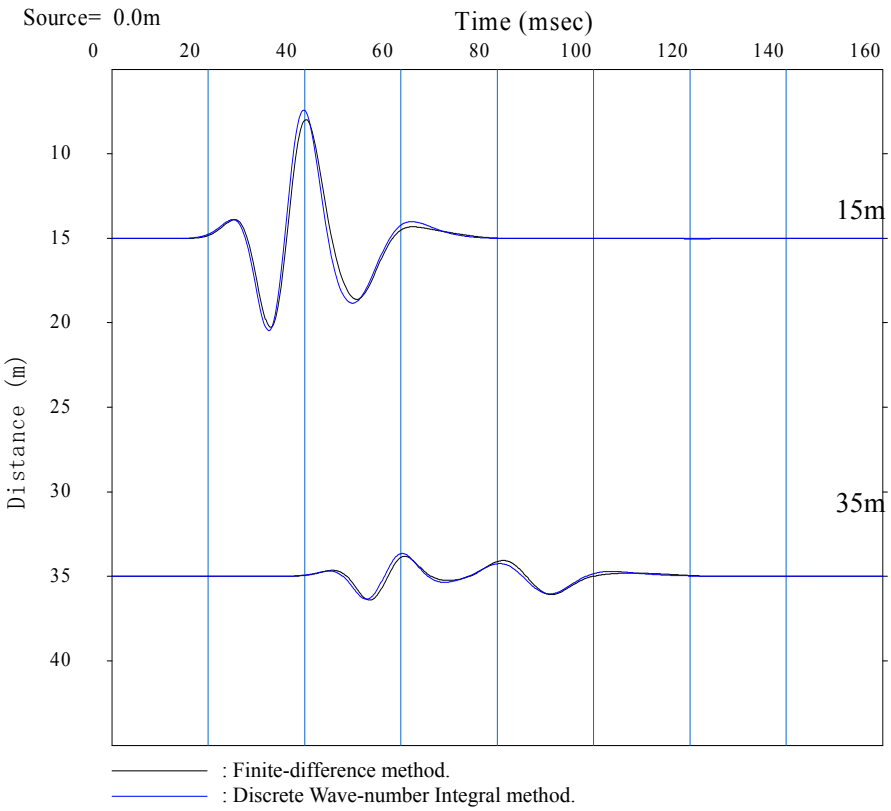

Figure 2.4.7. Comparison of finite-difference solutions (solid lines) with discrete wave-number integral method (dashed lines). Receivers located 15m and 35m from a source and vertical component of particle velocities are plotted.

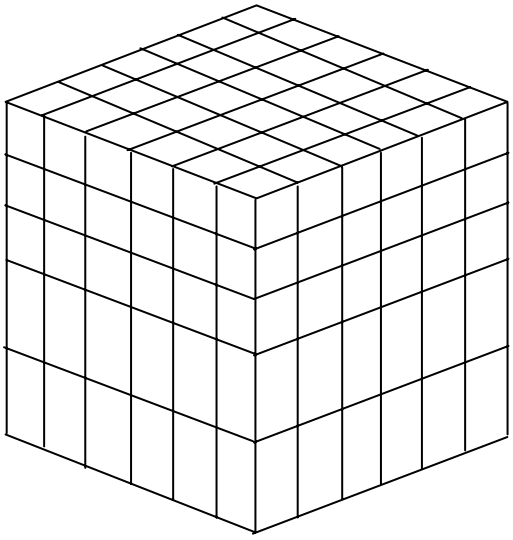

Figure 2.4.8. Nonuniform-grid spacing we have employed.

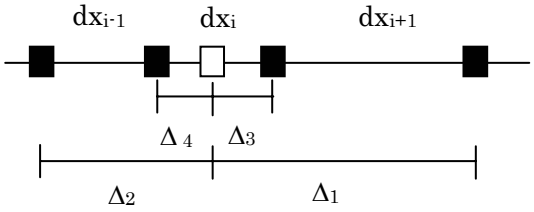

Figure 2.4.9. Definition of grid spacing in the nonuniform staggered grid.

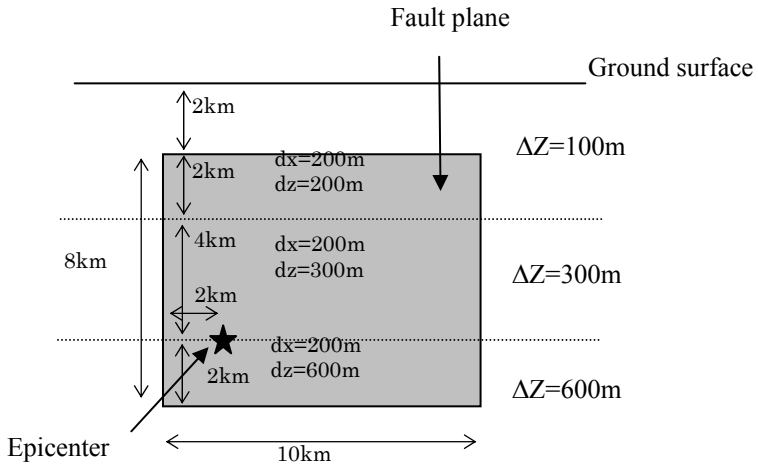

a)Cross section

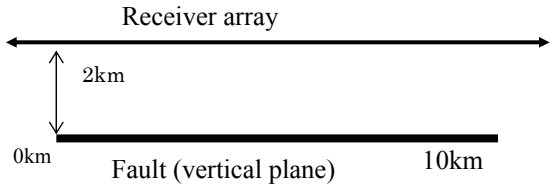

b)plan view

Figure 2.4.10. Finite-difference model used in the comparison of nonuniform-grid computation with uniform one. Δ_z indicates grid spacing in z direction. Dx and dz indicate source spacing in x and z directions respectively. In the uniform-grid spacing, Δ_z was set to 100m and dx and dz were set to 200m.

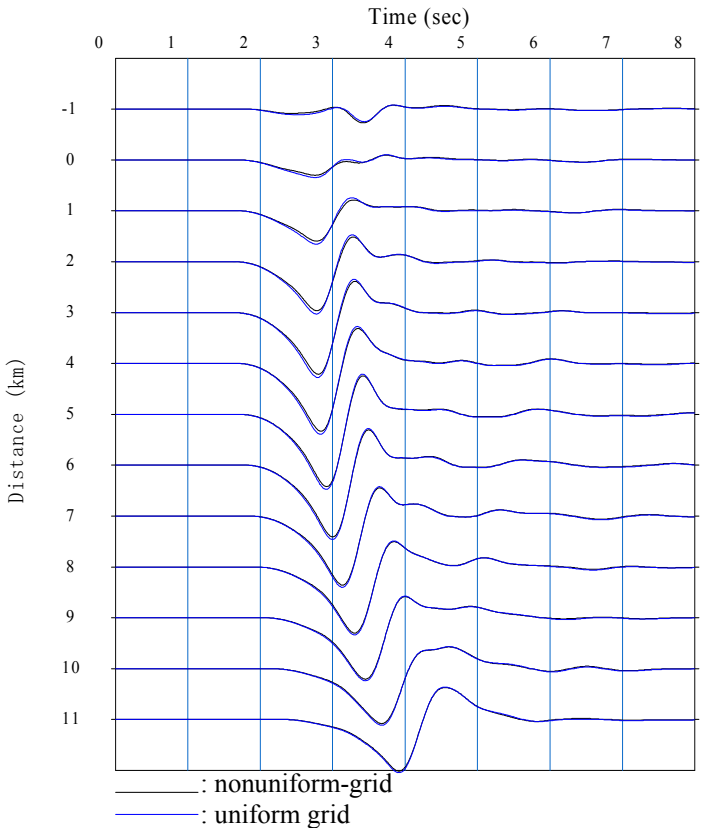

Figure 2.4.11. Comparison of nonuniform-grid computation (solid lines) with uniform grid computation (dashed line). Vertical component of particle velocities are plotted.

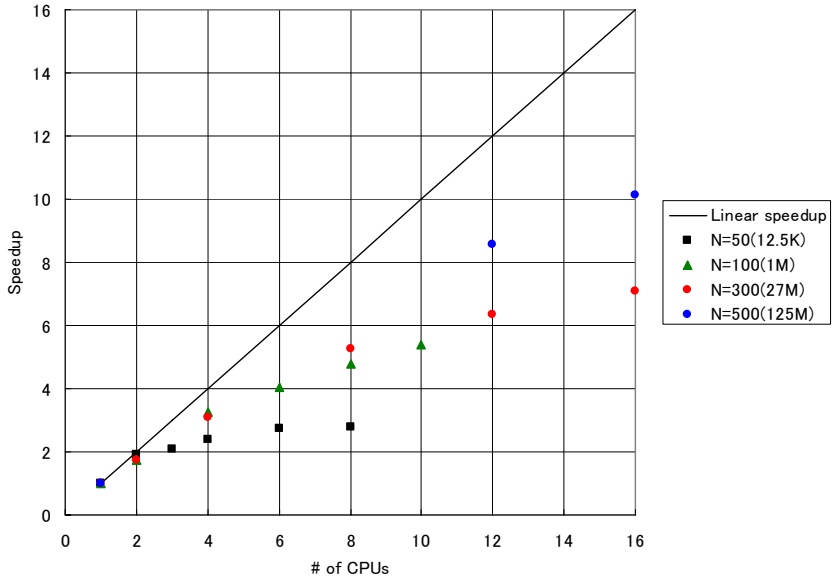

Figure 2.4.12. Example of computation time using PC-cluster. N indicates the number of grids on an edge. The total number of grids is mentioned in parentheses.

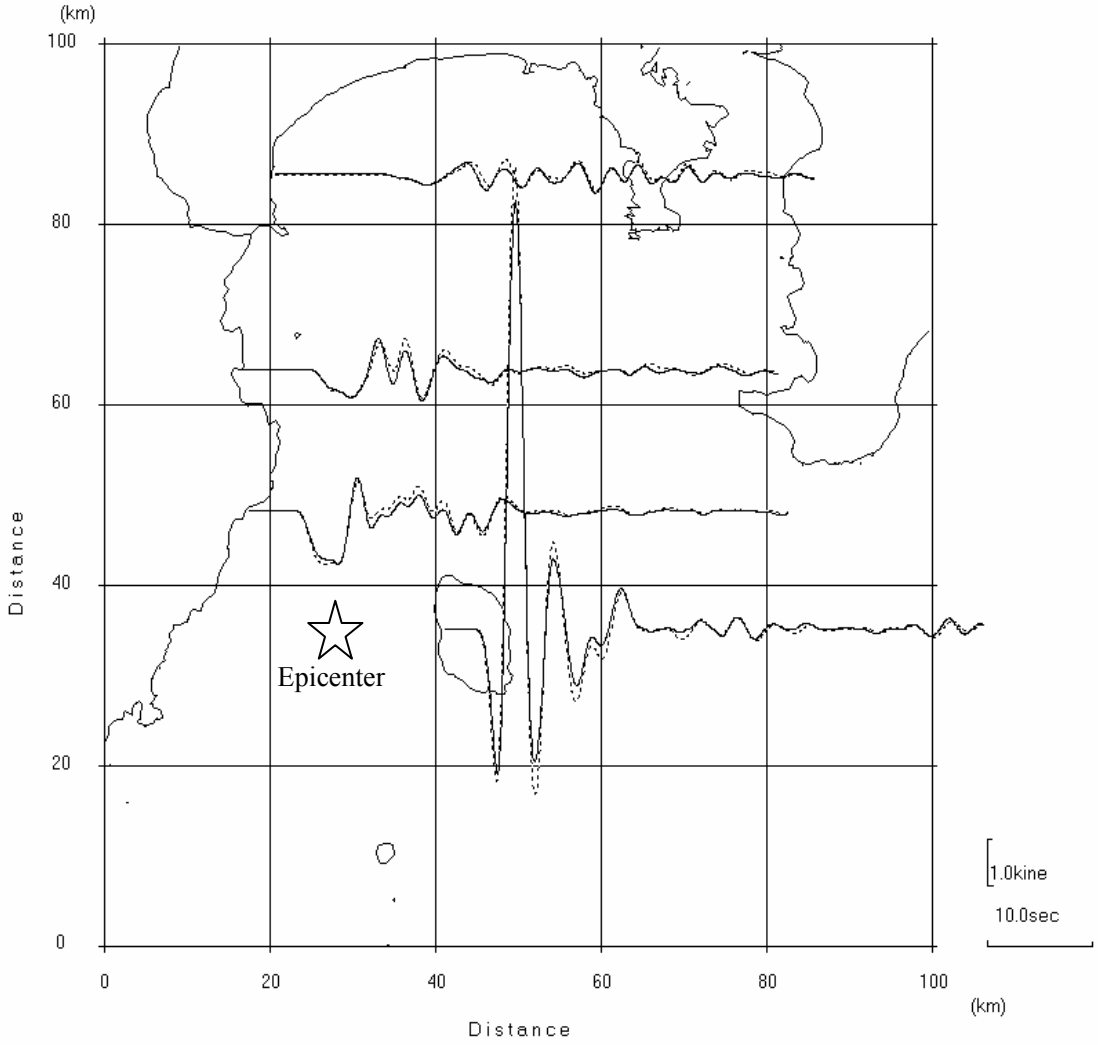

Figure 2.4.13. Comparison of nonuniform-grid computation (solid lines) with uniform grid computation (dashed line) in the simulation of an earthquake. Horizontal (North-south) component of particle velocities are plotted.

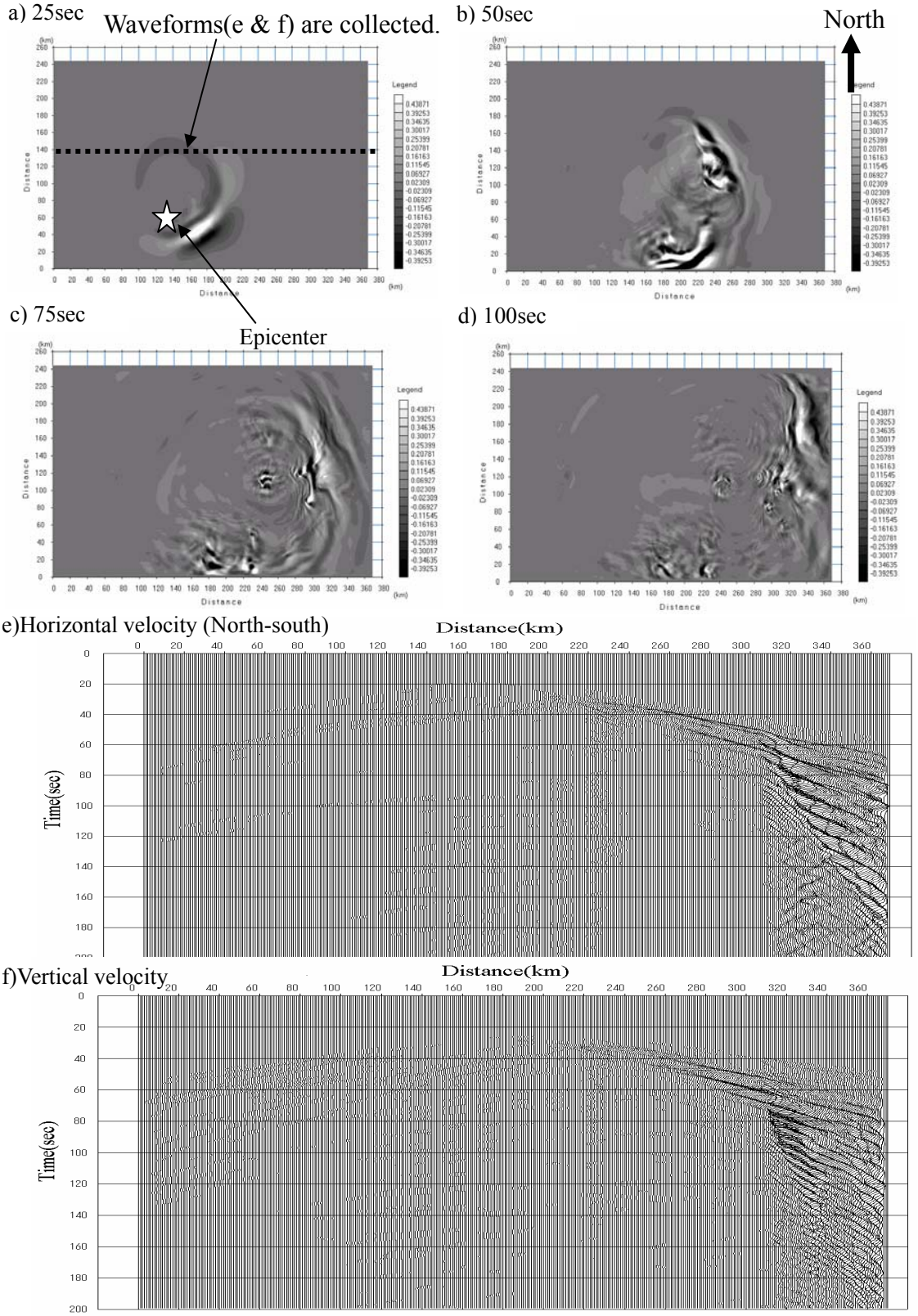

Figure 2.4.14. Snapshots (a to d) and waveforms (e and f) from the simulation. Horizontal (North-south) component of particle velocities collected at the ground surface were plotted in snapshots. Waveforms are collected at the distance of 170km in North-south direction.

2.5 Numerical Simulation of Surface-wave Propagating with 2D Structures

2.5.1 Introduction

Surface wave methods have been applied to both engineering and earth science problems to image the S-wave velocity of the Earth. In the early 1980s, a spectral analysis of surface waves (so called SASW) was introduced to engineering problems. Park et al (1999a, 1999b) have improved the SASW to the multi-channel analysis of surface waves (MASW) and Xia et al. (1999a, 1999b) generated two-dimensional S-wave velocity map by the MASW. The surface wave methods, such as the SASW or the MASW, can estimate S-wave velocity models that are extremely valuable in geotechnical work. Therefore, the surface wave methods have been increasingly used in various civil engineering and environmental investigations.

The surface wave methods for near-surface problems are relatively new technique. Therefore, the methods have several important problems that should be solved. The methods use the dispersive character of Rayleigh waves, especially fundamental mode of surface waves. Body waves and higher mode surface waves can contaminate the surface wave and the separation of the fundamental mode surface waves from the body waves and higher mode surface waves becomes difficult in the surface wave method analysis. The analysis of the surface wave methods is usually based on the inversion of dispersion curves in which one-dimensional models are assumed (Xia et al., 1999a, 1999b). The real subsurface structure can be, however, three-dimensional. The analysis of dispersion curves may have some difficulties in complex near-surface velocity models. The number of theoretical studies about surface wave propagation in the heterogeneous near-surface region is relatively few. For example, the effect of two- and three-dimensional structures to the method has not been investigated.

In order to improve the accuracy and reliability of the surface wave methods, we have to understand fundamental characters of surface waves. We believe that numerical waveform modeling technique, such as finite-difference methods, can be one

of the valuable tools for this objective. In this section, we will perform several numerical simulations by a finite-difference method to study surface wave propagation characters in two-dimensional models, and apply the surface wave method to the field observation data, on the basis of numerical simulations.

2.5.2 Slope Model

A two-layer model in which an interface is dipping by 5 degrees is adopeed in the first simulation. Figure 2.5.1 shows the velocity model used in the simulation. Two sources are placed at the distance of 100m(A) and 500m(B). Model parameters are listed in Table 2.5.1.

Table 2.5.1. Model parameters for the slope model.

	Vp(m/s)	Vs(m/s)	Density (kg/m^3)
1^{st} layer	2000	1000	2000
2^{nd} layer	3000	1730	2800

Waveform was calculated by finite-difference method employing two-dimensional, velocity-stress staggered grid (Levander, 1988). The source is a point explosion with an 18 Hz Ricker wavelet. Figure 2.5.2 shows the wave-field snapshots (vertical component of particle velocities) of 300msec. Figure 2.5.3 shows the waveforms collected at the receivers on the surface. Vertical component of particle velocities is plotted.

Nine couples of traces are extracted from each shot gather. Each couple consists of two traces to be 20 m of separation. Two shot gathers have 18 couples, and 18 dispersion curves were calculated from the couples. Extracted couples and corresponding dispersion curve numbers (used in Figure 2.5.4) are also shown in Figure 2.5.3. Dispersion curves are calculated through a cross correlation method (Guo and Liu, 1999).

From the two shot gathers, nine receiver-pairs are selected and dispersion curves are obtained. Figure 2.5.4a and b show dispersion curves of nine receiver-pairs for the source A and B respectively. Distance labels in the figure indicate the center of

two traces that were used for the dispersion curve calculation. From Figure 2.5.4, we can see that the dispersion curves have different characters along the survey line. The results indicate that a two-dimensional velocity model can be imaged from these dispersion curves. Figure 2.5.5 shows the dispersion curves of the same receiver-pairs for the source A and B, and their averages. For the source A and B, the two dispersion curves are almost identical, if we neglect calculation error associated with numerical calculation. It indicates that the character in dispersion curves neither depends on the offset distance between source and receiver nor the direction of wave propagation, but only depends on the velocity model beneath the receivers.

One-dimensional velocity models were obtained through the inversion of dispersion curves. A non-linear least square method is used for inversion. Unknown parameters are S-wave velocities for the first and the second layers, and the interface depth. As the initial model, true S-wave velocity values and the interface depth of 20m were assumed. P-wave velocities and densities are fixed as true values. Figure 2.5.6 shows the inverted interface depth and S-wave velocity. We can see that the inverted depth is very close to the real model.

In the practical survey, it may be difficult to apply the above procedure, due to various noises, such as body waves and higher mode surface waves. Park et al. (1999a, 1999b) proposed the multi-channel analysis of surface waves to separate a fundamental mode from higher modes objectively. Surface waves on a multi-channel record are converted directly into images of multi mode dispersion curves through a simple waveform transformation method. We have applied this method for analyzing surface waves. Figure 2.5.7 shows the velocity - frequency domain image of the phase velocity converted through the waveform transformation. A dispersion curve is picked as the maximum amplitude in each frequency. A picked phase velocity (a dispersion curve) is shown in Figure 2.5.7 as small dots. Figure 2.5.8 shows the dispersion curves for two sources. Two dispersion curves are almost identical in spite of opposite wave propagation direction. Figure 2.5.9 shows inverted results. Obtained one-dimensional velocity models give the average depth of the interface.

2.5.3 Step Model

The next model is a three-layer model whose interfaces have a clear step in the middle of the model (Figure 2.5.10). Model parameters are listed in Table 2.5.2.

Table 2.5.2. Model parameters for the step model.

	Vp(m/s)	Vs(m/s)	Density (kg/m^3)
1^{st} layer	500	100	1000
2^{nd} layer	750	160	1500
3^{rd} layer	1500	250	2000

The end-on spread is used for data collection. Forty-eight receivers are placed on the surface with 1m intervals. Sources are placed on the surface from 5.8m to 65.8m with 2m interval so that the 31 common shot gathers were calculated. The source is a point explosion with an 18 Hz Ricker wavelet.

Figure 2.5.11 shows the vertical component of particle velocities calculated through the finite-difference method. The phase velocity changes around 60m where the step exists. It is interesting to note that clear surface wave reflection is generated at the step. Dispersion curves were calculated from each shot gather through the waveform transformation method described in the previous section. Figure 2.5.12 shows an example of dispersion curve image transformed from a shot gather as well as the picked phase velocity (small dots). Figure 2.5.13 shows dispersion curves for all sources. It is clear that the dispersion curves have large difference whether a receiver spread placed left side or right side of the step.

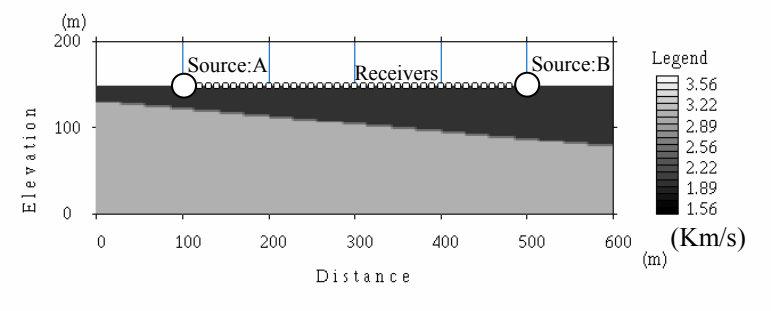

Fig.2.5.1. The slope model used in the numerical simulation. The figure shows the P-wave velocity model.

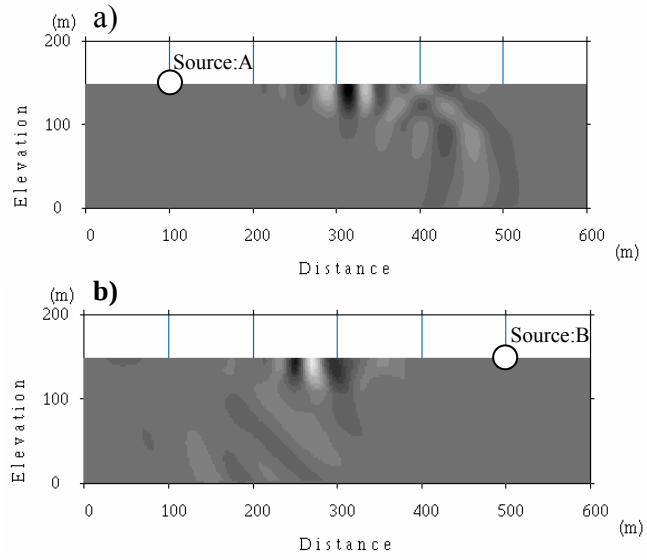

Fig.2.5.2. Wave-field snapshots of 300msec. The vertical component of particle velocities is shown. (a) Wave-field by the source A. (b) Wave-field by the source B.

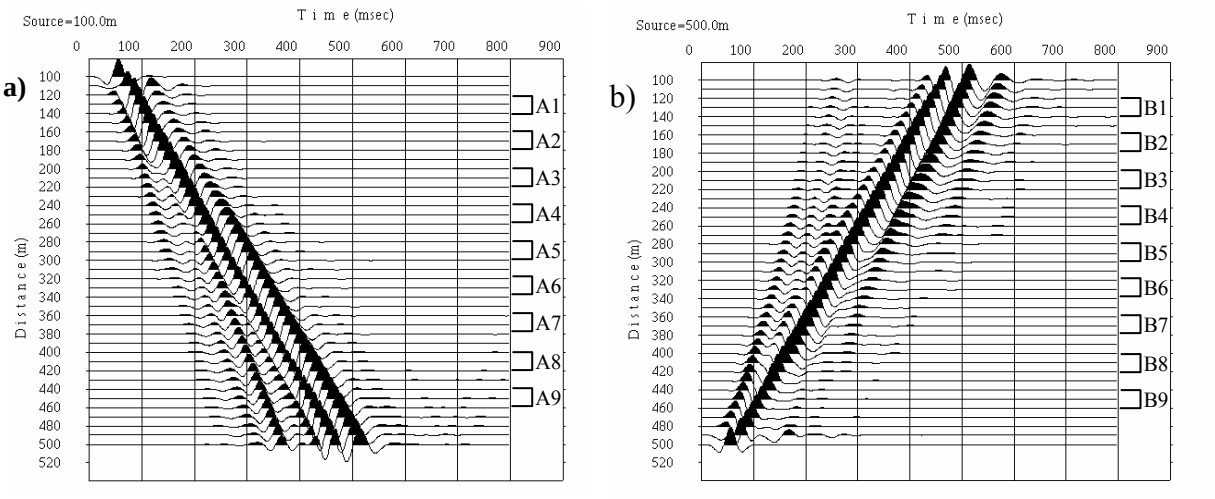

Fig.2.5.3. Waveforms collected at the receivers on the surface. Vertical component of particle velocities is plotted. Waveforms are normalized by each trace. (a) Waveforms from the source A. (b) Waveforms from the source B. Labels A1 to B9 show the dispersion curve numbers used in Figure 2.5.4 and Figure 2.5.5.

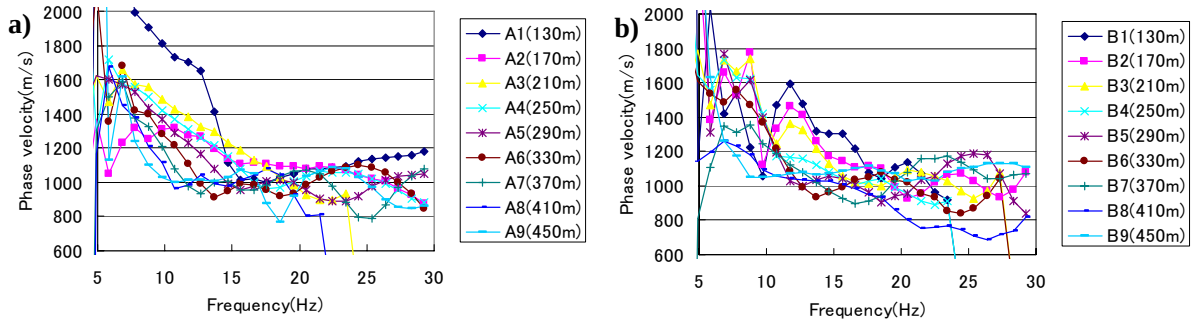

Fig.2.5.4. Dispersion curves calculated from theoretical waveforms. (a) Dispersion curves for the source A. (b) Dispersion curves for the source B.

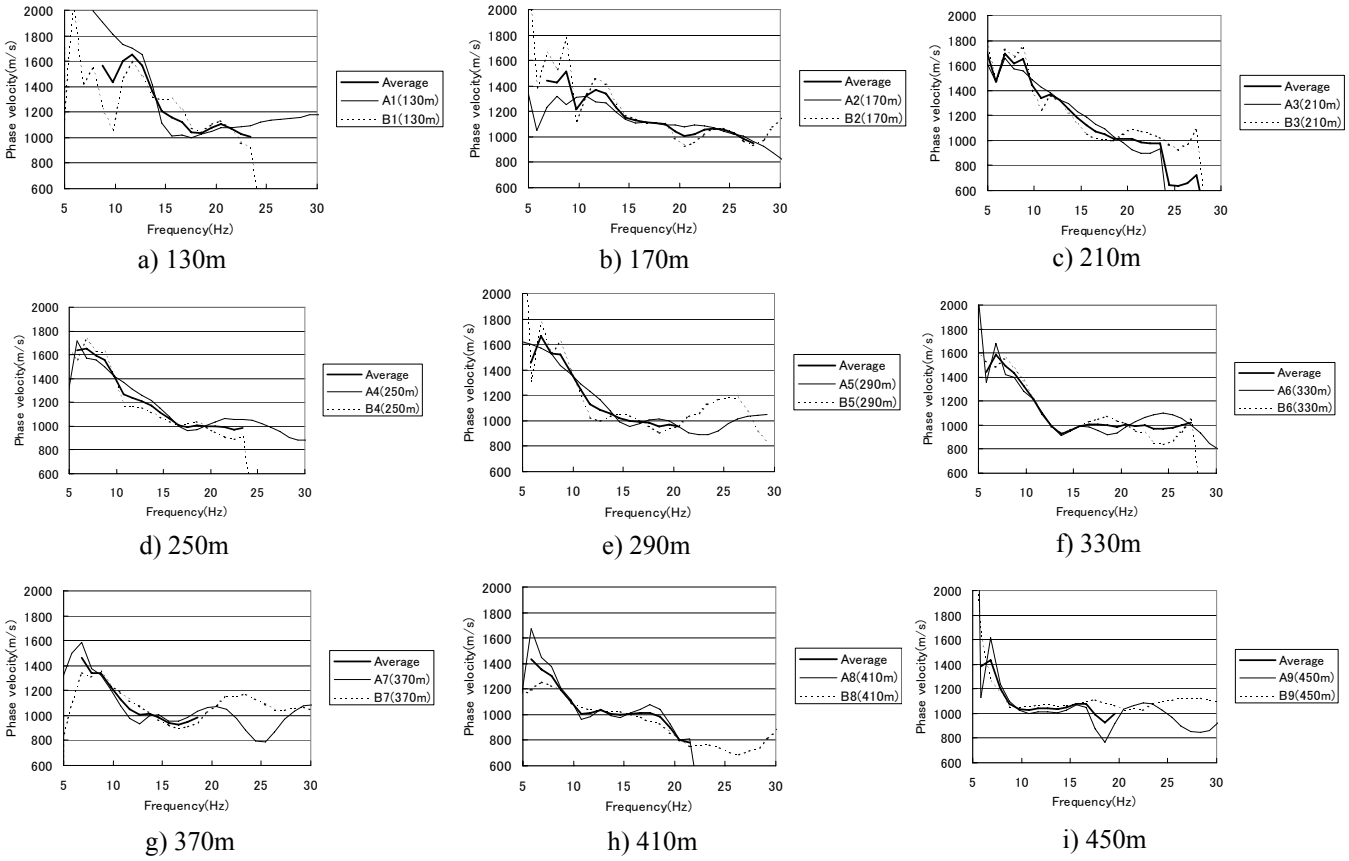

Fig.2.5.5. Two dispersion curves calculated from same receivers. Thin lines: dispersion curves for the source A. Dotted lines: dispersion curves for the source B. Thick lines: average.

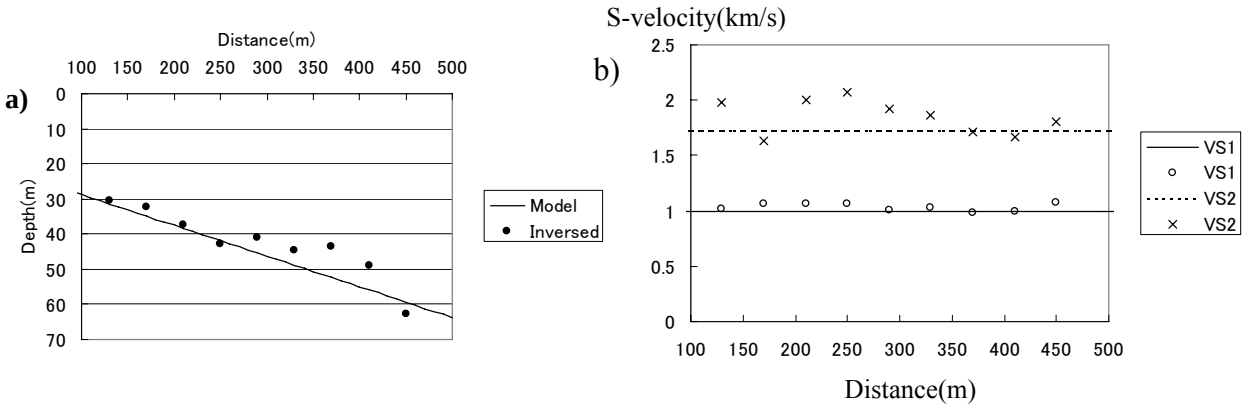

Fig.2.5.6. Inverted results. (a) Inverted interface depth. A solid line indicates the model. (b) Inverted S-wave velocity. A solid line indicates the velocity of the first layer. A dotted line indicates the velocity of the second layer.

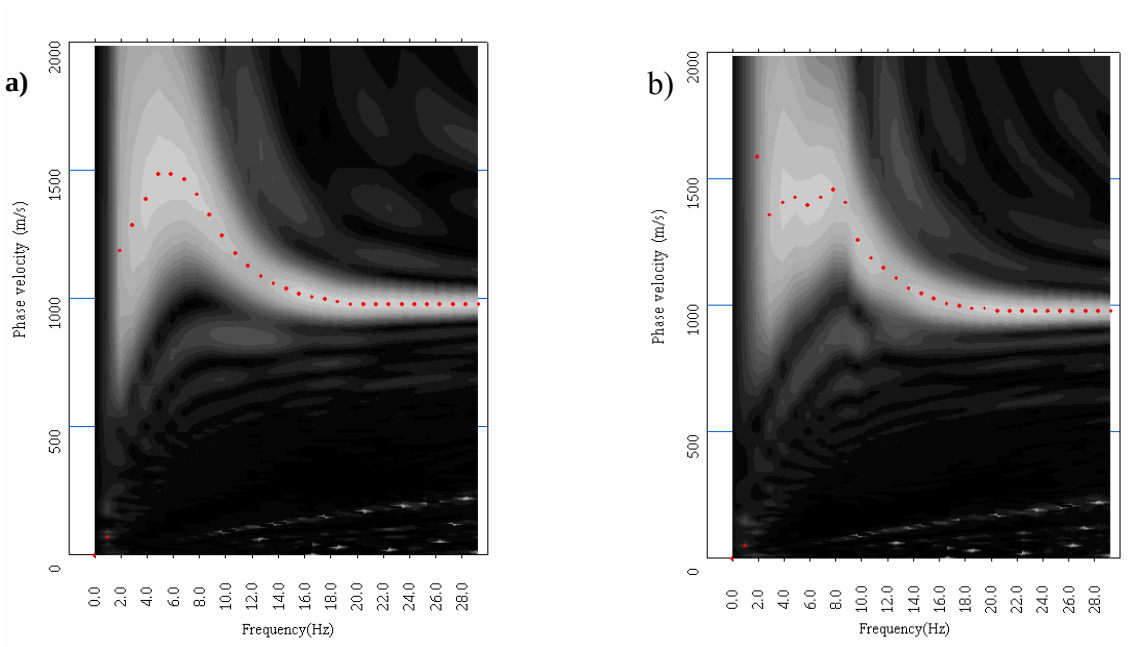

Fig.2.5.7. Phase velocity - frequency images converted through the multi-channel analysis of surface waves. (a) Dispersion curve image for the source A. (b) Dispersion curve image for the source B. Each small dot in the figure indicates maximum amplitude at the frequency.

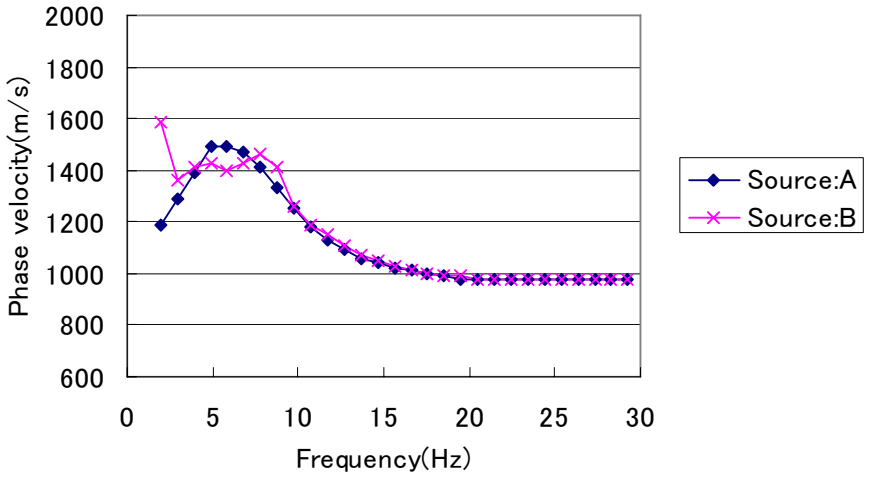

Fig.2.5.8. Dispersion curves for the two sources calculated through the multi-channel analysis of surface waves.

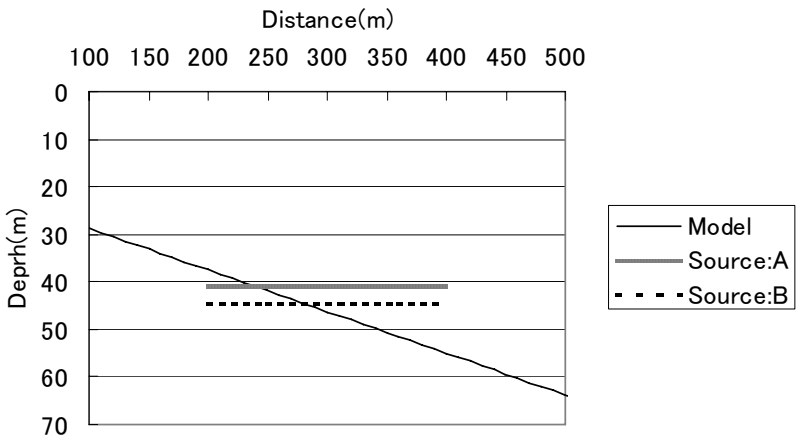

Fig.2.5.9. Inverted result of the dispersion curves calculated through the multi-channel analysis of surface waves. Inverted velocities from the source A are 1055m/s and 1727m/s, from the source B are 1041m/s and 1651m/s. The results are close to the true velocities (1000m/s and 1730m/s).

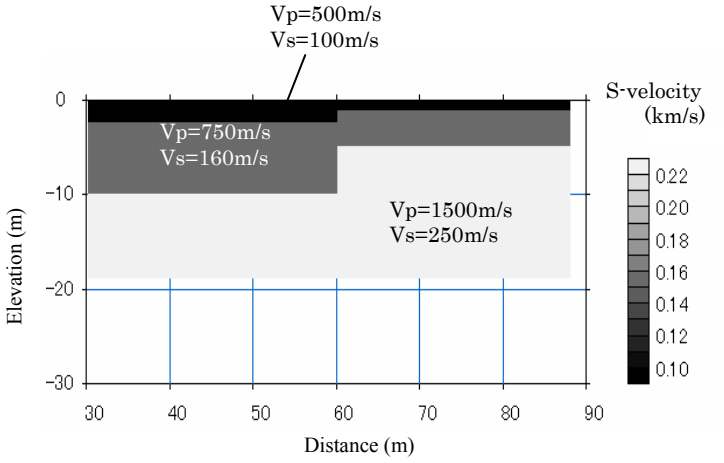

Fig.2.5.10. The step model used in the numerical simulation. The figure shows the S-wave velocity model.

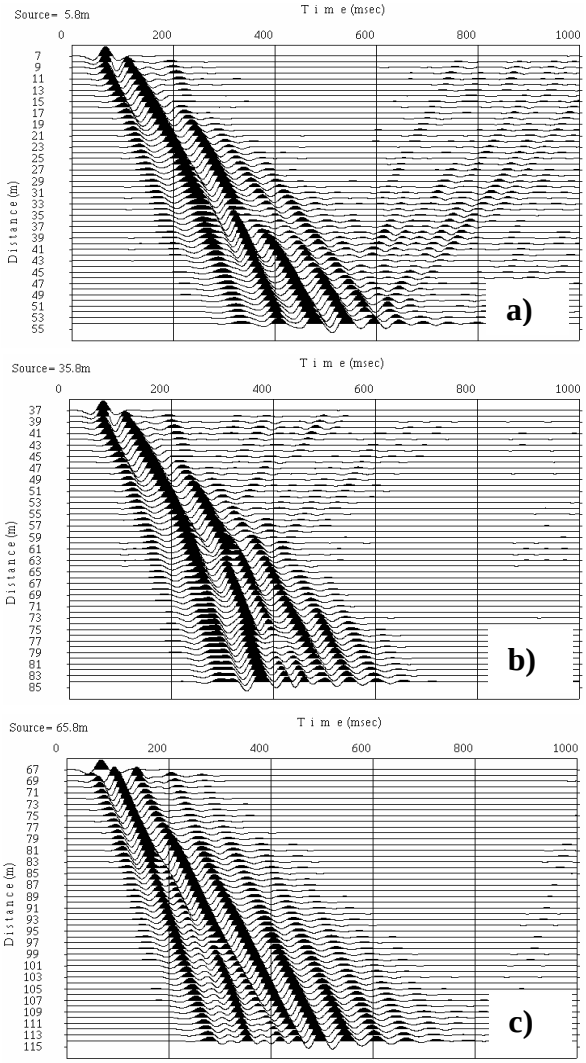

Fig.2.5.11. Examples of theoretical waveforms calculated through the finite-difference method. Vertical component of particle velocities is plotted. Receiver spread is on the left side of the step (a), on the step (b), on the right side of the step (c).

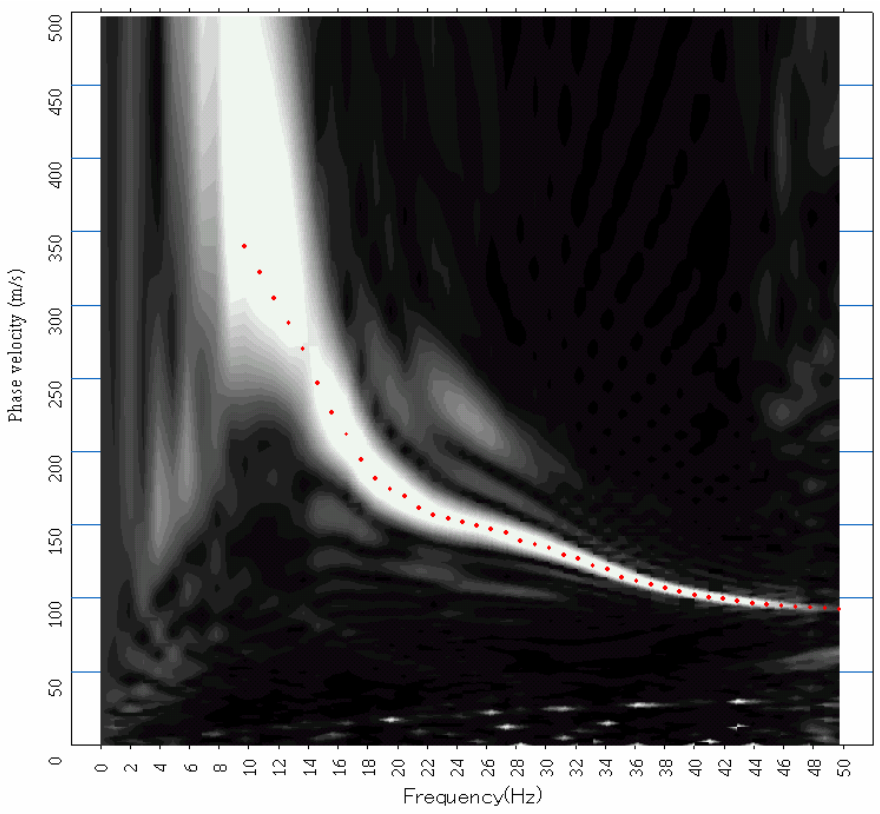

Fig.2.5.12. Image of dispersion curve (shot point 65.8m).

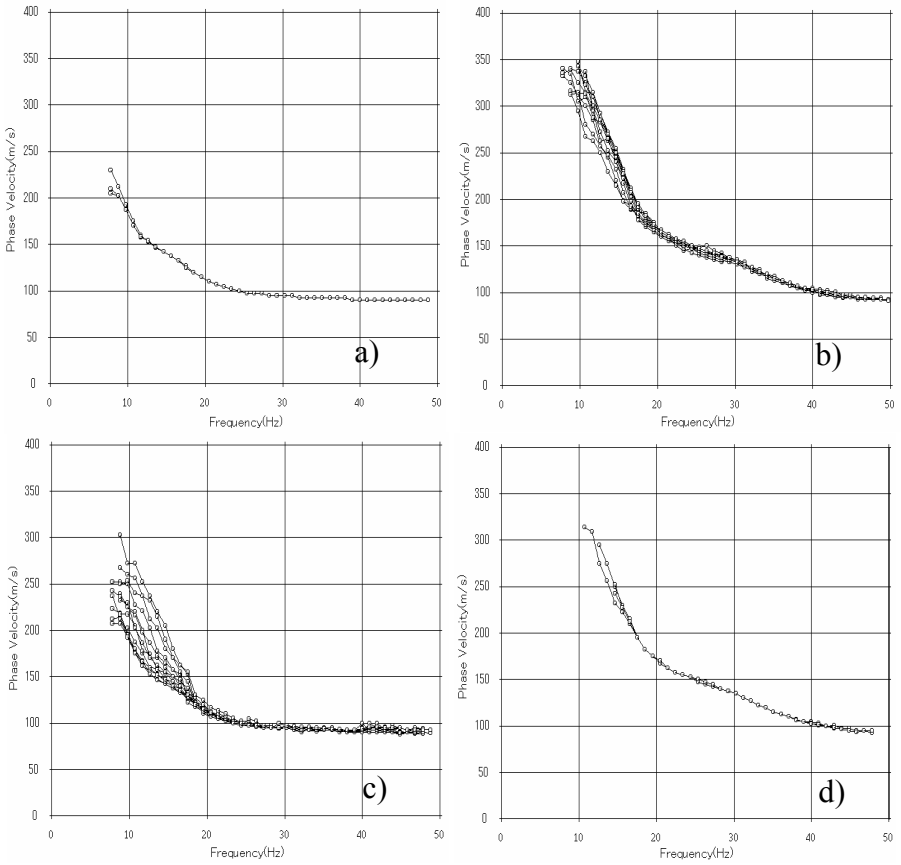

Fig.2.5.13. Dispersion curves calculated from 31 common source gathers. (a) A receiver spread is on the left side of the step. (b) A receiver spread is on the step (spread center is 36.5～60.5m). (c) A receiver spread is on the step (spread center is 62.5～82.5m). (d) A receiver spread is on the right side of the step.

2.6 Calculating Phase-velocity from Multi-channel Surface-wave Data

The simplest method to obtain phase-velocity is calculating the cross-correlation of two traces recorded at different position (i.e., Guo and Liu, 1999). Let us start with two traces *f(t)* and *g(t)* obtained at two receives with separation Δx. Two traces are transformed info frequency domain by the Fourier transform (equation 2.6.1) and written as $F(\omega)$ and $G(\omega)$ using angular frequency ω.

$$F(\omega)=\frac{1}{2\pi}\int_{-\infty}^{+\infty} f(t)\cdot\exp^{-i\omega t}dt$$

$$G(\omega)=\frac{1}{2\pi}\int_{-\infty}^{+\infty} g(t)\cdot\exp^{-i\omega t}dt \qquad (2.6.1)$$

Cross-correlation of the two traces ($CC_{fg}(\omega)$) can be defined in frequency domain as,

$$CC_{fg}(\omega)=F(\omega)\cdot\overline{G(\omega)}=A_f(\omega)A_g(\omega)\cdot\exp^{i\Delta\phi(\omega)} \qquad (2.6.2)$$

where, $A_f(\omega)$ and $A_g(\omega)$ are amplitude of $F(\omega)$and $G(\omega)$ respectively, $\overline{G(\omega)}$ is the complex conjugate of $G(\omega)$. $\Delta\phi(\omega)$ is the phase-spectrum of the cross-correlation $CC_{fg}(\omega)$ and it is equal to the phase-difference of two traces. $\Delta\phi(\omega)$ can be simply calculated from the the cross-correlation $CC_{fg}(\omega)$ as follows:

$$\Delta\phi(\omega)=\arctan\left(\frac{\mathrm{Re}\left(CC_{fg}(\omega)\right)}{\mathrm{Im}\left(CC_{fg}(\omega)\right)}\right). \qquad (2.6.3)$$

Phase-velocity $c(\omega)$ is directly related to the phase-difference $\Delta\phi(\omega)$.

$$c(\omega)=\frac{\omega\cdot\Delta x}{\Delta\phi(\omega)} \qquad (2.6.4)$$

This method has, however, serious limitations, such as receiver spacing must be chosen carefully in order to avoid phase wraparound, the method cannot distinguish the fundamental mode of dispersion curve from other modes or body waves, and the method cannot be applied two more than three traces.

McMechan and Yedlin(1981) proposed the method that can calculate phase-velocity directly from a multi-channel common shot gather transforming time-domain data (time vs. distance) to frequency domain (phase-velocity vs. frequency) using a τ-p transform and the Fourier transform. The method is much better than the cross-correlation so that the method enable us to calculate the phase-velocity directory from multi-channel (more than three traces) waveform data and to separate the fundamental mode of phase-velocity curve from higher modes and body waves visually. Park et al.(1999a) also proposed a waveform transformation, so called Multi-channel Analysis of Surface Waves (MASW), that can calculate phase-velocity directly from a multi-channel common shot gather similar to the McMechan's method. McMechan and Yedlin(1981) calculate the apparent velocity (p) firstly and transform it to the frequency domain secondary. On the contrary, Park et. al.(1999a) transform a shot gather into the frequency-domain firstly and calculate phase-velocity using phase shift secondary. Figure 2.6.1 shows the outline of two phase-velocity calculation methods. Park et al.(1999a) shows that the later one give us clear phase-velocity curve even if the number of traces is limited. We have compared two methods and drawn same conclusion. The computation procedure of the later one is also much simpler than the first one. For the sake of computation time saving and simpler coding, the later method overcomes the first one. We will use the later method in this study. Computation procedure of The Multi-channel Analysis of Surface Waves proposed by Park et. al.(1999a) can be summarized as follows:

1. Each trace in observed shot gathers is transformed into frequency domain by the Fast Fourier Transform (FFT).

$$F(x,\omega) = \frac{1}{2\pi}\int_{-\infty}^{+\infty} f(x,t)\cdot e^{-i\omega t}\,dt \qquad (2.6.5)$$

where, x is the distance, t is time, ω is frequency, $f(x,t)$ is a shot gather in time-domain and $F(x,\omega)$ is the shot gather in frequency-domain.

2. The shot gather in frequency-domain integrated over the spacing with respect to apparent velocities (c : phase-velocity).

$$F(c,\omega) = \int_{-\infty}^{+\infty} \frac{F(x,\omega)}{|F(x,\omega)|} e^{i\omega\frac{x}{c}} dx \qquad (2.6.6)$$

3. The integration is repeated through all apparent velocities to be calculated.

4. Absolute value is calculated and plotted on phase-velocity (c) vs. frequency domain.

$$p(c,\omega) = |F(c,\omega)| \qquad (2.6.7)$$

Figure 2.6.2 shows the example of phase-velocity transformation. Top figure (a) shows a time-domain shot gather and bottom figure (b) shows its phase-velocity image in frequency domain.

5. Finally, phase-velocities are determined as the maximum amplitude in each frequency.

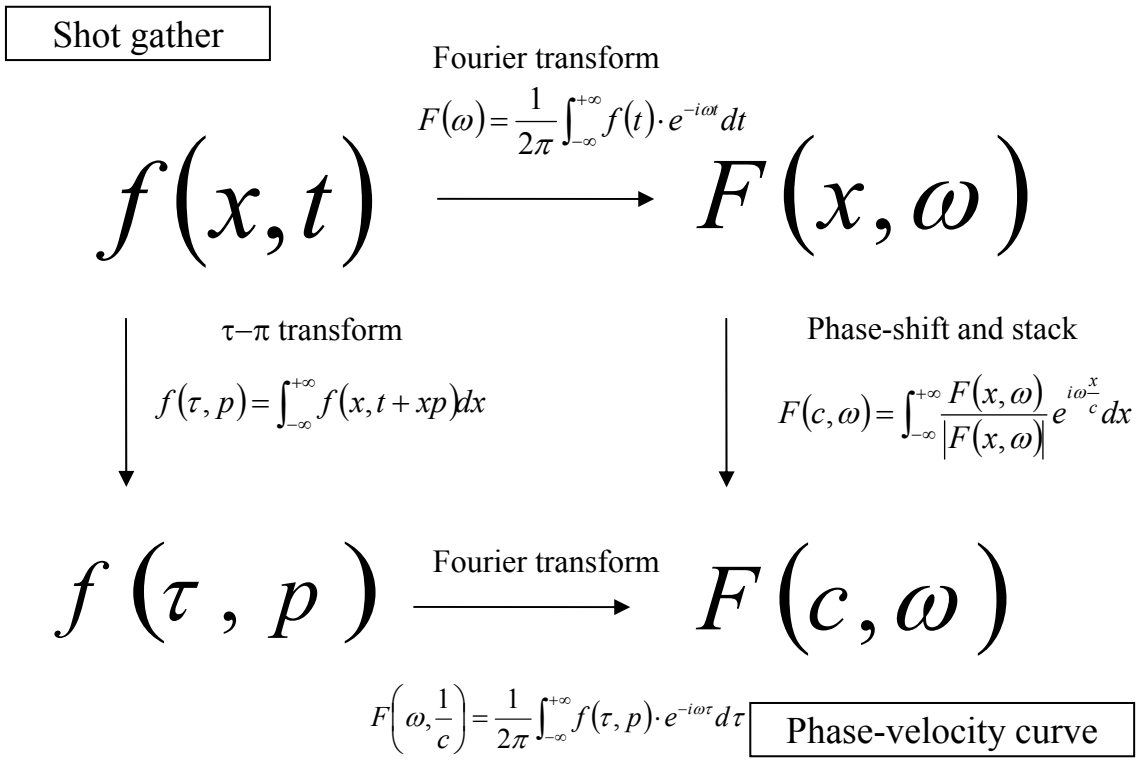

Figure 2.6.1 Outline of two transformation methods.

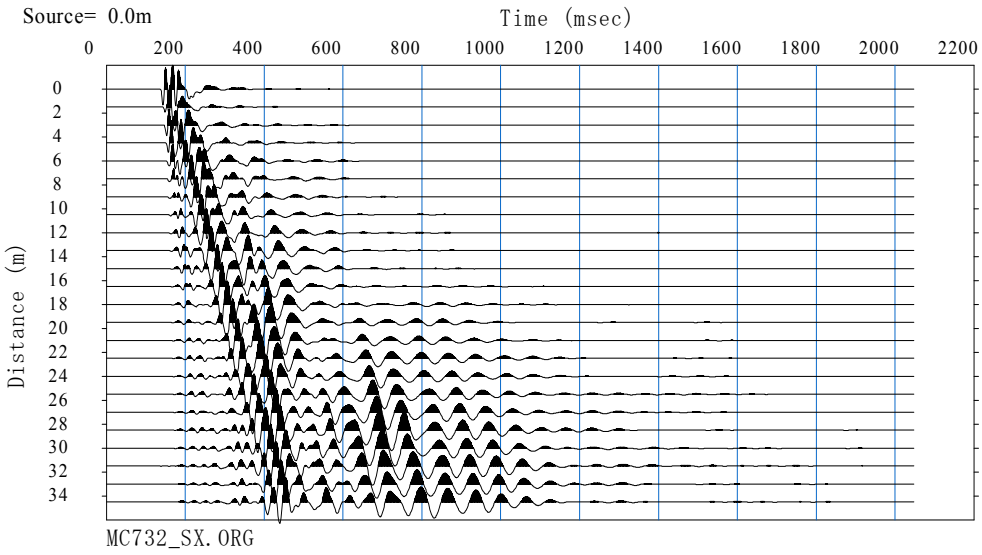

a) Time-domain shot gather.

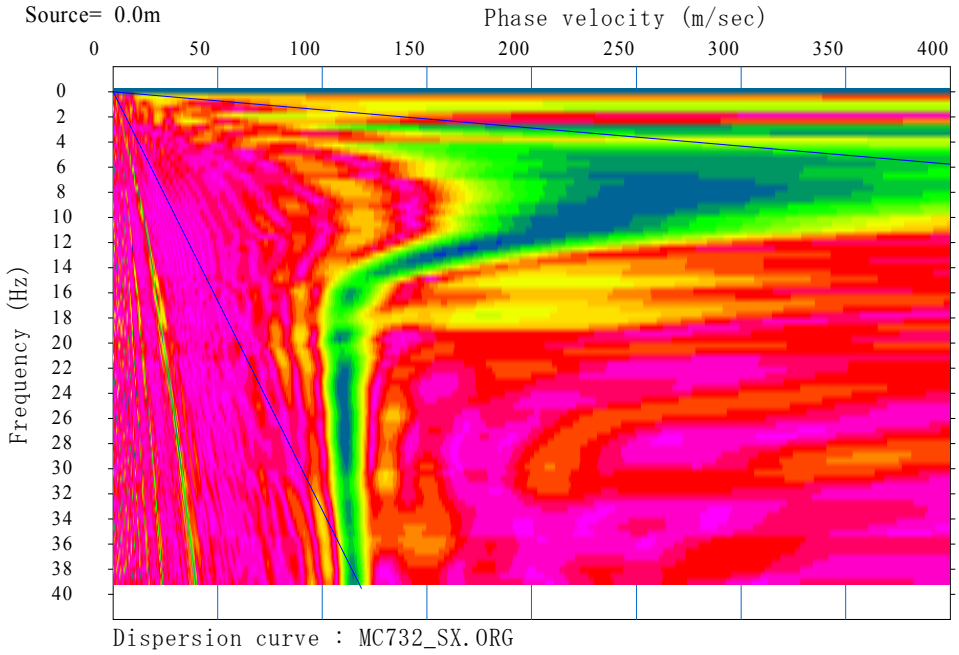

b) phase-velocity image in frequency domain.

Figure 2.6.2 Example of phase-velocity transformation. Time-domain shot gather (top) and its phase-velocity image in frequency domain (bottom).

2.7 Phase-velocity Analysis of Micro-tremors

A micro-tremor is weak vibration on the ground surface and mainly consists of surface-waves. S-wave velocity model of the ground can be obtained by analyzing the phase-velocity of the micro-tremor data. In order to calculate the phase-velocity of micro-tremors by the multi-channel analysis of surface-waves, the propagating direction of micro-tremors has to be known. Micro-tremors, however, do not propagate specific direction and it is impossible to determine propagating direction. Aki (1957) proposed a spatial auto correlation (SPAC) method in which micro-tremor data is statistically analyzed, for calculating the phase velocity of surface-waves in micro-tremor data. The SPAC method can be summarized as follows.

Let us start with two traces *f(t)* and *g(t)* obtained at two receives with separation Δx (Figure 2.7.1). Two traces are transformed info frequency domain by the Fourier transform and written as $F(\omega)$ and $G(\omega)$. Cross-correlation of the two traces ($CC_{fg}(\omega)$) can be defined as,

$$CC_{fg}(\omega) = F(\omega)\cdot\overline{G(\omega)} = A_f(\omega)A_g(\omega)\cdot\exp^{i\Delta\phi(\omega)}. \tag{2.7.1}$$

where, $A_f(\omega)$ and $A_g(\omega)$ are amplitude of $F(\omega)$and $G(\omega)$ respectively. $\Delta\phi(\omega)$ is phase-difference of two traces. Complex coherence of two traces $COH_{fg}(\omega)$ is defined as,

$$COH_{fg}(\omega) = \frac{CC_{fg}(\omega)}{A_f(\omega)A_g(\omega)}. \tag{2.7.2}$$

Phase-velocity ($c(\omega)$) can be calculated from phase-difference ($\Delta\phi(\omega)$) as,

$$c(\omega) = \frac{\omega\cdot\Delta x}{\Delta\phi(\omega)}. \tag{2.7.3}$$

where, Δx is separation of two receivers. Using the equation (2.7.3), Phase difference ($\Delta\phi(\omega)$) can be written as,

$$\Delta\phi(\omega) = \frac{\omega \cdot \Delta x}{c(\omega)}. \tag{2.7.4}$$

Substituting this into the equation (2.7.1) gives,

$$CC_{fg}(\omega) = F(\omega) \cdot \overline{G(\omega)} = A_f(\omega) A_g(\omega) \cdot \exp^{i\left(\frac{\omega \cdot \Delta x}{c(\omega)}\right)}. \tag{2.7.5}$$

Using the equation (2.7.5), the equation (2.7.2) can be rewritten as,

$$COH_{fg}(\omega) = \frac{CC_{fg}(\omega)}{A_f(\omega) A_g(\omega)} = \exp^{i\left(\frac{\omega \cdot \Delta x}{c(\omega)}\right)}. \tag{2.7.6}$$

Taking real part of this gives,

$$\mathrm{Re}\left(COH_{fg}(\omega)\right) = \cos\left(\frac{\omega \cdot \Delta x}{c(\omega)}\right). \tag{2.7.7}$$

The equation (2.7.7) means that the real part of complex coherence for two traces goes to cosine function.

The spatial auto-correlation (SPAC) for two dimensional array is defined as the directional average of complex coherence, left side of the equation (2.7.7), as,

$$SPAC(r, \omega) = \frac{1}{2\pi} \int_{\varphi=0}^{\varphi=2\pi} COH(r, \varphi, \omega) d\varphi. \tag{2.7.8}$$

where, r is separation of two receivers or radius of a circle, φ is direction of two sensors. The equation (2.7.8) means that calculating complex coherence for two sensors with separation r and direction φ, and averaging complex coherence along a circle (Figure 2.7.2).

The directional average of trigonometric functions goes to Bessel function as,

$$J_0(kr) = \frac{1}{2\pi} \int_{\varphi=0}^{\varphi=2\pi} e^{ikr\cos\varphi} d\varphi. \tag{2.7.9}$$

where, k is wave number. Using the equation (2.7.9), directional average of right side of

equation (2.7.7) can be written as,

$$J_0\left(\frac{\omega \cdot r}{c(\omega)}\right) = \frac{1}{2\pi}\int_{\varphi=0}^{\varphi=2\pi} \cos\left(\frac{\omega \cdot r}{c(\omega)}, \varphi\right) d\varphi . \qquad (2.7.10)$$

From the equation (2.7.8) and (2.7.10)

$$\mathrm{Re}\left(SPAC(r,\omega)\right) = J_0\left(\frac{\omega}{c(\omega)} r\right) \qquad (2.7.11)$$

where, $c(\omega)$ is phase-velocity at angular frequency ω. The left term of the equation (2.7.11) can be calculated from observed microtremor-data. Phase-velocity is calculated by comparing the spatial autocorrelation in left term and Bessel function in right term of the equation (2.7.11) changing the phase-velocity $c(\omega)$ in the right term of the equation. The velocity that minimize error in the equation (2.7.11) can be considered as the phase-velocity at the angular frequency ω.

The spatial auto correlation defined as the equation (2.7.8) can be only applied to isotropic arrays, such as circles or triangles, and cannot be applied to anisotropic arrays, such as lines or L-shapes, in order to calculate directional average expressed as the equation (2.7.8). However, if we assume that micro-tremors do not come from some specific direction and come from all directions equally, the directional average in the equation (2.7.8) can be calculated even if arrays are anisotropic. Generally, the micro-tremor's direction of propagation is not stable and averaging enough long time of micro-tremor data enables us to calculate the directional average of the equation (2.7.8) correctly. In this paper, we acquired enough long time micro-tremor data (at least 10 minutes) and averaged identical receiver spacing complex coherence in order to calculate spatial autocorrelation using anisotropic array.

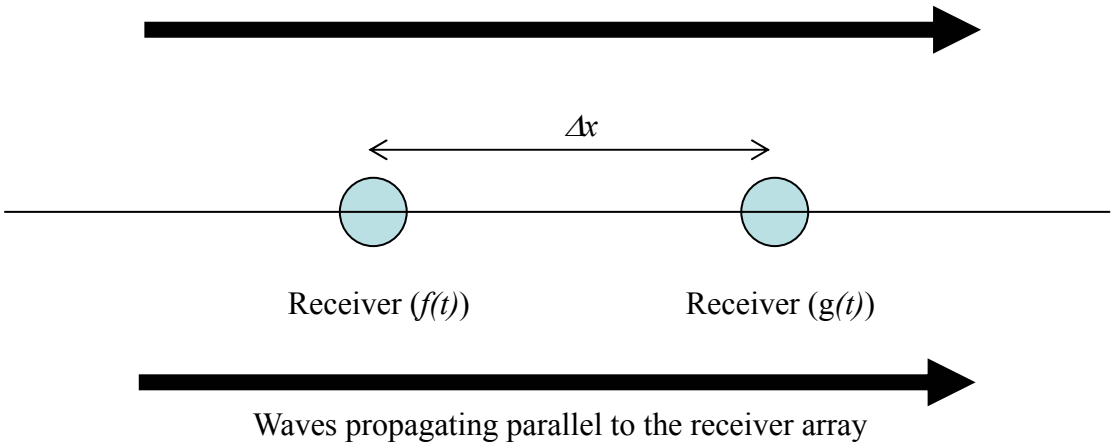

Figure 2.7.1. Two receives with separation Δx

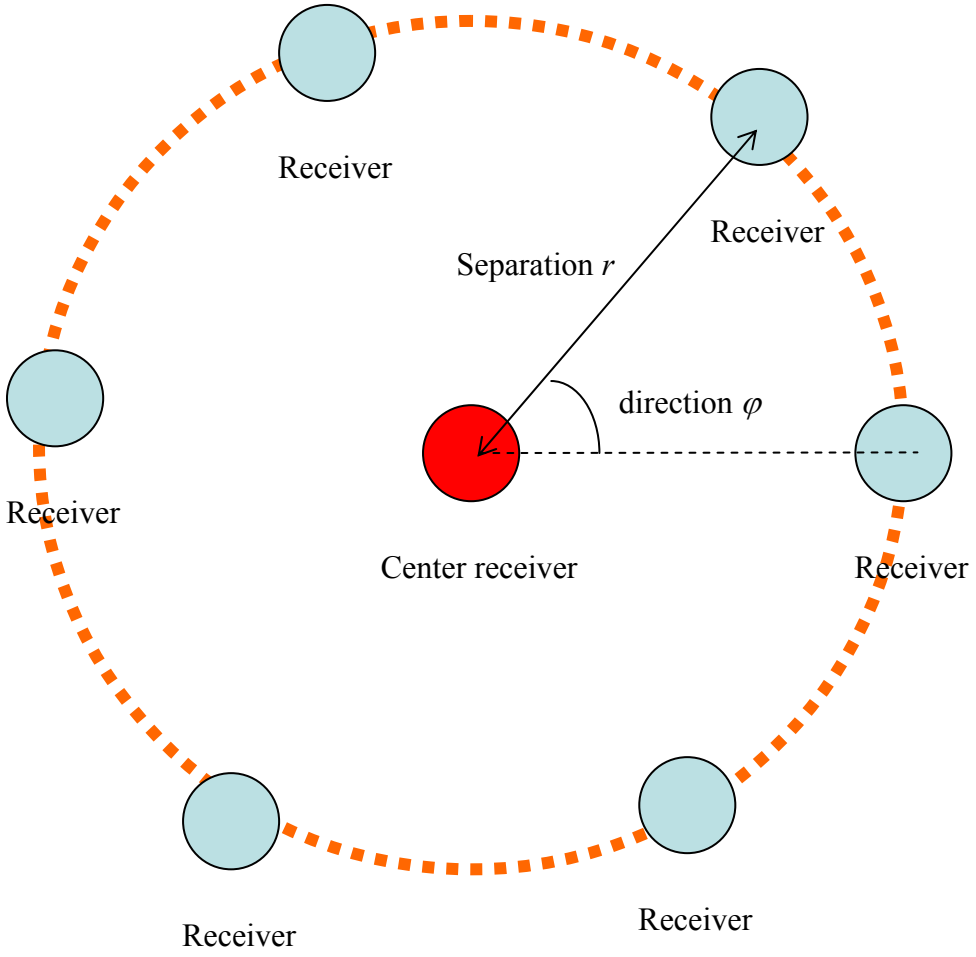

Figure 2.7.2. Receives on a circle.

2.8 Dispersion Curve Inversion

2.8.1 Introduction

S-wave velocity model is obtained from phase-velocity curves, calculated through waveform processing explained in previous sections, by a non-linear inversion. There are so many non-linear inversion methods, such as a least square method, a Genetic algorithm, a simulated annealing etc.. For the sake of simplicity and stability, a traditional non-linear least square method will be employed for the inversion in following chapters. Generally, the number of layers (usually 3 to 5 layers) is fixed and both S-wave velocity and thickness of each layer are estimated in the inversion of phase-velocity curve (e.g. Xia et al., 1999b). However, the method cannot avoid non-uniqueness in determination of the number of layers. The method has to solve two different parameters, such as S-velocity and thickness. In order to solve the inversion stably and uniquely, we fix the number of layers (10 to 15 layers) and thickness of each layers through iteration. S-wave velocity for each layer is only handled as unknown parameters. P-wave velocity and density are linearly related to the S-wave velocity with empirical equations (Kitsunezaki et al., 1990; Ludwig et al.(1970)) in each step of iteration. Computation procedure is summarized as follows.

2.8.2 Inversion for One Phase-velocity Curve

At first, we describe the inversion for one phase-velocity curve. A one-dimensional *M* layers S-wave velocity model to be inverted can be written as vector *x* (Figure 2.8.1).

$$x^T = \left(Vs_1, Vs_2, \cdots, Vs_M\right) \tag{2.8.1}$$

Where, $Vs_1, Vs_2, \cdots Vs_M$ are S-wave velocity for 1st layer, 2nd layer, Mth layer respectively. Objective function in inversion is,

$$\sum_i^N \left(f_i^{obs} - f_i^{cal}\left(Vs_1, Vs_2, \cdots Vs_N\right)\right)^2 = \sum_i^N \left(f_i^{obs} - f_i^{cal}\left(x\right)\right)^2 \longrightarrow Minimize \tag{2.8.2}$$

.

where N is the number of observed phase-velocity data, f^{obs} are phase-velocities obtained from observed waveform data and f^{cal} are theoretical phase-velocities for the S-wave velocity model.. A theoretical phase-velocity curve is calculated by the compound matrix method proposed by Saito and Kabasawa (1993). We use the following notation for phase-velocity f^{cal}.

$$f_i = f_i^{cal}(x) \qquad (i=1 \text{ to } N : N \text{ is the number of observed phase-velocities}) \qquad (2.8.3)$$

Then, a Jacobian matrix can be written as;

$$a = \begin{pmatrix} \frac{\partial f_1}{\partial Vs_1} & \frac{\partial f_1}{\partial Vs_2} & \cdot & \frac{\partial f_1}{\partial Vs_M} \\ \frac{\partial f_2}{\partial Vs_1} & \frac{\partial f_2}{\partial Vs_2} & \cdot & \frac{\partial f_2}{\partial Vs_M} \\ \frac{\partial f_3}{\partial Vs_1} & \frac{\partial f_3}{\partial Vs_2} & \cdot & \frac{\partial f_3}{\partial Vs_M} \\ \cdot & \cdot & \cdot & \cdot \\ \frac{\partial f_N}{\partial Vs_1} & \frac{\partial f_N}{\partial Vs_2} & \cdot & \frac{\partial f_N}{\partial Vs_M} \end{pmatrix}. \qquad (2.8.4)$$

We can see that the unknown vector x is in derivatives and it makes the inversion non-linear. Therefore, an initial model has to be constructed and the model is modified so that the residual between observed and theoretical phase-velocities to be small. In actual calculation, elements of the Jacobian matrix a are calculated numerically using a finite-difference method (Xia et al., 1999a). A residual between observed and theoretical phase-velocities can be expressed as vector y;

$$y^T = \begin{pmatrix} f_1^{obs} - f_i^{cal}(x) \\ f_2^{obs} - f_2^{cal}(x) \\ f_3^{obs} - f_3^{cal}(x) \\ \cdot \\ f_N^{obs} - f_N^{cal}(x) \end{pmatrix} \qquad (2.8.5)$$

A correction vector Δx can be calculated by least square method as follows;.

$$\left(a^T a + \varepsilon I\right)\Delta x = a^T y \quad . \tag{2.8.6}$$

Where, ε is a damping parameter that makes calculation stable. In the l^{th} iteration, new estimated model x^{l+1} is calculated as;

$$x^{l+1} = x^l + \gamma \Delta x \quad , \tag{2.8.7}$$

where γ is stabilizer and smaller than 1. The method constructing the initial model (x^0) will be described later.

Generally, the inversion of geophysical exploration cannot be solved stably because the geometry of sources and receivers is limited. Therefore, spatial regularization is included in order to solve the inversion stably. Our inversion of phase-velocity curve may be not stable because it includes many layers as unknowns. Following vertical regularization is included in order to make inversion stable.

$$\left(a^T a + \alpha r_v^T r_v + \varepsilon I\right)\Delta x = a^T y \tag{2.8.8}$$

Where, r_v is the difference between S-wave velocity of two successive layers as follows,

$$r_v x = \begin{pmatrix} 1 & -1 & 0 & \cdot & 0 & 0 \\ 0 & 1 & -1 & \cdot & 0 & 0 \\ 0 & 0 & 1 & \cdot & 0 & 0 \\ \cdot & \cdot & \cdot & \cdot & \cdot & \cdot \\ 0 & 0 & 0 & \cdot & 1 & -1 \end{pmatrix} \begin{pmatrix} Vs_1 \\ Vs_2 \\ Vs_3 \\ \cdot \\ Vs_{M-1} \\ Vs_M \end{pmatrix} = \begin{pmatrix} 0 \\ 0 \\ 0 \\ 0 \\ 0 \end{pmatrix} . \tag{2.8.9}$$

α is weight of regularization and large α makes inverted model smoother.

2.8.3 Inversion for Multi Phase-velocity Curve

A two-dimensional analysis proposed by Xia et al.(1999a) performs

one-dimensional inversion successively and aligns one-dimensional S-wave velocity model horizontally as a “pseudo” two dimension velocity model. This method, however, inverts dispersion curves individually and slight difference in dispersion curves may result in large difference between S-wave velocity models. Such unstable inversion makes unnatural horizontal discontinuity in inverted two-dimensional velocity model. In order to avoid such horizontal discontinuity, we invert dispersion curves with horizontal regularization. Feng et al. (2001) has successfully applied horizontal regularization to the dispersion curves obtained through micro-tremors array measurements. We have applied similar horizontal regularization to the dispersion curves obtained through the surface-wave method so that a two-dimensional velocity model is horizontally continuous. In the inversion, all dispersion curves in a survey line are included in one Jacobian matrix and a horizontal regularization matrix is solved simultaneously as follows.

There is a survey line that includes K dispersion curves obtained from each shot gather or CMPCC gather (explained in the Chapter 3). Jacobian matrices for each shot gather (or CMPCC gather) $a_1, a_2, a_3, \cdots a_K$ an be expressed as a single matrix A as,

$$A = a_1 + a_2 + a_3 + \cdots + a_K = \begin{pmatrix} a_1 & \mathrm{O} & \mathrm{O} & \mathrm{O} & \mathrm{O} \\ \mathrm{O} & a_2 & \mathrm{O} & \mathrm{O} & \mathrm{O} \\ \mathrm{O} & \mathrm{O} & a_3 & \mathrm{O} & \mathrm{O} \\ \mathrm{O} & \mathrm{O} & \mathrm{O} & \cdot & \mathrm{O} \\ \mathrm{O} & \mathrm{O} & \mathrm{O} & \mathrm{O} & a_K \end{pmatrix} \quad . \tag{2.8.10}$$

A correction vector Δx, a residual vector y and a vertical regularization vector r_v for each shot gather can be also expressed as single matrices,

$$X = x_1 + x_2 + x_3 + \cdots + x_K \tag{2.8.11}$$
$$\Delta X = \Delta x_1 + \Delta x_2 + \Delta x_3 + \cdots + \Delta x_K \tag{2.8.12}$$
$$Y = y_1 + y_2 + y_3 + \cdots + y_K \tag{2.8.13}$$
$$R_v = r_{v1} + r_{v2} + r_{v3} + \cdots + r_{vK} \quad . \tag{2.8.14}$$

Using above notation, a following simultaneous equation is solved in each step of iteration.

$$\left(A^T A + \alpha R_v^T R_v + \beta R_h^T R_h + \varepsilon I\right)\Delta X = A^T Y \tag{2.8.15}$$

Where, R_h is the difference between horizontally successive S-wave velocity models as follows.

$$R_h X = \left(\begin{array}{cccc|cccc|c|cccc} 1 & 0 & \cdot\cdot & 0 & -1 & 0 & \cdot & 0 & \cdot\cdot & 0 & 0 & \cdot & 0 \\ 0 & 1 & \cdot & 0 & 0 & 1 & \cdot & 0 & \cdot\cdot & 0 & 0 & \cdot & 0 \\ \cdot & \cdot & \cdot & \cdot & \cdot & \cdot & \cdot & \cdot & \cdot\cdot & \cdot & \cdot & \cdot & \cdot \\ 0 & 0 & \cdot & 1 & 0 & 0 & \cdot & -1 & \cdot\cdot & 0 & 0 & \cdot & 0 \\ \hline 0 & 0 & \cdot & 0 & 1 & 0 & \cdot & 0 & \cdot\cdot & 0 & 0 & \cdot & 0 \\ 0 & 0 & \cdot & 0 & 0 & 1 & \cdot & 0 & \cdot\cdot & 0 & 0 & \cdot & 0 \\ \cdot & \cdot & \cdot & \cdot & \cdot & \cdot & \cdot & \cdot & \cdot\cdot & \cdot & \cdot & \cdot & \cdot \\ 0 & 0 & 0 & 0 & 0 & 0 & \cdot & 1 & \cdot\cdot & 0 & 0 & \cdot & 0 \\ \hline \cdot & \cdot & \cdot & \cdot & \cdot & \cdot & \cdot & \cdot & \cdot\cdot & \cdot & \cdot & \cdot & \cdot \\ \hline 0 & 0 & \cdot & 0 & 0 & 0 & \cdot & 0 & \cdot\cdot & -1 & 0 & \cdot & 0 \\ 0 & 0 & \cdot & 0 & 0 & 0 & \cdot & 0 & \cdot\cdot & 0 & -1 & \cdot & 0 \\ \cdot & \cdot & \cdot & \cdot & \cdot & \cdot & \cdot & \cdot & \cdot\cdot & \cdot & \cdot & \cdot & \cdot \\ 0 & 0 & \cdot & 0 & 0 & 0 & \cdot & 0 & \cdot\cdot & 0 & 0 & \cdot & -1 \end{array}\right) \left(\begin{array}{c} Vs_{11} \\ Vs_{21} \\ \cdot \\ Vs_{M1} \\ \hline Vs_{12} \\ Vs_{22} \\ \cdot \\ Vs_{M2} \\ \hline \cdot \\ \hline Vs_{1K} \\ Vs_{2K} \\ \cdot \\ Vs_{MK} \end{array}\right) = \left(\begin{array}{c} 0 \\ 0 \\ 0 \\ 0 \\ 0 \\ 0 \\ 0 \\ 0 \\ \cdot \\ 0 \\ 0 \\ 0 \\ 0 \end{array}\right) \quad (2.8.16)$$

α and β are weight of regularization and large α and β values make inverted model smoother. We put depth dependent in the horizontal regularization matrix R_h so that deeper region is smoother, in order to take account the resolution is lower in deeper region.

2.8.4 Initial Model

An initial model is constructed by simple depth transformation as follows (See Figure 2.8.3). At first, wavelength is calculated from frequency and phase-velocity (Figure 2.8.3 (a)). Next, depth is defined as 1/3 of wavelength and plotted on depth-velocity chart with its phase-velocity (Figure 2.8.3 (b)). It is well known that the phase-velocity of Rayleigh wave approximately reflects the average S-wave velocity down to the depth of 1/2 to 1/4 wavelength. This procedure is so called “wavelength transformation” in terms of apparent depth (D_A) and Rayleigh wave velocity (VR).

$$D_A = a * \lambda = a * \frac{c}{f} \qquad (a \text{ is } 1/2 \text{ to } 1/4) \qquad (2.8.17)$$

$$VR = c = b * Vs \qquad (b \text{ is } 0.9 \text{ to } 0.95) \qquad (2.8.18)$$

Where, c is phase-velocity and f is frequency, and λ is wave length. b is defined based on the relationship between S-wave velocity and phase-velocity of Rayleigh waves in homogeneous half space (see Figure 2.3.4).

An S-wave velocity model is defined based on this apparent depth (D_A) and phase-velocity (c) or Rayleigh wave velocity (V_R) (Figure 2.8.3 (c)). Figure 2.8.4 shows the comparison of observed and theoretical dispersion curve for initial model based on 1/3 wavelength transformation. We can see that the theoretical dispersion curve fir initial model is not far from the observed data. It implies that the S-wave velocity model obtained through the 1/3 wavelength transformation is very good as an initial model.

Ground surface

Vs_1
Vs_1
Vs_3
.
.
Vs_M

Figure 2.8.1 A one-dimensional *M* layers S-wave velocity model.

Ground surface

Vs_{11}	Vs_{12}	Vs_{13}	. . .	Vs_{1K}
Vs_{11}	Vs_{12}	Vs_{13}	. . .	Vs_{1K}
Vs_{31}	Vs_{32}	Vs_{33}	. . .	Vs_{3K}
.	.	.	. . .	.
.	.	.	. . .	.
Vs_{M1}	Vs_{M2}	Vs_{M3}	. . .	Vs_{MK}

Figure 2.8.2 A two-dimensional *M* layers S-wave velocity model.

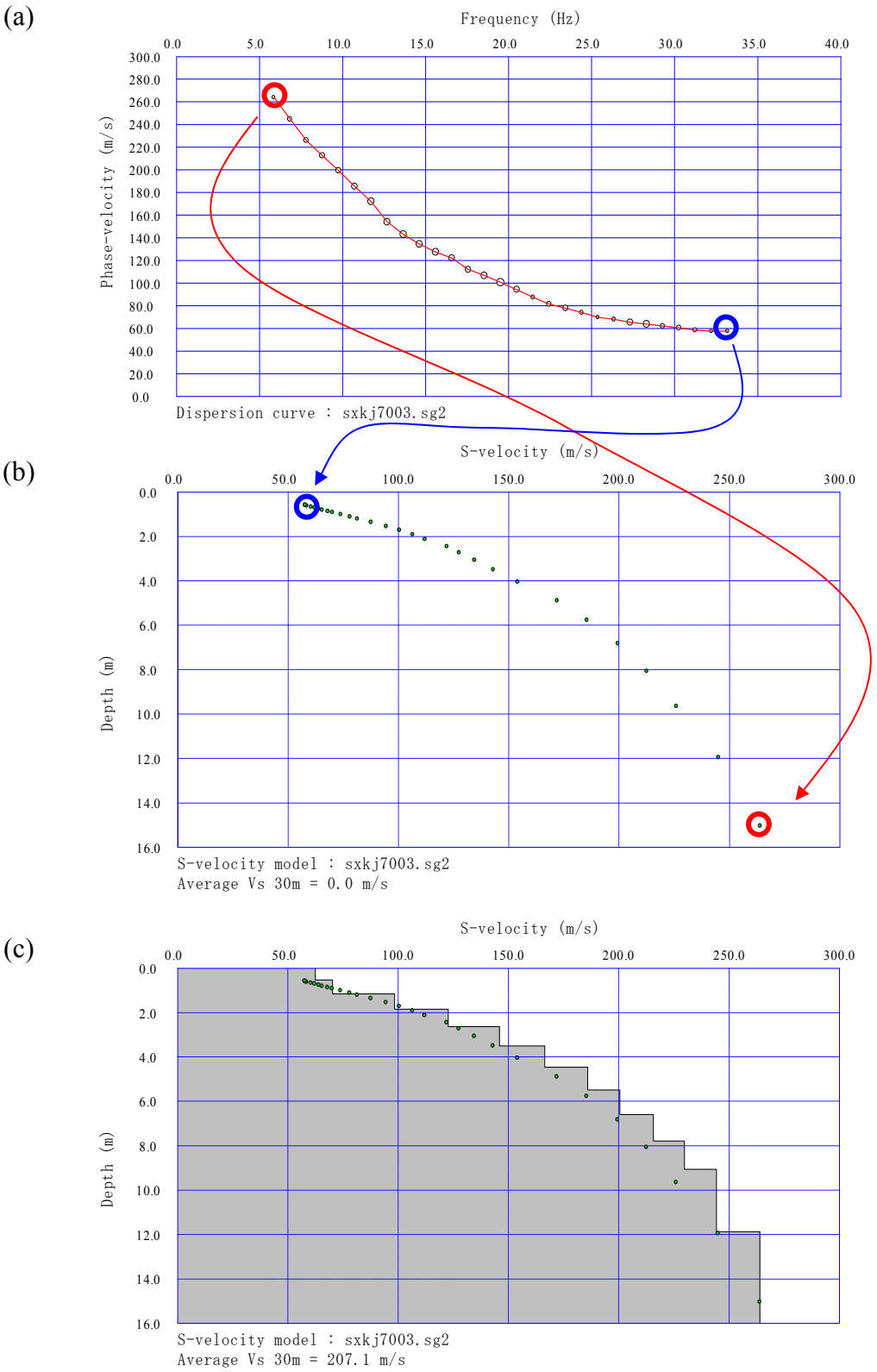

Figure 2.8.3 Initial model based on 1/3 wavelength transformation.

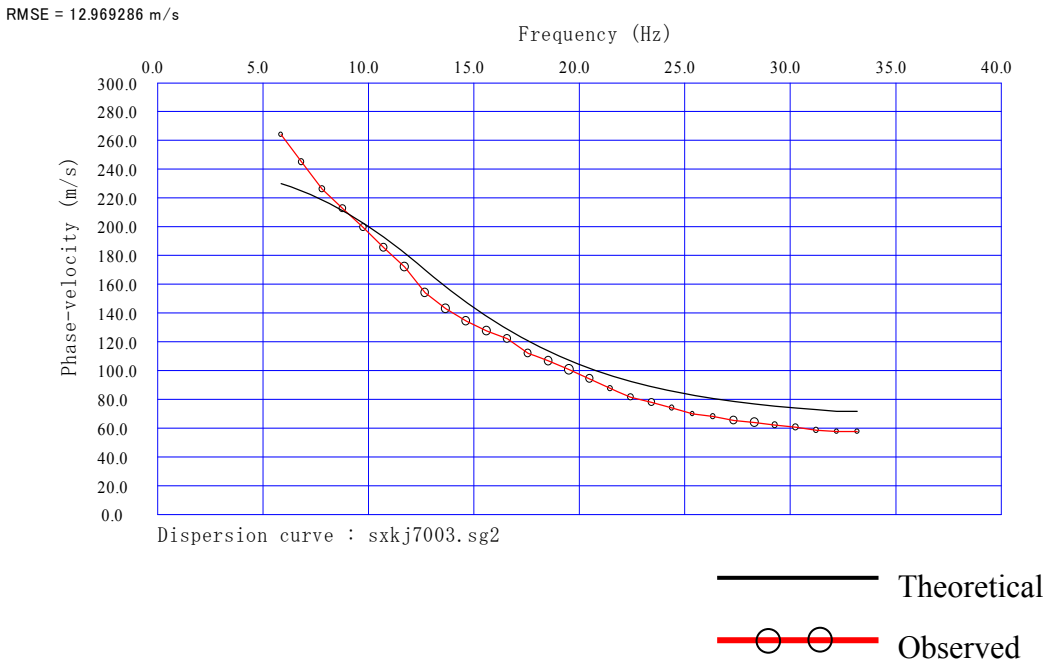

Figure 2.8.4 Comparison of observed and theoretical dispersion curve for initial model based on 1/3 wavelength transformation.

2.9 Summary

In the refraction or reflection seismic analysis, surface-waves have been considered as noise for long years and little attention has been given to the use of the surface-waves. We have reviewed fundamental theory behind surface wave propagation and its analysis in this chapter. Theoretical consideration and numerical examples have shown the surface-waves are understandable and sub-surface velocity model can be derived from the dispersion character of surface-waves. Dispersion curves can be obtained from both active and passive surface-wave data in terms of simple waveform transformation. Numerical examples have also shown that the amplitude of the surface-waves is relatively large in comparison with refraction and reflection waves. It indicates that the data acquisition of surface-waves is easy and implies that the surface-wave methods can be used for many geo-technical investigations as non-destructive testing. We are going to evolve the surface-wave methods so that the methods can rapidly two-dimensional S-wave velocity model in following chapters.

References

Aki, K., 1957, Space and time spectra of stationary stochastic waves, with special reference to microtremors, Bull. Earthq. Res. Ins., 35, 415-456,.

Aki, K. and Richards, P. G., 1980, Quantitative seismology, W. H. Freeman and company.

Aoi, S., and Fujiwara, H., 1999, 3D Finite-Difference Method Using Discontinuous Grids, Bull. Seism. Soc. Am. 89, 918-930.

Blanch, J. O., Robertsson, J. O. A. and Symes, W. W., 1993, Viscoelastic finite-difference modeling, Tech. Rep. 93-04, Department of Computational and Applied Mathematics, Rice University.

Blanch, J. O., Robertsson, J. O., and Symes, W. W., 1995, Modeling of a constant Q: Methodology and algorithm for an efficient and optimally inexpensive viscoelastic technique, Geophysics, 60, 176-184.

Bohlen, T. and Milkerite T., 2001, Parallel finite-difference modeling of seismic wave propagation in 3-D elastic random media, 71th Ann. Int. Meet., Soc. Expl. Geophys. Exp. Abst., 1147-1150.

Bouchon, M., 1979, Discrete wave number representation of elastic wave fields in three-space dimensions, J. Geophys. Res., 84, 3609-3614.

Carcione, J. M., Kosloff, D., and Kosloff, R., 1988, Wave propagation simulation in a linear viscoelastic medium, Geophys. J. Roy. Astr. Soc., 93, 393-407.

Carcione, J. M., 1993, Seismic modeling in viscoelastic media, Geophysics, 58, 110-120.

Cerjan, C., Kosloff, D., Kosroff, R. and Reshef, M., 1985, A nonreflecting boundary condition for discrete acoustic and elastic wave equations, Geophysics, 50, 705-708.

Christensen, R. M., 1982, Theory of viscoelasticity -An introduction: Academic Press, Inc.

Day, S. M., 1998, Efficient simulation of constant Q using coarse-grained memory variables, Bull. Seism. Soc. Am. 88, 1051-1062.

Day, S. M., and Minster, J. B., 1984, Numerical simulation of attenuated wavefields

using a Pade approximant method, Geophys. J. Roy. Astr. Soc., 78, 105-118.

De Lilla, A., 1997, Finite difference seismic wave propagation using discontinuous grid sizes, M.Sc. Thesis, Massachusetts Institute of Technology.

Emmerich, H., and Korn, M., 1987, Incorporation of attenuation into time-domain computations of seismic wave fields, Geophysics, 52, 1252-1264.

Falk, J., Tessmer, E., and Gajewski, D., 1995, Tube wave modeling by the finite-difference method with varying grid spacing, Technical report, Institute fur Geophysik, Universitat Hamburg, Internal report.

Feng, S., Sugiyama, T., and Yamanaka, H., 2001, Multi-site inversion in array micro tremor survey, Proceedings of the 104th SEJG Conference, 35-39.

Fukuyama, E. and Mikumo, T., 1993, Dynamic rupture analysis: Inversion for the source process of the 1990 Izu-Oshima, Japan, earthequake (M=6.5), J. Geophys. Res., 98, 6529-6542.

Graves, R. W., 1996, Simulating seismic wave propagation in 3D elastic media using staggered-grid finite differences, Bull. Seism. Soc. Am., 86, 1091-1106.

Guo, T., and Liu, L., 1999, Non-intrusive evaluation of submarine tunnel foundation using dynamic high-frequency surface wave prospecting, Proceedings of the symposium on the application of geophysics to engineering and environmental problems '99, 67-74.

Hayashi, K., Burns, D. R, and Toksöz, M N., 2001, Discontinuous grid finite-difference seismic modeling including surface topography, Bulletin Seismological Society of America, 91, 1750-1764.

Higdon, R. L. 1986, Absorbing boundary conditions for difference approximations to the multi-dimensional wave equation, Mathematics of computation 47, 437-459.

Higdon, R. L. 1987, Numerical absorbing boundary conditions for the wave equation, Mathematics of computation, 49, 65-90.

Higdon, R. L. 1990, Radiation boundary conditions for elastic wave equation, SIAM J. Numer. Amal. 27, 831-870.

Jastram, C., and Behle, A., 1992, Acoustic modeling on a grid of vertically varying spacing, Geophys. Prosp, 40, 157-170.

Jastram, C., and Tessmer, E., 1994, Elastic modeling on a grid with vertically varying spacing, Geophys. Prospect. 42, 357-370.

Kitsunezaki. C. ,N. Goto, Y. Kobayashi., T. Ikawa, M. Horike, T. Saito, T. Kurota, K. Yamane, and K. Okuzumi, 1990, Estimation of P- and S- wave velocities in Deep Soil Deposits for Evaluating Ground Vibrations in Earthquake, Sizen-saigai-kagaku,9-3,1-17 (in Japanese).

Levander, A. R., 1988, Fourth-order finite-difference P-SV seismograms, Geophysics, 53, 1425-1436.

Liu, H. P., Anderson, D. L. and Kanamori, H., 1976, Velocity dispersion due to anelasticity; implications for seismology and mantle composition, Geophys. J. R. Astr. Soc. 47, 41-58.

Ludwig, W. J., Nafe, J.E., and Drake, C.L.,1970, Seismic refraction, in the Sea vol. 4, part1, Wiley-interscience, 74.

McMechan, G. A., and Yedlin, M. J., 1981, Analysis of dispersive waves by wave field transformation : Geophysics 46, 869-874.

Moczo, P., 1989, Finite-difference technique for SH-waves in 2-D media using irregular grids – application to the seismic response problem, Geophys. J. Int. 99, 321-329.

Moczo, P., Labák, P. Kristek, J. and Hron, F., 1996, Amplification and differential motion due to an antiplane 2D resonance in the sediment valleys embedded in a layer over the half-space, Bull. Seism. Soc. Am., 86, 1434-1446.

Park, C. B., Miller, R. D. and Xia , J., 1999a, Multimodal analysis of high frequency surface waves, Proceedings of the symposium on the application of geophysics to engineering and environmental problems '99, 115-121.

Park, C. B., Miller, R. D., and Xia, J., 1999b, Multichannel analysis of surface waves, Geophysics, 64, 800-808.

Pipkin, A. C., 1986, Lectures on viscoelasticity theory, Springer Verlag, New York, Inc.

Pitarka, A., 1999, 3D elastic finite-difference modeling of seismic motion using staggered grids with nonuniform spacing, Bull. Seism. Soc. Am., 89, 54-68.

Robertsson, J. O. A., Blanch, J. O., and Symes, W. W., 1994, Viscoelastic finite-difference modeling, Geophysics, 59, 1444-1456.

Robertsson, J. O. and Holliger, A. K., 1997, Modeling of seismic wave propagation near the earth's surface, Physics of the Earth and Planetary Interiors, 104, 193-211.

Saito, M. and Kabasawa, H., 1993, Computation of reflectivity and surface wave dispersion curves for layered media 2. Rayleigh wave calculations, Butsuri-tansa, 46,

283-298, (in Japanese).

Strang, G., 1986, Introduction to applied mathematics, Wellweley-Cambridge Press.

Virieux, J., 1986, P-SV wave propagation in heterogeneous media: Velocity-stress finite difference method, Geophysics, 51, 889-901.

Xia, J., Miller, R. D., and Park, C. B. 1999a, Configuration of near surface shear wave velocity by inverting surface wave : Proceedings of the symposium on the application of geophysics to engineering and environmental problems '99, 95-104.

Xia, j., Miller, R. D. and Park, C. B., 1999b, Estimation of near-surface shear-wave velocity by inversion of Rayleigh waves, Geophysics, 64, 691-700.

Xu, T., and McMechan, G. A. 1998, Efficient 3-D viscoelastic modeling with application to near-surface land seismic data, Geophysics, 63, 601-612.

Yamada, N. and Yamanaka, H., 2001, Comparison of performances of 3D subsurface structural models in the southwestern part of the Kanto plain for strong motion simulation –Examination using an earthquake (M_{JMA} 4.1) in the west of Kanagawa prefecture of May 22, 1999-. Journal Seism. Soc. Japan, 53, 313-324 (in Japanese).

Chapter 3

Development of a Two-dimensional Surface-wave Method Using Active Sources

3.1 Introduction

Delineation of S-wave velocity structures down to the depth of 15m is very important for engineering and environmental problems. PS-loggings have been adopted to this purpose for years. However, the PS-logging is not convenient for survey that it requires a borehole. Drilling a borehole and operating a logging tool are a costly business. There have been growing demands for more convenient methods for surveying the shallow S-wave structures. It is well known that the dispersion of phase-velocity of surface-waves (Rayleigh wave) mainly reflects the S-wave velocity structure. A lot of studies have been made on the use of surface-waves for near-surface S-wave delineation in the past decade (e.g. Tokimatsu, 1997). For example, the spectral analysis of surface-waves (SASW) has been used for the determination of 1D S-velocity structures down to 100m (Nazarian et al., 1983). Most of such surface-wave methods employ a shaker or a vibrator as sources and calculate phase differences between two receivers using a simple cross-correlation technique.

Park et al.(1999a, 1999b) proposed a multi-channel analysis of surface-waves (MASW). Their method determines phase velocities directly from multi-channel surface-wave data after applying integral transformation to the frequency-domain waveform data. The integration converts time-domain waveform data (time-distance) into a phase-velocity frequency image directly. The MASW is much better than the SASW because the MASW can visually distinguish a fundamental mode of Rayleigh wave dispersion curve from other modes, such as higher modes and body waves. In addition to this, the MASW can avoid spatial aliasing, which is a problem in the SASW. Xia et al.(1999) and Miller et al.(1999) applied the MASW method to shot records continuously and delineated 2D S-wave velocity structures.

In order to determine phase-velocities in low frequency region precisely, Park et al.(1999a) pointed out that it is essential for MASW method to expand a receiver array as longer as we can. However, a larger receiver array may decrease the lateral resolution of the survey because the conventional MASW method provides an averaged velocity model over a total span of the array. A smaller array is better for increasing lateral resolution. Improving lateral resolution has a trade-off relationship with accuracy

of phase velocity. We have developed a CMP cross correlation analysis method to overcome this trade-off (Hayashi and Suzuki, 2004). The point about our method is calculating phase-velocity in small receiver separation and handling different shot records together.

3.2 Concept of CMP Cross-correlation Analysis

3.2.1 Common Mid Point Cross Correlation

Figure 3.2.1a shows an example of multi-channel surface-wave observation by using an impulsive source. Dispersive later phases can be observed and their apparent velocities change suddenly at the middle of the spread, indicating a lateral change in velocity structure around the middle point of the spread (Distance=185m). Figure 3.2.1b shows a phase-velocity versus frequency image converted by MASW. A dispersion image split into two or three curves, indicating no unique phase velocity. The characteristics in the dispersion image are similar to those of a finite-difference numerical model having a lateral velocity change (Hayashi, 2001).

We may say that a P-SV shot record, which uses vertical force as source and vertical receiver, mainly contains surface waves (Rayleigh waves) and waves travel with horizontal direction. If we assume that waves travel only horizontal direction and S-wave velocity changes mainly horizontal direction, we can say that phase of each trace can be represented by linear summation of phase-difference between receivers and phase associated with source (Figure 3.2.2). We shall focus on two traces *f (t)* and *g(t)* in one shot record obtained at receivers i and receiver i+1 in Figure 3.2.2. Phase of two traces ($\phi_f(\omega)$ and $\phi_g(\omega)$) can be represented as follows:

$$\phi_f(\omega) = \phi s(\omega) + \Delta\phi sr_1(\omega) + \Delta\phi r_1 r_2(\omega) + \Delta\phi r_2 r_3(\omega) + \cdots \Delta\phi r_{i-1} r_i(\omega) \quad (3.2.1)$$

$$\phi_g(\omega) = \phi s(\omega) + \Delta\phi sr_1(\omega) + \Delta\phi r_1 r_2(\omega) + \Delta\phi r_2 r_3(\omega) + \cdots \Delta\phi r_{i-1} r_i(\omega) + \Delta\phi r_i r_{i+1}(\omega). \quad (3.2.2)$$

Cross-correlation of two traces only stores phase-difference between two traces as follows:

$$\Delta\phi_{fg}(\omega) = \phi_g(\omega) - \Delta\phi_f(\omega) = \Delta\phi r_i r_{i+1}(\omega) \quad (3.2.3)$$

where, $\Delta\phi_{fg}(\omega)$ is phase of cross-correlation. It means that calculating cross-correlations

remove phase associated with source wavelet and phase-difference between source and receivers. Therefore, we can handle different shot records together in phase-velocity calculation using cross-correlations. No studied have ever tried to handle different shot records together in phase-velocity calculation using cross-correlations. For example, a multi-channel analysis of surface-waves (MASW) proposed by Park et al. (1999a and 1999b) handles multi traces together. However their method cannot handle multi shots together. We calculate phase-velocity from multi shot records as follows.

The MASW can be considered as the summation of cross-correlations of all wave traces. Dispersion relationships are obtained by using the pairs of each observation points. Then structures are estimated at the midpoints of an entire array spread. Figure 3.2.3(a) illustrates a relationship between locations of observation points and estimated velocity structure. The horizontal location of estimated velocity structure corresponds to the mid-points of an entire array spread. If we wish to improve resolution of phase velocity determination, we must use many pairs. However, spreading of the correlation distance degrades lateral resolution. Thus there is a trade off between the number of correlation pairs and the correlation distance for improving phase velocity measurement.

In order to improve the lateral resolution, we must use cross-correlation that has the same common-mid-point locations, as shown in Figure 3.2.3(b). Hereafter, we use the term "CMPCC" to refer to the cross-correlations that have common-mid-point. If we use CMPCC of one shot gather, other cross-correlations that have different mid-points are thrown away. Let us take Figure 3.2.3(a) for example. Ten pairs can be extracted from five traces, but only two traces can be grouped for CMPCC as shown in Figure 3.2.2c. To increase the number of CMPCC data, we use a multi-shot method and move the observation line and shot points, like reflection seismic method. CMPCC points can be increased as shown in Figure 3.2.3(d).

Data acquisition for CMPCC method is similar to a 2D seismic reflection survey. Source-receiver geometry is based on the end-on-spread and both source and receivers moves up along a survey line. Receivers can be fixed at the end of a survey line (Figure 3.2.4). CDP cables and a CDP switch used in the 2D seismic reflection survey enable us to perform data acquisition easily. Ideally, source interval and receiver interval should be identical. However, considering the resolution of surface-waves and

the efficiency of data acquisition, it is better to select that the source interval is larger than the receiver interval.

3.2.2 Analysis

We have developed CMPCC analysis and apply it to multi-channel and multi-shot surface-wave data. The procedure of CMPCC analysis is summarized as follows:

1. In each shot gather, cross-correlations are calculated for every pairs of two traces (Figure 3.2.5(a)). For example, 276 cross-correlations ($=_{24}C_2$) are calculated from a shot gather that includes 24 traces.

2. From cross-correlations for every pairs of all shot gathers, correlations having common mid-point are grouped together.

3. In each common mid-point, cross-correlations that have an equal spacing are stacked in the time domain (Figure 3.2.5(b), (c)). Even if each source wavelet and its phases are different, cross-correlations can be stacked because the correlation stores only phase-differences between two traces. The phase-differences contained in the source wavelet has been removed by cross-correlation if we assume two traces only contain waves propagating horizontal direction as mentioned before.

4. The cross-correlations that have different spacing should not be stacked in the time domain. The different-spacing cross-correlations are ordered with respect to their spacing in each common mid-point (Figure 3.2.5(d)). Resultant cross-correlation gathers resembles to the shot gathers. However, it contains only characteristic phase differences in each CMP location, and can be handled as shot gathers in the phase-velocity analysis. We named it CMPCC gather.

5. The MASW is applied to the CMPCC gathers for calculating phase-velocities. First, each trace is transformed into frequency domain by FFT. Then, frequency-domain data

is integrated over the spacing with respect to phase-velocities. Using these procedures, the CMPCC gathers in the spacing and time domain can be transformed into phase-velocity and frequency domain directly.

6. Phase-velocities are determined as the maximum amplitude in each frequency.

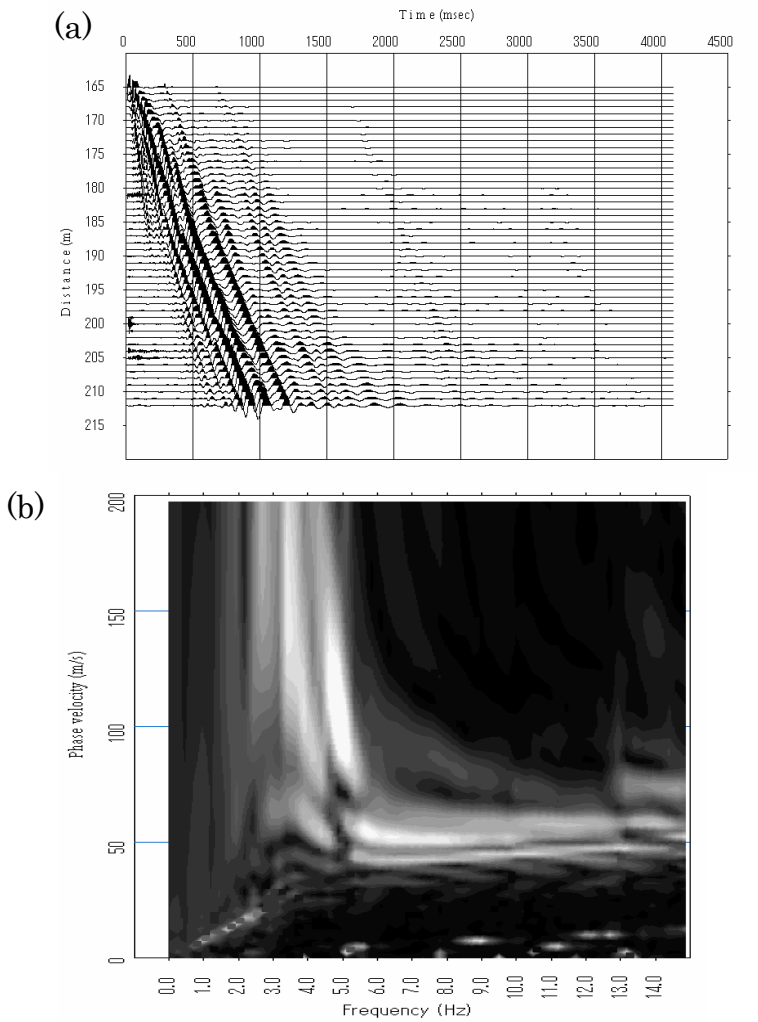

Figure 3.2.1. (a) An example of observed shot records. (b) Its phase-velocity frequency image. White indicates largest amplitude.

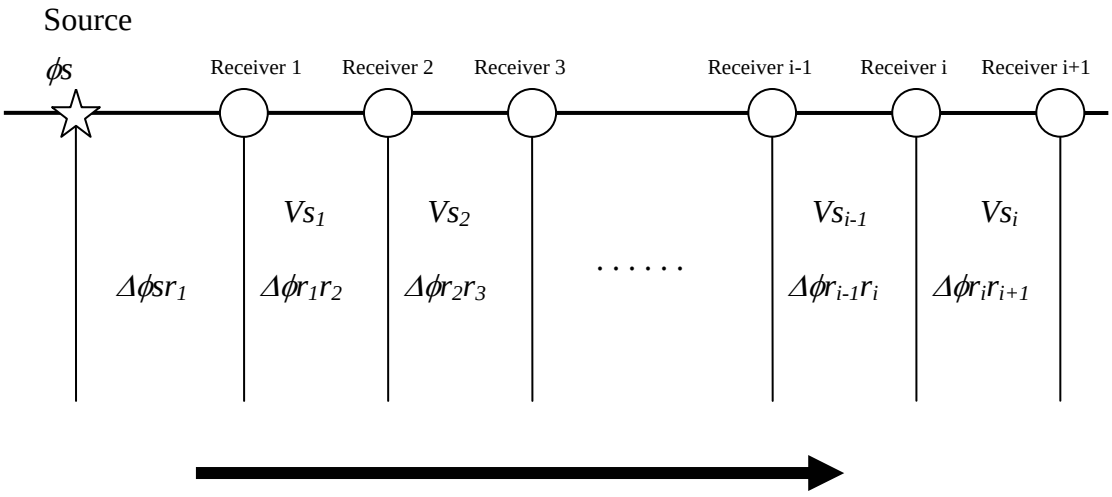

Waves travel with horizontal direction.

ϕs : Phase associated with source wavelet.
$\Delta\phi sr_1$: Phase difference between source and receiver 1.
$\Delta\phi r_1r_2$: Phase difference between receiver 1 and 2.
$\Delta\phi r_2r_3$: Phase difference between receiver 2 and 3.
$\Delta\phi r_{i-1}r_i$: Phase difference between receiver i-1 and i.
$\Delta\phi r_ir_{i+1}$: Phase difference between receiver i and i+1.

Figure 3.2.2 Linear summation of phase-difference between receivers and phase associated with source.

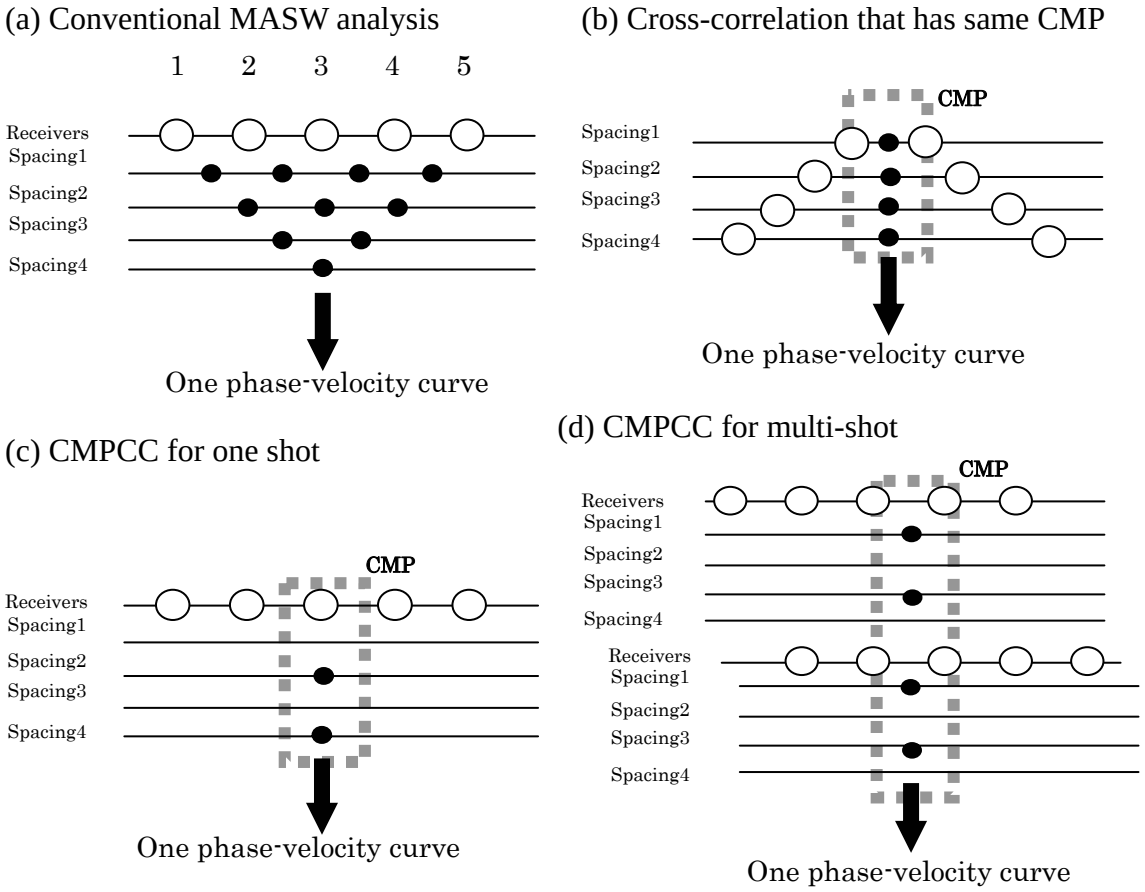

Figure 3.2.3. Concept of CMP analysis in surface-wave method. The open circles indicate receiver locations and the solid circles indicate the mid-points of cross-correlations. Spacing 1, 2, 3, … mean the receiver distances for calculating cross-correlation; for example, spacing 1 corresponds to the pairs 1-2, 2-3, 3-4 and 4-5, whereas spacing 2 corresponds to the pairs 1-3, 2-4 and 3-5. (a) Location of observation points and estimated velocity structure in conventional MASW analysis. (b) Cross-correlation that has same CMP locations (CMPCC). (c) CMPCC for one shot. (d) CMPCC for multi-shot.

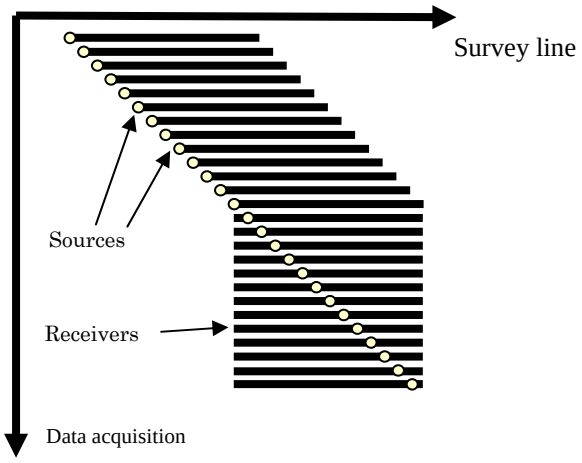

Figure 3.2.4. A source-receiver geometry of moving-source observation for CMP analysis of surface-waves.

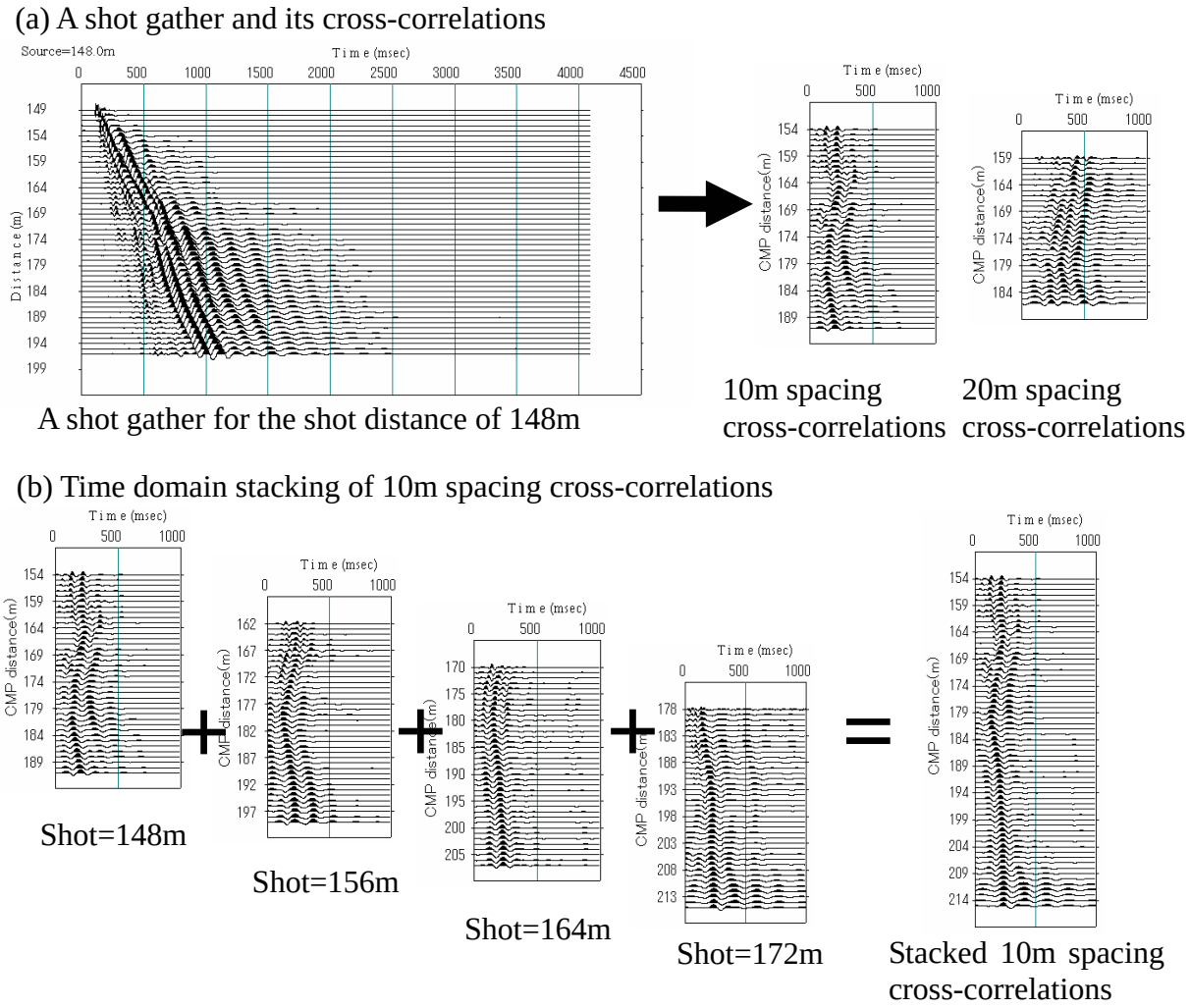

Figure 3.2.5. An example of data processing of CMPCC analysis for four shots. (a) Calculation of cross-correlations from one shot gathers (step1). (b) and (c) Time domain stacking of cross-correlations that have identical spacing (step3). (d) Different spacing cross-correlations are ordered with respect to the lateral distances. The CMPCC gathers are obtained for each distance. All shot-gathers in survey line are used and cross-correlations are calculated for every pairs of two traces.

(c) Time domain stacking of 20m spacing cross-correlations

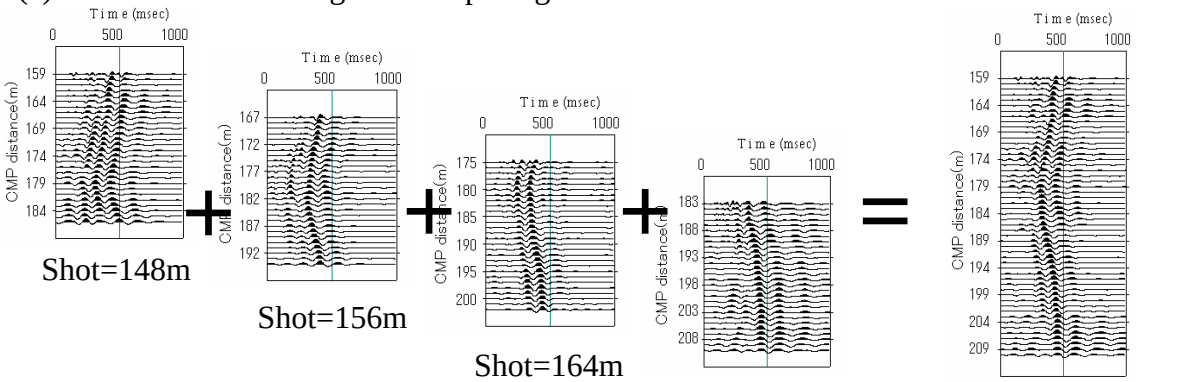

(d) Different spacing cross-correlations are ordered with respect to their spacing

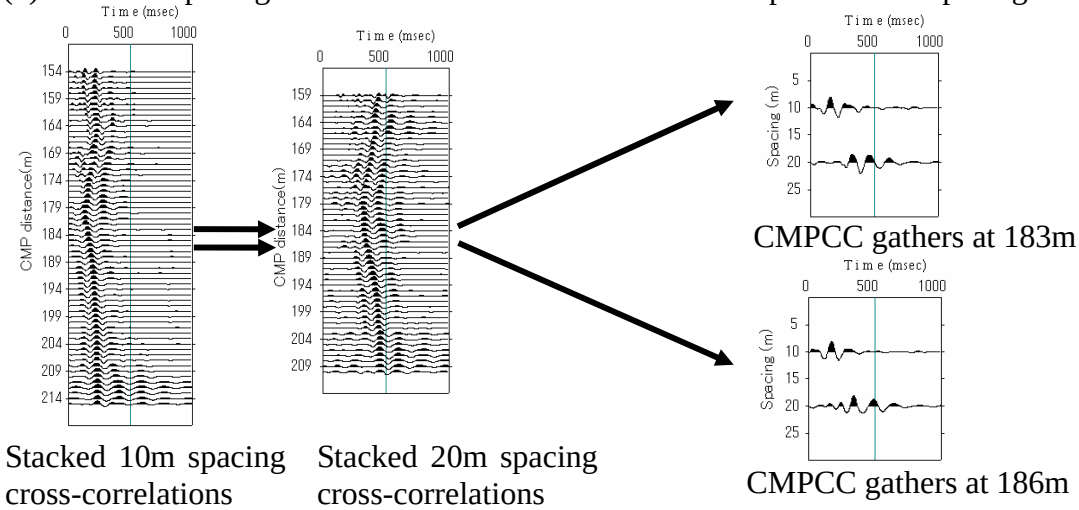

Figure 3.2.5. Continued.

3.3 Numerical Experiments

A numerical test was performed in order to evaluate the applicability of CMPCC method. Figure 3.3.1 and 3.3.2 show a velocity model used in the numerical test and the source-receiver geometry, respectively. The model is a three-layer structure having a step discontinuity at the distance of 60m. The velocity model is same as the step model used in the Chapter 2.5 and model parameters are listed in the Table 2.5.2. A stress-velocity, staggered grid, 2D finite-difference method (Levander, 1988), described in the Chapter 2.4, is used for waveform calculation. Figure 3.3.3(a) shows a shot gather. Apparent velocity of time-domain waveforms changes abruptly at the distance of 60m, corresponding to the step. A phase-velocity and frequency image for shot location at 35.8m is shown in Figure 3.3.3(b). A phase-velocity curve in the phase-velocity frequency image split into two curves in the frequency range from 15 to 40Hz. The CMPCC analysis was applied to this data. All shot gathers were used in the analysis. Figure 3.3.4 shows resultant CMPCC gathers in which common-mid-point cross-correlations are ordered with respect to their spacing. We can see that obvious change of apparent velocity is not identified in the time domain waveform data of CMPCC gathers. In the phase-velocity frequency images, the energy concentrates in one phase velocity curve.

A non-linear least square method (Xia et al., 1999) was applied to dispersion curves for reconstructing 2D S-wave velocity profile. An initial model was generated by a simple wavelength-depth conversion. The number of layers is fixed as 15, and only S-wave velocities are changed throughout reconstruction. Figure 3.3.5 shows the inverted S-wave velocity profile by conventional MASW analysis (a) and the CMPCC method (b). The step discontinuity at the middle of the section is more clearly imaged by CMPCC analysis, compared with the reconstructed image by MASW analysis.

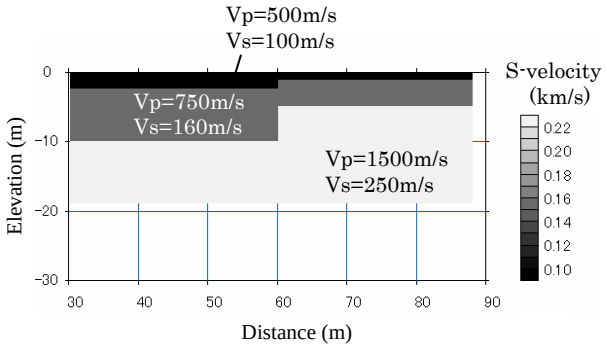

Figure 3.3.1. Velocity model used in a numerical test.

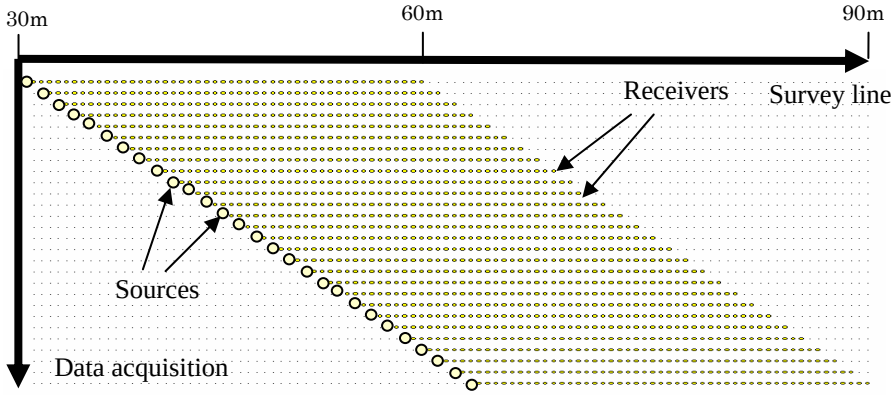

Figure 3.3.2. Source-receiver geometry used in a numerical test.

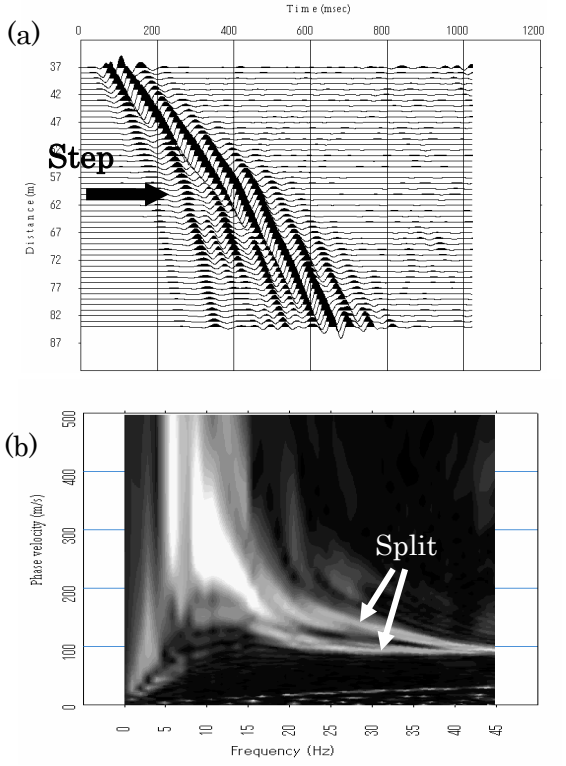

Figure 3.3.3 Shot gathers (a) of 35.8m shot and its phase-velocity frequency image (b).

(a) CMP distance of 50.8m (b) CMP distance of 70.8m

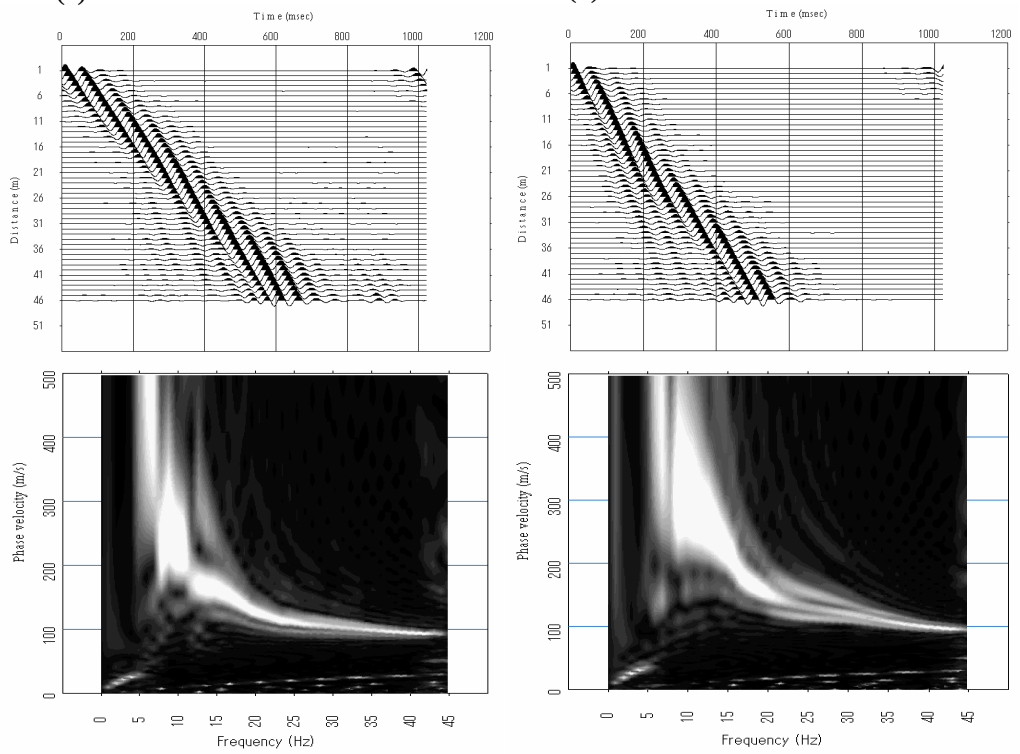

Figure 3.3.4. CMPCC gathers obtained through the CMPCC analysis (top) and their phase-velocity frequency images (bottom). The data correspond to two lateral distances: 50.8m (a) and 70.8m (b). The velocity structure laterally changes between those distances.

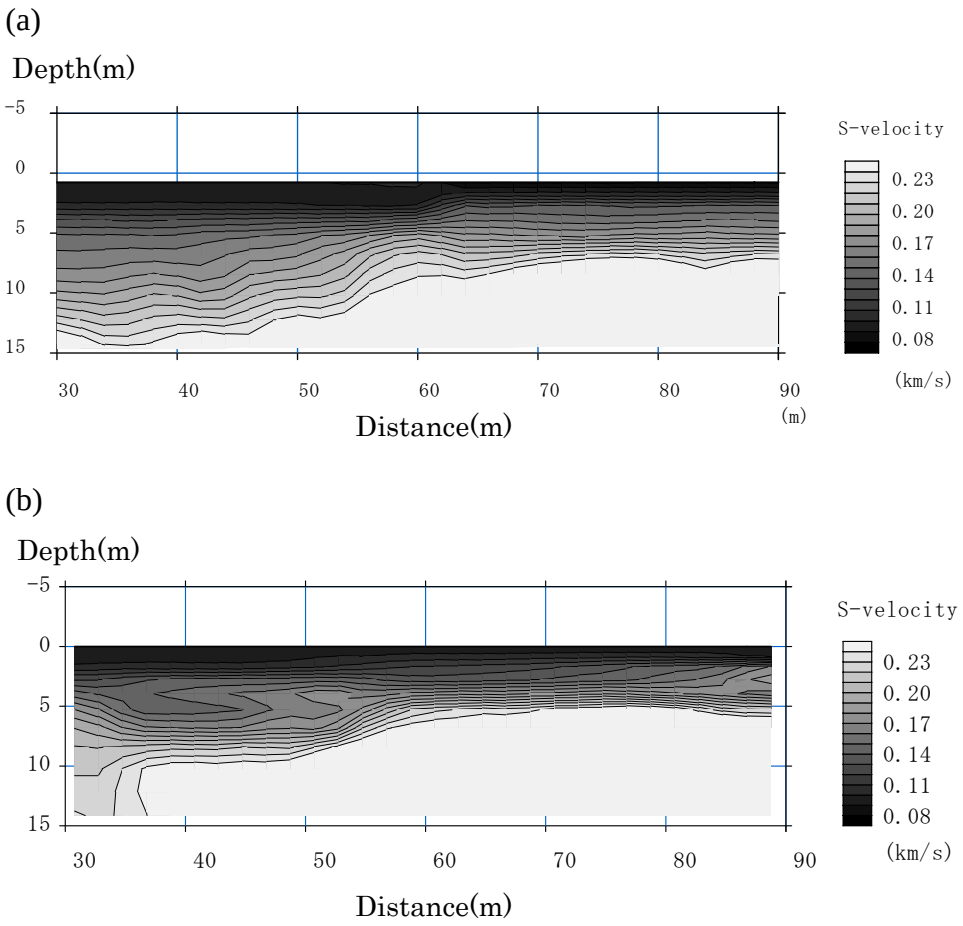

Figure 3.3.5. Reconstructed S-wave structure obtained from (a) Conventional MASW method and (b) CMPCC method.

3.4 Physical Model Experiments

3.4.1 Introduction

In the early 1980s, a spectral analysis of surface waves (so called SASW) was introduced (Nazarian et al., 1983). Park et al. (1999a, 1999b) have improved the SASW to the multi-channel analysis of surface waves (MASW) and Xia et al. (1999a) generated two-dimensional S-wave velocity map by the MASW. The surface wave methods, such as the SASW or MASW, can estimate S-wave velocity models that are extremely valuable in engineering geophysics. Therefore, the surface wave methods have been increasingly used in various civil engineering and environmental investigations.

However, the surface wave methods for near-surface problems are relatively new technique. Therefore, the methods have several important difficulties that should be solved as follows. The methods use the dispersive character of Rayleigh waves, especially fundamental mode of surface waves. Body waves and higher mode surface waves can contaminate the data in the surface wave methods, and the separation of surface waves corresponding to fundamental mode waves from those unfavorable waves may be one of the difficulties in the surface wave analysis. The surface wave method relies on a one-dimensional analysis of dispersion curves (Xia et al., 1999a, 1999b). Therefore, the analysis of dispersion curves may have some difficulties in two- and three-dimensional velocity models. The number of theoretical studies about surface wave propagation in the heterogeneous near-surface region is relatively small. For example, only few attempt have so far been made at the effect of two- and three-dimensional models on the method.

In order to improve the accuracy and reliability of the surface wave methods, we have to understand fundamental characters of surface waves. Both numerical modeling, such as finite-difference methods, and physical modeling can be valuable tools for these purposes. In this paper, we will perform physical modeling by a Laser Doppler Vibrometer (LDV) in order to investigate the fundamental characters in the surface waves, such as Rayleigh wave dispersion, in one-dimensional models.

3.4.2 Experiment Using a Laser Doppler Vibrometer

As is well known, a light beam reflected from a moving object has a Doppler shift f_D:

$$f_D = 2V/\lambda \tag{3.4.1}$$

where V and λ denote the velocity of object along the beam and the wavelength of light respectively. We employed a LDV LV-1300(ONO sokki Inc.), which is used for measuring vibration of factory product. The Doppler shifted frequency f_D is converted to a voltage signal that indicates actual vibrations. Since the velocity is directly converted to the frequency shift, there is neither the mechanical nor the electrical coupling between the material's surface vibration and the observed signal. Nishizawa et al.(1997) used LDV for measuring seismic waves at the surface of the rock prisms and have proved it can be used as a precise receiver for ultrasonic waves (300KHz to 2MHz) generated by the PZT.

Figure 3.4.1 is a schematic diagram of the measurement system. The detail of the system is described in Nishizawa et al.(1997). A source is a 5-mm PZT having a 2MHz characteristic frequency. We used driving pulses that consists of a single-cycle sine wave with 100 to 500KHz frequency and 100V peak to peak amplitude. A thin reflection sheet is glued to the model surface to enhance the reflection beam.

3.4.3 Homogeneous Models

In the first example, homogeneous half space models are used. Square prisms made of acrylic and gabbro were used as homogeneous models. The size of model is 300*300*90mm. Source-receiver configuration is shown in Figure 3.4.2. Waveforms were collected at the surface of the models with 4mm distance interval. The first receiver was placed 4mm apart from the source. Since a source and receivers are placed on the surface of homogeneous models, this example can be tested as the Lamb's

problem.

Figure 3.4.3 shows the vertical component of particle velocities and its power spectrum for the acrylic model. 100 and 250 KHz single-cycle sine waves were used as driving pulses. Small amplitude first arrival with the velocity of 2.7km/s and large amplitude later phase with the velocity of 1.25km/s are clearly observed. Figure 3.4.4 shows the vertical component of particle velocities and its power spectrum for the gabbro model. 100 and 250 KHz single-cycle sine waves were used as driving pulses. Large amplitude later phase with the velocity of 3.2km/s is clearly observed. First arrival cannot be clearly seen from Figure 3.4.4 due to low gain. The velocity for the first arrival seems to be 5.6km/s from a figure with high gain. In the waveforms for the 250KHz pulse, clear later phase with a hyperbolic curve can be observed beyond 100μs. This phase seems to be reflected surface waves (Rayleigh waves) from the edge of the model. Figure 3.4.5 shows the phase velocity – frequency images of waveform data converted through the multi-channel analysis of surface waves (MASW) (Park et al., 1999a).

From these figures, waveforms for this example can be characterized as follows. Waveforms consist of small amplitude first arrival and large amplitude later phase. It is obvious that the former is direct P-waves and the latter is surface waves (Rayleigh waves). The amplitude of Rayleigh waves is much larger than that of direct P-waves. Both P-waves and Rayleigh waves have little dispersion. These characters agree with the analytical solution of Lamb's problem (Saito, 1993). Figure 3.4.6 shows synthetic waveform calculated by three-dimensional finite difference method. We can see that the observed waveform data for acrylic model agree with synthetic waveform very well. We can be fairly certain that the measurement system with the PZT and the LDV has generated and measured correct surface waves.

3.4.4 Two-layer Models

1) Horizontal two-layer model

In the next example, horizontal two-layer models are used. The models consist of acrylic as a low-velocity first layer and mortar as a high-velocity second layer. Two

models are used in the experiment and the thickness of first layer is 5mm and 10mm respectively. Source-receiver configuration is the identical with the first example. 100 and 500 KHz single-cycle sine waves were used as driving pulses.

Figure 3.4.7 shows the vertical component of particle velocities and its phase velocity image for a model with 5mm thickness first layer. In the case of a 100KHz pulse, two clear later phases are observed. The phase velocity for the faster one is about 1.9km/s and the slower one is about 1.25km/s. These two later phases that can be considered as surface waves, compose a clear dispersion curve on the phase velocity image. We can say with fair certainty that the curve is the fundamental mode of Rayleigh wave dispersion curves. In the case of a 500KHz pulse, waveform appearance is too complicated to identify phase velocity. However, the dispersion curves appeared on the phase velocity image is almost identical with the 100KHz case. It is amazing that such different waveforms have almost identical phase velocity images. This result shows the accuracy of the measurement system as well as the robustness of the phase velocity – frequency transformation method through MASW (multi-channel analysis of surface waves).

Figure 3.4.8 shows the vertical component of particle velocities and its phase velocity image for a model with 10mm thickness first layer. A clear dispersion curves can be seen on the phase velocity image. However, the phase velocity for the second layer cannot be easily determined from the dispersion curves in comparison with the 5mm case.

The result indicates that the velocity model is more important than the frequency contents of the source in order to image clear dispersion curves. Park et al. (1999a) shows that the resolution of phase velocity image increases as the number of traces increases to include further offset. It seems reasonable to suppose that the resolution of dispersion curves is determined by velocity models, the number of traces and the inclusion of further offset. The frequency contents of the source may have small effect on the dispersion curves as long as the data acquisition is precise.

Dispersion curves are picked as the maximum amplitude in each frequency on the phase velocity images. Picked dispersion curves are shown in Figure 3.4.9. A non-linear least square method is applied to the dispersion curves in order to obtain velocity models. The number and thickness of layer, and densities are fixed during the

iteration. P-wave velocities are linearly related to S-wave velocities by two constants. Therefore, only S-wave velocities are unknown in the inversion. The inverted velocity models (S-wave velocity) are shown in Figure 3.4.10. Almost correct layer thickness (5mm and 10mm) was obtained by the inversion. The result shows the reliability of the whole process of surface wave analysis including both the computation of dispersion curves from waveforms and its inversion.

3.4.5 Two-layer Model with a Step

In the final example, a two-dimensional model is used. The model is two-layer model with a step. Figure 3.4.11 shows the vertical section along a receiver array and the location of sources and receivers. There is a 5mm step in the middle of the model. The receiver array is placed perpendicular to the step. The sources are placed at the beginning (A) and end (B) of the receiver array.

Figure 3.4.12 shows the vertical component of particle velocities and its phase-velocity frequency image. Both waveforms appearance suddenly changes at the step in the time domain data. In the wave forms for source-B (Figure 3.4.12c)) , we can see wave forms that has reversed apparent velocity. This reversed waveforms seems to be reflected surface-waves as numerical simulation shown in the previous chapter (Hayashi and Suzuki, 2001). Figure 3.4.12(b) and (d) shows phase-velocity frequency image for each source. Although the time domain data looks different, frequency domain phase velocity image looks almost identical. In the phase-velocity frequency images, two dispersion curves can be seen. Phase velocity changes at the frequency of 50KHz in one dispersion curve and it changes at 120KHz in another one. Considering the phase-velocity frequency images shown in Figure 3.4.7 and Figure 3.4.8, we can say that the first one (changes at 50KHz) corresponds to a dispersion curve for 10mm thickness acrylic layer and second one (changes at 120KHz) corresponds to the one of 5mm thickness.

Theoretical waveforms for the two-dimensional model have been calculated by two-dimensional finite-difference method. In the viscoelastic calculation, quality factor (Q) is assumed to be 10 for first layer (acrylic) and 100 for second layer (mortar).

Figure 3.4.13 shows the comparison of observed and theoretical data with and without viscoelastic term. Theoretical surface-wave amplitude without viscoelastic terms much larger to the viscoelastic calculation. On the contrary, waveforms include viscoelastic attenuation agree with observed data very well.

3.4.6 Application of CMPCC Analysis to Physical Model Data

We have applied CMPCC analysis to LDV data for the two-dimensional model. Figure 3.4.14 shows source-receiver geometry. Survey line length is 110mm and the step is placed at the distance of 55mm (see Figure 3.4.15). Source pulse is 50KHz. Twenty-three shot gathers are analyzed together. Figure 3.4.16 shows the example of observed waveform data using the LDV and PZT. It is clear that the features of waveform data changes at the step placed at 55mm. Twenty-two CMPCC gathers are calculated 5mm distance interval. Figure 3.4.17 shows the example of CMPCC gathers. (a) and)b) shows the CMPCC gathers for the CMP distance of 27.5m (left side of the step). (c) and (d) shows the CMPCC gathers for the CMP distance of 72.5m (right side of the step). We can see that the dispersion curves in the phase-velocity frequency images have clear difference between left and right side of the step. Dispersion curves are calculated for all 22 CMPCC gathers. Figure 3.4.18 shows these dispersion curves. In the figure, difference of color indicates the difference of CMPCC location. Red to yellow curves are placed in left side of the step and green to blue curves are placed in right side of the step.

A non-linear least square method was applied to all dispersion curves for reconstructing 2D S-wave velocity model. An initial velocity model was generated by a simple wavelength-depth conversion described in the previous chapter. The number of layers is fixed as 15, and only S-wave velocities are changed throughout reconstruction. Figure 3.4.19 shows the initial and inverted S-wave velocity profile. The step discontinuity at the middle of section (55mm) is clearly imaged by CMPCC analysis.

3.4.7 Conclusions

The physical modeling of surface waves using the LDV and PZT was performed

and the fundamental characters in the surface waves were studied. The waveforms from the modeling for homogeneous half space agreed with the analytical solution of Lamb's problem. It proves that the LDV can measure and the PZT can generate the surface waves. Clear dispersion curves were obtained from the waveforms for two-layer models. It shows the accuracy of the measurement system as well as the robustness of the phase velocity – frequency transformation method. Correct velocity models were obtained by the inversion of the dispersion curves. We may say that the reliability of surface-wave methods has been shown by this physical modeling.

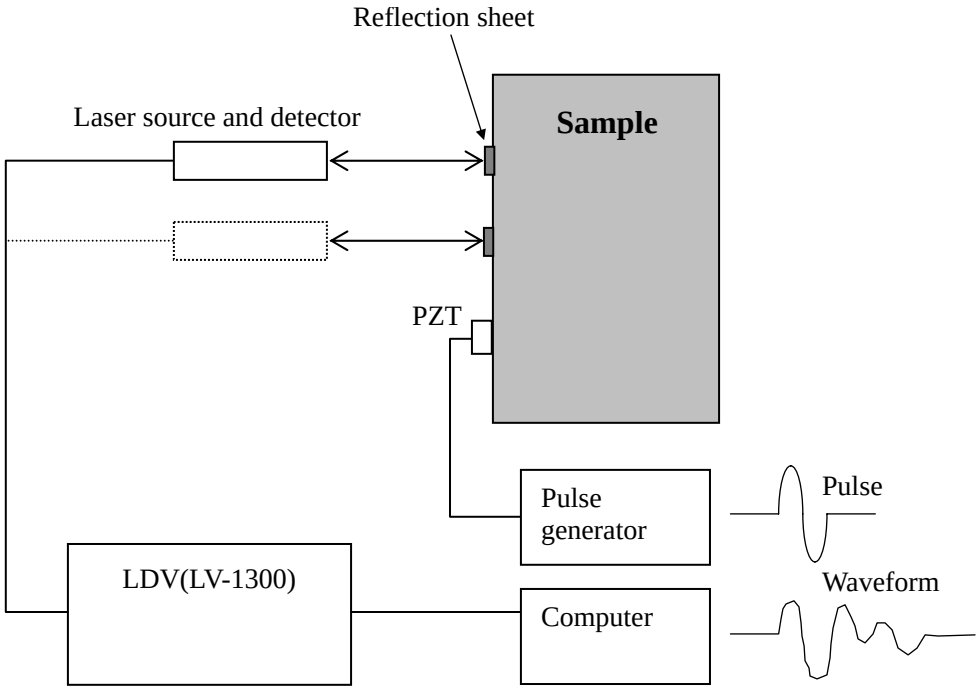

Figure 3.4.1. Schematic diagram of the measurement system using a laser Doppler vibrometer (LDV) and a piezoelectric transducer (PZT). The PZT is mounted on the surface for generating elastic waves. The laser beam illuminates the high-gain reflection sheet, which reflects the beam in an incident direction.

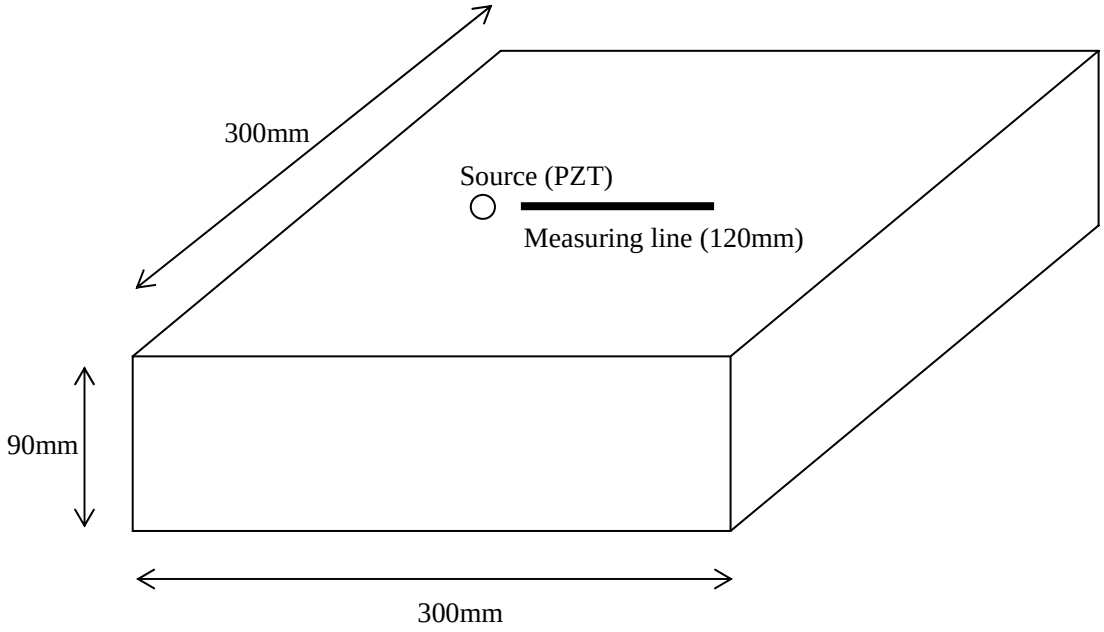

Figure 3.4.2. Source-receiver configuration used in the experiment. A source and a measuring line are placed in the middle of the models. Waveforms are collected at the surface of the models with 4m distance interval.

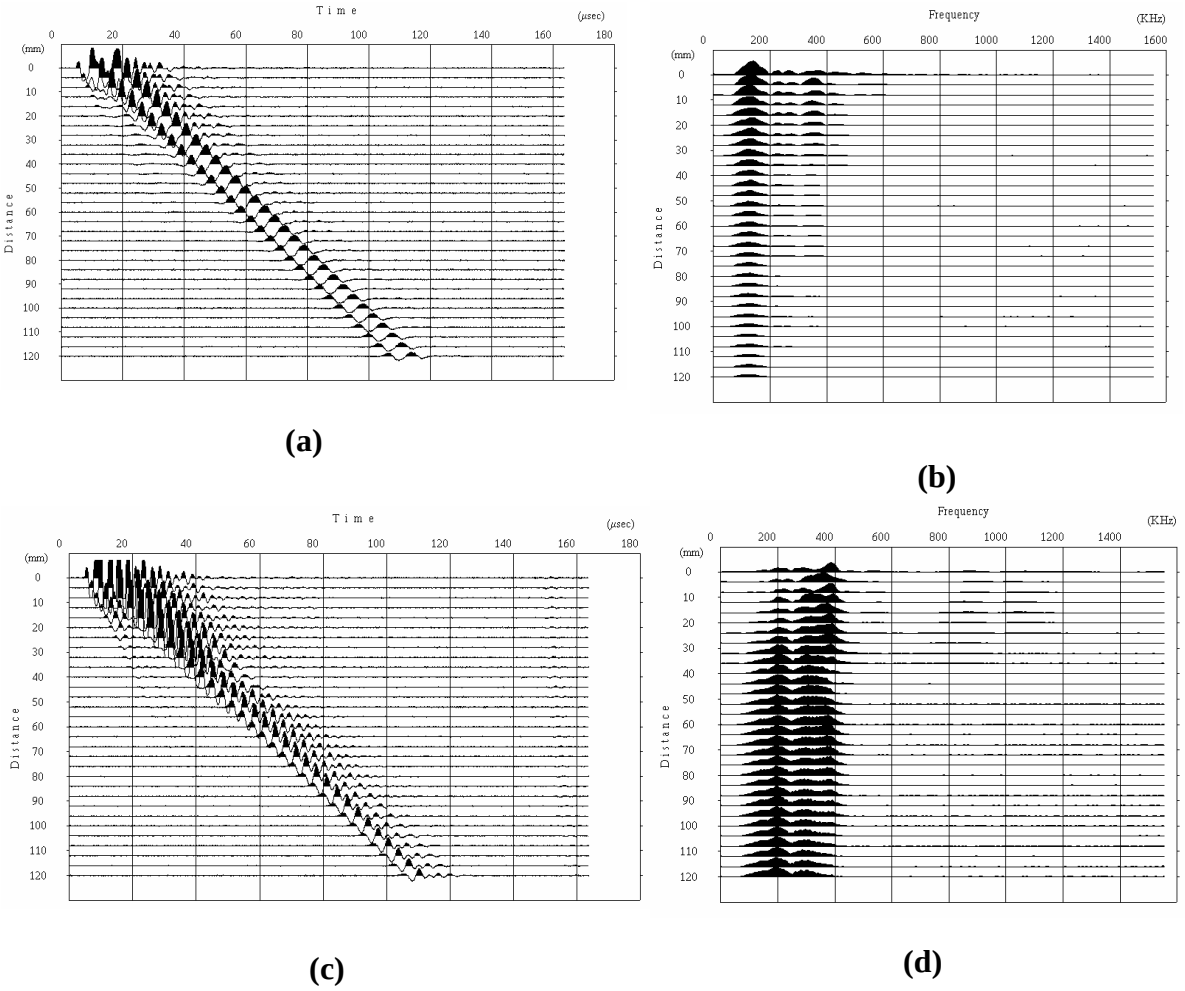

Figure 3.4.3. Vertical component of particle velocities and its power spectrum for the acrylic model. (a) Waveforms and (b) power spectrum for 100KHz pulse. (c) Waveforms and (d) power spectrum for 250KHz pulse.

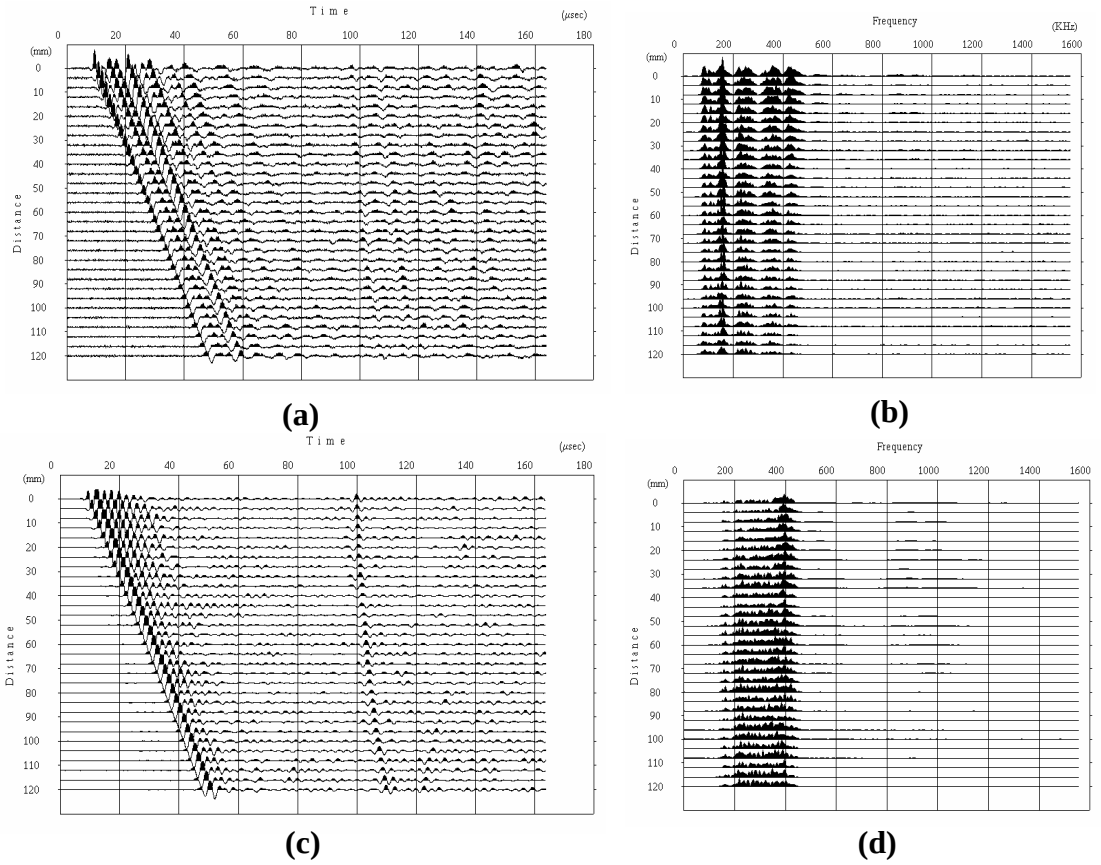

Figure 3.4.4. Vertical component of particle velocities and its power spectrum for the gabbro model. (a) Waveforms and (b) power spectrum for 100KHz pulse. (c) Waveforms and (d) power spectrum for 250KHz

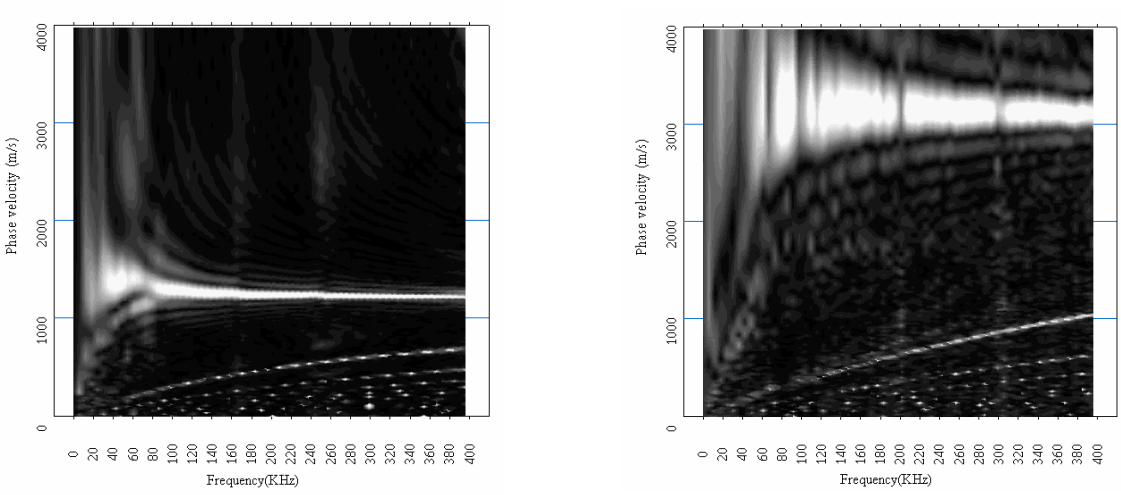

Figure 3.4.5. Phase velocity images converted through the multi-channel analysis of surface waves. (a) Waveforms for acrylic model. (b) Waveforms for gabbro model.

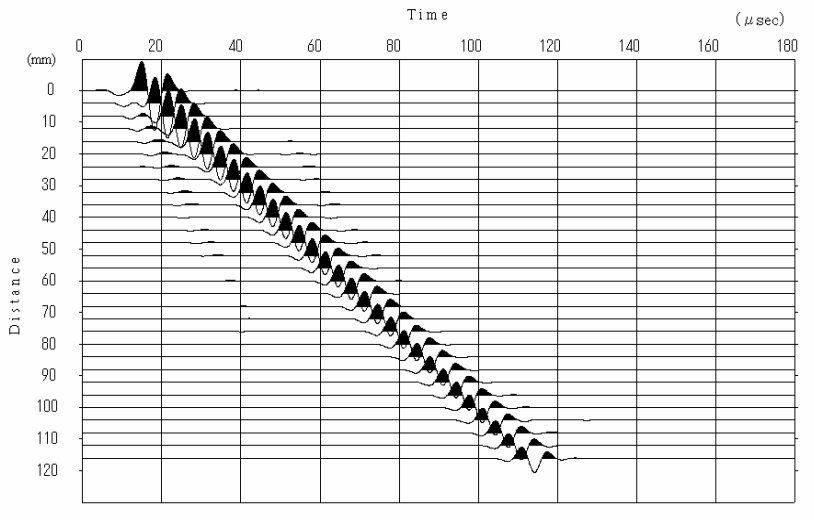

Figure 3.4.6. Synthetic waveform calculated by 3D elastic finite-different method. Vp=2500m/s, Vs=1300m/s, density=1500kg/m^3, grid spacing=0.5m. P-wave source with 100KHz Ricker-wavelet is used.

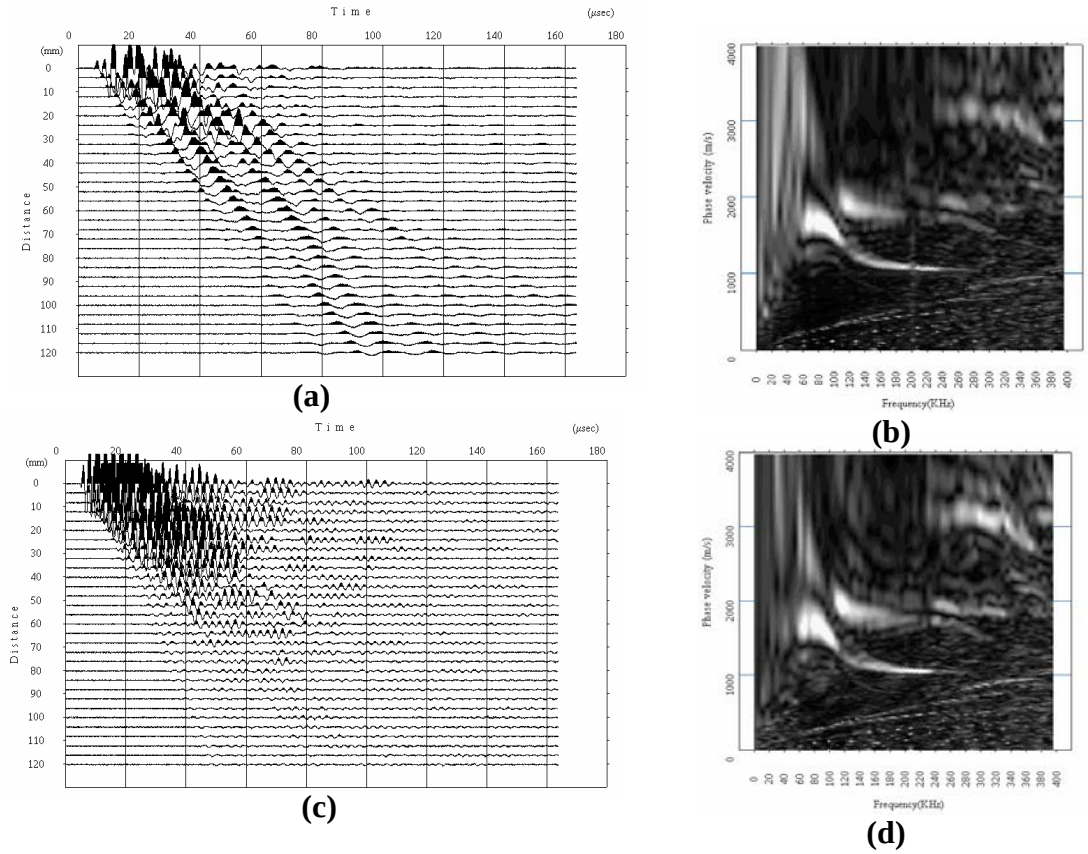

Figure 3.4.7. Vertical component of particle velocities and its phase-velocity images for a model with 5mm thickness first layer. (a) Waveforms and (b) a phase-velocity image for 100KHz pulse. (c) Waveforms and (d) a phase-velocity image for 500KHz pulse.

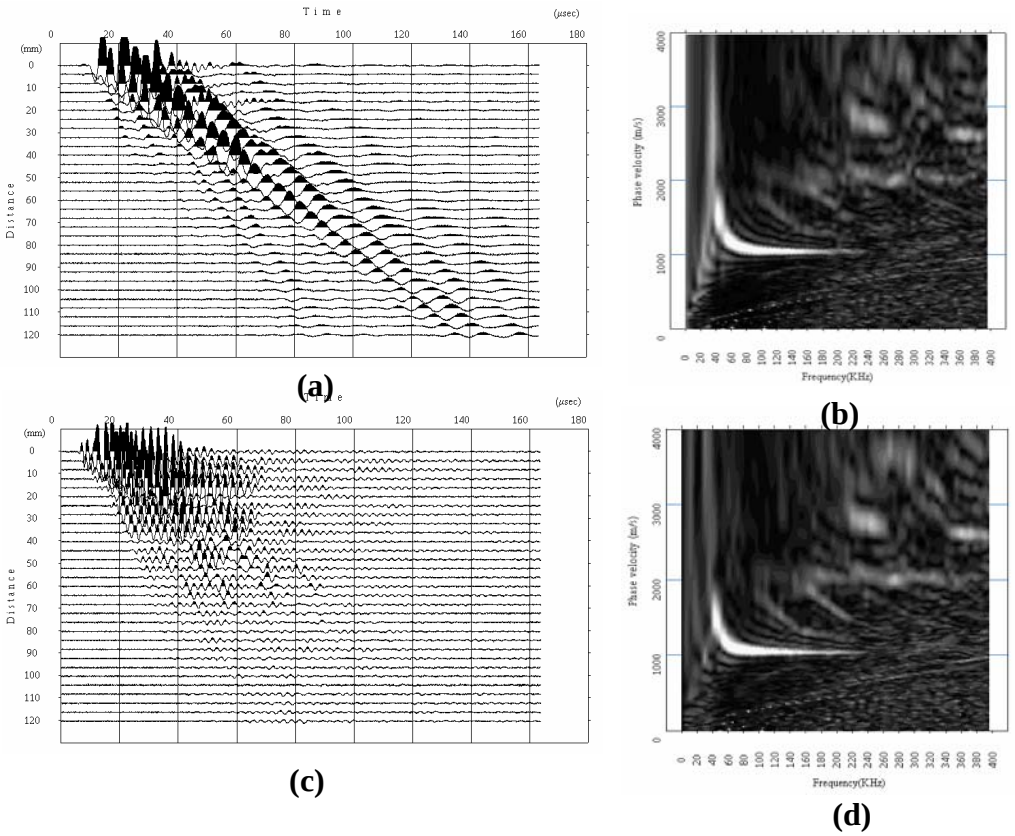

Figure 3.4.8. Vertical component of particle velocities and its phase-velocity images for a model with 10mm thickness first layer. (a) Waveforms and (b) a phase-velocity image for 100KHz pulse. (c) Waveforms and (d) a phase-velocity image for 500KHz pulse.

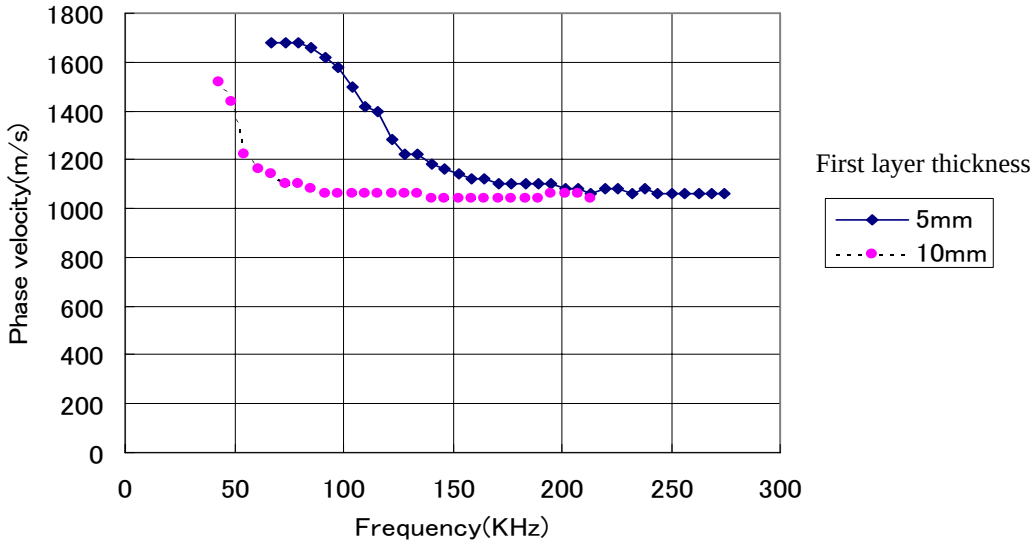

Figure 3.4.9. Dispersion curves for the two-layer models. Phase velocities are picked as the maximum amplitude in each frequency on the phase velocity images.

(a) **(b)**

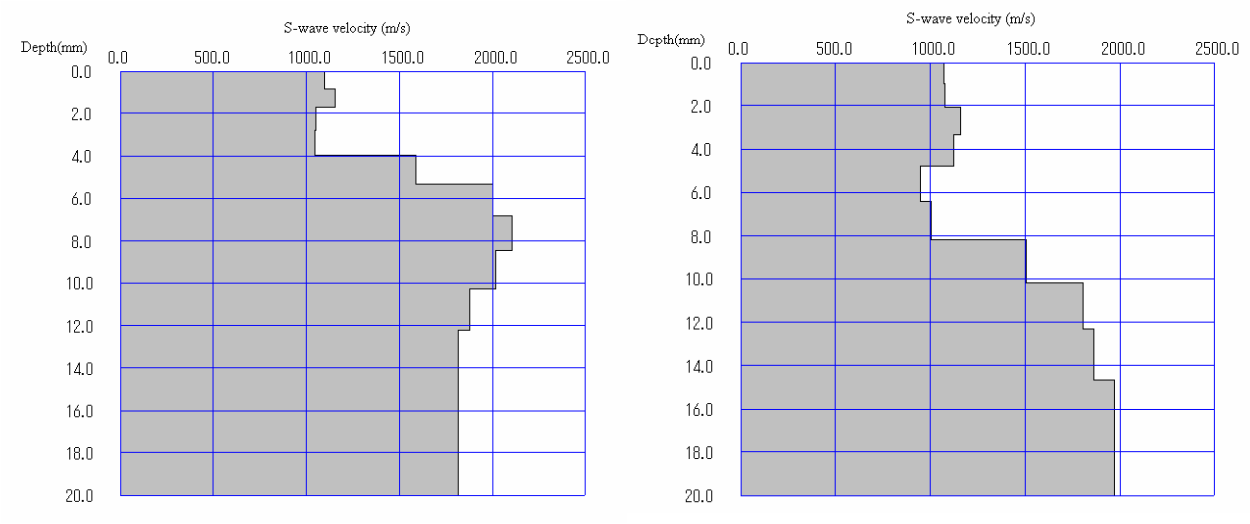

Figure 3.4.10. Inverted velocity models (S-wave velocity) for the two-layer models. (a) A inverted model for a model with 5mm thickness first layer. (b) A inverted model for a model with 10mm thickness first layer.

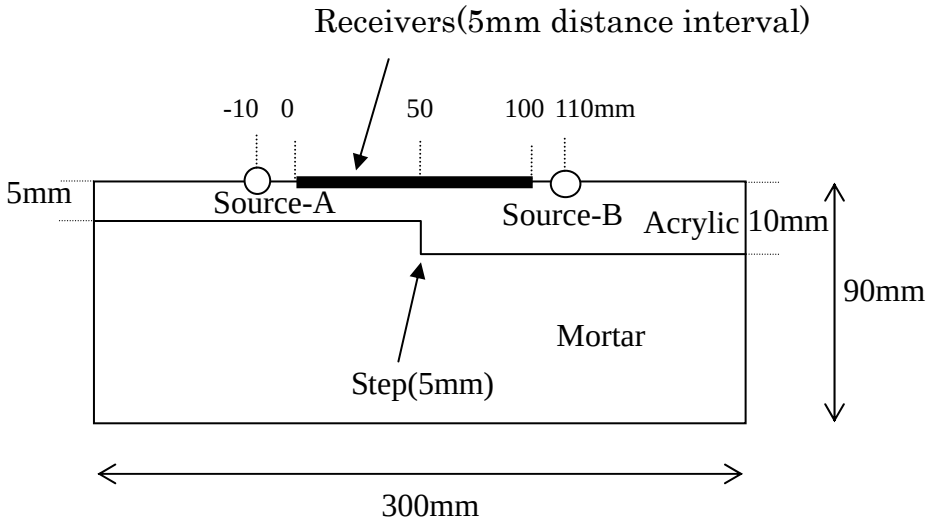

Figure 3.4.11. A two-dimensional model used in the experiment.

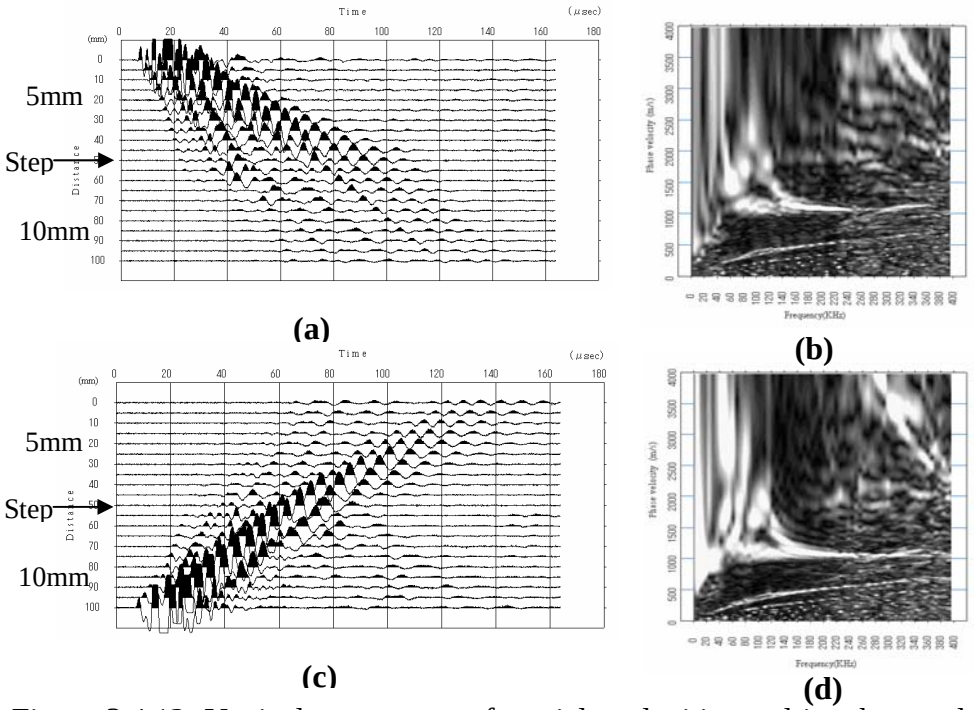

Figure 3.4.12. Vertical component of particle velocities and its phase-velocity images for a two-dimensional model with a 125KHz pulse. (a) Waveforms and (b) a phase-velocity image for the source A. (c) Waveforms and (d) a phase-velocity image for the source B.

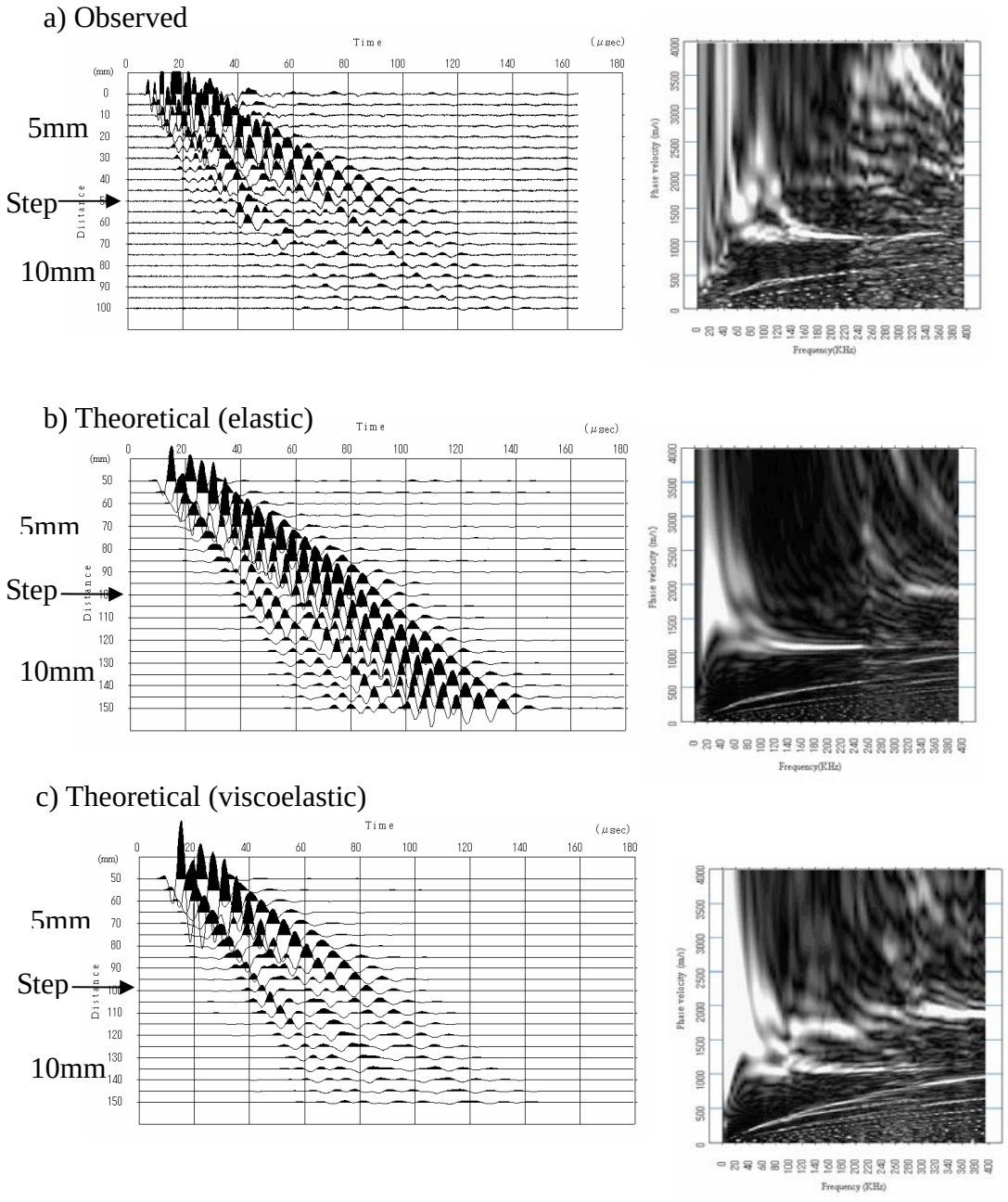

Figure 3.4.13. Comparison of observed and theoretical data for two-dimensional model. a) Observed data. b) Theoretical data calculated by finite-difference method. c) Theoretical data calculated by finite-difference method including viscoelastic attenuation. Quality factor (Q) is assumed to be 10 for first layer (acrylic) and 100 for second layer (mortar).

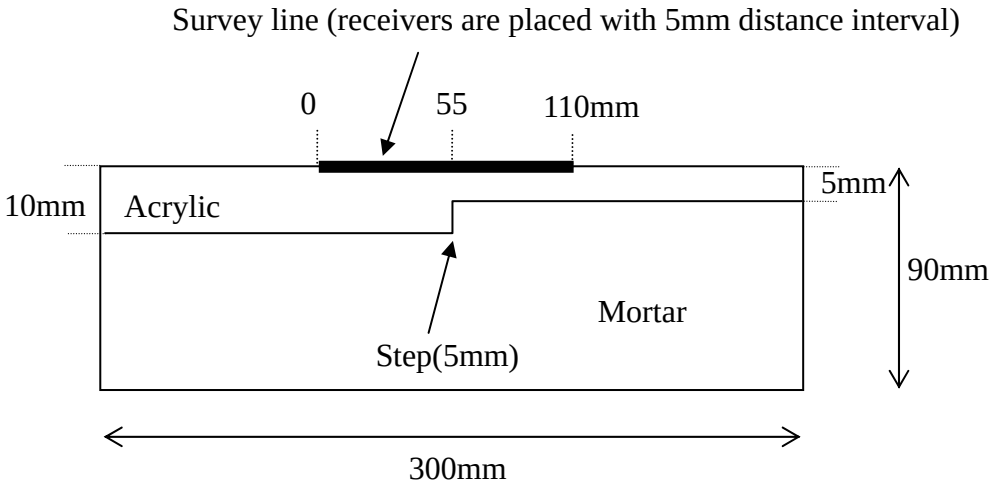

Figure 3.4.14. A two-dimensional model used in the experiment of CMPCC analysis.

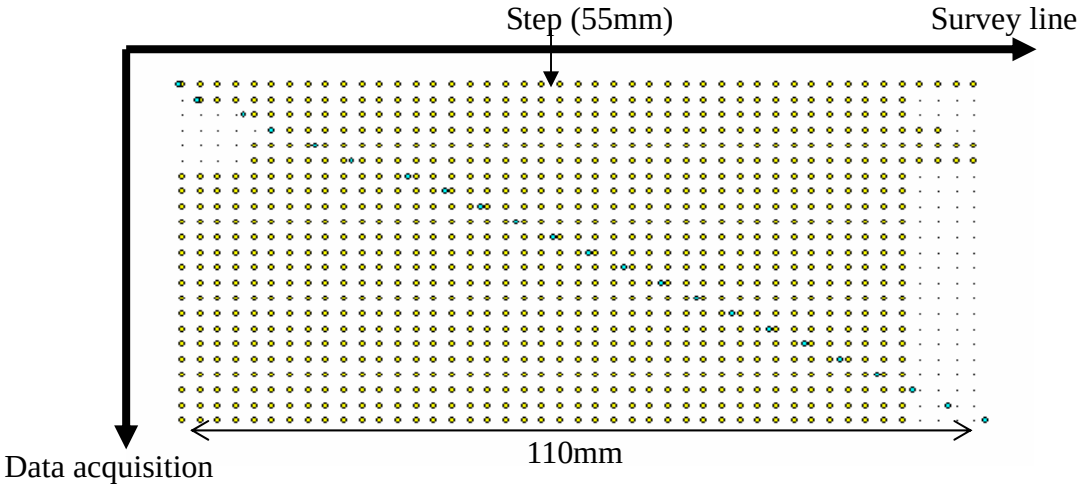

Figure 3.4.15. Source and receiver geometry for CMPCC analysis. Blue circles indicate sources and yellow circles indicate receivers.

a) Source = -0.5m

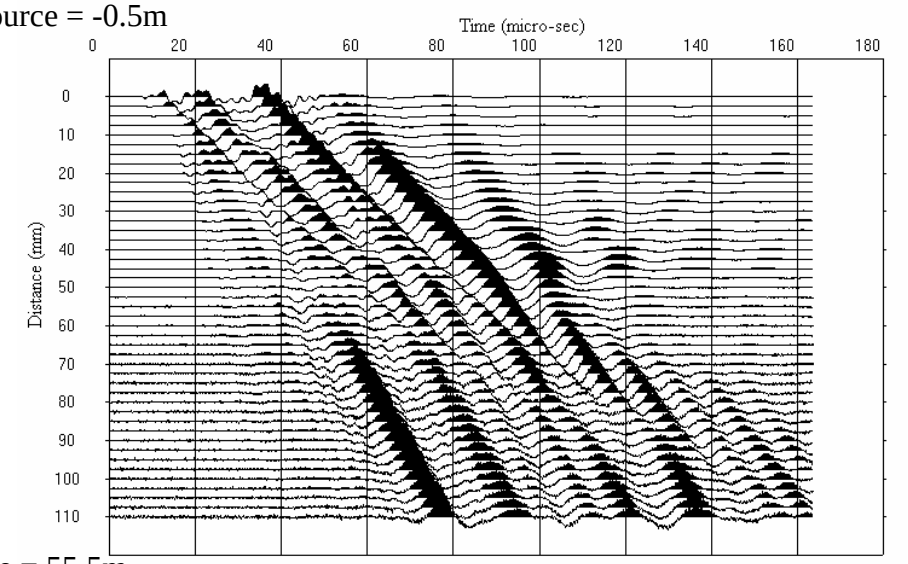

b) Source = 55.5m

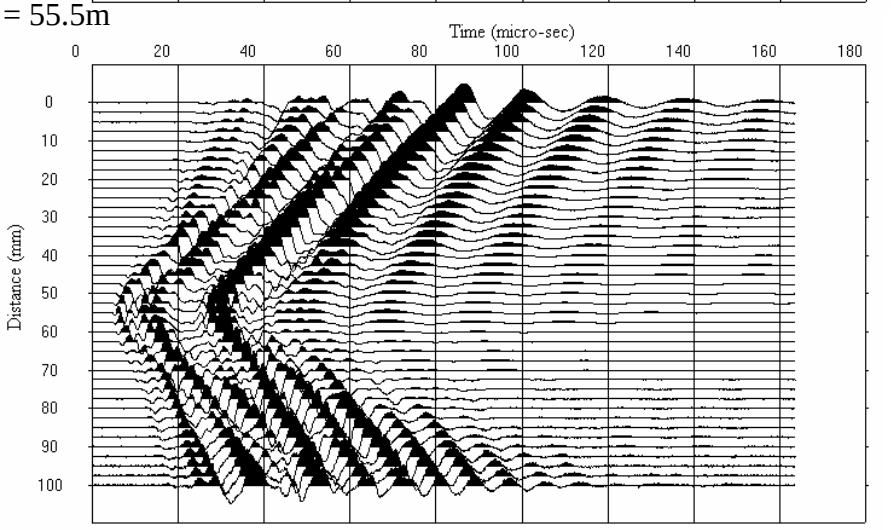

c) Source = 101.5m

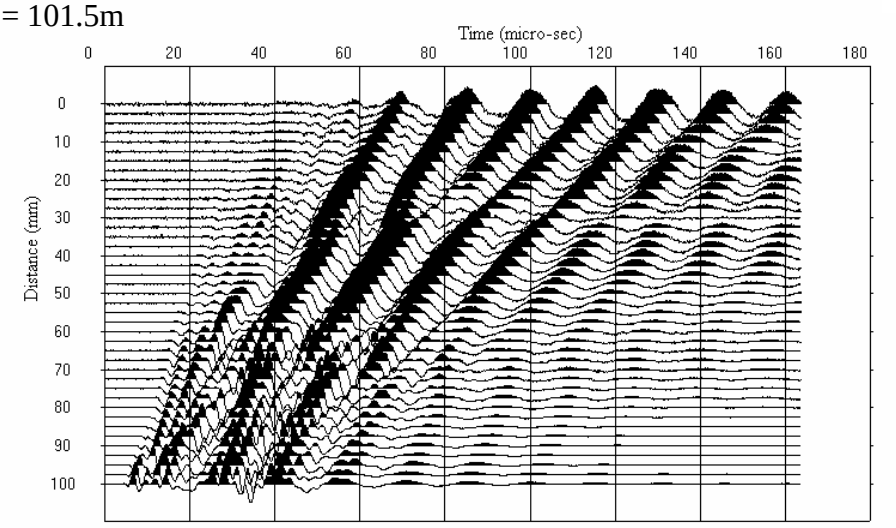

Figure 3.4.16. Example of observed waveform data using the LDV and PZT for 2D model.

a)

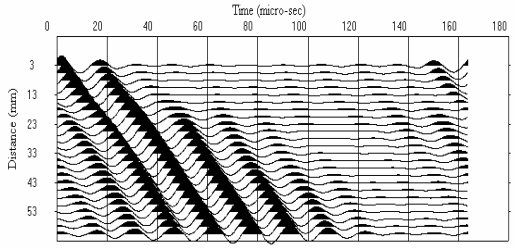

b)

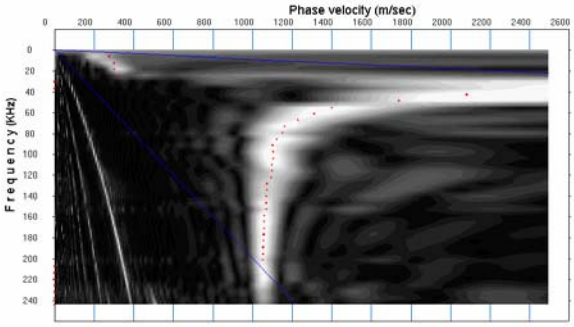

c)

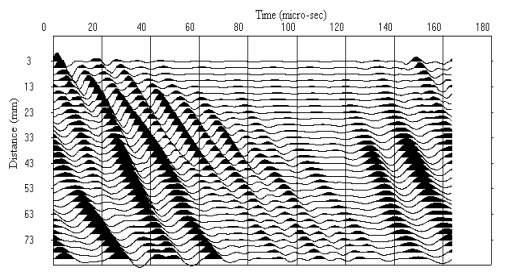

d)

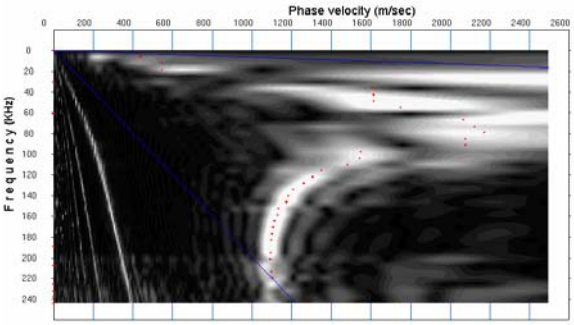

Figure 3.4.17 Example of CMPCC gathers. (a) Waveforms and (b) phase-velocity frequency image for the CMP distance of 27.5m. (c) Waveforms and (d) phase-velocity frequency image for the CMP distance of 72.5m.

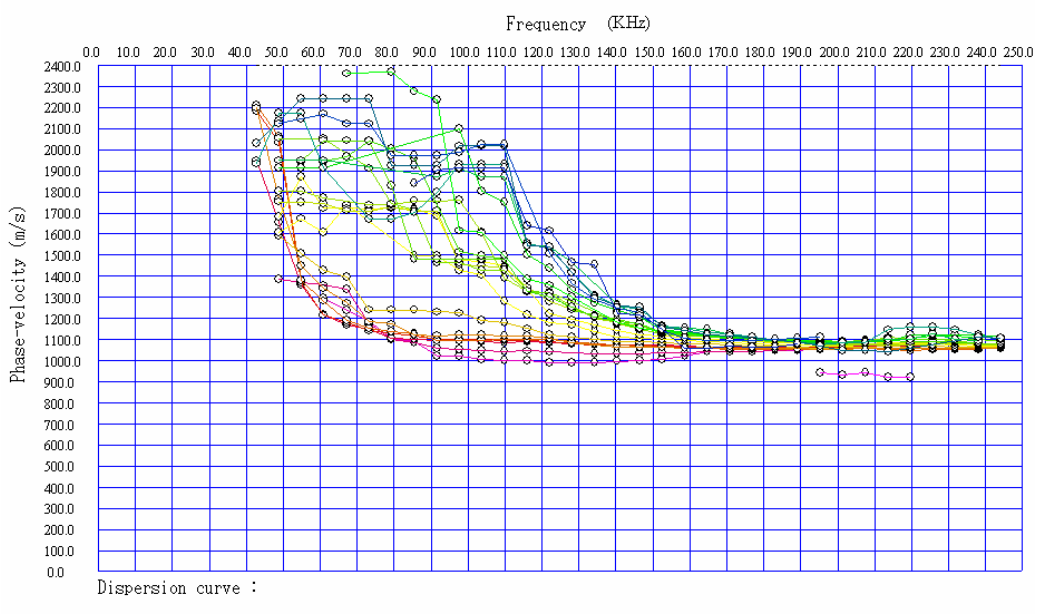

Figure 3.4.18. All dispersion curves calculated from CMPCC gathers. Difference of color indicates the difference of CMPCC location. Red to yellow curves are placed in left side of the step and green to blue curves are placed in right side of the step.

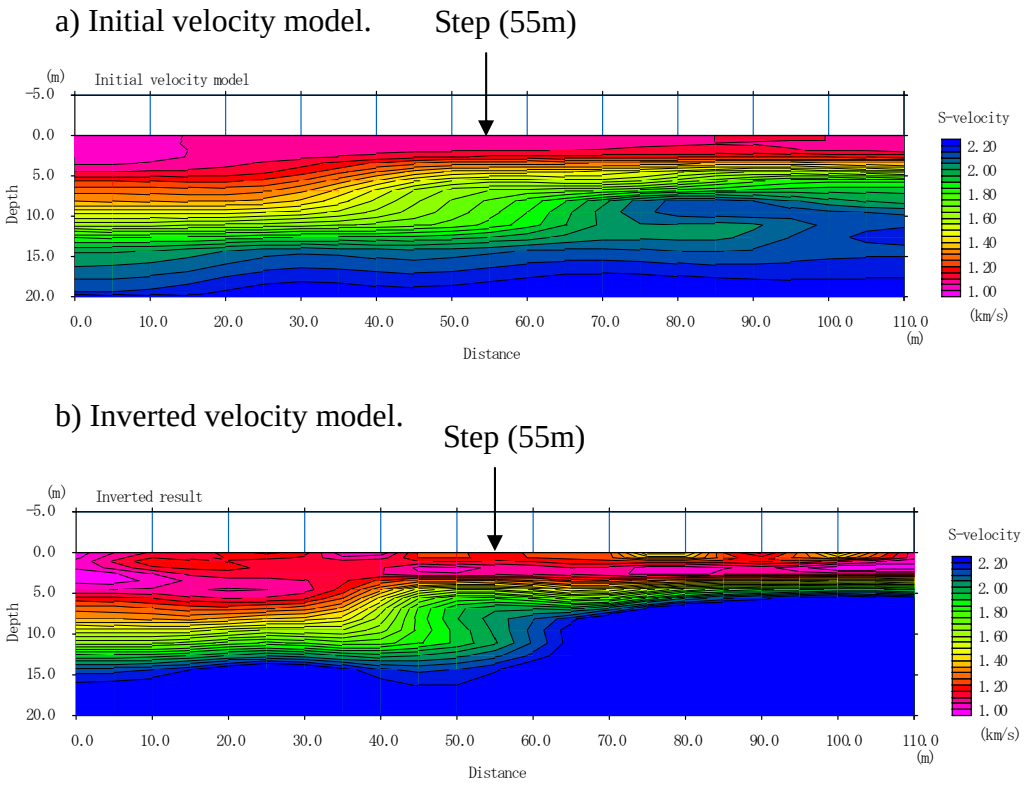

Figure 3.4.19. Initial (a) and inverted (b) S-wave velocity profile.

3.5 Field Experiments

The CMPCC analysis was applied to the field surface-wave data. The survey site is located in the Hokkaido Island, Japan and observed surface-wave data are shown in the Figure 3.2.1. The purpose of the survey was to detect a burred channel. The survey line was placed on a flood plain along the river. A 10kg sledgehammer was used as a source. Sources were moved with 4m intervals. Forty-eight geo-phones (4.5Hz) were deployed with 1m intervals. Figure 3.5.1 shows the sledge hammer and the geophone. The nearest source-to-receiver offset was 1m. Fifty-two shot gathers were recorded by an OYO-DAS1 seismograph.

Figure 3.5.2 shows the resultant CMPCC gathers and their phase-velocity frequency images. The CMPs are at the 173m (a) and 201m (b), placed in the first half and latter half of the spread, respectively. Any changes in surface-wave velocity are not apparent in the time domain waveform data of CMPCC gathers. In the phase-velocity frequency images, it is obvious that the energy concentrates in one phase velocity curve.

A 2D S-wave velocity model was reconstructed by applying the inversion method described in the previous chapter. The number of layers is also fixed as 15. Figure 3.5.3 shows the reconstructed S-wave velocity model obtained from MASW (a) and CMPCC (b). N-value curves obtained through an automatic ram-sounding are superimposed to the reconstructed structures. The 2D S-wave velocity structure reconstructed by the CMPCC analysis well coincides with N-value curves.

Variation of N-value curves along the line suggest that the velocity structure should changes horizontally between S2 (120m) and S1 (200m). In the S-wave velocity structure from the surface-wave method, the depth of low velocity layer (alluvium sediments) changes at the distance of 175m. Based on the interpretation of the S-wave velocity structure obtained through the surface-wave method together with N-value curves, we can conclude that there is a buried channel filled with alluvium sediments, away beyond the distance of 175m (Figure 3.5.3c).

(a)

(b)

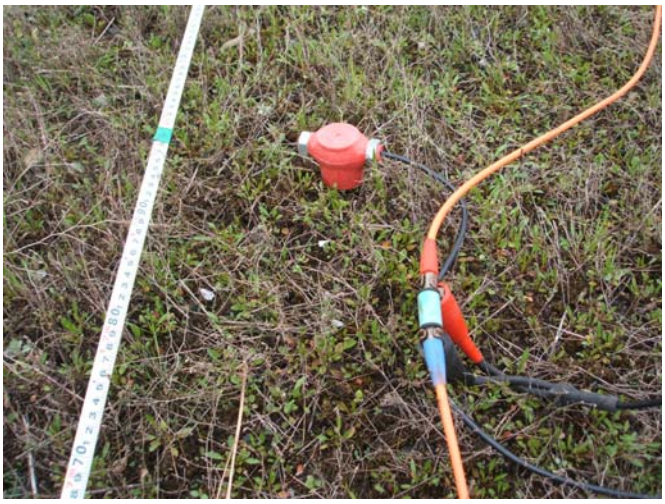

Figure 3.5.1. A sledge hammer (a) and a geophone (b) used in a surface-wave method.

(a)CMP distance of 173m　　(b)CMP distance of 201m

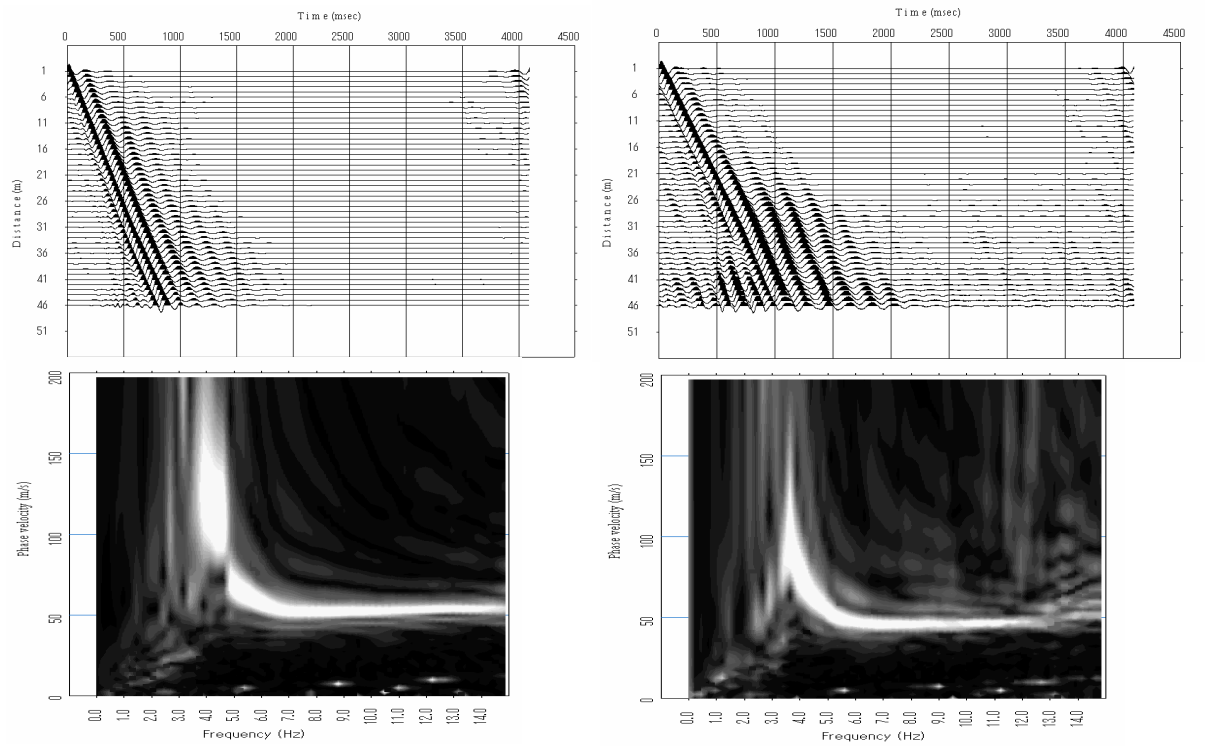

Figure 3.5.2. Result of CMPCC analysis for waveform data shown in the Figure 3.2.1. CMPCC gathers (top) and their phase-velocity frequency images (bottom). CMP distances are 173m (a) and 201m (b).

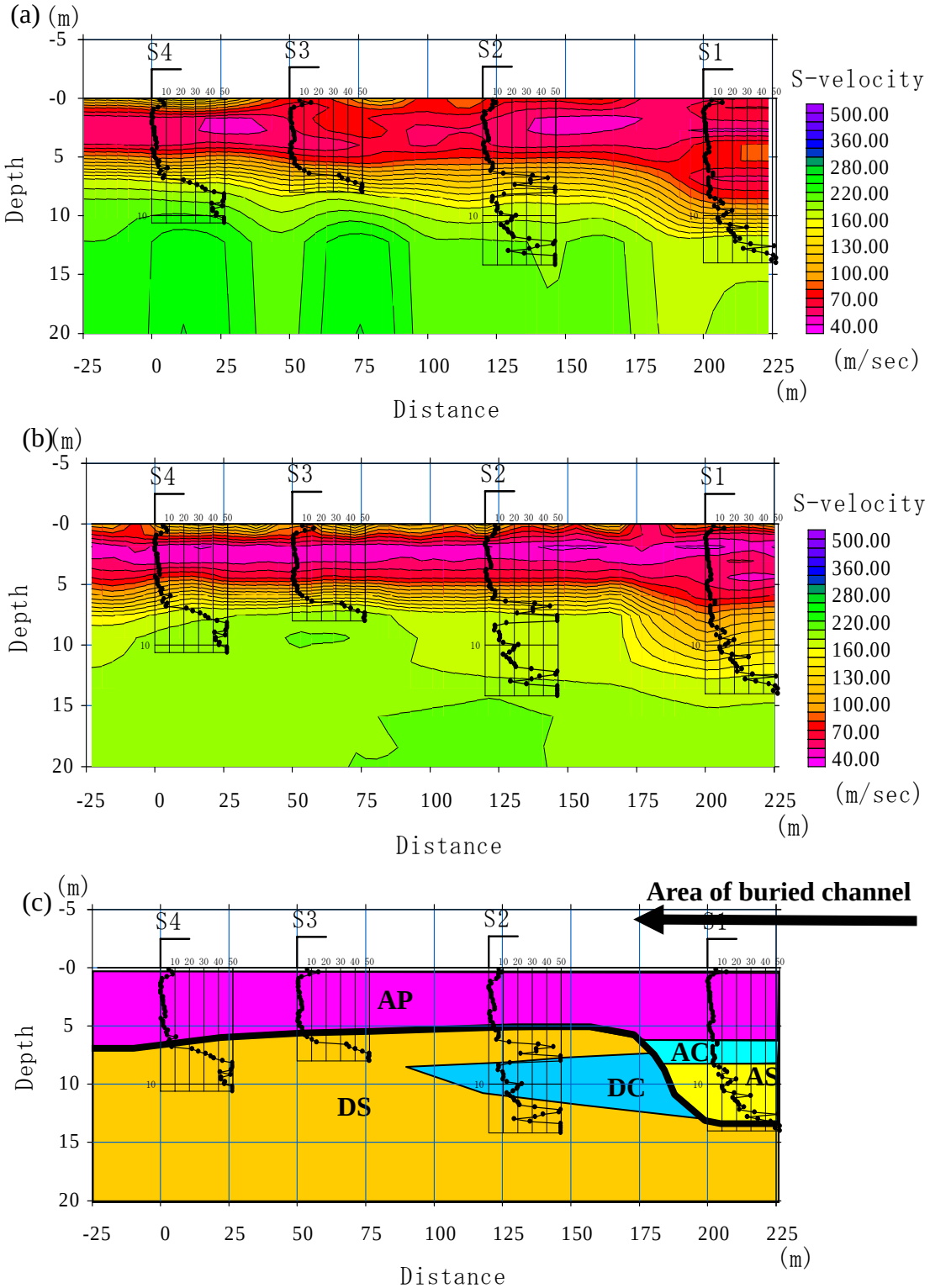

Figure 3.5.3. Reconstructed S-wave velocity structure by (a) Conventional MASW method and (b) CMPCC method, together with a geological section (c) estimated from N-values obtained by an automatic ram-sounding: The surface geology consist of AP: alluvium peat, AC: alluvium clay, AS: alluvium sand, DC: diluvium clay, and DS: diluvium sand.

3.6 Summary

One of the notable features of the CMPCC analysis is that the method does not require any summation and average of phase differences. The reason is that the CMPCC analysis processes the multi-channel and multi-shot waveform data into the cross-correlations. The conventional SASW method determines phase-velocities from different spacing cross-correlations separately. The SASW cannot determine high-frequency phase velocities from large-spacing cross-correlations due to a spatial aliasing. Therefore, the SASA uses only limited information in whole waveform data. On the contrary, the MASW analysis is better than SASW because the methods can determine phase-velocities precisely using whole waveform data (McMechan and Yedlin, 1981; Park et al., 1999a, 1999b). The CMPCC analysis is a further extension of the MASW and enables us to determine phase-velocities from multi-shot data directly by using the CMPCC gathers. The method not only improves accuracy and resolution in the MASW method but also enables the SASW method to perform pseudo multi-channel analysis for distinguishing a fundamental mode from higher modes visually.

References

Guo, T., and Liu, L., 1999, Non-Intrusive Evaluation of Submarine Tunnel Foundation Using Dynamic High-Frequency Surface Wave Prospecting, Proceedings of the symposium on the application of geophysics to engineering and environmental problems '99, 67-74.

Hayashi, K., and Suzuki, H., 2001, Surface wave propagation in two-dimensional models and its application to near-surface S-wave velocity delineation, Proceedings of the 5th SEGJ international symposium, 385-392.

Hayashi, K., and Suzuki, H., 2004, CMP cross-correlation analysis of multi-channel surface-wave data, Butsuri-Tansa, 57, 7- 13.

Levander, A. R., 1988, Fourth-order finite-difference P-SV seismograms, Geophysics, 53, 1425-1436.

McMechan, G. A., and Yedlin, M. J., 1981, Analysis of dispersive waves by wave field transformation : Geophysics 46, 869-874.

Miller, R. D., Xia, J., Park, C. B. and Ivanov, J. M., 1999, Multichannel analysis of surface waves to map bedrock : The Leading Edge, 18, 1392-1396.

Nazarian, S., Stokoe, K. H., and Hudson, W. R., 1983, Use of spectral analysis of surface waves method for determination of moduli and thickness of pavement system : Transport. Res. Record, 930, 38-45.

Nishizawa, O., Satoh, T., Lei, X. and Kuwahara, Y., 1997, Laboratory studies of seismic wave propagation in inhomogeneous media using a laser Doppler vibrometer, BSSA, 87, 809-823.

Park, C. B., Miller, R. D., and Xia, J., 1999a, Multimodal analysis of high frequency surface waves : Proceedings of the symposium on the application of geophysics to engineering and environmental problems '99, 115-121.

Park, C. B., Miller, R. D., and Xia, J., 1999b, Multichannel analysis of surface waves : Geophysics, 64, 800-808.

Saito, M., 1993, Branch line contribution in Lamb's problem, BUTSURI-TANSA, 46, 372-380 (in Japanese).

Tokimatsu, K., 1997, Geotechnical site-characterization using surface-waves,

Earthquake geotechnical engineering, Ishihara (ed.), Balkema, Rotterdam, .1333-1368.

Xia, J., Miller, R. D., and Park, C. B. 1999a, Configuration of near surface shear wave velocity by inverting surface wave : Proceedings of the symposium on the application of geophysics to engineering and environmental problems '99, 95-104.

Xia, j., Miller, R. D. and Park, C. B., 1999b, Estimation of near-surface shear-wave velocity by inversion of Rayleigh waves, Geophysics, 64, 691-700.

Chapter 4

Development of a Passive Surface-wave Method Using Micro-tremors

4.1 Introduction

The Earth's surface is always vibrating weakly. This vibration is called as microtremor. The microtremor are generated by the various sources, such as winds, ocean waves at the seashore, traffic noises, heavy machinery factories and household appliances. Because the microtremor are generated by sources on the ground surface, the microtremor mainly consist of surface-waves, and the vertical component of the microtremor can be considers as Rayleigh waves. Therefore, it is reasonable that the dispersion curve of the vertical component of the microtremor is the dispersion curve of Raylegh waves.

Micro-tremors consist of wide frequency range of surface waves from the period of 0.1 second to 10 seconds. Therefore, S-wave velocity model down to several kilometers can be obtained using the microtremor. A passive surface-wave method, so called micro-tremors array measurements (MAM), is a seismic exploration method in which the micro-tremors are observed by multi-receives and its phase-velocity is analyzed. The first researcher to give much attention to the high frequency surface-waves is Aki. He investigated the micro-tremors as surface-waves and presented the theory of Spatial Auto Correlation (Aki, 1957). Okada (2003) had developed a large scale microtremor array measurements, using long period microtremor. Figure 4.1.1 shows the schematic diagram of passive surface-wave method using micro-tremors. The penetration depth of the method is from 100m to several kilometers. We have employed the Okada's method and applied it to shallower problems, such as geo-technical, environmental, and earthquake engineering. Our depth of interests is from several ten meters to 100m.

Only few attempts have so far been made at the applicability of the passive method for shallow S-wave velocity investigations. Therefore, we have applied the method to many sites and evaluated the applicability of the method. In this Chapter, we are going to show the result of evaluation of applicability for passive surface-wave method. Unlike the active surface wave methods, the MAM does not need any sources and needs two-dimensional arrays, such as triangles, circles or crosses. Because the sources of the microtremor are distributed randomly in space, the microtremor does not have any specific propagation directions. Therefore, two dimensional arrays are required for calculating the phase-velocity of the microtremor and statistic analysis approach, so called Spatial Auto Correlation (SPAC) is used in phase-velocity calculation. The mathematical description of SPAC is mentioned in the Chapter 2.

Theoretically, isotropic arrays, such as a circle or an equilateral triangle, are preferable in the SPAC analysis. However, the isotropic arrays required wide space and it is difficult to obtain such wide space in urban area. Recently, several theoretical studies have been made on the applicability of irregular arrays (e.g. Yokoi et al., 2006). The use of irregular arrays will enable us to apply the passive methods in urban area. Our evaluation has mainly focused on the applicability of irregular arrays, such as L-shape and linear arrays.

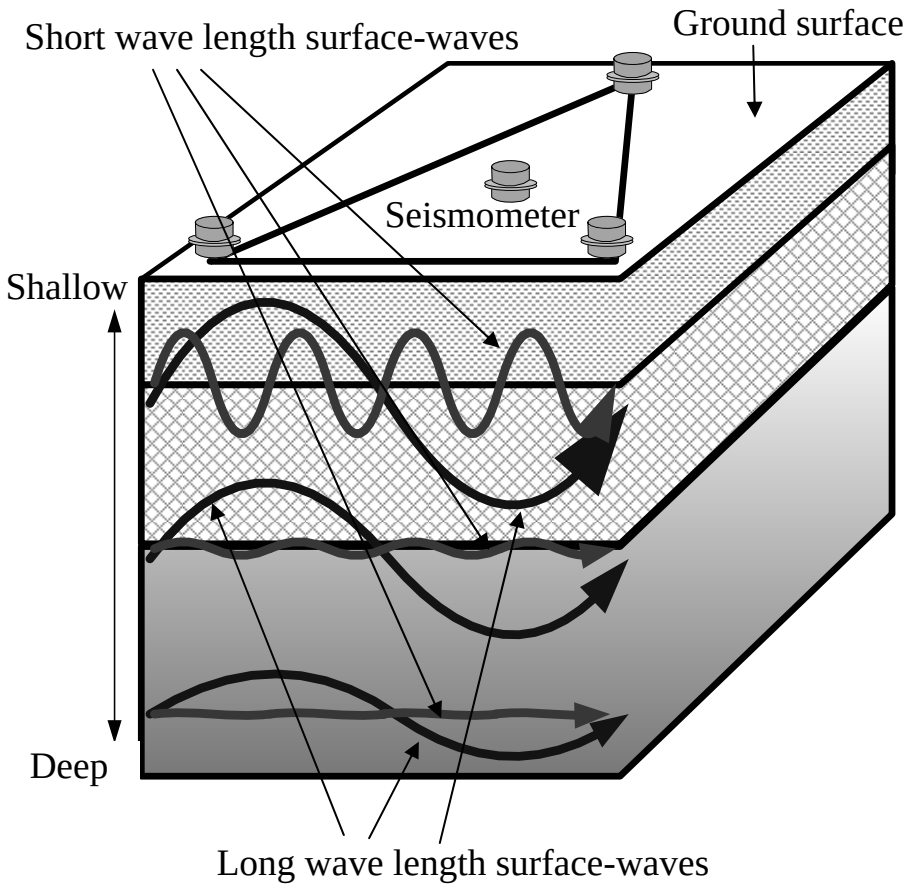

Figure 4.1.1. Schematic diagram showing microtremor array measurements. Amplitude of shorter wave length surface-waves decay rapidly with depth whereas one of longer wave length keep amplitude even if deeper part. Therefore, shorter wave-length surface-waves reflect shallow S-wave velocity and longer one reflect deeper S-wave velocity. S-wave velocity profile can be estimated be measuring phase-velocity for different wave-length (frequency).

4.2 Field Experiments at the Leaning Tower of Pisa, Italy

4.2.1 Introduction

The basic field experiments of a passive surface-wave method were carried out at the Leaning Tower of Pisa, Italy. There are several purposes in the experiments. The first purpose is evaluating the appropriate data length. Cleary, the longer data is the better for statistical analysis in the spatial auto correlation. However, long data acquisition decreases the convenience of the method. Recording micro-tremor data with appropriate data length is very important in practical survey. The second purpose is evaluating the effect of array shape on dispersion curves. Isotropic arrays, such as circle or triangle are theoretically best for passive analysis. However, sometimes it is difficult to use such isotropic arrays in urban area. Irregular arrays enable us to use the passive method in urban area. Therefore, we have to investigate the applicability of irregular arrays. Artificial noise is also important issue. The effect of artificial noise, such as traffic noise, on passive data analysis has never been examined. Around the Leaning Tower of Pisa, there is a lot of in-situ S-wave velocity information, such as cross-hole, SCP. Therefore, the site was very good place to evaluate the accuracy and reliability of the method. We have investigated these issues at the Leaning Tower of Pisa and compared the result with existed S-wave information. In this chapter, the result of simple experiments will be summarized, S-wave velocity model at the Tower will be investigated in the next chapter.

We have performed 7 passive arrays at different site using different shapes. Figure 4.2.1 shows the location and shape of passive arrays around the Tower. At the north and east side of the tower, we measured three different shape arrays.

4.2.2 Effect of Data Length on Phase-velocity Calculation

Geophones that have natural frequency of 2Hz were used as receivers. And an OYO McSEIS-SXW was used for data acquisition. Figure 4.2.2 shows the example of

waveform data. One data-file contains about 30 seconds of microtremor data and 300 data-files were continuously recorded. Total data length is about 3 hours. Dispersion curves were calculated for different record length data, such as 1, 5, 10, 20 and 300 data-files, it results in 33 seconds, 2.5 minutes, 5 minutes, 10 minutes and 3 hours respectively.

In the analysis of passive surface-wave data, we use a spatial auto correlation method, so called ‘SPAC’. In the SPAC method, we compare coherence calculated from observed waveform data with Bessel functions calculated from assumed phase velocity. Figure 4.2.3 shows the coherence obtained from different record length data. Theoretically, coherence curves must be smooth curves as Bessel function. It is clear that coherence curves go to smoother as data length goes to longer. Smooth coherence curve means S/N ratio is high. We can say that long data can increase S/N ratio in the SPAC analysis.

A phase-velocities giving minimum error between coherence curves and Bessel functions, are defined as a dispersion curve. Figure 4.2.4 shows dispersion curves obtained from different record length data. We can see that, 33 seconds data, shown as blue dots, includes a lot of noise. However, it is clear that the dispersion curves go smoother as data length goes longer. Figure 4.2.5 shows the root mean square (RMS) error against data length. The RMS error decreases as data length increases. It is also clear that the RMS error for 10minutes and that of 3 hours are almost identical. These results lead to the conclusion that approximately 10 minutes record is enough for phase-velocity analysis using the spatial auto correlation.

4.2.3 Effect of Data Length on Phase-velocity Calculation

Next, dispersion curves obtained through different shapes will be investigated. Figure 4.2.6 shows the comparison of dispersion curves using different array shapes at north site and east site. At the north site, three different shape arrays give almost identical dispersion curve. At the east site, two different shape arrays give almost identical dispersion curve. These results lead to the conclusion that the effect of array shape on dispersion curve calculation was not significant in the site. The result of

similar tests at many places in the world will be discussed in the Chapter 4.3.

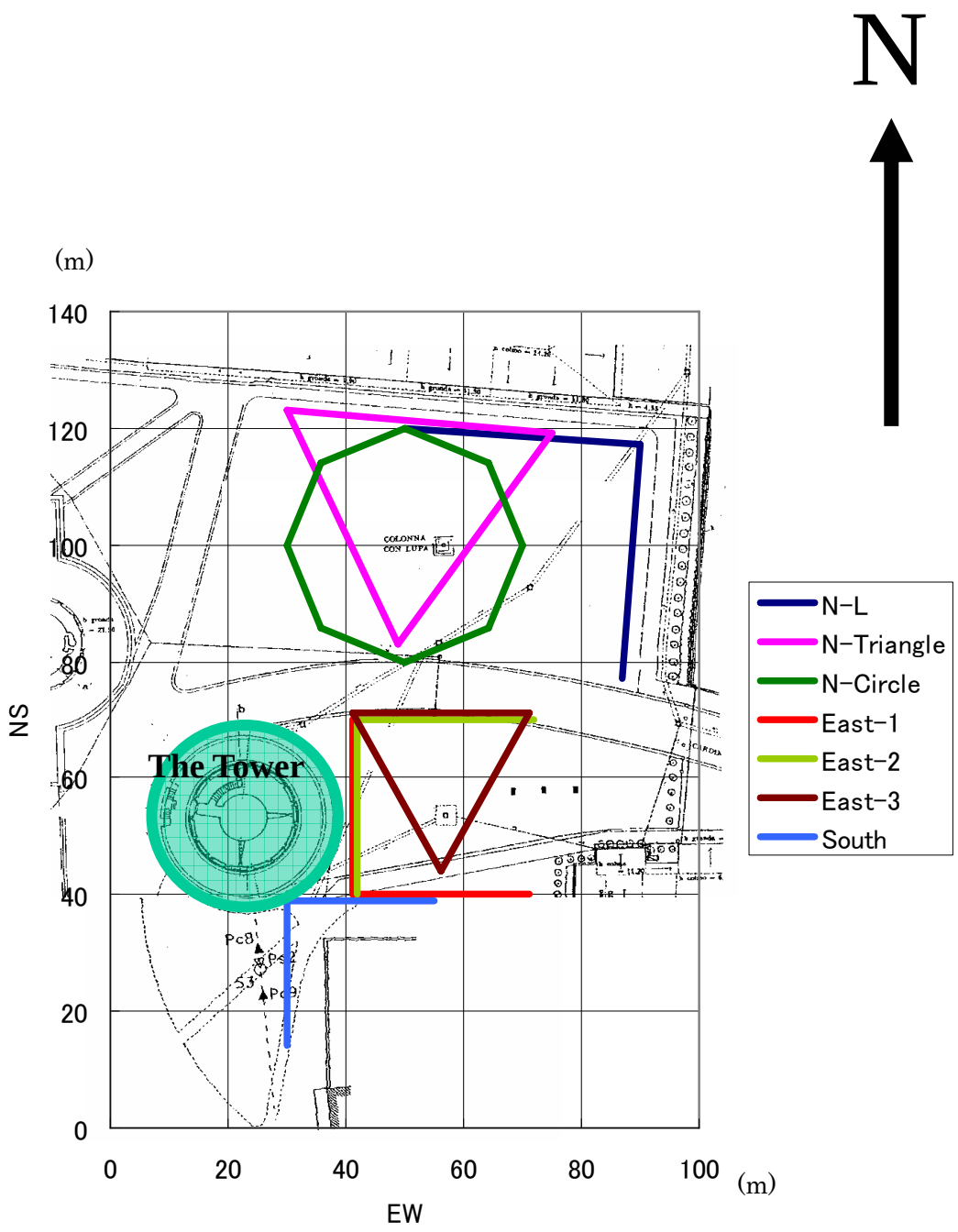

Figure 4.2.1 Location and shape of passive arrays.

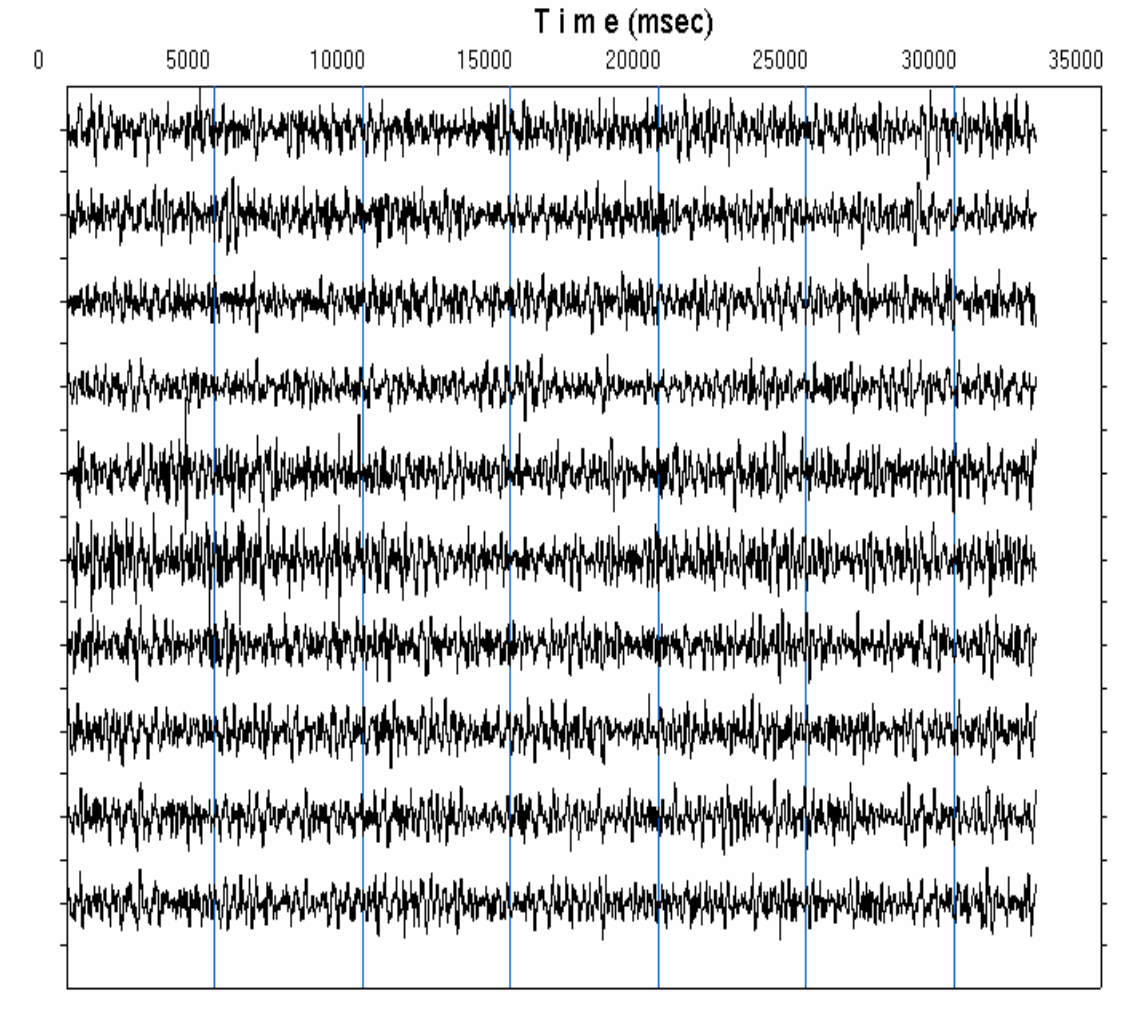

Figure 4.2.2 Example of waveform data.

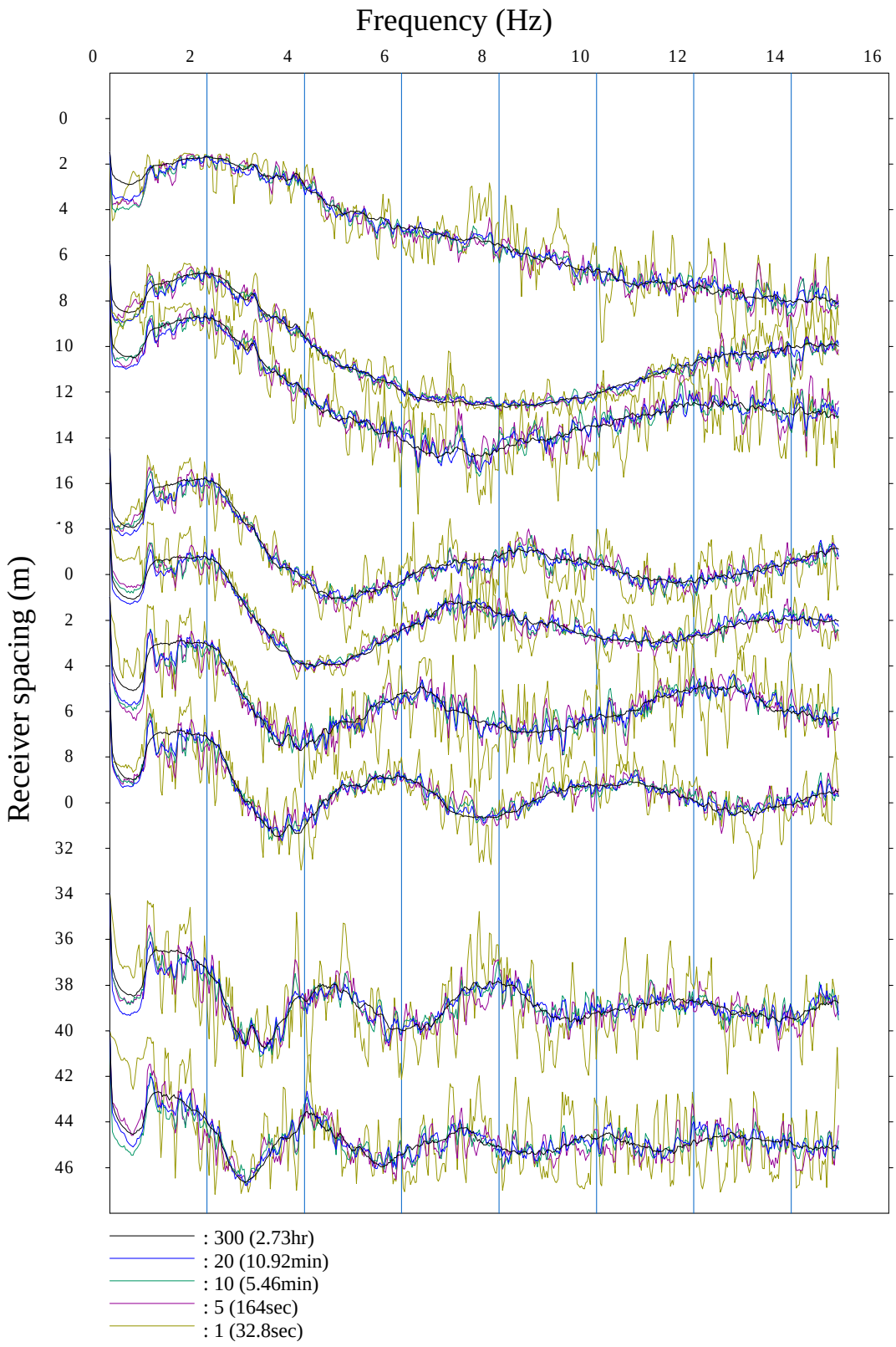

Figure 4.2.3 Coherence obtained from different record length data.

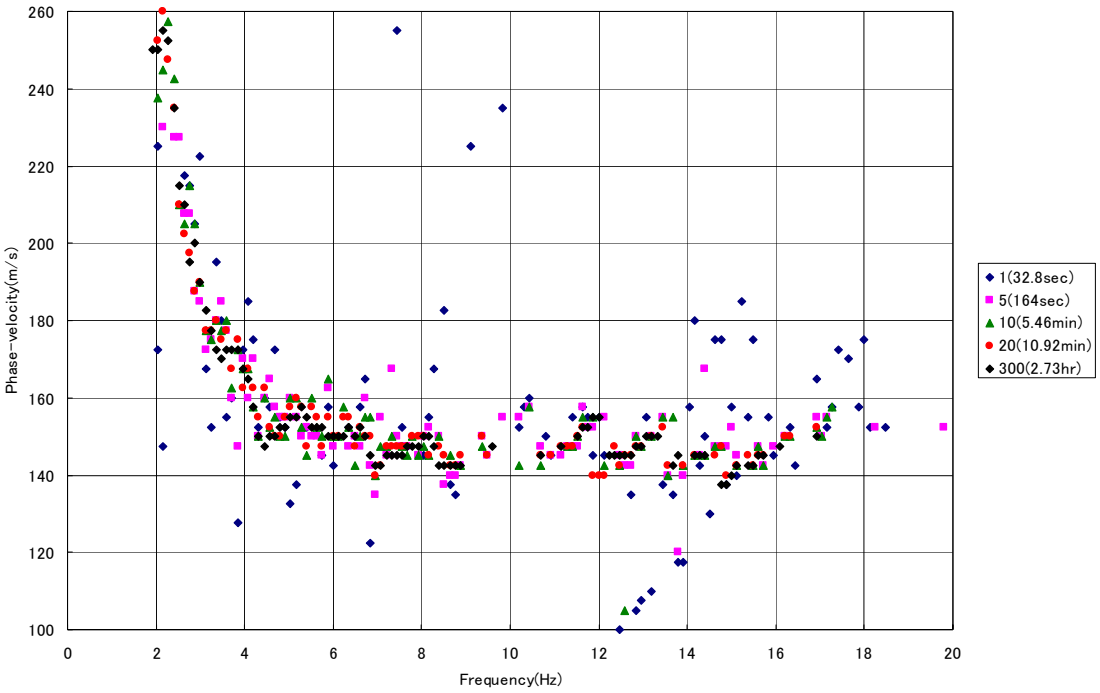

Figure 4.2.4 Dispersion curves obtained from different record length data.

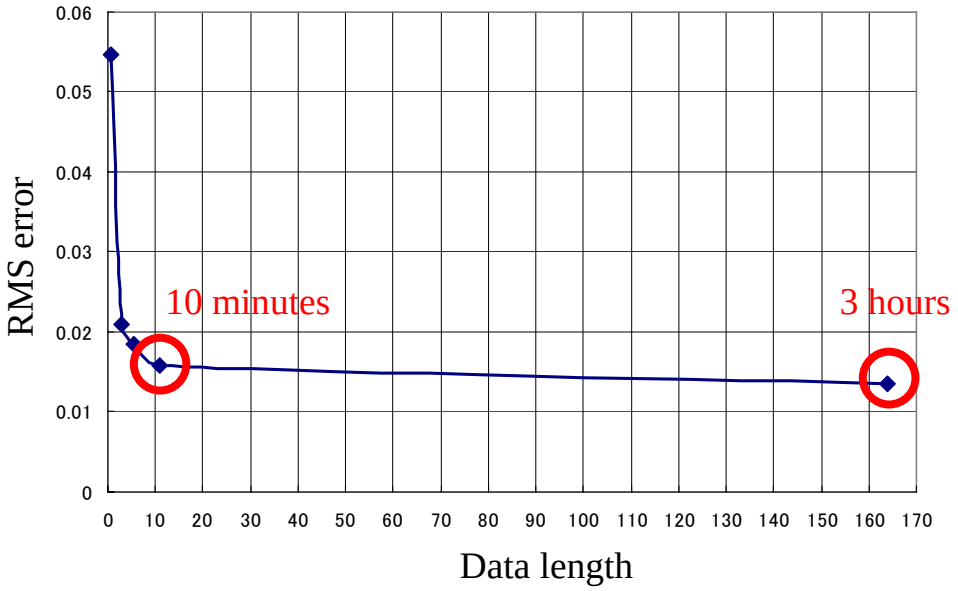

Figure 4.2.5 Root mean square error against data length.

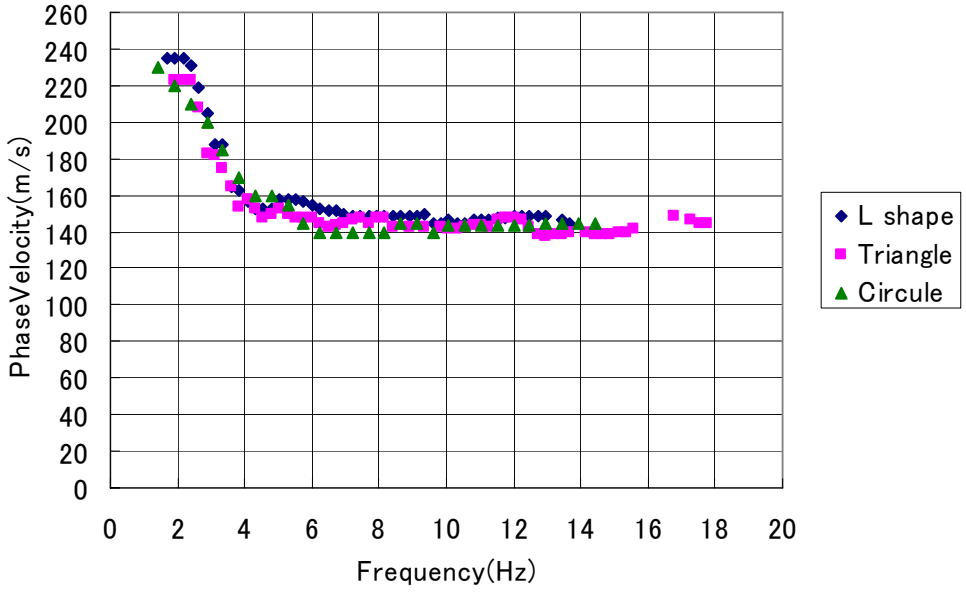

Dispersion curves obtained at North site.

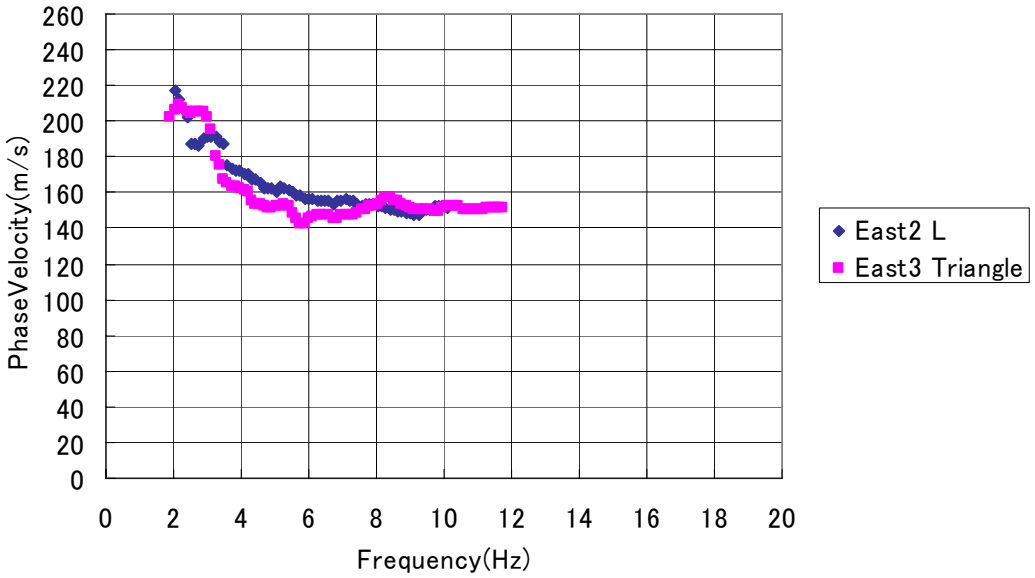

Dispersion curves obtained at East site.

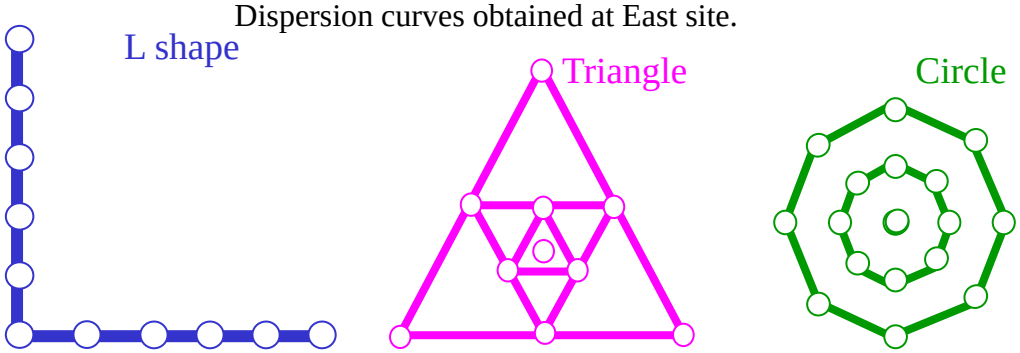

Figure 4.2.6 Comparison of dispersion curves using different array shapes at north site (top) and east site (bottom).

4.3 Effect of Array Shape and Comparison with an Active Method

The result of the field tests in the Leaning Tower of Pisa shown in Chapter 4.2implies that a high-frequency (2-10Hz) micro-tremor array measurement (MAM) is fairly robust and stable so that the effect of shape of array or traffic noise may be negligible. In order to confirm this assumption, we have performed similar tests many places in the world. Active method dispersion curves were also compared with passive one.

4.3.1 Data Acquisition in Nagoya City, Japan

Passive and active dispersion curves were compared at two parks in the downtown of Nagoya city in Japan. The site is placed in alluvium plain. Triangle and L-shape arrays were used for passive data acquisition. The size of triangle array was 50m and that of L-shape array was 75m. In the passive method, 10 geophones were uses in the triangle array and 11 geophones were used in the L-shape array (see Figure 4.3.1). Geophones that have natural frequency of 2Hz were used as receivers. In the active method, 24 geophones were deployed with 1m receiver intervals. Geophones that have natural frequency of 4.5Hz were used as receivers and a 10 kg sledge hammer was used as a source. An OYO McSEIS-SXW was used for data acquisition.

Figure 4.3.1 shows the dispersion curves obtained through both passive and active surface-wave methods. We can see that the triangle and L-shape dispersion curves are almost identical. In the frequency range between 8 to 15 Hz, passive dispersion curves agree with active one very well. It strongly implies that the passive and active methods measure the same mode dispersion curves.

4.3.2 Data Acquisition in Tsukuba City, Japan

Passive and active dispersion curves were compared at Tsukuba city in Japan. The site is placed in diluvium terrace covered with Kanto loam. Triangle and

L-shape arrays were used for passive data acquisition. The size of array was 50m for both L-shape and triangle arrays. In the passive method, 10 geophones were uses in the triangle array and 11 geophones were used in the L-shape array (see Figure 4.3.2). Geophones that have natural frequency of 2Hz were used as receivers. Data length is about 10 minutes. In the active method, 24 geophones were deployed with 1m receiver intervals. Geophones that have natural frequency of 4.5Hz were used as receivers and a 10 kg sledge hammer was used as a source. An OYO McSEIS-SXW was used for data acquisition. A large scale micro-tremors array measurement was also performed at the site. Triangle arrays were used and maximum array size was 1km. Long period seismometers were used as receivers.

Figure 4.3.2 shows the dispersion curves obtained through both passive and active surface-wave methods. We can see that the triangle and L-shape dispersion curves are almost identical. At the frequency of 5Hz, passive dispersion curves agree with active one very well. In the frequency range of 2 to 7Hz, small scale passive method dispersion curves (both triangle and L-shape) agree with that of large scale passive method. In conclusion, dispersion curves obtained through three different scale surface-wave methods agreed on one dispersion curve. We may, therefore, reasonably conclude that the dispersion curve obtained through the passive and active surface-wave method was the fundamental mode of Rayleigh wave dispersion curve.

4.3.3 Data Acquisition at the Dolphin Park in Los Angeles City, U.S.

Passive and active dispersion curves were compared at the Dolphin Park in the downtown of Los Angeles city in the U.S. Triangle and linear arrays were used for passive data acquisition. Data length is about 10 minutes. The size of triangle array was 60m and the length of linear array was 110m. In the triangular array, two types of data acquisition were performed. In the first one, 4 geophones that have natural frequency of 1Hz were used. Next one, 10 geophones that have natural frequency of 4.5Hz were used (see Figure 4.3.3). The 4.5 Hz geophones were also used in the linear array and the active method. The linear array is also used for the active method. A 10 kg sledge hammer was used as a source in the active method. An OYO McSEIS-SXW was

used for data acquisition.

Figure 4.3.3 shows the dispersion curves obtained through both passive and active surface-wave methods. We can see that the triangle and linear array dispersion curves are almost identical. It must be noted that the dispersion curves obtained by 4.5Hz geophones is almost identical down to the frequency of 2Hz. More noteworthy is that the dispersion curve obtained by linear array agrees with that of triangular array down to the frequency of 2 Hz. It implies that high frequency micro-tremors come from outside of the array almost isotropically. The active dispersion curve agrees with passive one in the frequency range from 5 to 10Hz as previous examples.

4.3.4 Data Acquisition in Redwood City, U.S.

Passive and active dispersion curves were compared at the park in the Redwood City in U.S.A. The site is placed in alluvium plain. Triangular array were used for passive data acquisition. The size of triangular array was 30m. Ten geophones were used in the passive method and 24 geophones were used in the active method (see Figure 4.3.4). Geophones that have natural frequency of 4.5Hz were used as receivers in both active and passive methods. A 10 kg sledge hammer and an industrial shaker were (Figure 4.3.5) used as sources in the active method. The shaker is traditionally used in the U.S. for a conventional surface-wave method known as the spectral analysis of surface-waves (SASW). An OYO McSEIS-SXW was used for data acquisition n both active and passive methods.

Figure 4.3.4 shows the dispersion curves obtained through both passive and active surface-wave methods. We can see that the passive dispersion curve agrees with that of the active method in the frequency range between 4 to 10 Hz. It is also important that the dispersion curve obtained through the sledge hammer agrees with that of the shaker. It confirms that an impulse source, such as the sledge hammer, can be used as the shaker that generate surface-waves as single frequency sinusoidal wave. Conventional surface-wave methods, such as SASW, have to use the shaker, which can generate sinusoidal waves, as a source. Because the SASW uses an industrial FFT analyzer, which cannot calculate phase-difference of impulsive waves generated by a

sledge hammer. The result of the example shows that the impulse source and multi-channel data acquisition can generate same dispersion curve as conventional method without the expensive shaker and FFT analyzer.

4.3.5 Data Acquisition at the Williams Park in San Jose City, U.S.

Passive and active dispersion curves were compared at the Williams Park in the San Jose City in U.S. Two types of active methods, MASW and SASW, were also compared. The MASW stands for the multi-channel analysis of surface-waves that we already explained in the previous chapters. The SASW stands for the spectral analysis of surface-waves in which a shaker and 2 or 3 geophones are used as receivers. The SASW has been traditionally performed in U.S. as a conventional surface-wave method.

The site is placed in alluvium plain and the United States Geological Survey (USGS) has performed a lot of geophysical inspections at there. There is borehole and PS logging was performed.

A triangular array was used for passive data acquisition. The size of triangular array was 50m. Ten geophones were used in the passive method and 24 geophones were used in the multi-channel analysis of surface-waves (see Figure 4.3.6). Geophones that have natural frequency of 4.5Hz were used as receivers in the passive method as well as the active method (MASW). A 10 kg sledge hammer was used as a source in MASW. An OYO McSEIS-SXW was used for data acquisition for the passive method and the MASW. For the SASW, the shaker was used as sources and two geophones that have the natural frequency of 1Hz were used as receivers. A FFT analyzer was used for data acquisition and phase difference calculation.

Figure 4.3.6 shows the dispersion curves obtained through the passive method (MAM) and the active methods (SASW and MASW). We can see that the three dispersion curves are almost identical in the frequency range between 4 to 10 Hz. The result confirm that the passive and active method measure same mode dispersion curves. It is also important that the dispersion curve obtained through the SASW agrees with that of the MASW. It means that the MASW in which an impulse source and

multi-channel data acquisition are used can generate same dispersion curve as the conventional SASW method as shown in the previous section.

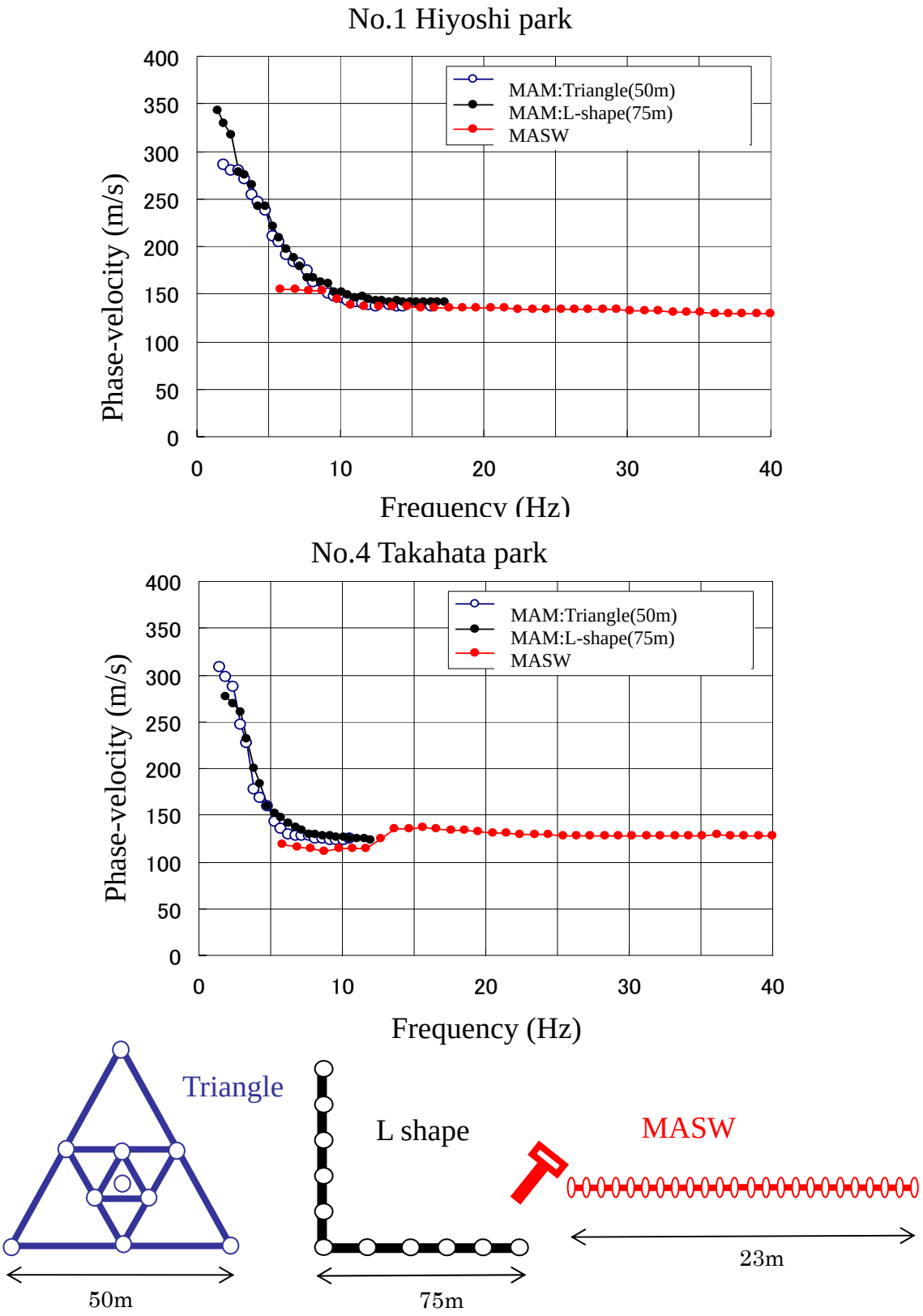

Figure 4.3.1 Comparison of passive and active dispersion curves in Nagoya, Japan.

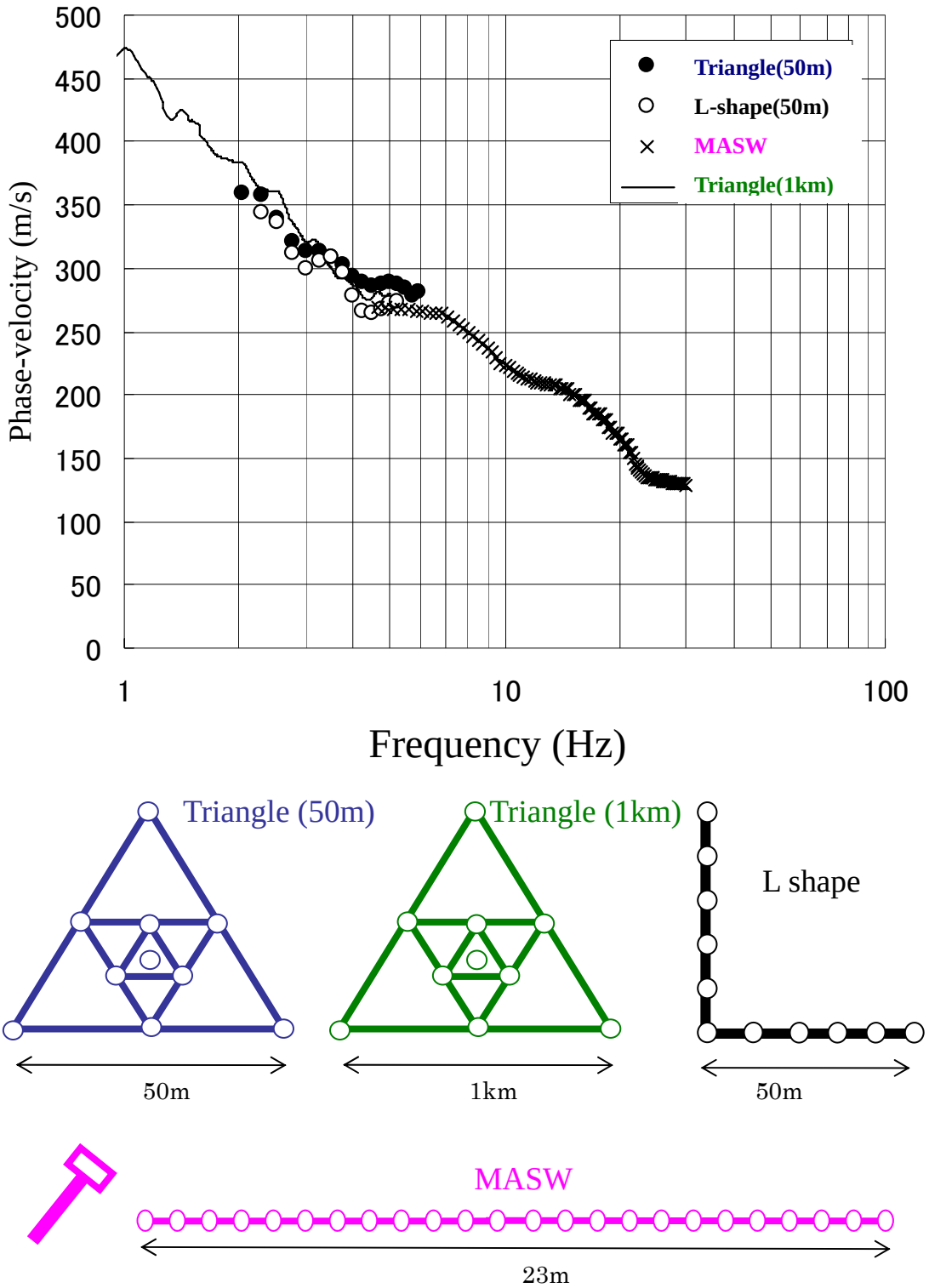

Figure 4.3.2 Comparison of passive and active dispersion curves in Tsukuba, Japan.

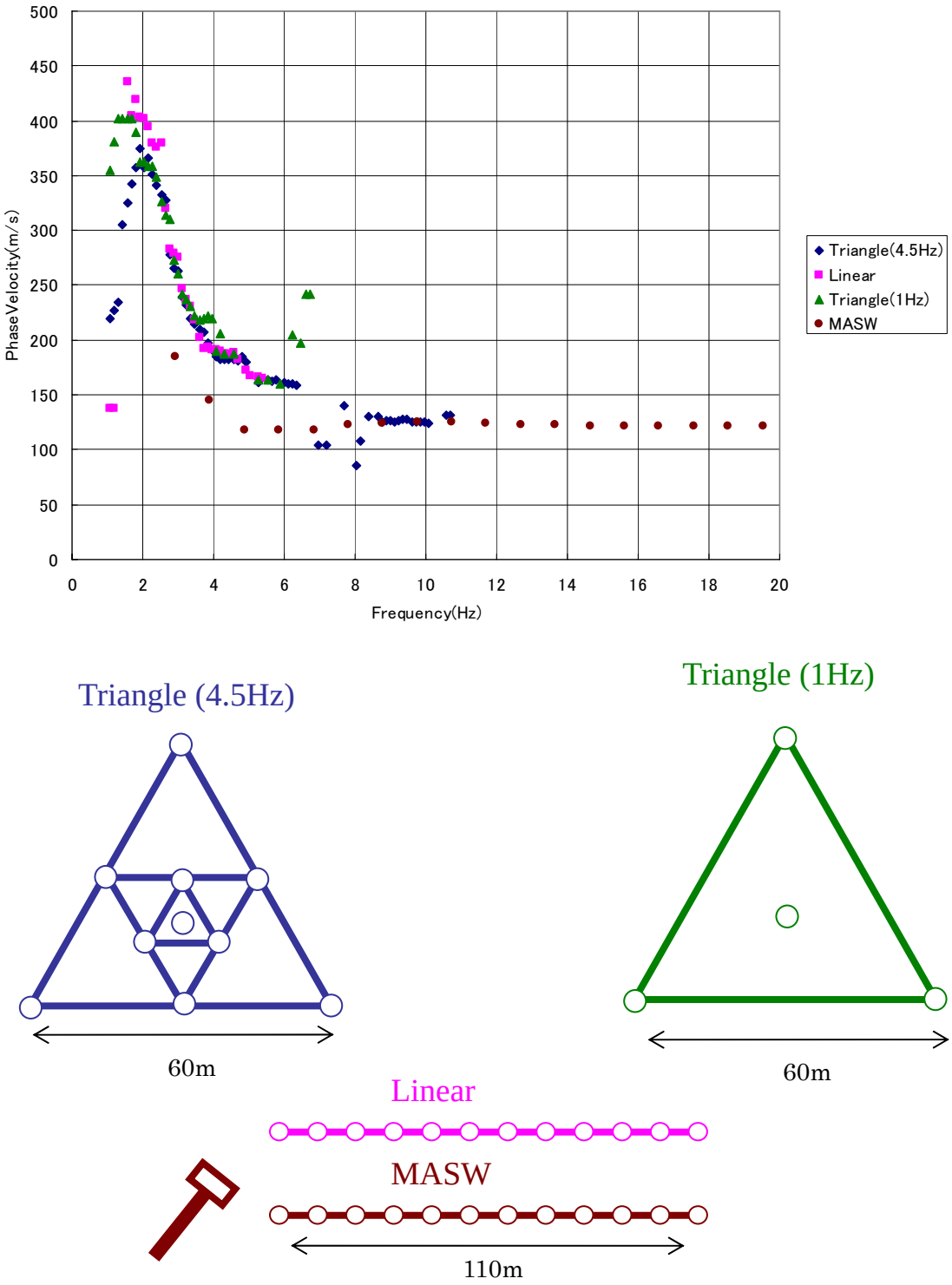

Figure 4.3.3 Comparison of passive and active dispersion curves in Los Angeles, U.S.

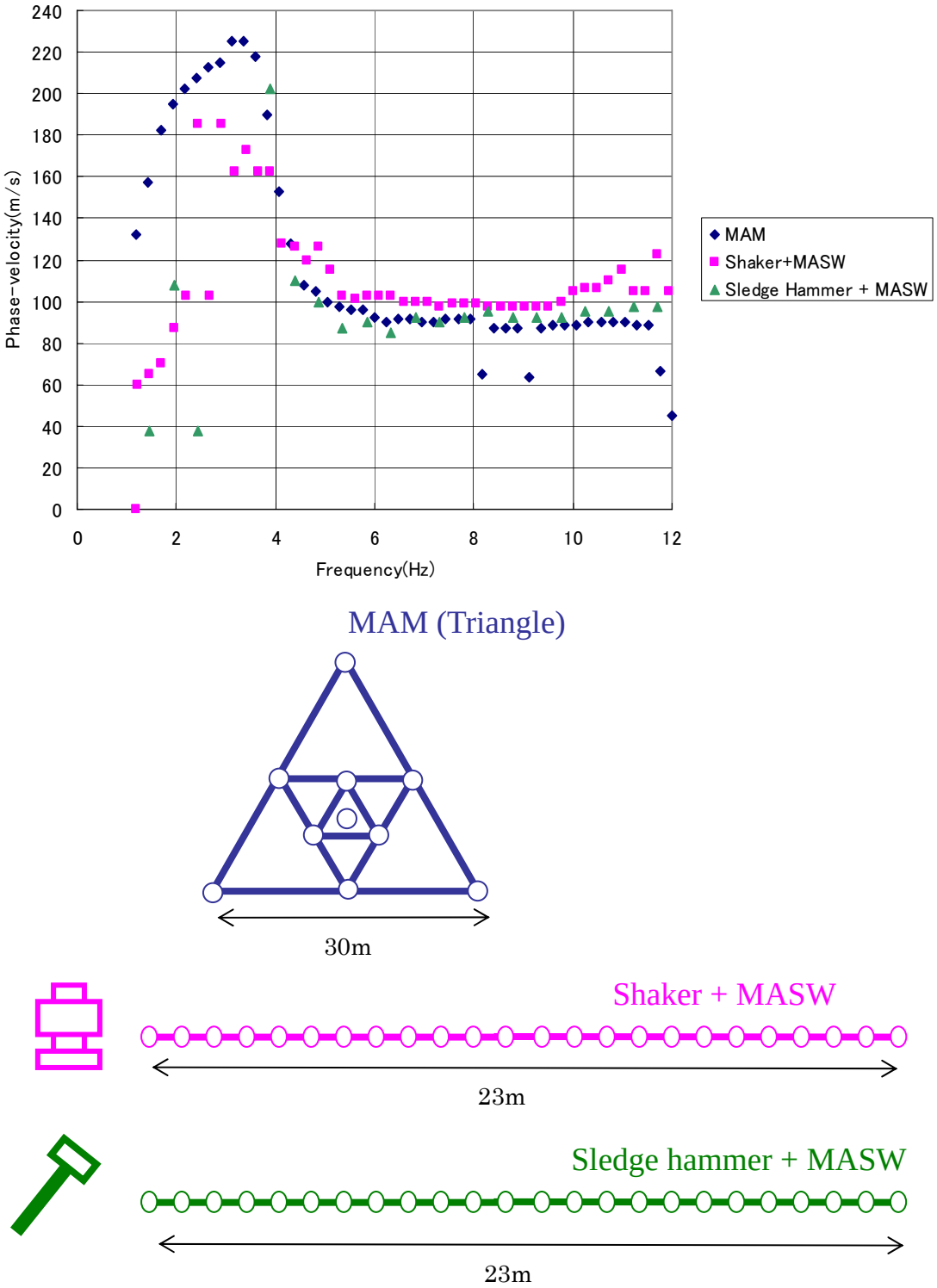

Figure 4.3.4 Comparison of passive and active dispersion curves in Redwood, U.S.

Figure 4.3.5 A typical shaker used in conventional surface-wave

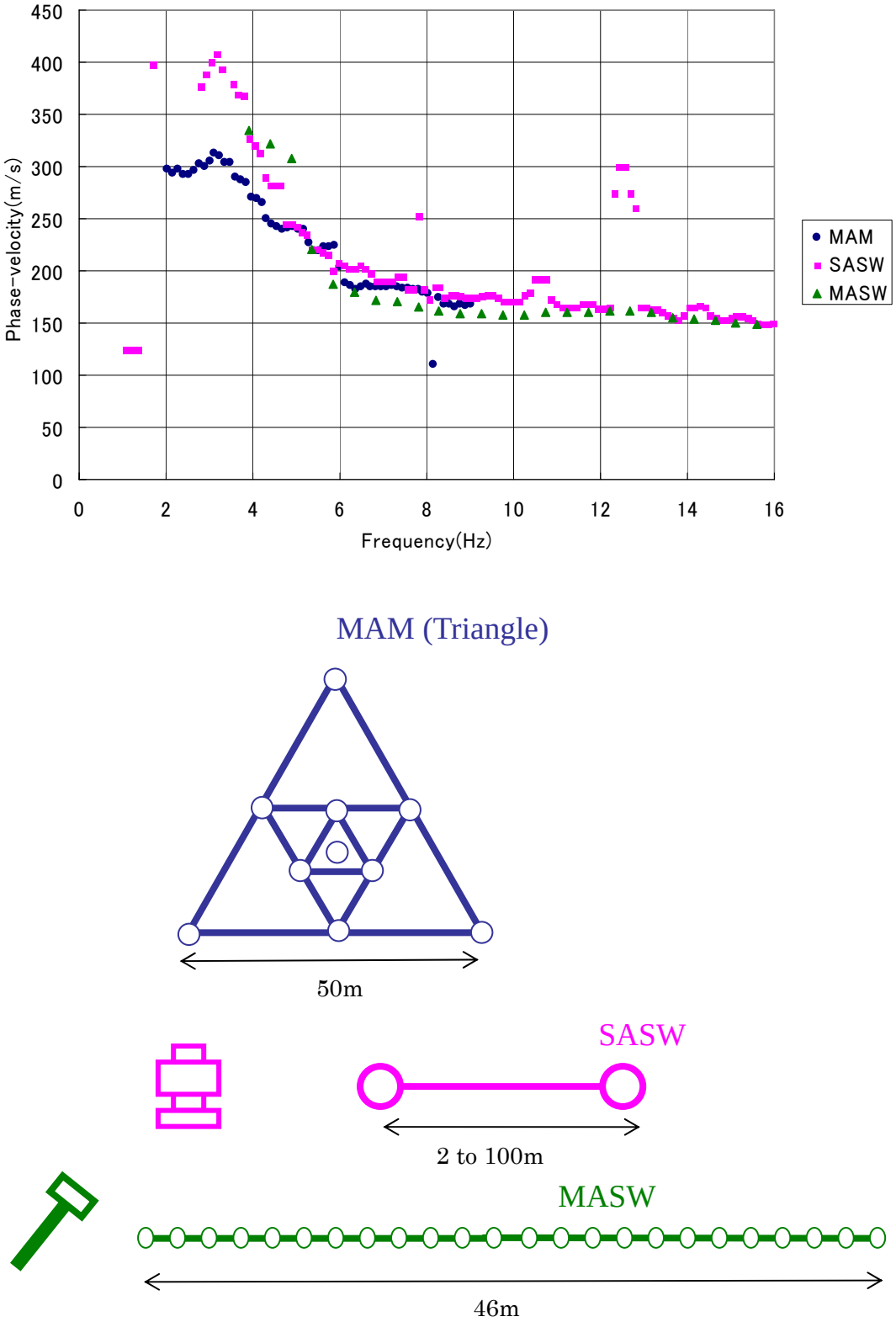

Figure 4.3.6 Comparison of passive and active dispersion curves in San Jose, U.S.

4.4 Summary

As shown in this chapter, we have applied a passive surface-wave method, so called small scale microtremor array measurements, to many sites and compared the results with the active surface-wave method. These results lead to the conclusion that small scale microtremor array measurements can be used for S-wave velocity delineation in civil engineering investigations. Irregular two-dimensional arrays, such as L-shaped array, provide almost same dispersion curves as one of isotropic arrays. Although an array is linear, microtremor data may provide correct dispersion curves at some of the sites. Penetration depth is almost same as the size of array. Arrays whose size of 50m and 2Hz geophones are enough for estimating S-wave velocity model down to the top of diluvium layer in most of sites. It seems that about 10 minutes of micro-tremor data is enough for 50m arrays.

The top of diluvium layer is very important because it is considered as the bedrock of most of the high-rise buildings. S-wave velocity down to the depth of 30m is also very important for evaluating the local site amplification of strong ground motion of earthquakes. Our field experiments show that the small scale micro-tremor array measurements can be used for such purposes. Penetration depth of active surface-wave methods with a sledge hammer or a weight drop is 10 to 20 m and not enough for bedrock investigations or local site amplification evaluation. The passive surface-wave method, together with the active method, enables us to estimate S-wave velocity models down to the depth of 50m non-destructively from the surface.

References

Aki, K., 1957, Space and time spectra of stationary stochastic waves, with special reference to microtremors, Bull. Earthq. Res. Ins., 35, 415-456.

Okada, H., 2003, The microtremor survey method, Society of Exploration Geophysicist, Tulsa.

Yokoi, T., Hayashi, K. and Aoike, K., 2006, A case study on dependence of the complex coherence function on the azimuth SPAC method of microtremor array measurement, Proceedings of the 114th SEGJ Conference, 138-141, (in Japanese).

Chapter 5

Application of Surface-wave Methods to Civil Engineering Investigations

5.1 Introduction

We have developed a surface-wave method in order to estimate the S-wave velocity structure of ground from the surface with small cost (Hayashi and Suzuki, 2004). A wide area must be investigated in geological and geotechnical investigations for civil engineering problems, such as levee inspections and the evaluation of reclaimed ground. Geophysical methods can play important roll in such wide area investigations. The surface-wave method is one of the attractive methods because it can estimate the stiffness of ground rapidly from the surface.

S-wave velocity structures down to the depth of several ten meters are very important in many engineering problems. For example, local site amplification of strong ground motion can be calculated from the S-wave velocity model down to several ten meters. Liquefaction resistance can be also calculated from S-wave velocity. In addition to that, the S-wave velocity well correlated to N-value (blow number) obtained from SPT. Therefore, the surface-wave method, in which S-wave velocity is obtained from surface, can be applied to many geological and geotechnical investigations for civil engineering problems.

5.2 Joint Analysis with Blow Counts in Housing Site Investigations

5.2.1 Introduction

In Japan, a Swedish weighted sounding test (SWS) or a standard penetrating test (SPT) are used for the site investigation of small buildings, such as individual houses in order to evaluate the depth to bedrock or the allowable bearing capacity of the ground. The result of SWS tests is only one-dimensional information and it is difficult to apply the SWS tests to the site in which geological condition is complex.

We have applied the surface-wave method to housing site investigations in order to estimate 2D or 3D structure of the ground even if complex geological condition. Data acquisition and analysis are based on the multi-channel analysis of surface-waves proposed by Park et al. (1999) and Xia et al. (1999) shown in previous Chapters. In order to increase lateral resolution, the CMP Cross-correlation analysis described in the Chapter three is also employed.

The surface-wave method gives us only S-wave velocity model not the N-value or the allowable bearing capacity. The vertical resolution of the surface-method is limited compare with the SWS and the SPT. However, the S-wave velocity obtained through the surface-wave method well correlated to N-value (blow count) obtained from the SPT or the SWS. Analyzing the surface-wave data together with the N-value obtained through the SPT or the SWS, accurate structure of the under ground may be obtained. In this section, we will propose the joint analysis method in which the surface-wave data and N-value are analyzed together and show the application of the method to a housing site investigation.

5.2.2 Data Acquisition

Data acquisition is same as we have already showed in previous Chapters. A

sledgehammer is used as source and twenty-four vertical component of geophones that has the natural frequency of 4.5Hz are used as receivers. Receiver spacing is 0.5 to 2 meters. Typical housing site is 20m square in Japan and receiver and shot spacing is usually about 1m in our survey. Receivers and shots are placed on a straight line. Figure 5.2.1 shows typical source-receiver geometry.

5.2.3 Analysis

A surface-wave data analysis presented in the Chapter 3 can be summarized as follows. At first, Common Mid Point Cross-correlation gathers are obtained from all shot gathers. A phase-velocity-frequency transformation Park et al.(1999) is applied to each CMPCC gather and dispersion curves are obtained for each CMPCC gather. Next, an S-wave velocity model is obtained using a non-linear least square method. The number of layers is fixed as 10 to 15, and only S-wave velocities are changed throughout inversion.

In the design works for individual houses in Japan, the most important geo-technical information is blow counts (N-value) obtained through the SWS tests and S-wave velocity is not used. However, surface-wave method gives us only S-wave velocity. Although blow counts generally correlate S-wave velocity, the correlation between blow counts and S-wave velocity much depends on soil condition at each site. Therefore, it is difficult to estimate the blow counts from S-wave velocity. In typical housing site investigations, two to four SWS tests are performed and one-dimensional blow counts information (converted from WSW and NSW) is obtained. Therefore, we combine the SWS tests that provide one-dimensional blow counts, and the surface-wave method that provides two-dimensional S-wave velocity model, and estimate two-dimensional blow counts profile of ground.

Unlike mountainous area, S-wave velocity does not always increase with depth in flat area. There are reversed layer, such as low velocity layer underneath high velocity layer, or thin embedded high velocity layer. In the surface-wave method, it is practically difficult to obtain velocity structures for reversed layer or embedded layers as unique solution, even if the model is one-dimensional. On the contrary, sounding

tests can delineate such complex geological structures. However, sounding tests cannot obtain 2D or 3D image of the ground. Considering such characteristics of surface-wave method and sounding tests, we will try to obtain geological model that satisfies both surface-wave method and sounding tests in the inversion of dispersion curves. Unknown information in proposed inversion is S-wave velocity model and relationship between S-wave velocity and the blow counts. We assume the blow counts and S-wave velocity have linear relationship in logarithm scale and the constants of the linear relationship can vary in each site. Analysis procedure is as follows.

1) We assume S-wave velocity and the blow counts (N-value) have following relationship.

$$Vs = c \cdot N^m \tag{5.2.1}$$

N is the blow counts (N-value), Vs is S-wave velocity, m and c are constants (m=0.314 and c=97m/s in Imai and Tonouchi (1982)).

2) At the CMP position on which SWS test was carried out, the blow counts profile is converted into one-dimensional S-wave velocity model based on the linear relationship between the blow counts and S-wave velocity. Two constants, m and c, are assumed by Imai and Tonouchi (1982).

3) A theoretical dispersion curve is calculated for 1D S-wave velocity model converted from the blow counts. The theoretical dispersion curve does not agree with an observed one. Therefore, two constants (m and c) in the equation (5.2.1) are modified by non-linear least square method so that residual between theoretical and observed dispersion curve decrease. If the number of layer is n, the objective function of inversion is;

$$\sum_i^N \left(f_i^{obs} - f_i^{cal}\left(Vs_1, Vs_2, \cdots Vs_n\right)\right)^2 = \sum_i^N \left(f_i^{obs} - f_i^{cal}\left(m, c\right)\right)^2 \longrightarrow Minimize \tag{5.2.2}$$

where, f^{obs} is phase-velocities obtained from observed data, f^{cal} is theoretical phase-velocities for estimated velocity model, Vs_1 *to* Vs_n are S-wave velocity calculated by the equation (5.2.1). Using this inversion, S-wave velocity models linearly related to the blow counts data with the equation (5.2.1) are obtained all CMP position that has the blow counts information.

4) One-dimensional S-wave velocity model obtained through above procedures are linearly interpolated and two-dimensional S-wave velocity profile beneath a survey line is constructed.

5) Using this 2D s-wave velocity model as initial model, a non-linear least square method is applied to all dispersion curves. In the inversion, horizontal regularization (Feng, 2001) is applied. Following equation is solved at each iteration step in the inversion;

$$\left(A^T A + \alpha R_v^T R_v + \beta R_h^T R_h + \varepsilon I\right)\Delta X = A^T Y \qquad (5.2.3)$$

where, A is a Jacobian matrix that consists of partial derivatives of phase-velocities, ΔX is a correction vector for S-wave velocity model, Y is a residual vector, R_v and R_h are vertical and horizontal regularization matrix respectively (equation (2.8.9) and equation (2.8.16)), I is a unit matrix, α, β and ε are constants.

6) At the CMP position on which SWS test was carried out, the blow counts are compared with inverted S-wave velocity models. Final constants, m and c for a relationship between S-wave velocity and blow counts are determined through this comparison using linear-least square method.

7) Two-dimensional S-wave velocity model is converted into blow counts profile using equation (5.2.1) and final constants, m and c.

5.2.4 Numerical Example

In order to evaluate the efficiency of the method, I have carried out a numerical test. The purpose of this test is;

1) Evaluating the applicability of a surface-wave method to delineate a two-dimensional model in small investigation site.
2) Evaluating the efficiency of joint analysis with blow counts.

Figure 5.2.2 shows the S-wave velocity model used in the test. The model is two layer model and S-wave velocity and the blow counts are summarized in table 5.2.1.

Table 5.2.1

	S-wave velocity (m/s)	Blow counts (N-value)
1st layer	100	3
2nd layer	300	15

There is a step at the middle of the model (30m). The blow counts profiles are obtained at the distance of 25m and 35m. Twenty-four receivers are placed from the distance of 18.4m to 41.4m with 1m spacing. The length of survey line is 24m. Twenty-five sources are placed from 18m to 42m with 1m spacing. Theoretical waveforms are calculated by 2D finite-difference method. Figure 5.2.3 shows the example of theoretical shot gather (shot position = 18m). CMPCC gathers are calculated with 2m spacing. Figure 5.2.4 shows the CMPCC gathers for the CMP distance of 25m and 35m and Figure 5.2.5 shows phase-velocity frequency images of CMPCC gathers. In the time domain data, waveform difference between two CMPCC gathers is not clear. However, we can see that the phase-velocity frequency images have clear difference. The dispersion curve for the CMPCC gathers of 25m is much faster than one of 35m. It implies that the CMPCC gathers reflect the velocity model underneath a CMP position even if such small survey line. Figure 5.2.6 shows all dispersion curves for CMPCC gathers. Red to yellow dispersion curves indicates first half and green to blue curves indicates latter half.

Dispersion curves clearly show the latter half of survey line is slower than first half. Figure 5.2.7 shows the inverted S-wave velocity model without blow counts information. The result implies horizontal variation of velocity model. However, it is difficult to decide the depth and velocity of second layer in the latter half of survey line. Figure 5.2.8 shows the inverted S-wave velocity model with blow counts information. In the latter half of the survey line, S-wave velocity for the second layer is estimated slower than true velocity, the depth of the second layer agrees with the true model. Figure 5.2.9 shows the blow counts profile converted from S-wave velocity model with estimated *m* and *c (m=0.43, c=62m/s)*. Even if the blow counts deeper than 8m are smaller than true value in the latter half of the survey line, we can say almost true N-value profile could be obtained.

5.2.5 Application to Housing Site Investigations

In order to evaluate the applicability of the method, we have carried out a surface-wave method and SWS tests at 33 sites, in Ibaraki and Chiba prefecture, Japan. Sites are individual housing sites and the size of investigation site is smaller than 20m square. Surface-wave data and N-value from SWS tests are analyzed together. Here is the example of tests.

The investigation site is on diluvium terrace in south part of Ibaraki prefecture, Japan. There is filling area in the housing site. The purpose of the investigation is the delineation of the filling area and the evaluation of filling material as the foundation of a house. A survey line is 23 m length and 24 receivers were deployed with 1m intervals. A sledge hammer is used as a source and 25 shots were deployed with 1m intervals. Figure 5.2.10 shows the example of shot gathers and Figure 5.2.11 shows the example of CMPCC gathers. Ten CMPCC gathers were obtained with 2m intervals. Figure 5.2.12 shows the example of phase-velocity images in frequency domain. The distance of CMP is 5m and 17m respectively. We can see that the phase-velocity of 17m CMPCC is much higher than that of 5m. Figure 5.2.13 shows the all dispersion curves calculated from CMPCC gathers. Difference of color indicates the difference of CMPCC location. Red to yellow curves are placed at the beginning of the survey line and green to blue

curves are placed at the ending of the survey line. It is clear that the phase-velocity of the dispersion curves increase with the distance of CMPCC location. It implies that the S-wave velocity structure of the site is laterally inhomogeneous and the S-wave velocity of the ground increases with distance from the survey origin.

A non-linear least square method (Xia et al., 1999) was applied to each dispersion curves for reconstructing 2D S-wave velocity profile. Figure 5.2.14 shows the result of analysis and the N-value obtained from SWS tests. The S-wave velocity model indicates there is low velocity area shallower than depth of 4m at the left side of the survey line. The SWS test labeled as 'C' confirm that the low velocity area exists there. The SWS test labeled as 'A' and 'B' indicate that a stiff layer exists at the depth of 2m. However, the S-wave velocity model obtained through the surface-wave method did not show the high velocity layer at there.

Figure 5.2.15 shows the result of analysis with the SWS tests and the N-value obtained from SWS tests. Figure 5.2.16 shows the estimated N-value model converted from S-wave velocity model. The conversion from S-wave velocity to N-value used constants (c=74.9m/s、m=0.0489) optimized by the non-linear least square method described above. In the Figure 5.2.15 and 5.2.16, we can clearly see the high-velocity thin layer at the depth of 2m.

Figure 5.2.17 shows the estimated geological model obtained through the surface-wave method and the SWS tests. The result of investigation can be summarized as follows. The investigation results indicate that the filling area extends from 0m to 10m. In the filling area, there is a layer that will be self-penetrated by load of 750 Newton at the Swedish sounding test labeled as 'C'. The S-wave velocity in the filling is less than 100m/s. The results imply that the filling area may cause deformation or settlement. This field survey example shows that the surface-wave method analyzing with SWS tests or SPT tests can image detailed velocity structure.

We have carried out the surface-wave method and SWS tests at 33 sites, in Ibaraki and Chiba prefecture, Japan. The surface-wave data was analyzed with N-value as described above. The relationship between N-value and S-wave velocity for 33 sites is shown in Figure 5.2.18. It is clear that the S-wave velocity increases with the N-value increases. Constants calculated from Figure 5.2.18 with a regression analysis are

c=76.7m/s and m=0.332. These constants are close to the constants (c=97m/s and m=0.314) presented by Imai and Tonouchi (1982).

5.2.6 Conclusions

The numerical and field examples presented in this Chapter shows that the surface-wave method can be applied housing site investigations in order to evaluate the allowable bearing capacity of the ground. The resolution of S-wave velocity model obtained through the surface-wave method is limited. Analyzing surface-wave data together with N-value can increase the resolution of the estimated S-wave velocity model. This approach also enables us to estimate engineering parameters, such as the allowable bearing capacity, that do not physically relate to S-wave velocity.

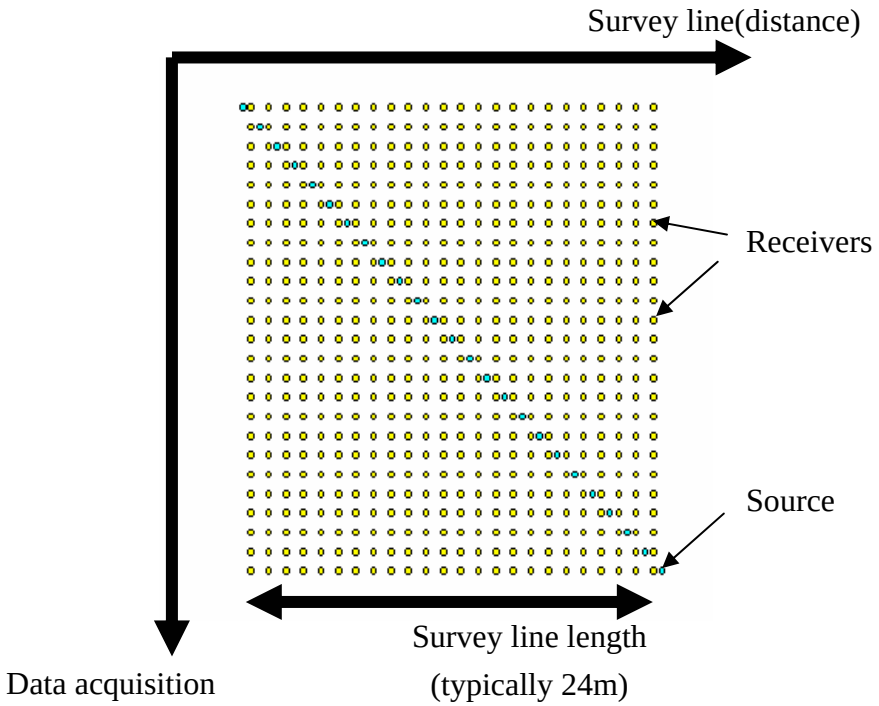

Figure 5.2.1.Typical source-receiver geometry used in housing site investigations.

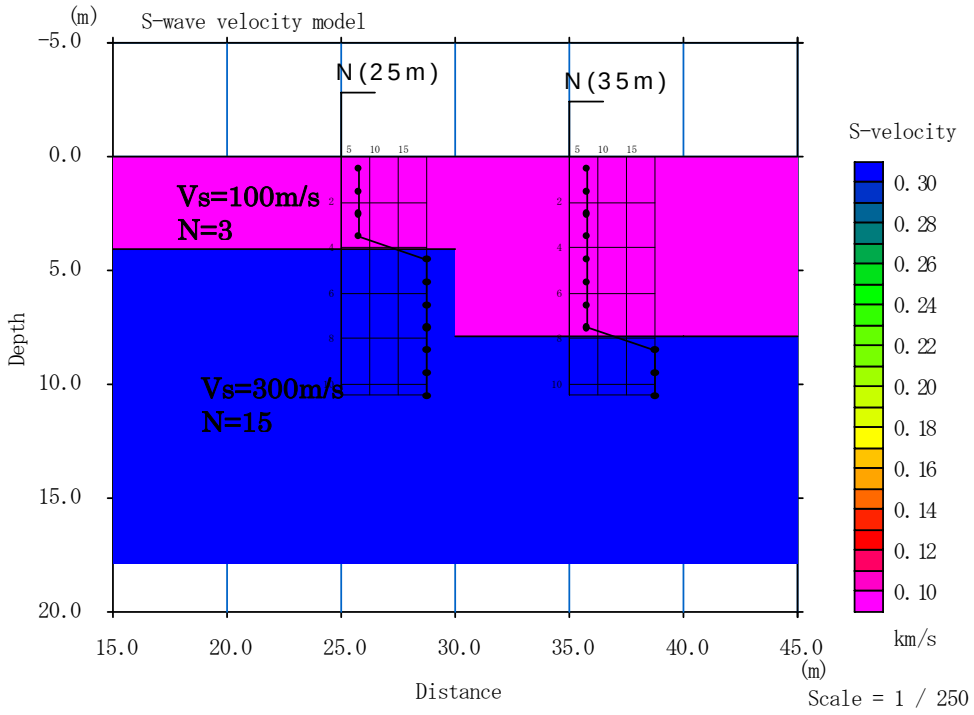

Figure 5.2.2 S-wave velocity model and N-value used in the numerical test.

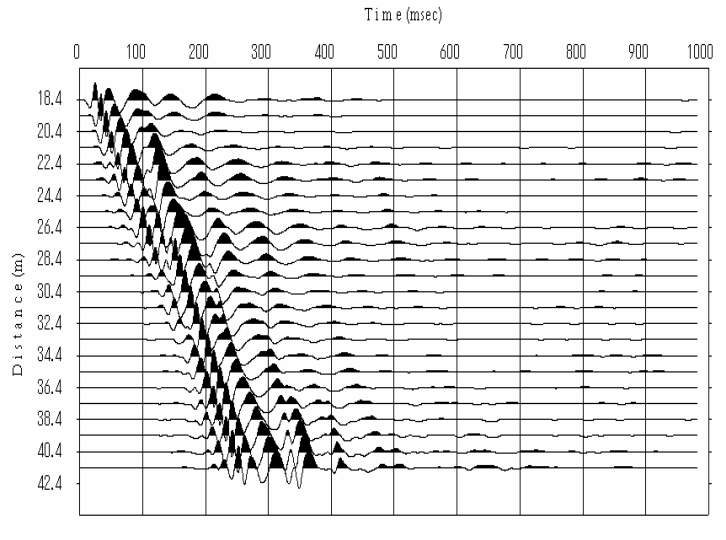

Figure 5.2.3. Example of theoretical waveform s calculated by finite-difference method. Vertical component of particle velocity is shown.

CMP=25m CMP=35m

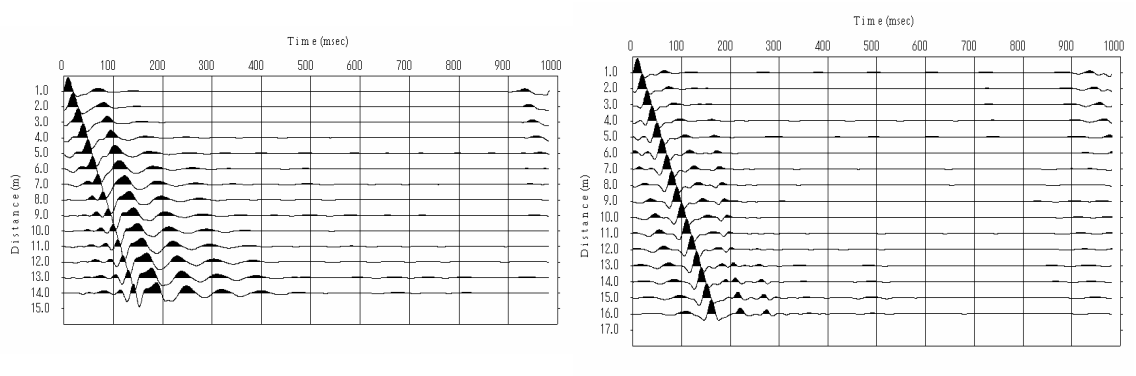

Figure 5.2.4. CMPCC gathers for the CMP distance of 25m(left) and 35m(right).

CMP=25 CMP=35m

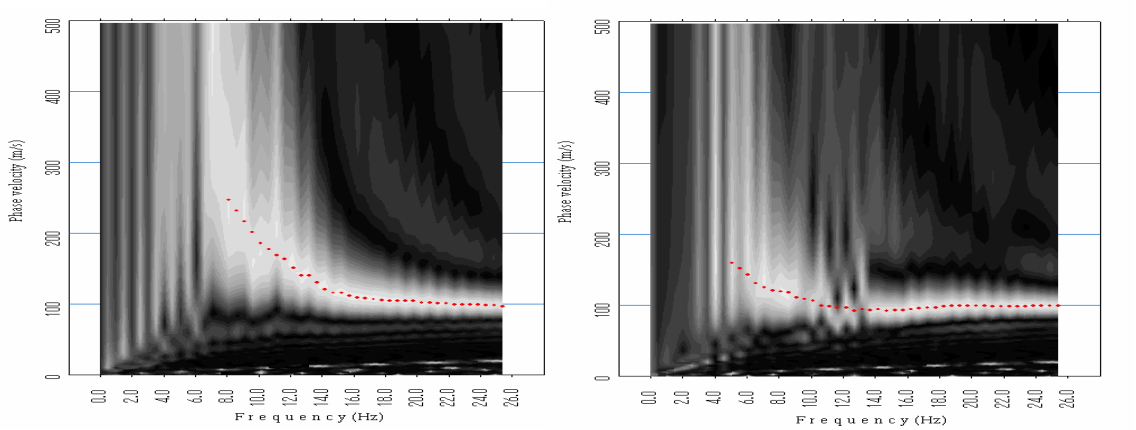

Figure 5.2.5. Phase-velocity frequency images of CMPCC gathers for the CMP distance of 25m(left) and 35m(right).

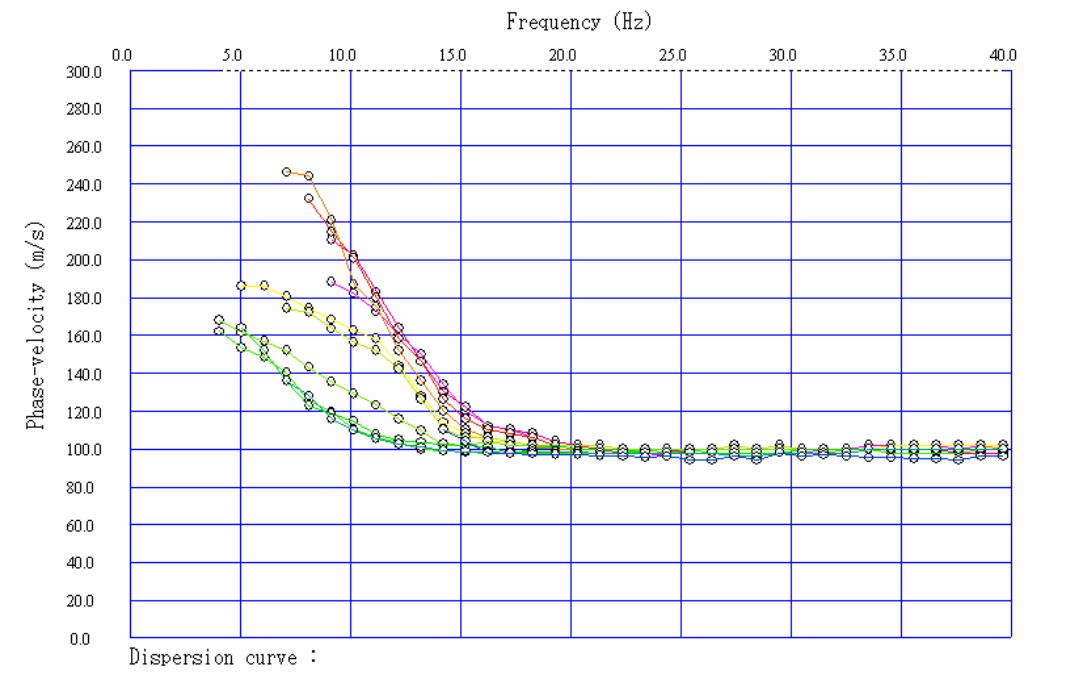

Figure 5.2.6. All dispersion curves for CMPCC gathers. Red to yellow dispersion curves indicates first half and green to blue curves indicates latter half.

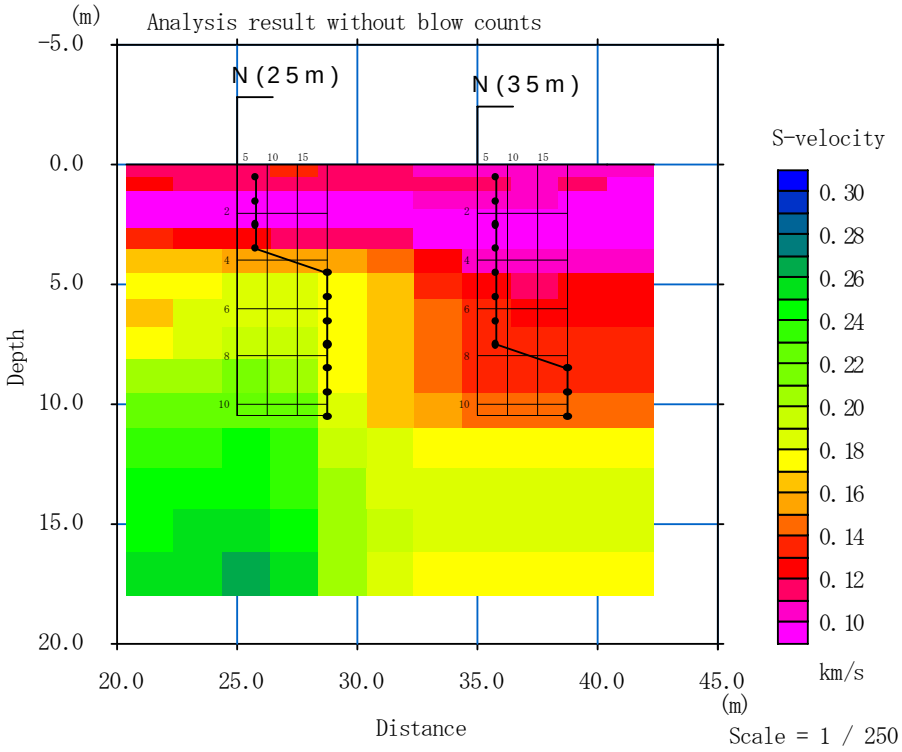

Figure 5.2.7. Inverted S-wave velocity model without the blow counts (N-value) information.

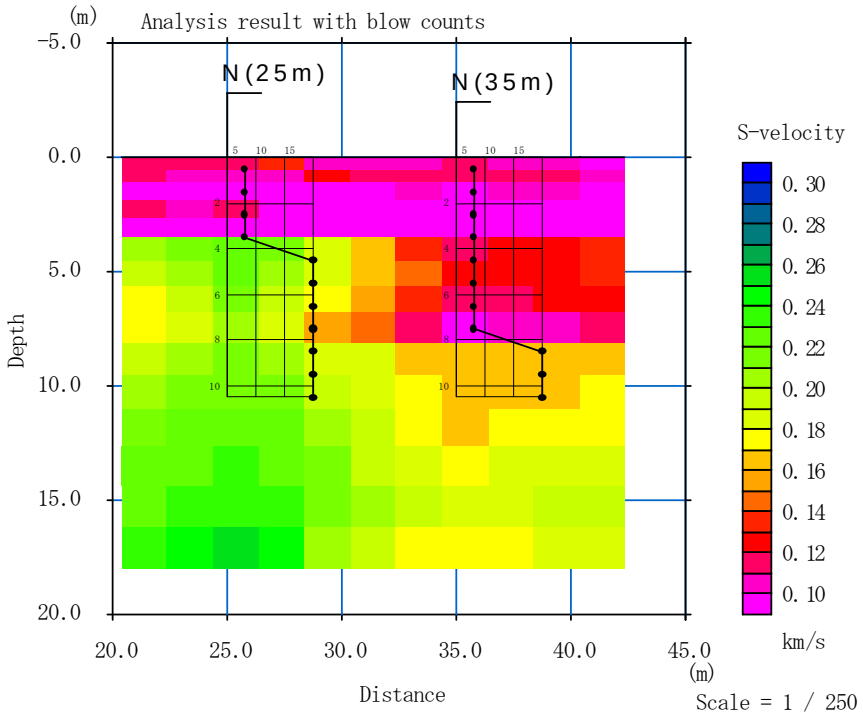

Figure 5.2.8. Inverted S-wave velocity model with the blow counts (N-value) information.

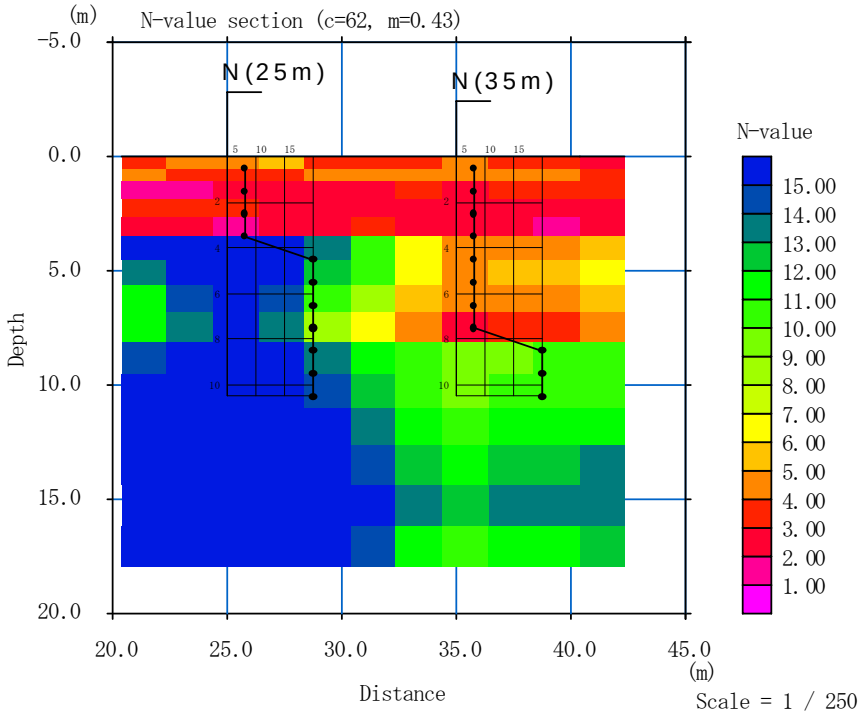

Figure 5.2.9. Converted N-value profile using estimated *m* and *c* *(m=0.43, c=62m/s)*..

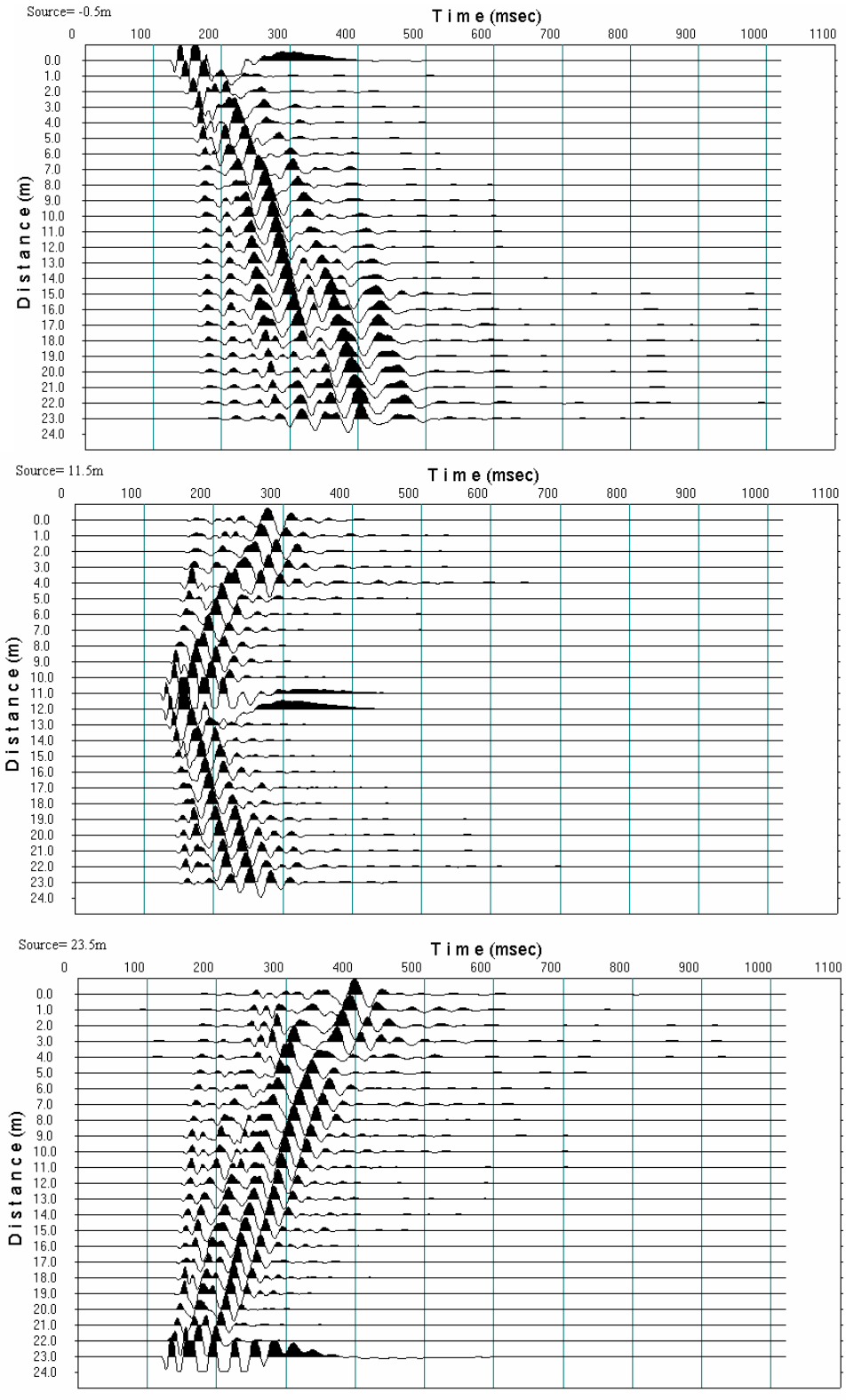

Figure 5.2.10. Example of shot gathers.

(a)

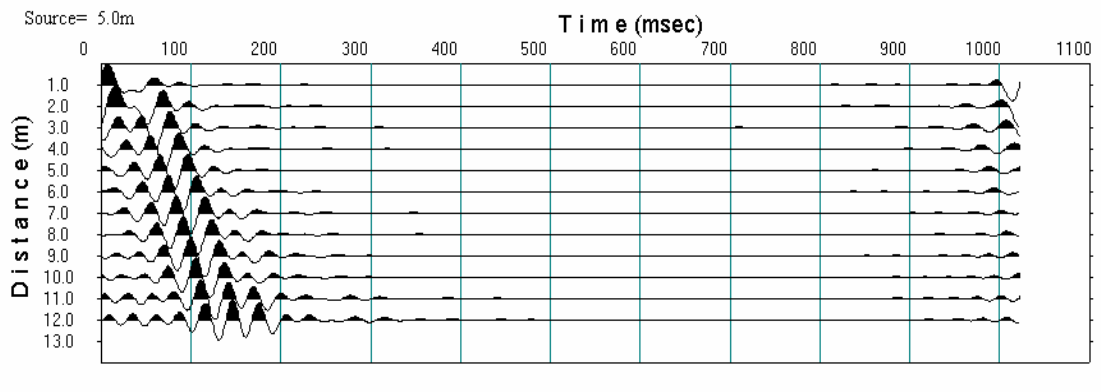

(b)

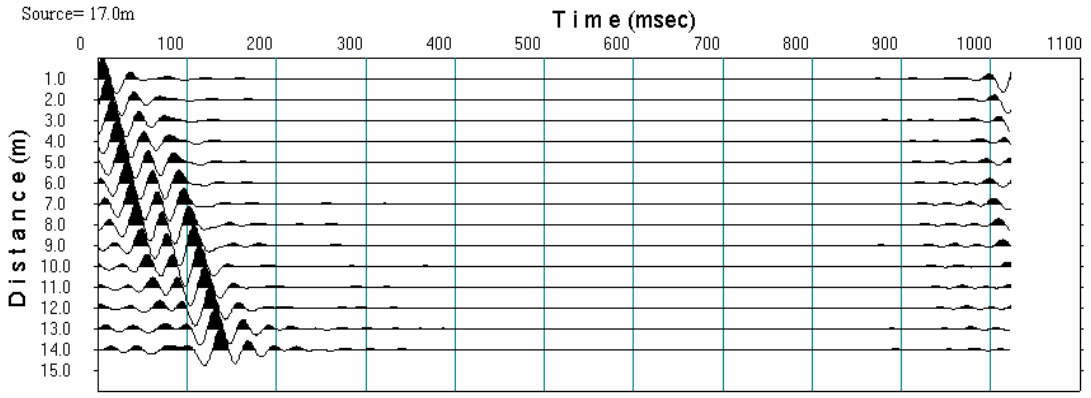

Figure 5.2.11. Example of CMPCC gathers.
(a) CMP location is 5m. (b) CMP location is 17m.

(a)

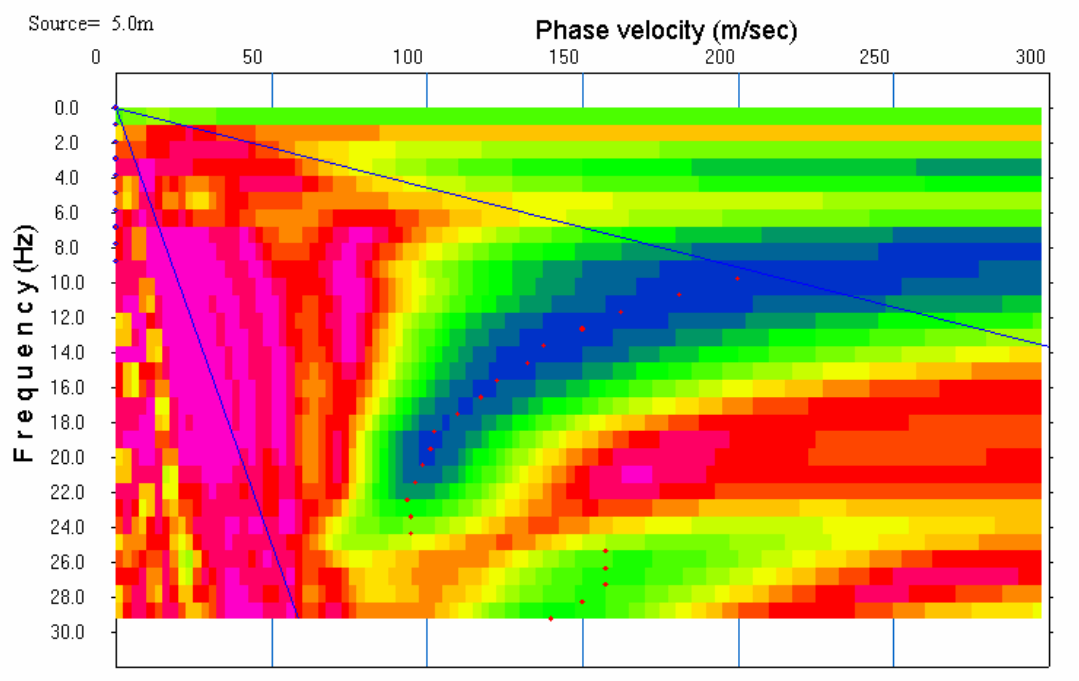

(b)

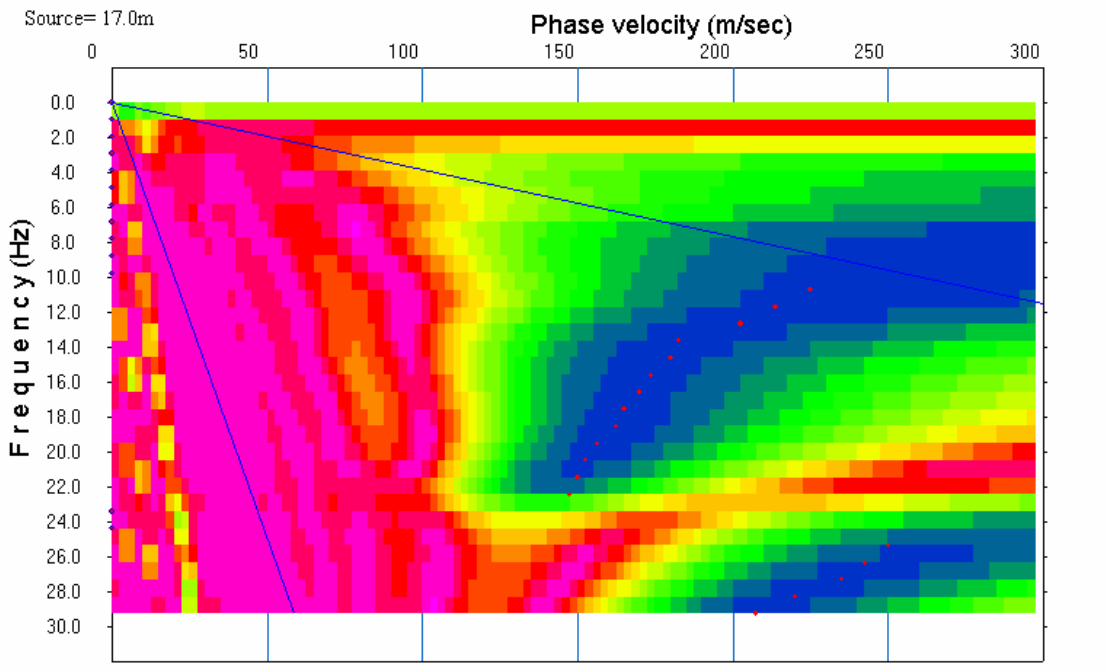

Figure 5.2.12 Example of phase-velocity images in frequency domain.
(a) CMP location is 5m. (b) CMP location is 17m.

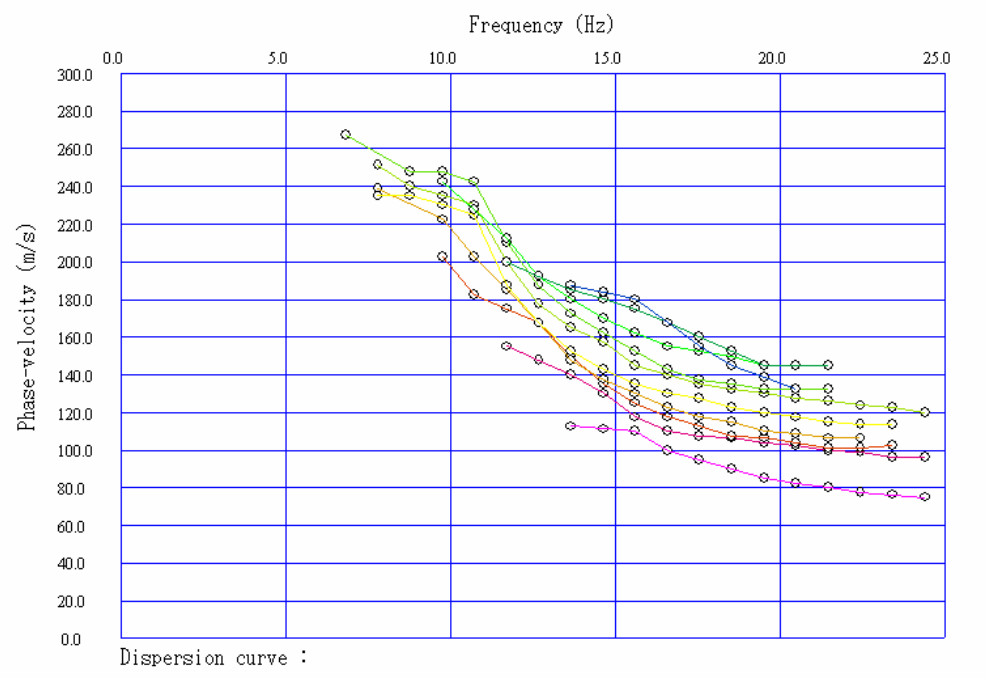

Figure 5.2.13. All dispersion curves calculated from CMPCC gathers. Difference of color indicates the difference of CMPCC location. Red to yellow curves are placed at the beginning of the survey line and green to blue curves are placed at the ending of the survey line.

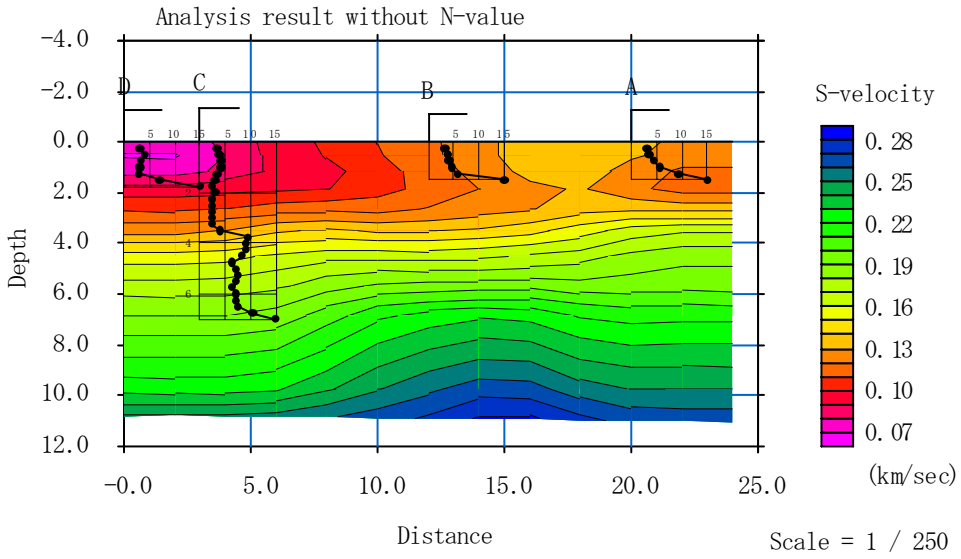

Figure 5.2.14. Result of surface-wave method and the N-value (blow counts) obtained from SWS tests.

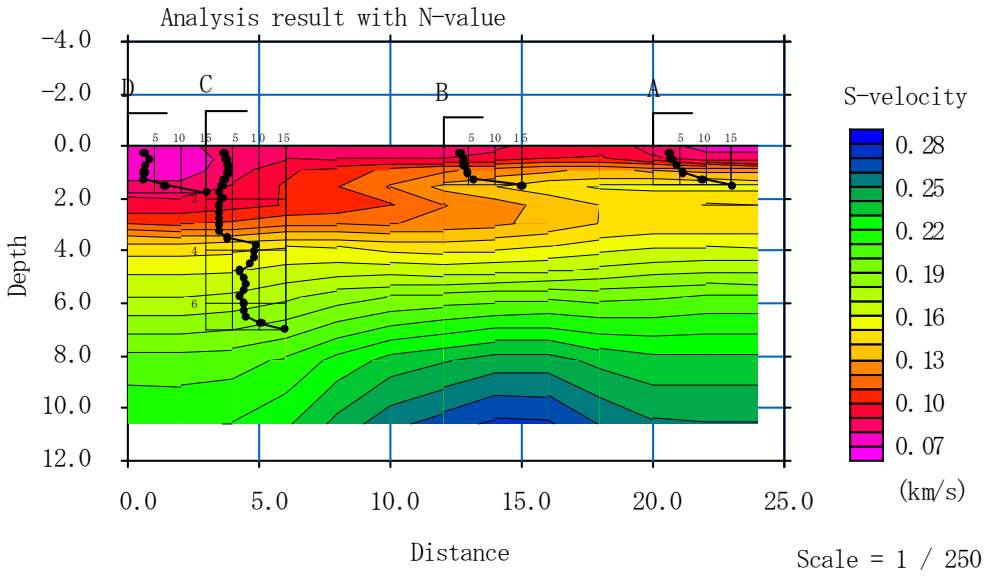

Figure 5.2.15. Result of analysis with the SWS tests and the N-value obtained from SWS tests.

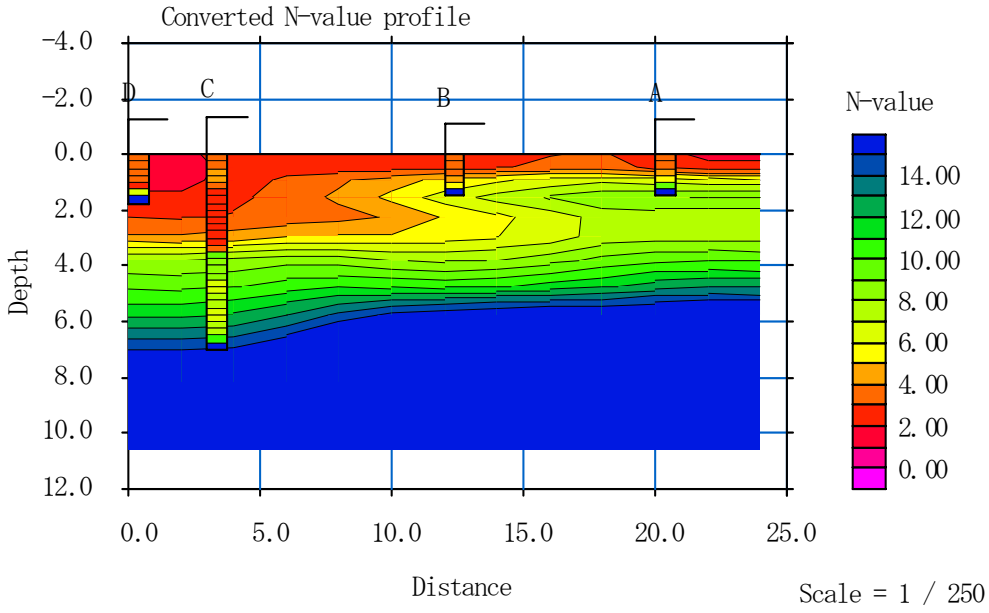

Figure 5.2.16. Estimated N-value model converted from S-wave velocity model

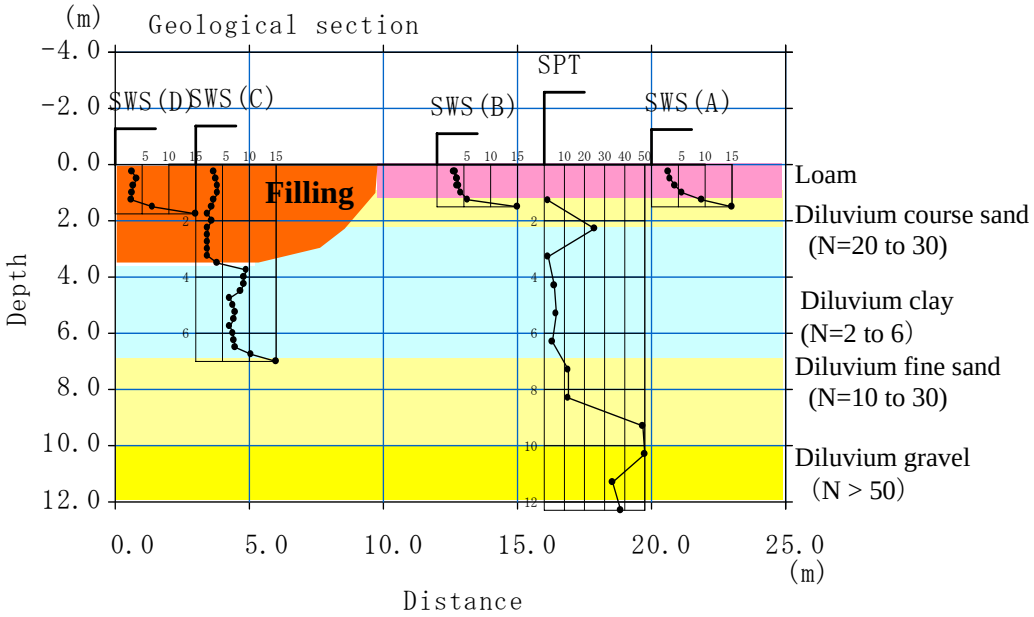

Figure 5.2.17. Estimated geological model obtained through the surface-wave method and the SWS tests

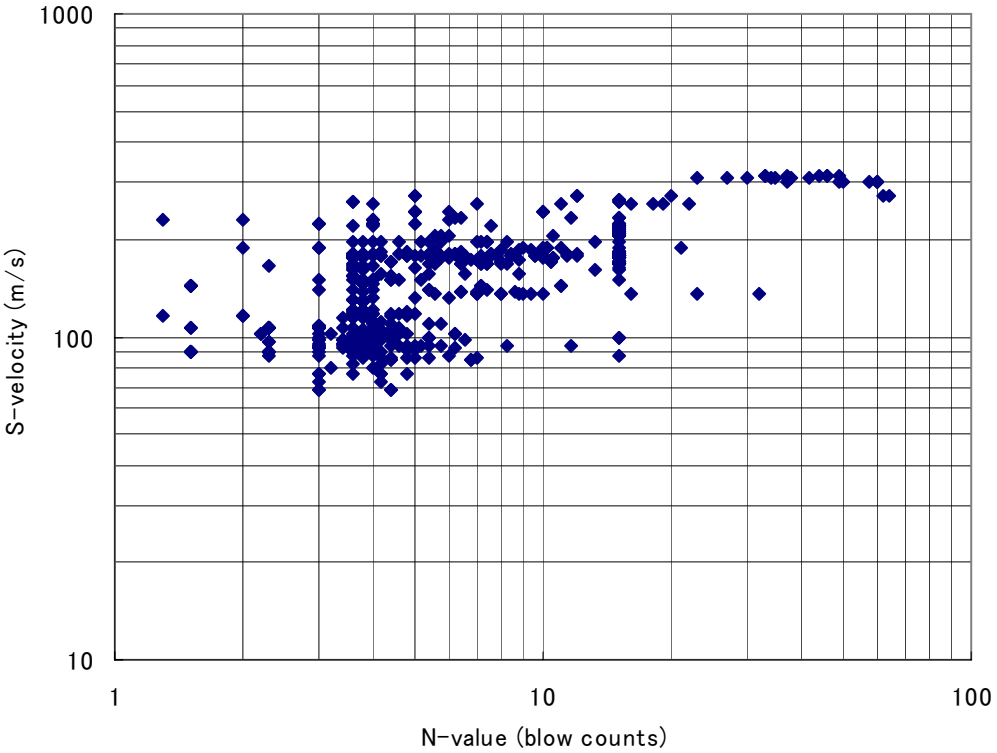

Figure 5.2.18. Relationship between N-value and S-wave velocity for 33 sites.

5.3 Joint Analysis of a Surface-wave Method and Micro-gravity Survey

This section presents a joint analysis of a surface-wave method and a micro-gravity survey for estimating both S-wave velocity and density model of the ground. The surface-wave and the micro-gravity surveies have been performed for delineating a buried channel filled with soft alluvium sediments (Hayashi et al., 2005a). A CMP cross-correlation analysis of surface-waves was applied to multi-shot and multi-channel surface-wave data and an S-wave velocity model was obtained. The micro-gravity survey has been performed on the same survey line and a clear low Bouguer anomaly area was detected. The gravity data was analyzed based on the S-wave velocity model obtained through the surface-wave analysis. The S-wave velocity model was converted into a density model by the information of laboratory soil tests. Gravity anomaly was calculated and compared with the observed data. The density model was modified for reducing residual with a least square method. A clear low-density area was obtained and it agrees with a low S-wave velocity area obtained from the surface-wave method.

5.3.1 Introduction

In the most of engineering and environmental investigations, several geophysical methods, drilling, logging and laboratory tests are used together. It is rare that only one geophysical exploration method is used in the investigation. Even if a lot of methods are applied to one site, individual exploration methods are analyzed separately. Only in the last stage of the exploration work, joint or integrated interpretation, such as interpretation of a seismic refraction method and a PS-logging, is usually carried out. However, the joint interpretation is usually performed just by empirically or visually and not performed mathematically and physically.

The most of geophysical exploration methods carried out on the surface and cross-hole tomography are essentially non-unique problem and it is difficult to obtain

a unique solution. Analyzed results usually depend on initial models and constraining conditions based on empirical and subjective knowledge. This situation reduces the quality and objectivity of the investigation. If we are able to analyze several geophysical exploration data together, subjectivity and non-uniqueness in each method can be reduced. Hence the quality of whole investigation will increase. This kind of approach is called joint analysis or joint inversion, and it has been applied to many problems recently. In this dissertation, we presents a micro-gravity analysis based on an S-wave velocity model obtained through a two-dimensional surface-wave method as an example of joint analysis.

5.3.2 Site Description

The purpose of investigation is delineating the extension of buried channels, down to a depth of 10 m. Existed drilling results indicated that the channels have been filled with soft sediments, such as alluvium clay and peat. Construction of banking and building is planned in this site. Ground subsidence associated with the construction was predicted and the detailed information of underground structure was required. A surface-wave method and a micro-gravity survey have been carried out for delineating a buried channel filled with soft alluvium sediments in the site.

There are many physical properties of material that can be obtained from surface geophysical exploration methods, such as resistivity, chargeability and P-wave velocity. It is well known that S-wave velocity and density well reflects material stiffness. The density is especially important for estimating subsidence associated with soft sediments layers. Gravity value measured on the surface directly reflects the underground density information. Recently, a gravity survey has been applied to engineering and environmental problems in a relatively very restricted survey area. The resolution of gravity survey for engineering and environmental problems is about 10 micro-gals. Such a small-scale gravity survey is called a micro-gravity survey. In the gravity survey, it is usually impossible to obtain a unique underground density model from gravity measurements on the surface. Horizontal heterogeneity of a density model can be detected in gravity survey. However, it is

difficult to obtain the vertical heterogeneity.

S-wave velocity (Vs) obtained through surface-wave methods, is calculated from rigidity or shear modulus (μ) and density (d) as the following equation:

$$Vs = \sqrt{\frac{\mu}{d}} . \tag{5.3.1}$$

It seems reasonable to suppose that a surface-wave method is more sensitive about vertical heterogeneity of the density than the micro-gravity survey. We have tried to combine the micro-gravity survey with the surface-wave survey and delineate a buried channel filled with soft alluvium sediments with high resolution and high accuracy.

The survey line length is 205m. In the micro-gravity survey, measurements were carried out by a Scintrex CG-3M with 2m intervals. In the surface-wave method, a 10kg sledgehammer was used as a source. Sources were moved with 1m intervals. Twenty-four geo-phones (4.5Hz) were deployed with 1m intervals. The nearest source-to-receiver offset was 0.5m. Two-hundreds and six shot gathers were recorded by an OYO-McSEIS-SXW seismograph with a roll-along switch.

5.3.3 Density Model Estimation from Gravity Data Using a Least Square Method

In the analysis of micro-gravity survey, we need the several basic corrections, such as a tide correction, an instrumental height correction, and a Bouguer correction, applying to observed gravity data at first. The reduced gravity data is called Bouguer anomaly. It is difficult to estimate a near-surface density model directly from gravity data because the Bouguer anomaly reflects deeper horizontal density heterogeneity too. Then, we applied wave length filter that removes short and long wave length anomaly from the Bouguer anomaly. The short wave length anomaly is noise, and the longer wave length anomaly reflects deeper horizontal density variation trend. The resultant filtered gravity anomaly distribution reflects density heterogeneity

associated with only near-surface region. In the following sections, we shall use the term “gravity anomaly” to refer to relative gravity values that is the filtered Bouguer anomaly. Applying this wave length filter, we can quantitatively connect gravity anomaly observed on the surface with near-surface density heterogeneity as shown in the Figure 5.3.1.

A near-surface density model is defined as two-dimensional model expressed by rectangle cells (Figure 5.3.2). Gravity anomaly ($g(x_{ij})$) on the surface can be calculated as

$$g(x_i) = \sum_{j=1}^{m} d_j \cdot f_{ij} \,, \tag{5.3.2}$$

where m is the number of cells, d_j is the density at the j_{th} cell, x_i is position of the i_{th} observation point. f_{ij} are constants that can be defined by relative position of cells and observation points (Banerjee and Gupta, 1977). In the case of n observation points, equation (5.3.2) can be expressed as matrix notation as follows:

$$\begin{bmatrix} f_{1,1} & f_{1,2} & \cdot & f_{1,m} \\ f_{2,1} & f_{2,2} & \cdot & f_{2,m} \\ \cdot & \cdot & \cdot & \cdot \\ f_{n,1} & f_{n,2} & \cdot & f_{n,m} \end{bmatrix} \begin{bmatrix} d_1 \\ d_2 \\ \\ d_m \end{bmatrix} = \begin{bmatrix} g(x_1) \\ g(x_2) \\ \cdot \\ g(x_n) \end{bmatrix}. \tag{5.3.3}$$

In the following sections, we will express equation (5.3.3) as

$$\boldsymbol{FD} = \boldsymbol{G} \,. \tag{5.3.4}$$

$\boldsymbol{F}$, $\boldsymbol{D}$ and $\boldsymbol{G}$ are matrix notation of f_{ij} , d_j and $g(x_i)$ respectively. Because f_{ij} are constants with no relation to density d_j, an underground density model ($\boldsymbol{D}$) can be simply estimated from observed gravity anomaly ($\boldsymbol{G_{obs}}$) by a linear least square method as follows:

$$\boldsymbol{D} = \left(\boldsymbol{F}^{\boldsymbol{T}}\boldsymbol{F} + \boldsymbol{\varepsilon I}\right)^{-1}\boldsymbol{F}^{\boldsymbol{T}}\boldsymbol{G}_{\boldsymbol{obs}} \,, \tag{5.3.5}$$

where $\boldsymbol{I}$ is a unit matrix and ε is a damping parameter. Generally, the equation (5.3.5) is not stable and the damping parameter must be large. Larger damping parameter results in stable solution but larger residual. Then we apply an iterative method. At first, we calculate a stable solution with a large damping parameter. Next, we reduce residual between observed and theoretical gravity anomaly iteratively as follows. Residual between observed and theoretical data is

$$\boldsymbol{R} = \boldsymbol{G}_{obs} - \boldsymbol{F}\boldsymbol{D}\,, \tag{5.3.6}$$

where $\boldsymbol{R}$ is a residual vector that relates to a density model correction vector $\Delta\boldsymbol{D}$ by,

$$\boldsymbol{F}\Delta\boldsymbol{D}=\boldsymbol{R}. \tag{5.3.7}$$

Therefore, model correction vector $\Delta\boldsymbol{D}$ can be calculated by the following equation:

$$\Delta\boldsymbol{D} = \left(\boldsymbol{F}^{T}\boldsymbol{F} + \varepsilon\boldsymbol{I}\right)^{-1}\boldsymbol{F}^{T}\boldsymbol{R}\,. \tag{5.3.8}$$

An iterative correction is repeated till residual become enough small. In this investigation, we expressed the density model as horizontal direction 100 cells by vertical direction 15 cells. The number of cells or unknown (m) is 1,500. The number of observed gravity data (n) is 200. About the boundary conditions, density beneath the model is assumed to be zero and the density left and right side of the model is assumed to be the density of left and right end of the model, respectively.

Figure 5.3.3 shows a distribution of gravity anomaly at the site and an analysis result (density model). The density model obtained through the method is just relative density. Therefore we assume maximum density is to be 2.0g/cc in the Figure 5.3.3. Multi-channel and multi-shot surface-wave data were acquired on the same survey line. We applied a CMP cross-correlation analysis (CMPCC) of surface-waves (Hayashi and Suzuki, 2003) to the surface wave data. Figure 5.3.4 shows the S-wave velocity model obtained through the CMPCC analysis. As

mentioned above, the analysis of gravity data does not have a unique solution, the density model (***D***) that satisfies gravity anomaly (***G***) may not be true and it may be meaningless in an investigation. In the Figure 5.3.3, low-density area in the density model agrees with low gravity area. However, vertical resolution is poor and the density model does not agree with the S-wave velocity model. Therefore, we have tried to obtain the density model that consits with S-wave velocity model better than the Figure 5.3.3.

5.3.4 Analysis with an Initial Model Based on a S-wave Velocity Model

Generally, S-wave velocity and density are well correlated (Ludwig et al.,1970). Then, we have tried to obtain a density model using the S-wave velocity model obtained from surface-wave data. Laboratory tests had been carried out for soil samples obtained from existed drillings in the site. The results reported that the density of peat was 1.25 g/cc and the density of alluvium clay is 2.0g/cc.

At first, we assumed the correlation between S-wave velocity and density from the laboratory tests and the surface-wave method. The minimum and maximum S-wave velocity obtained through the surface-wave data analysis are 0.06 km/sec and 0.26 km/sec respectively. We assume these minimum and maximum S-wave velocities correspond to the density of peat 1.25g/cc and the density of clay 2.0g/cc obtained through laboratory tests. Using this minimum and maximum S-wave velocity and density, we assumed density of the site (d (g/cc)) linearly correlates to S-wave velocity (Vs (km/s)) as the following equation:

$$d(g/cc) = 3.75Vs(km/\sec) + 1.025. \qquad (5.3.9)$$

Figure 5.3.5 shows a density model converted from the S-wave velocity model using the equation (5.3.9) and the theoretical gravity anomaly calculated from this density model and it is compared with observed data. We can see that the residual is small and the density model converted from the S-wave velocity model almost satisfies the observed gravity anomaly.

Next, we modified the density model iteratively by the equation (5.3.8) using the residual vector $\boldsymbol{R}$ calculated by the equation (5.3.6). Figure 5.3.6 shows the final density model obtained through the iterative correction and the comparison between the observed and theoretical data. We can see that the residual is enough small and the density model satisfies the observed gravity anomaly distribution. In addition to that, it should be noted that the density model is consistent with the S-wave velocity model very well.

5.3.5 Conclusions

We have estimated the near-surface density model that satisfies observed gravity anomaly based on the S-wave velocity model obtained from the surface-wave data. The density model satisfies the observed gravity anomaly, and consists with S-wave velocity model and the result of laboratory tests as well. The purpose of the investigation is delineating a buried channel placed at the distance from 130m to 180m. The channel filled with low S-wave velocity and low density soft sediments was found by drilling at the distance of 150m. The main interest in the survey was where the left end of the channel was placed. The result of surface-wave method indicates that the buried channel is placed in the internal from 130m to 180m and it does not extend before 130m. The density model obtained from micro-gravity data confirms the S-wave velocity model, and it also indicates the channel was filled very low density sediments that might cause serious ground subsidence associated with the future construction.

We inverted the surface-wave data and micro-gravity data separately in this study. However, it is possible to invert surface-wave and gravity data simultaneously using two unknown parameters, density and rigidity. S-wave velocity can be calculated from density and rigidity from the equation (5.3.1). We would like to develop a simultaneous inversion, so called joint inversion, not joint analysis presented here.

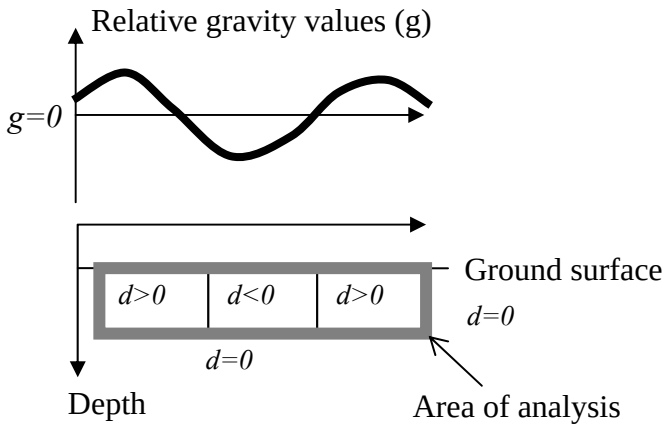

Figure 5.3.1. Gravity observed on the surface and a near-surface density model.

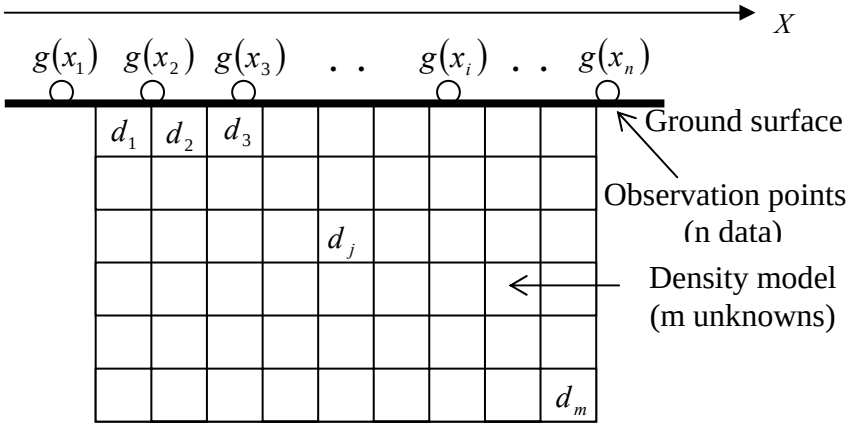

Figure 5.3.2. Two-dimensional density model used in an analysis.

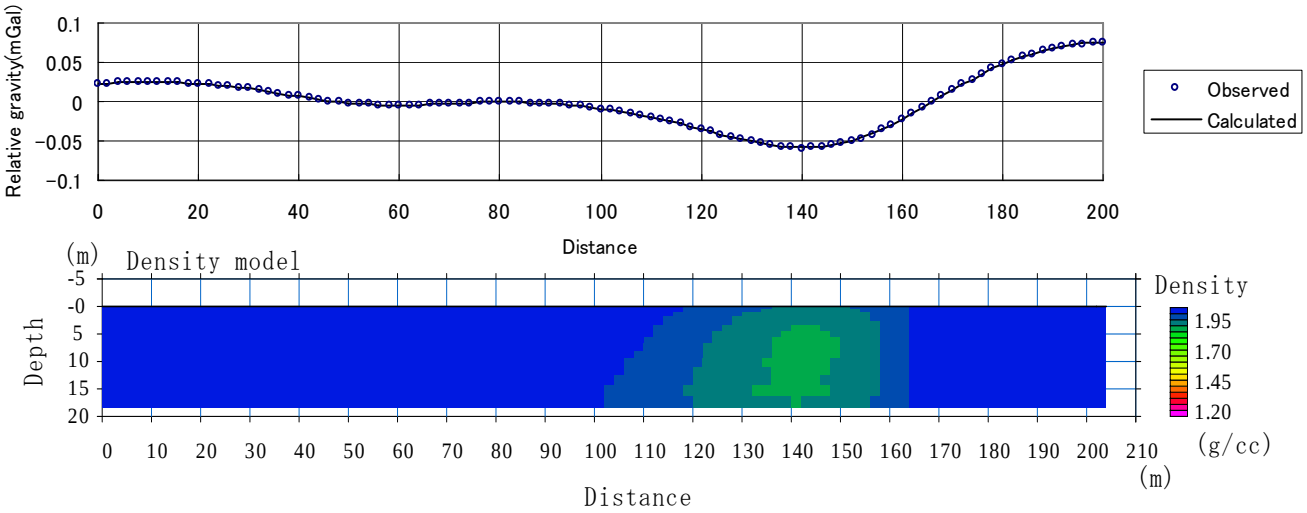

Figure 5.3.3. Observed gravity anomaly distribution compared with calculated one (top) and a density model obtained through a linear least square method (bottom).

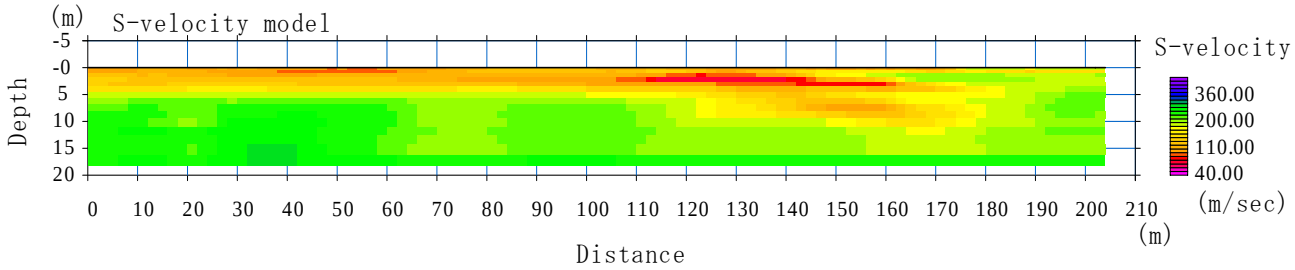

Figure 5.3.4. S-wave velocity model obtained by a surface-wave method.

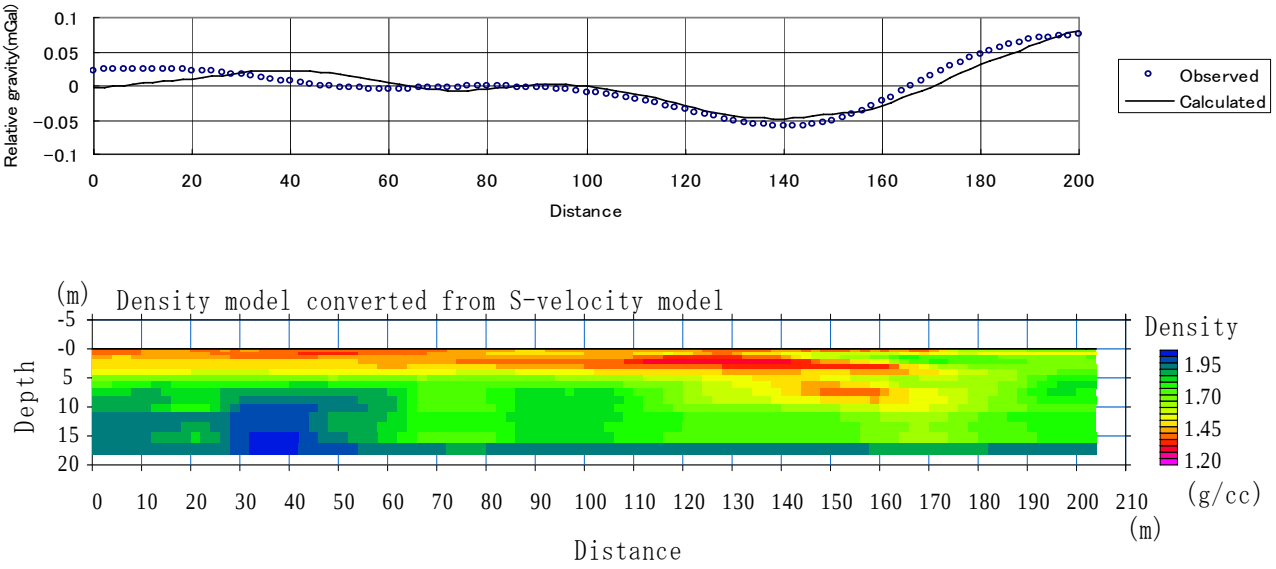

Figure 5.3.5. Observed gravity anomaly distribution compared with calculated one (top) and a density model converted from the S-wave velocity model (bottom).

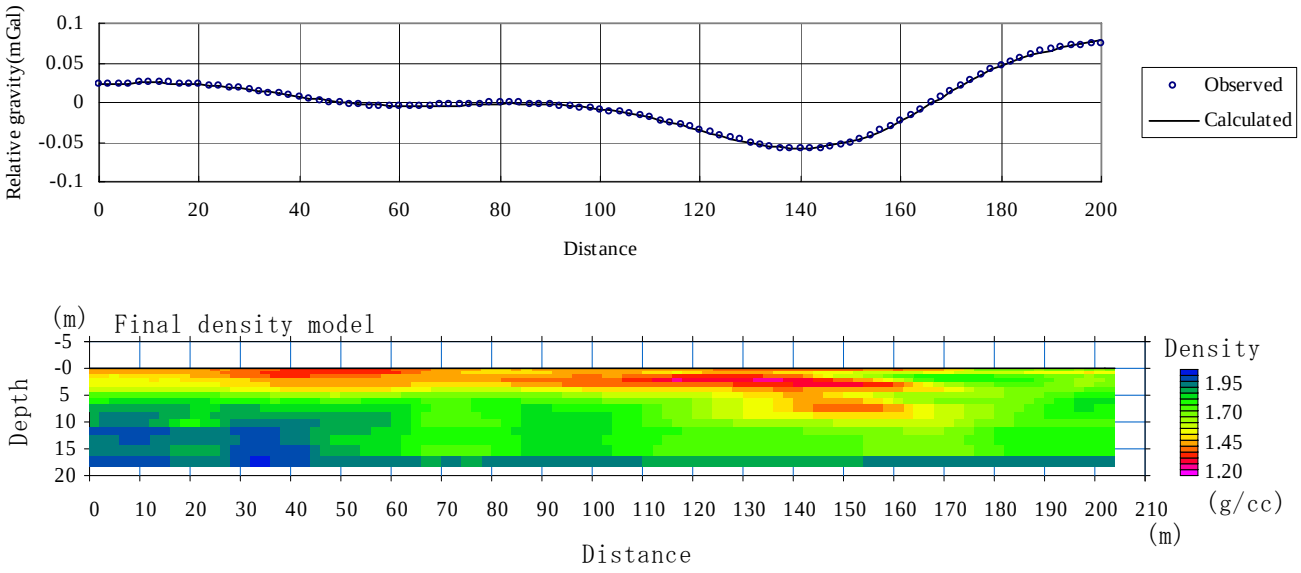

Figure 5.3.6. Observed gravity anomaly distribution compared with calculated one (top) and a final density model obtained through the iterative analysis based on the initial density model converted from the S-wave velocity model (bottom).

5.4 Application to Historical Site Investigations

5.4.1 Introduction

In recent years, conservation of antiquities attracts much interest. Over the past few years, a considerable number of geophysical studies have been made for the conservation of antiquities. The advantage of geophysical methods for antiquities is the methods are non-destructive and there is a little fear to hurt precious historic environment. In this Chapter, the example of application of the geophysical method to historical site will be presented.

The investigation site is Pisa, Italy. Active and passive surface-wave methods were applied to the geotechnical investigation around The Leaning Tower of Pisa (Figure 5.4.1). The purpose of the investigation is delineating two and three dimensional heterogeneity around the Tower. In order to evaluate the stability of the Tower, detailed geological structure around the foundation of the Tower becomes very important. Therefore, many geo-technical and geophysical investigations have been conducted for many years. However, three-dimensional geological model around the Tower seems to be not clear in spite of many investigations. The efficiency of the surface-wave method is that the method can delineate 2D or 3D information of the site quickly from the ground surface. In-situ measurements, such as sampling, sounding and logging, are accurate but only provide one-dimensional information of the ground. The surface wave methods can interpolate existing 1D in-situ information and delineate detailed 2D and 3D geological model around the Tower.

5.4.2 One-dimensional S-wave Velocity Models Using Passive and Active Data

Figure 5.4.2 shows the investigation site. For the sake of simplicity, the investigation site will be divided into three portions, such as north, east and south as shown in the figure. In the north side of the Tower, a spectral analysis of surface-waves

(SASW) has been carried out (Foti, 2003). In the east side of the Tower, cross-hole measurements have been carried out. In the south side and around the Tower, seismic corn penetrating tests (SCPT) have been carried out. In the investigation, the sampling and sounding were also carried out at the south side of the Tower.

Figure 5.4.3 shows the location and shape of passive arrays. We have carried out 7 passive arrays at different site using different shapes. At the north and east site, three different shape arrays were used. At the south site, one array was carried out. Figure 5.4.4 shows the survey lines active method. We have carried out the active method on 9 survey lines. Dispersion curves were not clear at the 'E-2' and 'S-2' lines. These two lines placed just beside the Tower. S-wave velocity model around the Tower may not be a simple horizontal layered model. This complicated S-wave velocity model may cause the un-clear dispersion curves. Therefore, surface-wave data obtained from other 7 survey lines will be discussed in this Chapter.

In the passive method, geophones that have the natural frequency of 2Hz were used as receivers. Sampling time was 2msec and data length was about 10 minutes. In the active method, geophones that have the natural frequency of 4.5Hz were used as receivers. Sampling time was 1 msec and data length was about 1 second. A 10 kg sledge hammer was used as a source. Receiver and source intervals were 1m or 2m. An OYO McSEIS-SXW was used for the passive and active data acquisition.

Figure 5.4.5 shows all dispersion curves obtained through passive methods. Clearly, south site and 'East 1' array has different dispersion curves compared with other arrays. 'East-1' array is on the boundary of east and south site. Therefore, we will group 'South' array and 'EAST 1' array as 'South site' in following discussions. In each sites, we averaged all dispersion curves. Figure 5.4.6 shows averaged dispersion curves for there sites, such as north, east and south, dispersion curves obtained through active method performed at each area were also shown. We can see that the passive and active dispersion curves agree with very well around 10Hz. Therefore, we combined active and passive dispersion curves together.

For the moment, we shall focus on the comparison of our surface-wave data with the result of other geophysical experiments. At first, we will compare our dispersion curves with the surface-wave data presented by Foti (2003). Figure 5.4.7 shows the comparison of dispersion curves with Foti (2003). The surface wave-data

presented by Foti (2003) was acquired in the north-site. We can see that our north site dispersion curves almost agree with the results by Foti (2003). In our dispersion curves, highest phase velocity obtained through a passive method is 240m/s at the frequency of 2Hz. The highest velocity is much higher than that of Foti (2003) obtained through an active method. It implies that the penetration depth of our surface-wave method is deeper than that of Foti (2003).

A non-linear least square inversion (Xia et al., 1999) was applied to combined dispersion curves in order to obtain S-wave velocity model. In the inversion, unknown parameters were only S-wave velocity of each layer and thickness of layer was fixed through iterations. An initial S-velocity model is generated by a wavelength-depth conversion in which 1/3 of wavelength is considers as depth. Figure 5.4.8 shows the resultant S-wave velocity model for the north site. In this figure, green circles indicate apparent depth calculated from the dispersion curve using the wavelength-depth conversion. In the north site, the S-wave velocity from surface to the depth of 20m is about 150m/s. The S-wave velocity bellower than the depth of 20m is increasing with depth gradually. Figure 5.4.9 shows the comparison of observed dispersion curve with theoretical data. The theoretical dispersion curve is phase-velocity for the fundamental mode of Rayleigh waves. It is clear that the theoretical data agrees with observed data very well. Figure5.4.10 shows the phase-velocity and relative amplitude for the fundamental and higher modes of Rayleigh waves. Solid lines indicate phase-velocity and dashed lines indicate relative amplitude. Blue circles indicate the phase-velocity which gives maximum amplitude in each frequency. We can confirm that the observed dispersion curve mainly consists of the fundamental mode of dispersion curve. It indicates our inversion, in which only fundamental mode of Rayleigh waves was considered, was appropriate in this site.

Next, we will focus on the east and south site data. Similar to the north site, the least square inversion was applied to the east and south site dispersion curves. Figure 5.4.11 shows resultant S-wave velocity models for the east site. Figure 5.4.12 and 5.4.13 shows the comparison of observed dispersion curve to fundamental and higher modes dispersion curves respectively. Figure 5.4.14 shows resultant S-wave velocity models for the south site. Figure 5.4.15 and 5.4.16 shows the comparison of observed

dispersion curve to fundamental and higher modes dispersion curves respectively. The result of surface-wave method for the east and south site can be summarized as follows.

At the east site, S-wave velocity from the depth of 3 to 7m is relatively high compare with other sites. At the south site, S-wave velocity from the depth of 7 to 15m is relatively high, compare with other sites. Three S-wave velocity models for three sites, such as north, east and south sites, imply that the S-wave velocity of the site varies not only vertical direction but also horizontal direction.

Figure 5.4.17 shows the S-wave velocity models for three sites together with the S-wave velocity model obtained through a cross-hole measurement. The cross-hole measurement was performed at the east site. In the velocity model from cross-hole measurement, S-wave velocity from the depth of 5 to 8m is relatively high. This character, high velocity layer is embedded in shallower than 10m, is similar to our S-wave velocity model for the east site. Figure 5.4.18 shows the S-wave velocity models for three sites together with the S-wave velocity models obtained through Seismic Corn Penetrating Tests (SCPTs). The SCPTs were performed around the Tower. In the velocity models from SCPTs, S-velocity from the depth of 7 to 13m is relatively high. This character, high velocity layer is embedded around the depth of 10m, is similar to our S-wave velocity model for the south site. In conclusion, our S-wave velocity models obtained through the passive and active surface-wave method agree with existed data very well.

5.4.3 Two-dimensional S-wave velocity Models Using Active Data

Figure 5.4.19 shows the example of waveform data for the active surface-wave method. We can see that the waveform were different by sites. North and east site's wave forms are more complicated than south rite's waveform data. It implies that a velocity model at the south site is relatively simple compare with the north and east sites. The CMPCC analysis was applied to the waveform data and dispersion curves were calculated with 2m or 4m spacing along the survey lines, in order to delineate horizontal heterogeneity of the site. Figure 5.4.20 shows the example of dispersion curves for the east and south sites. It seems that the south site dispersion curves are simpler than that of the east sites. We have applied one-dimensional non-linear least square method to

each dispersion curve. Resultant one-dimensional velocity models are shown as two-dimensional models. Figure 5.4.21 shows the two-dimensional S-wave velocity models in the north site. In the north site, S-wave velocity from surface to the depth of 2m is relatively high. All four S-wave velocity models are almost identical in the north site. Figure 5.4.22 shows the S-wave velocity models for the east and south sites. In the east site, S-wave velocity from the depth of 2m to 6m is relatively high in E-1 line. In the E-3 line that places south-north direction, S-wave velocity changes horizontal direction. In the south site, S-wave velocity from surface to the depth of 8m is relatively low compare with the north and east sites.

5.4.3 Interpolated Three-dimensional Velocity Model Image around the Tower

Resultant one and two dimensional S-wave velocity models are interpolated and a three dimensional S-wave velocity model was constructed. Figure 5.4.23 shows the plan views of interpolated S-wave velocity model with 2 or 5m depth spacing. In the shallow region, from the surface to the depth of 3m, S-wave velocity is higher at north side and lower at south side of the Tower. In the depth of 3 to 7m, S-wave velocity is higher at east side of the Tower. In the depth of 7 to 20m, S-wave velocity is higher at south side and lower at north side of the Tower. The plan views clearly show that S-wave velocity around the Tower changes not only vertically but also horizontally.

The result of the surface-wave investigation around The Leaning Tower of Pisa can be summarized as follows:

1) The highest phase velocity obtained through a passive method is 240m/s at the frequency of 2Hz.

2) Dispersion curves at the north side of the Tower agree with the dispersion curves obtained by Foti (2003).

3) Dispersion curves at the east side of the Tower agree with the S-wave velocity model obtained through the cross-hole measurements.

4) Dispersion curves at the south side of the Tower agree with the S-velocity models obtained through the Seismic Corn Penetrating Tests.

5) S-wave velocity down to the depth of 20m varies between 130 to 200m/s not only vertically but also horizontally.
6) In the shallow region, down to 3m, S-wave velocity is higher at north side and lower at south side of the Tower.
7) In the depth of 3 to 7m, S-wave velocity is higher at east side of the Tower.
8) In the depth of 7 to 20m, S-wave velocity is higher at south side and lower at north side of the Tower.

The surface-wave methods could delineate detailed S-wave velocity model around The Leaning Tower of Pisa. The geological condition of the Tower foundation is very important for the stability of the tower. The S-wave velocity model obtained through the surface-wave method can contribute important information toward the understanding of the Tower foundation.

Figure 5.4.1 The Leaning Tower of Pisa, Italy.

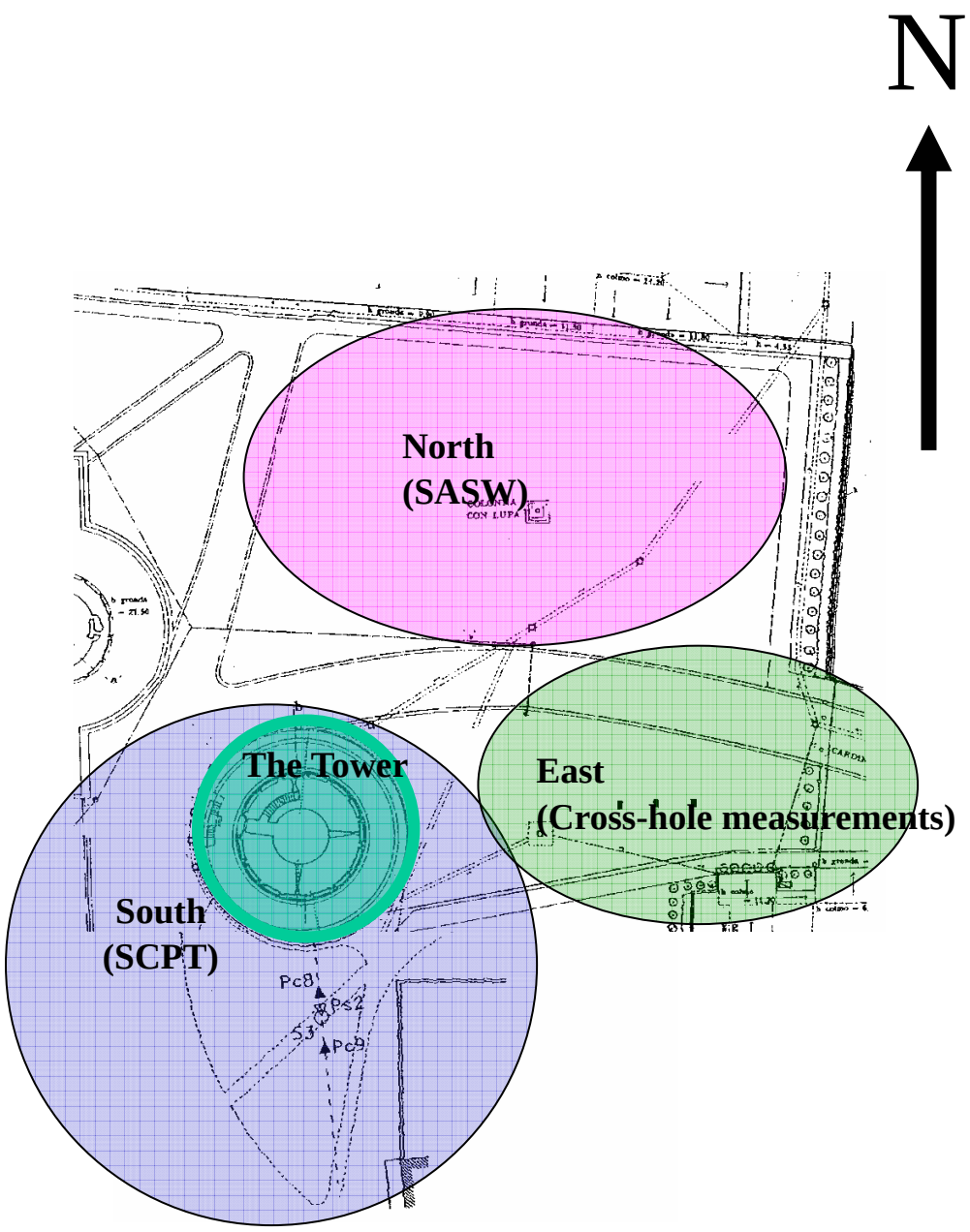

Figure 5.4.2 Description of the site and S-wave velocity measurements already performed at the site.

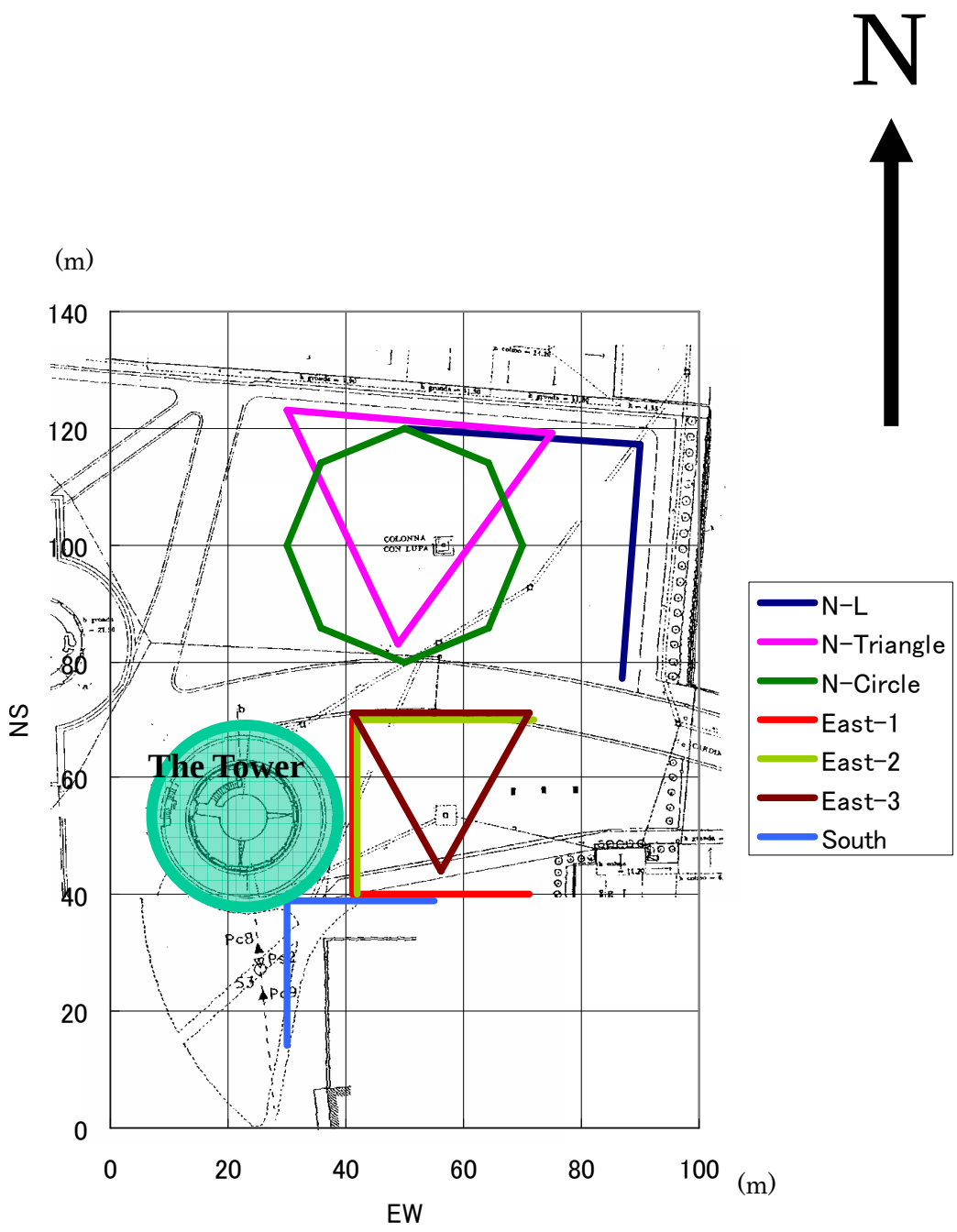

Figure 5.4.3 Location and shape of passive arrays.

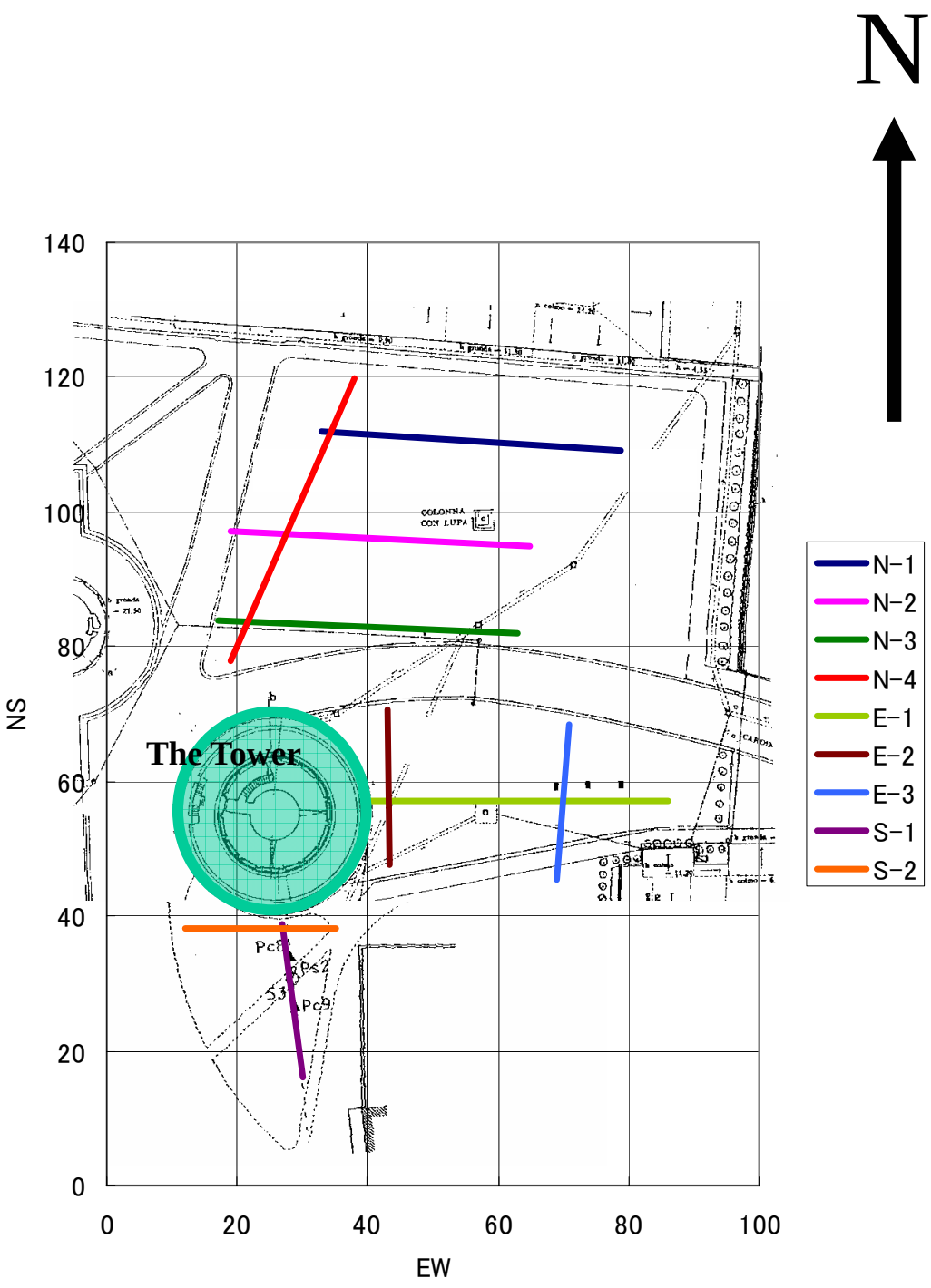

Figure 5.4.4 Location of active method survey lines.

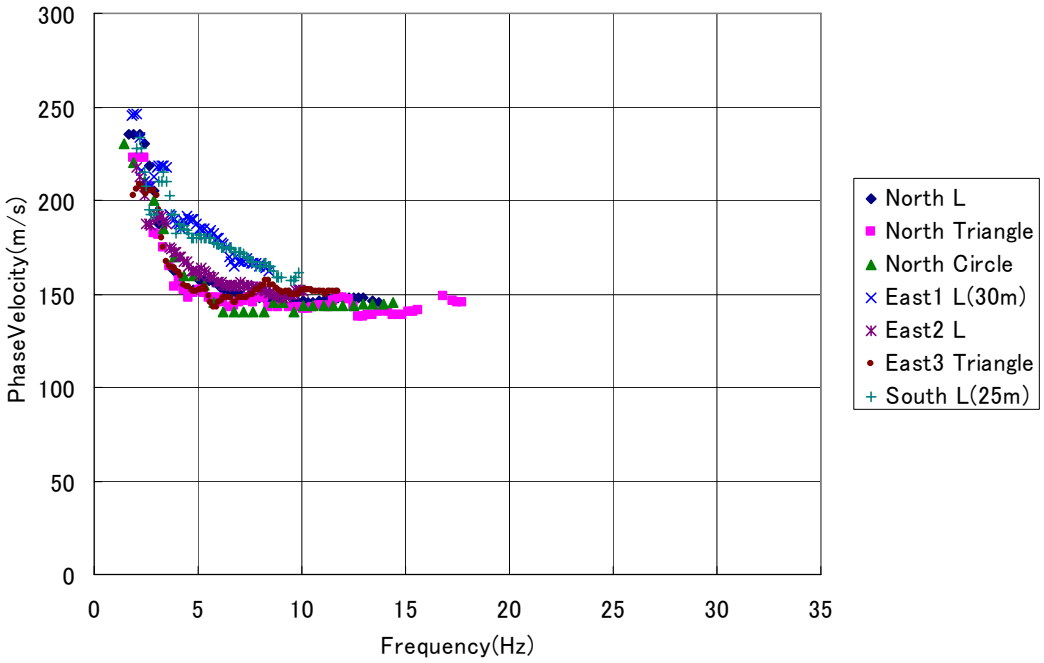

Figure 5.4.5 All dispersion curves obtained through passive method.

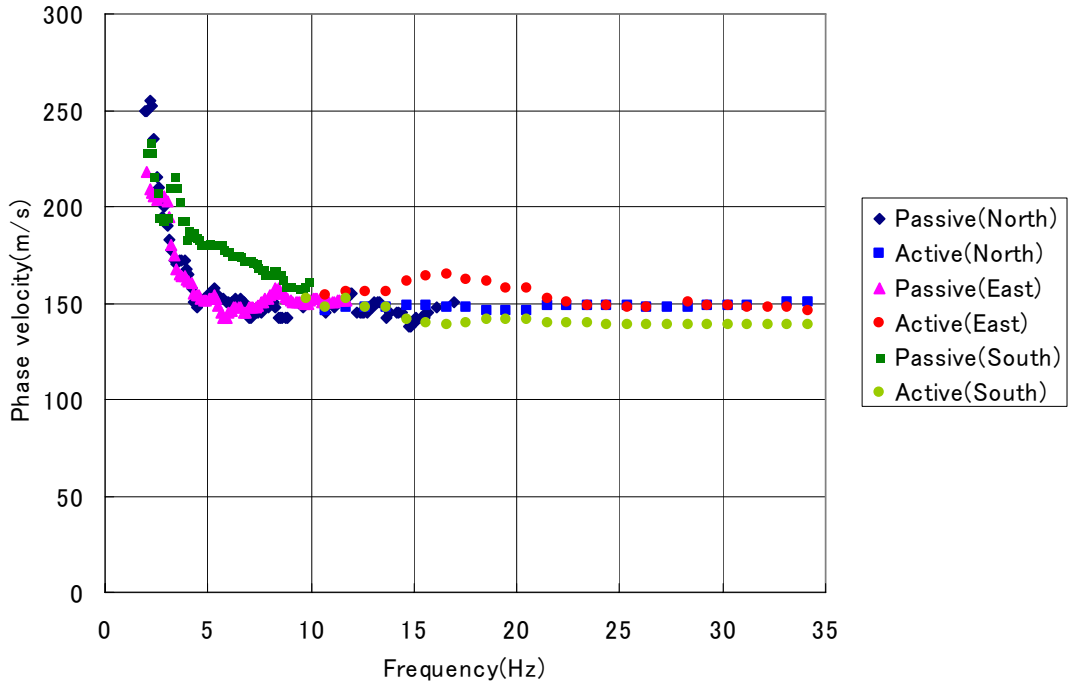

Figure 5.4.6 Averaged dispersion curves for three sites.

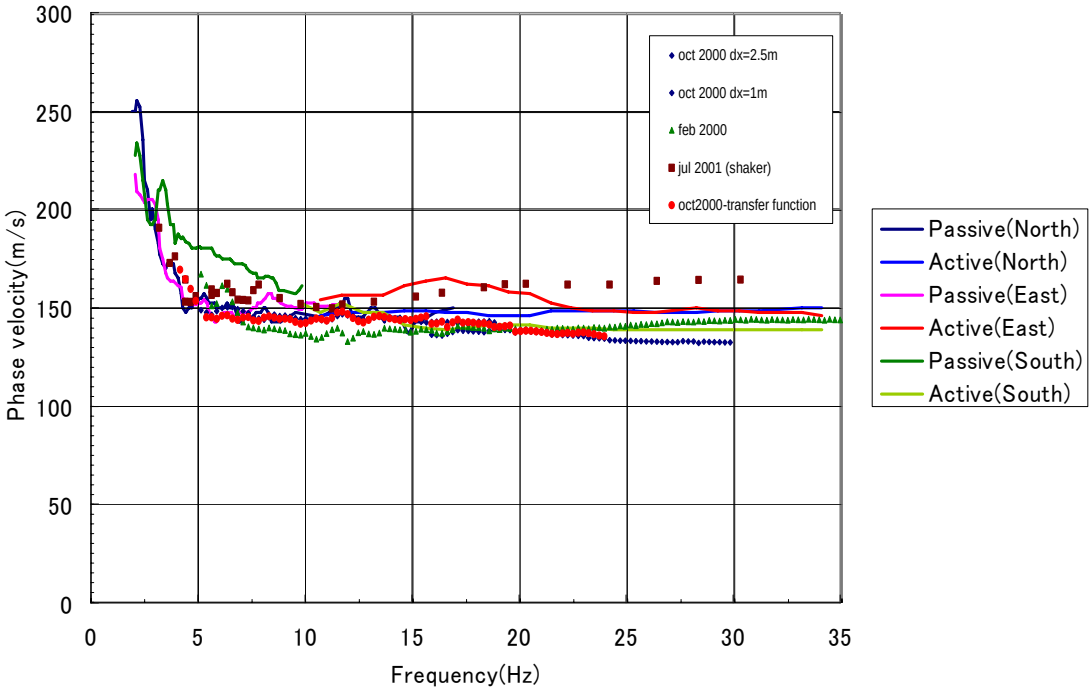

Figure 5.4.7 Comparison of dispersion curves with Foti (2003).

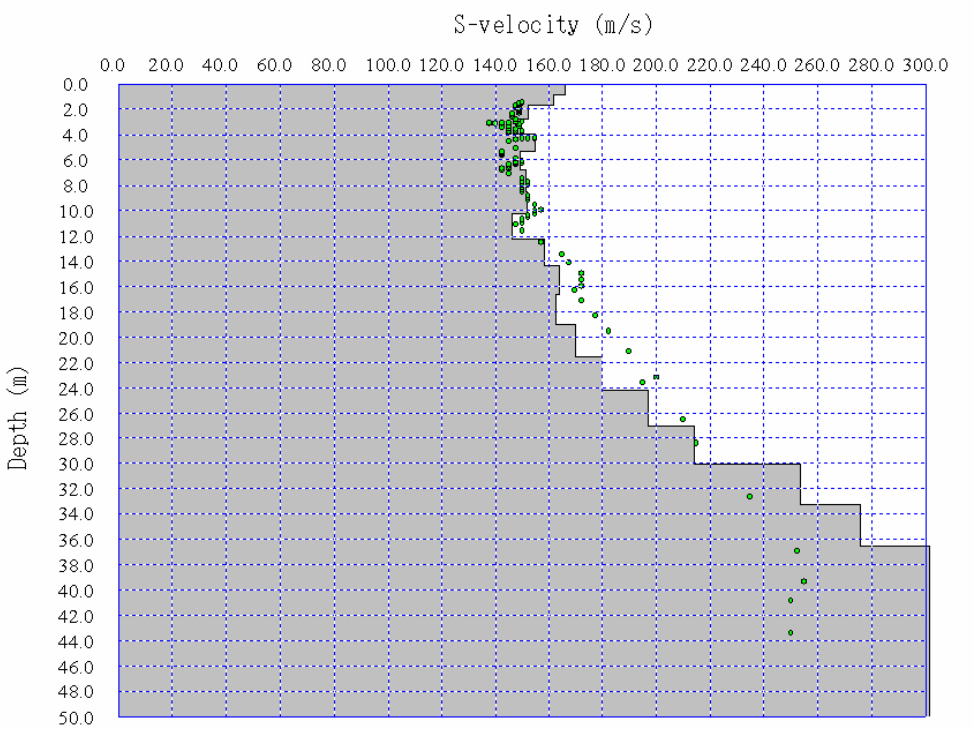

Figure 5.4.7 Resultant S-wave velocity model for the north site.

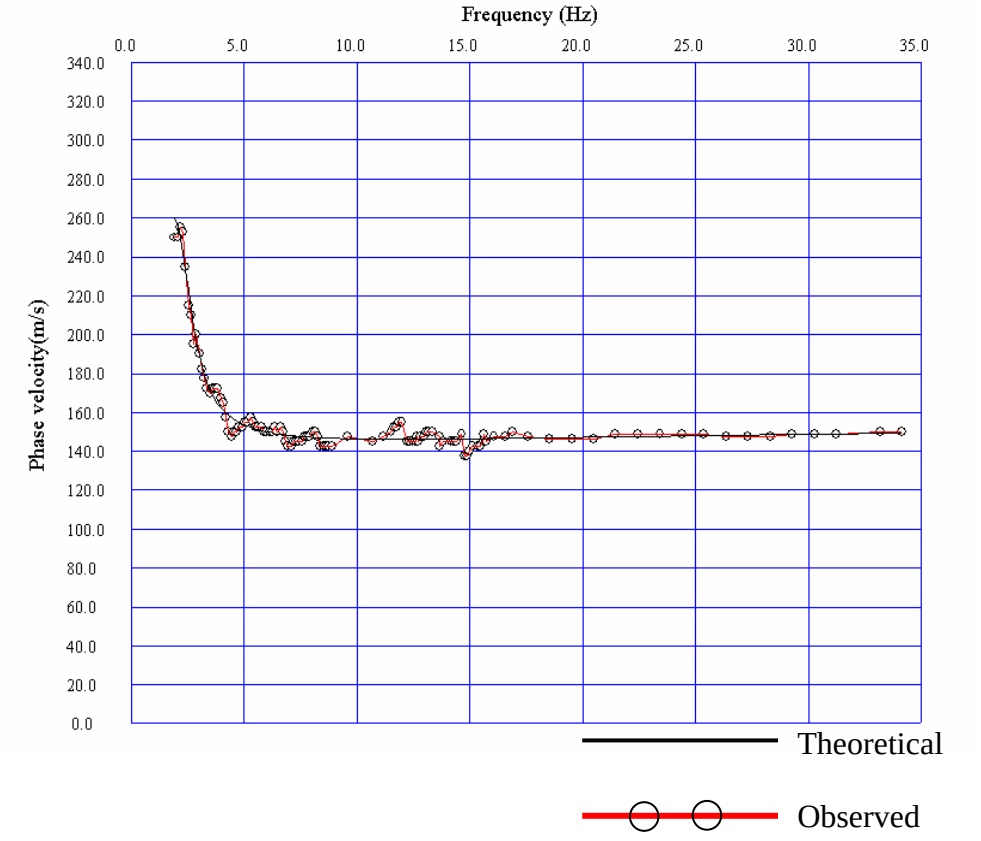

Figure 5.4.8 Comparison of observed dispersion curve with theoretical data. (north site)

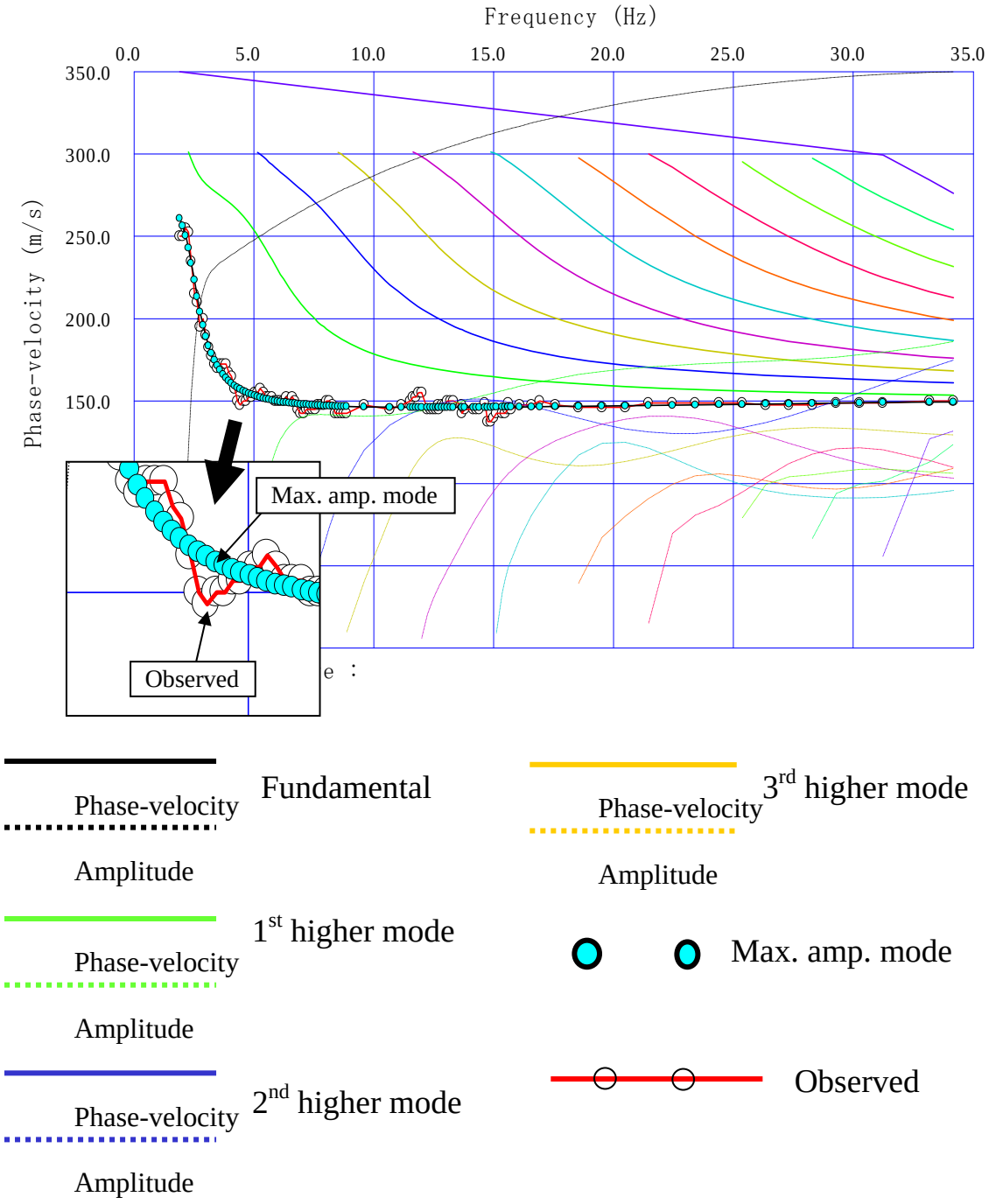

Figure 5.4.10 Phase-velocity and relative amplitude for fundamental and higher mode of Rayleigh waves (north site).

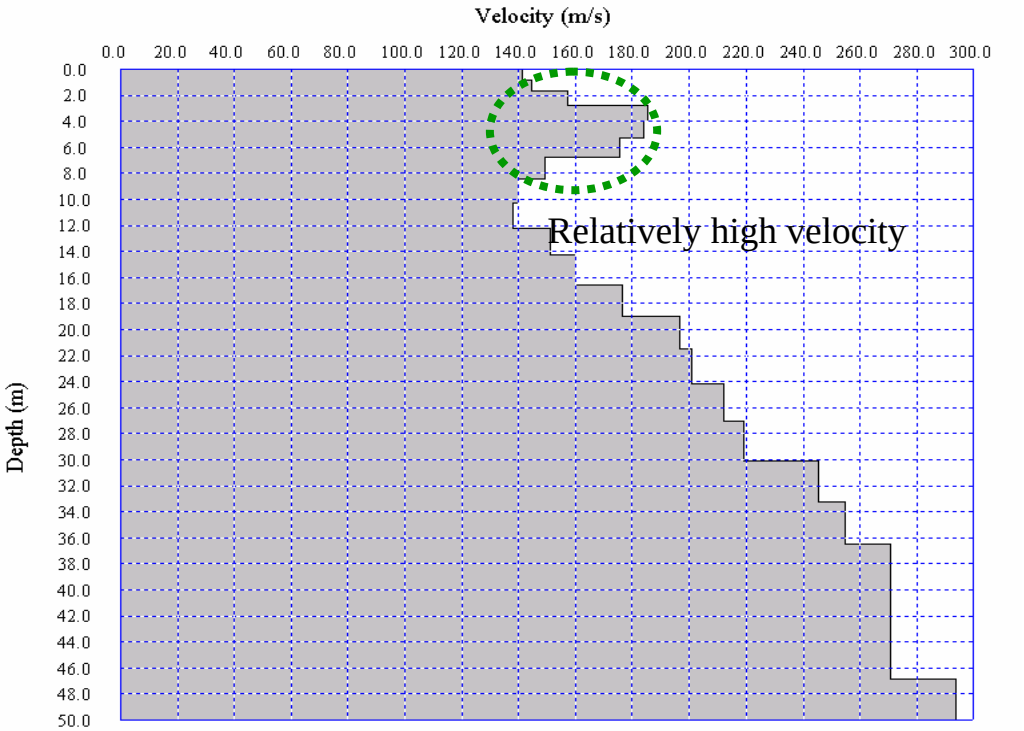

Figure 5.4.11 Resultant S-wave velocity model for the east site.

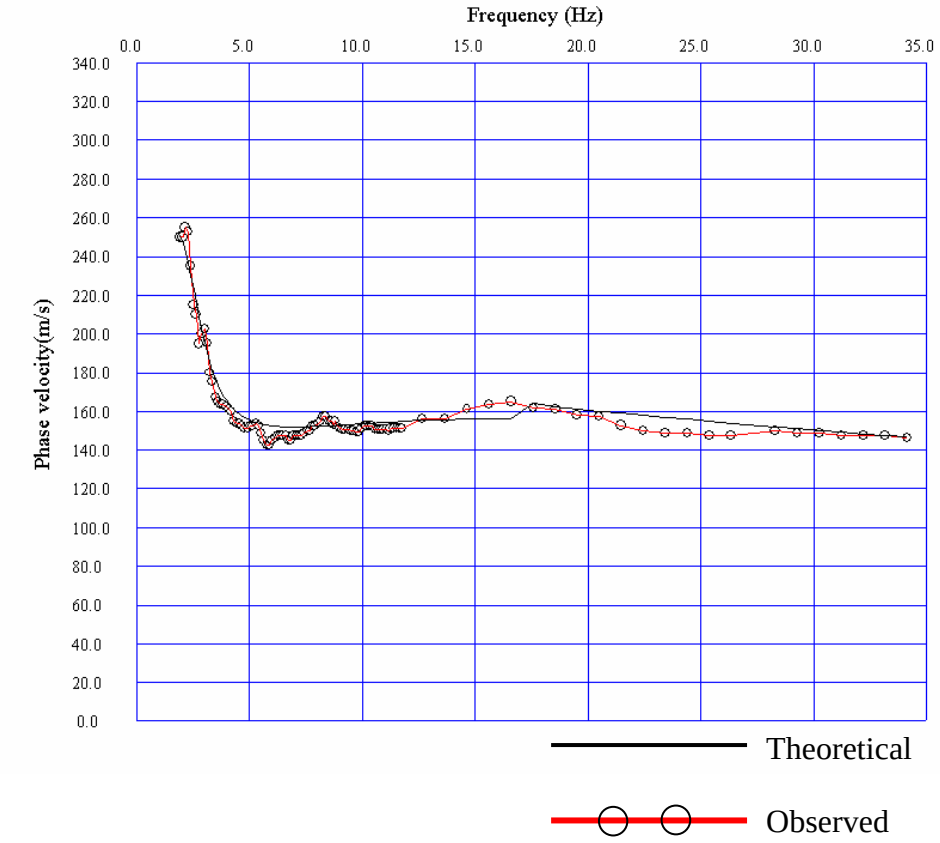

Figure 5.4.12 Comparison of observed dispersion curve with theoretical data (east site).

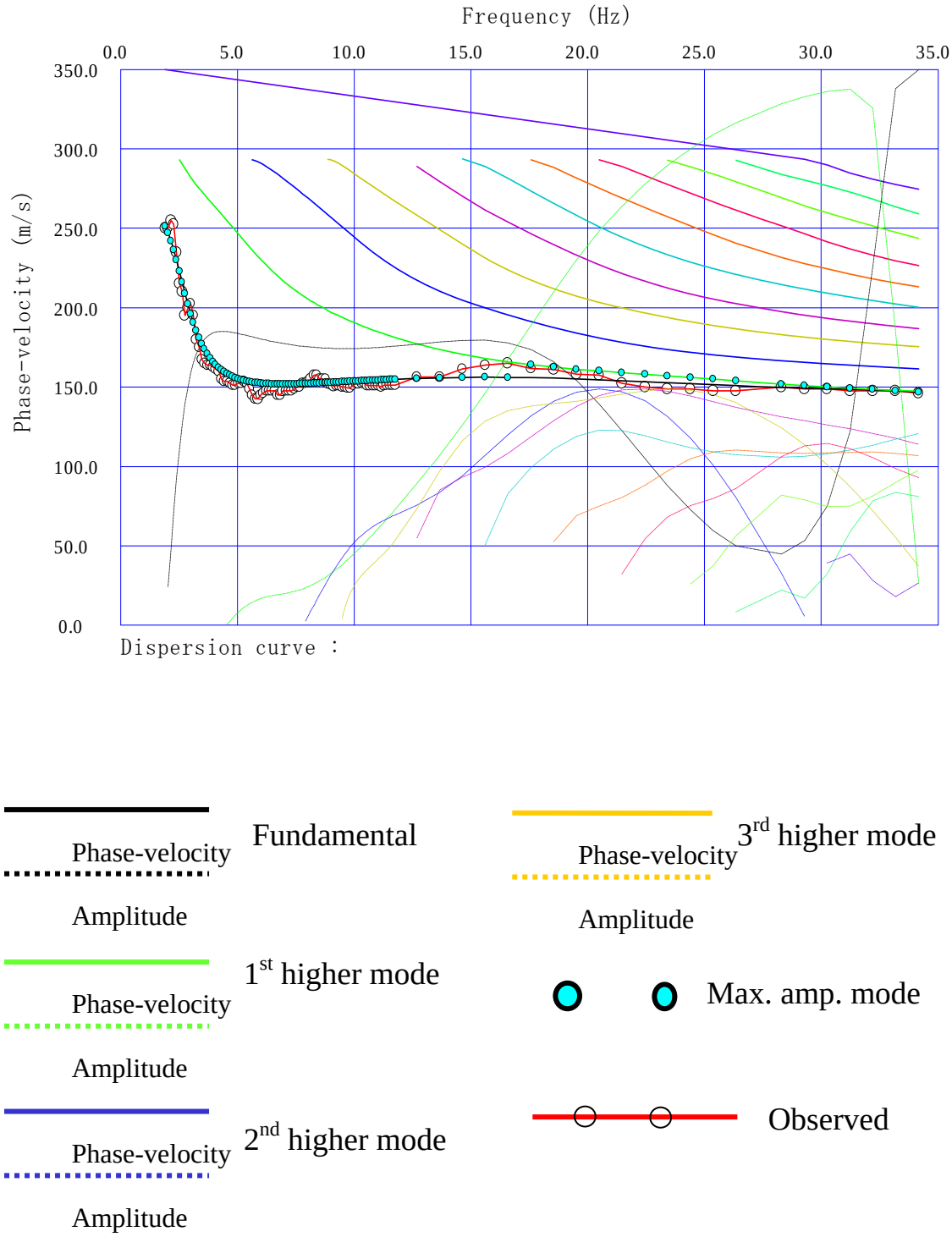

Figure 5.4.13 Phase-velocity and relative amplitude for fundamental and higher mode of Rayleigh waves (east site).

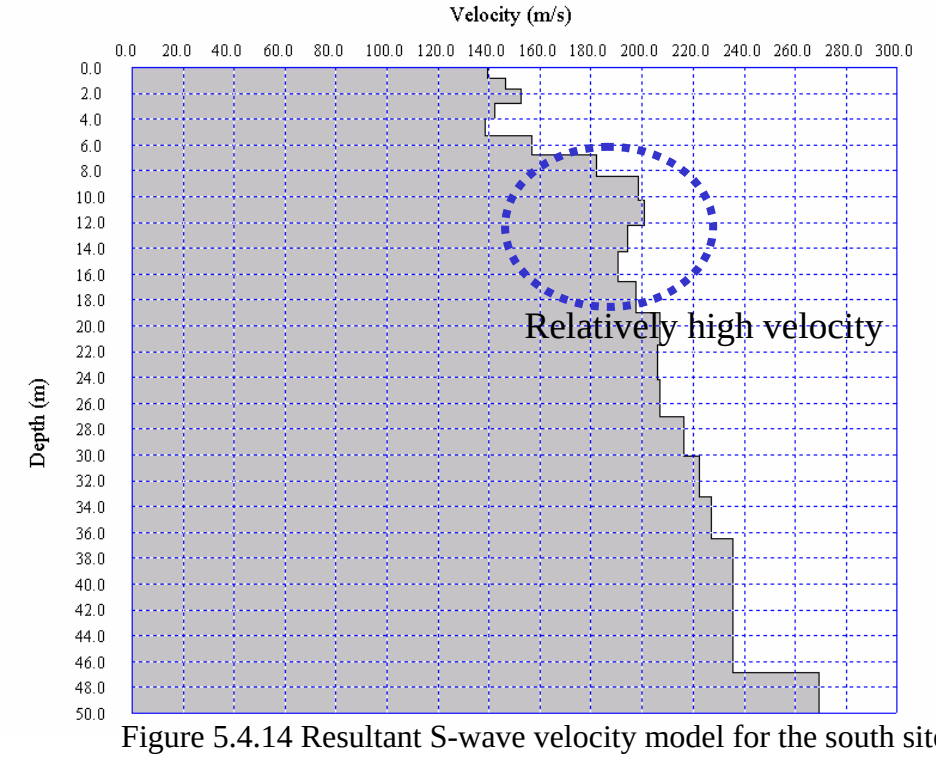

Figure 5.4.14 Resultant S-wave velocity model for the south site.

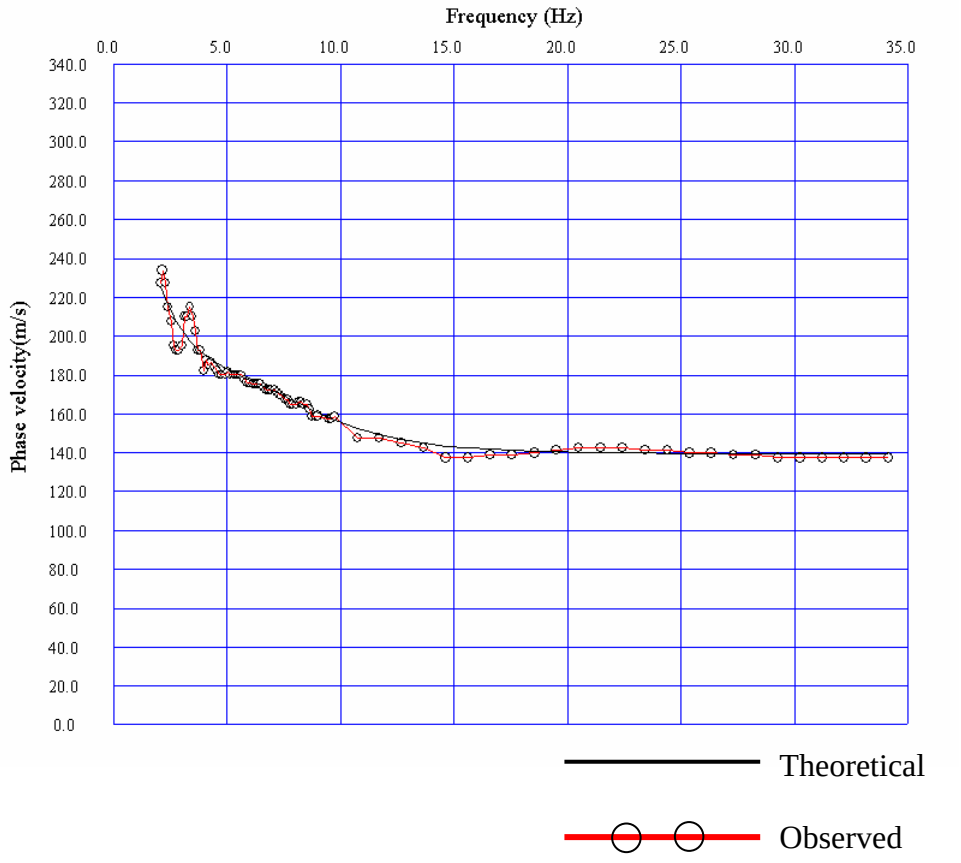

Figure 5.4.15 Comparison of observed dispersion curve with theoretical data (south site).

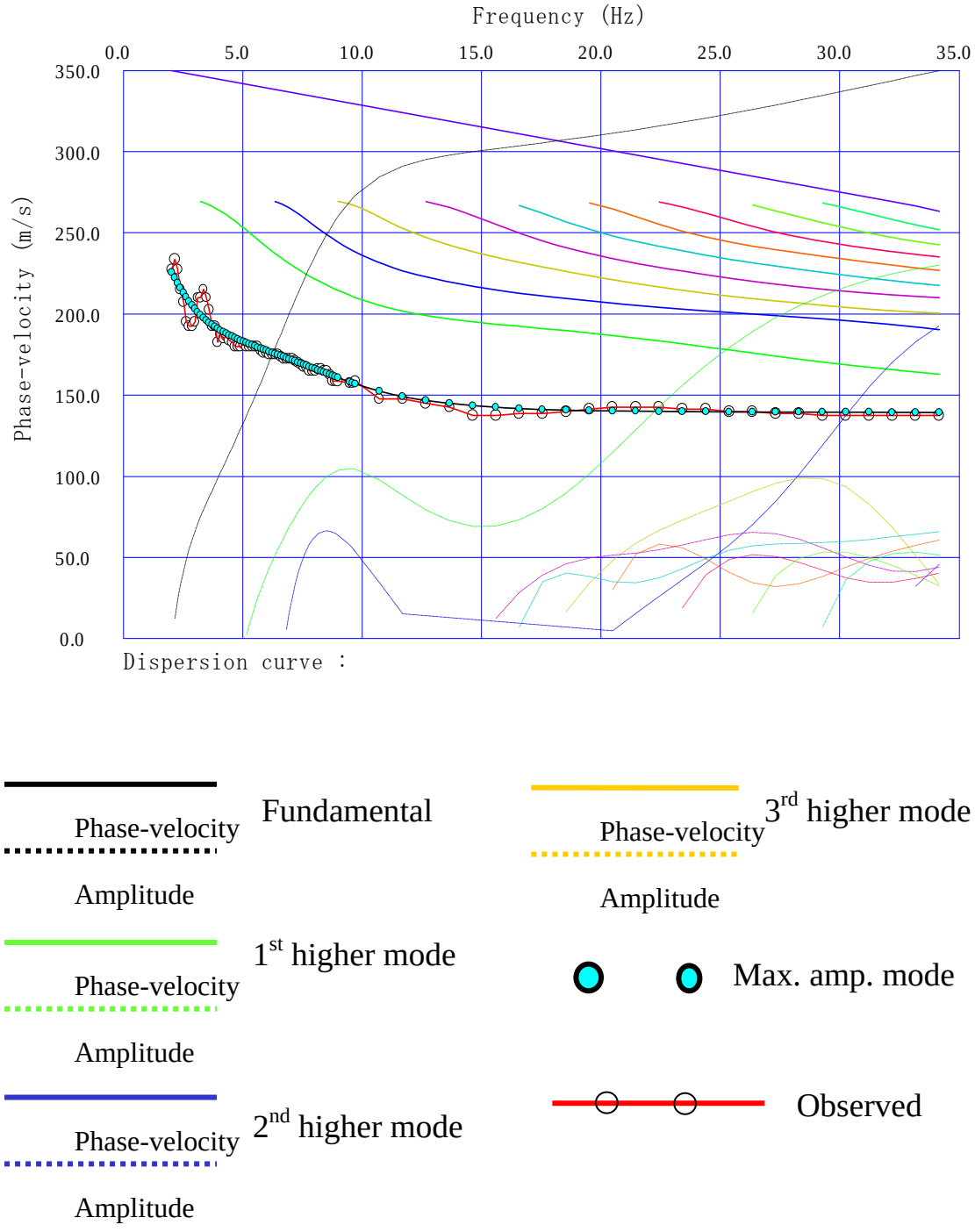

Figure 5.4.16 Phase-velocity and relative amplitude for fundamental and higher mode of Rayleigh waves (south site).

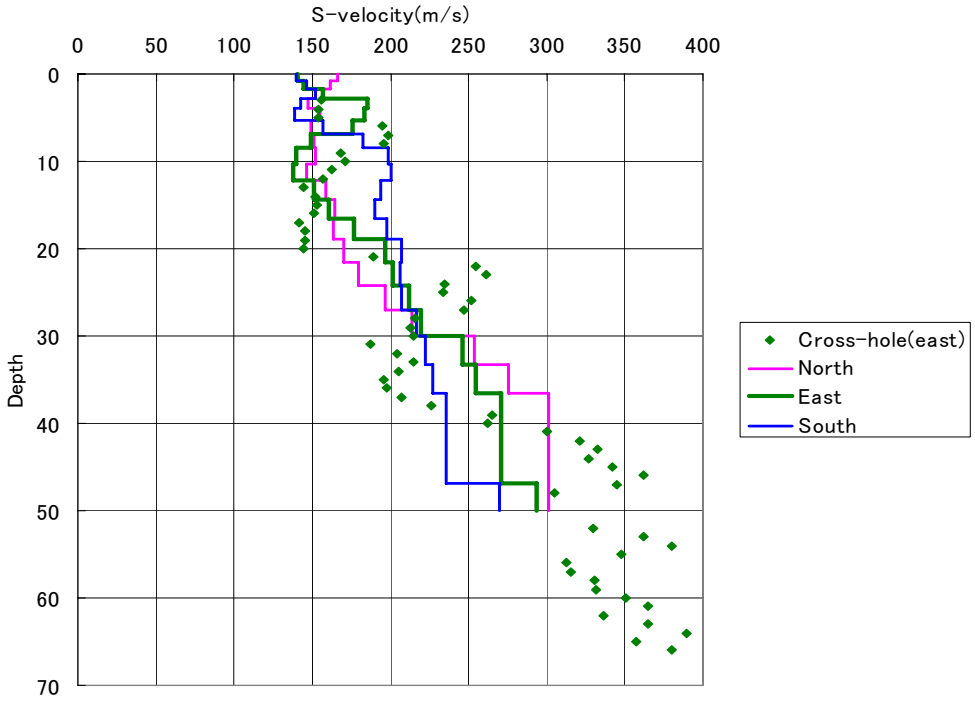

Figure 5.4.17 S-wave velocity models obtained through the surface-wave method compared with that of cross-hole measurements.

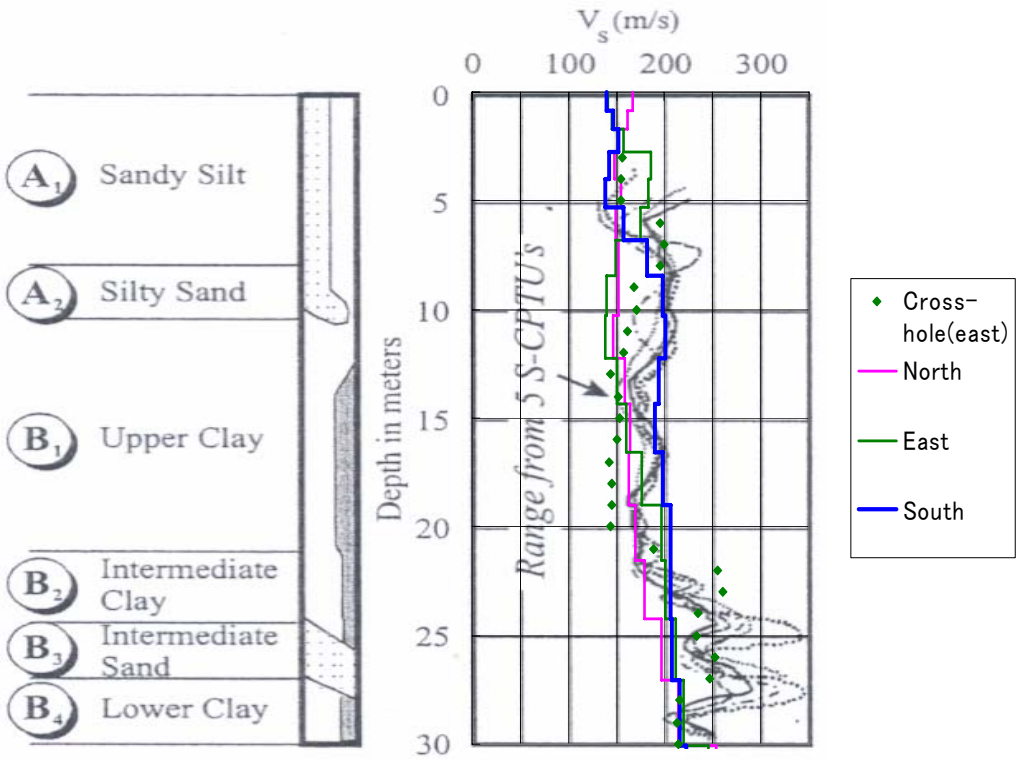

Figure 5.4.18 S-wave velocity models obtained through the surface-wave method compared with that of CPT tests.

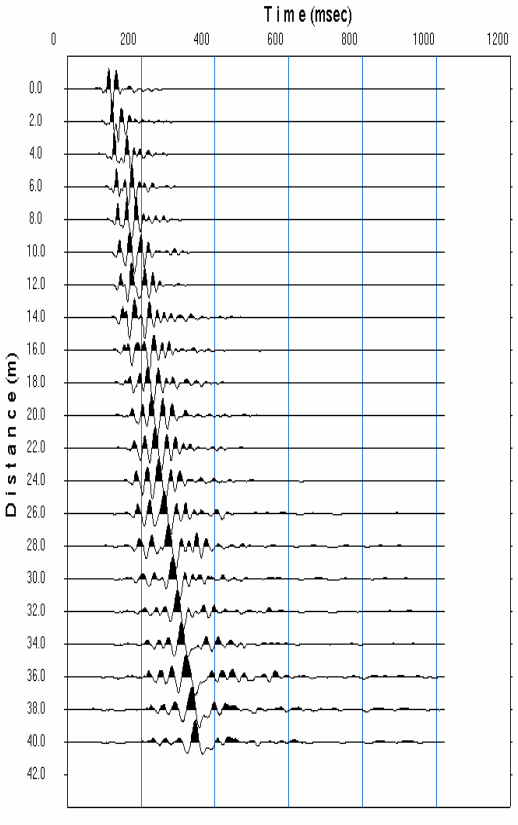

1) North site.

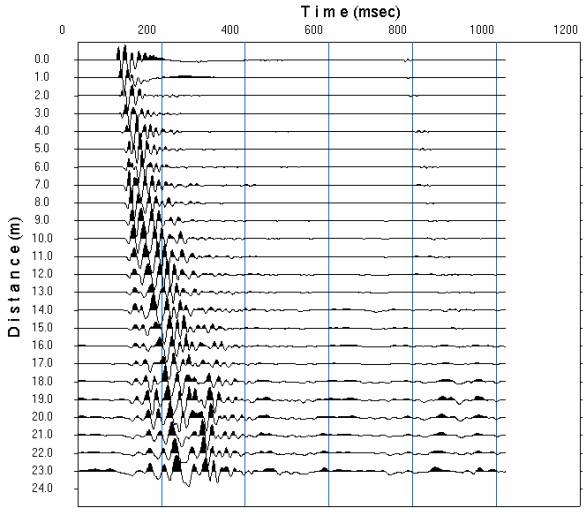

2) East site.

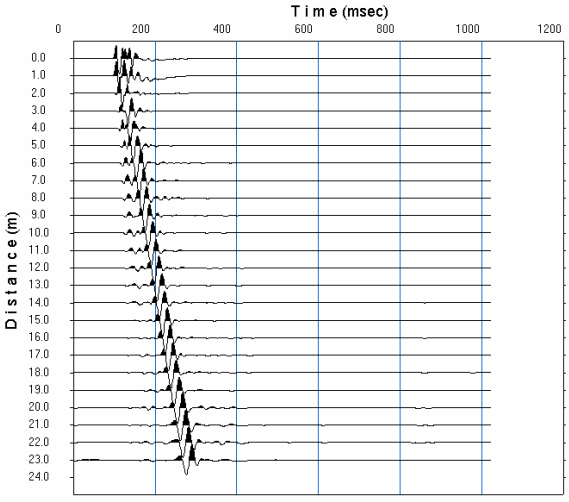

3) South site.

Figure 5.4.19 Example of waveform data for active surface-wave method.

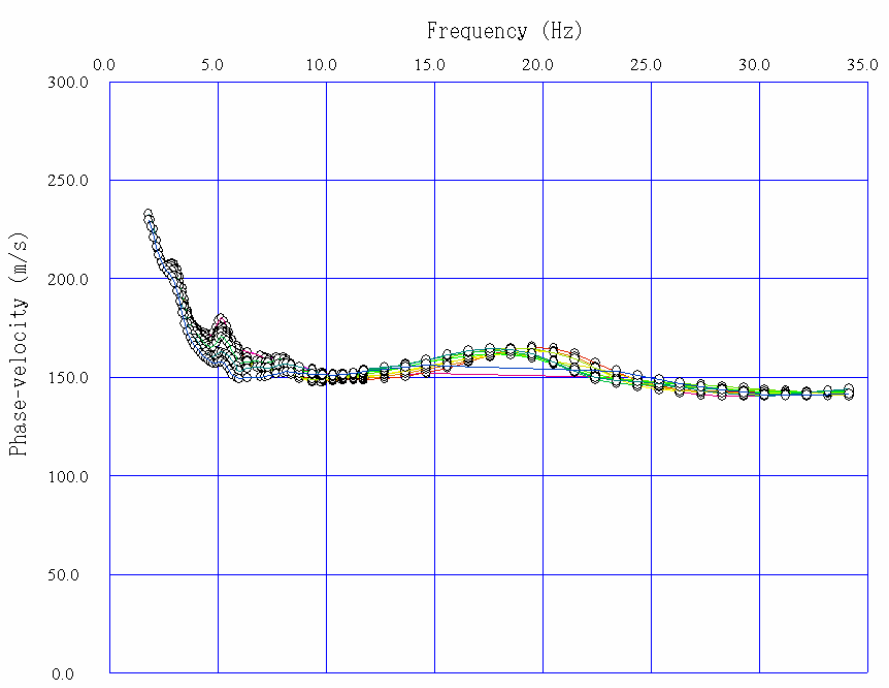

1) East site

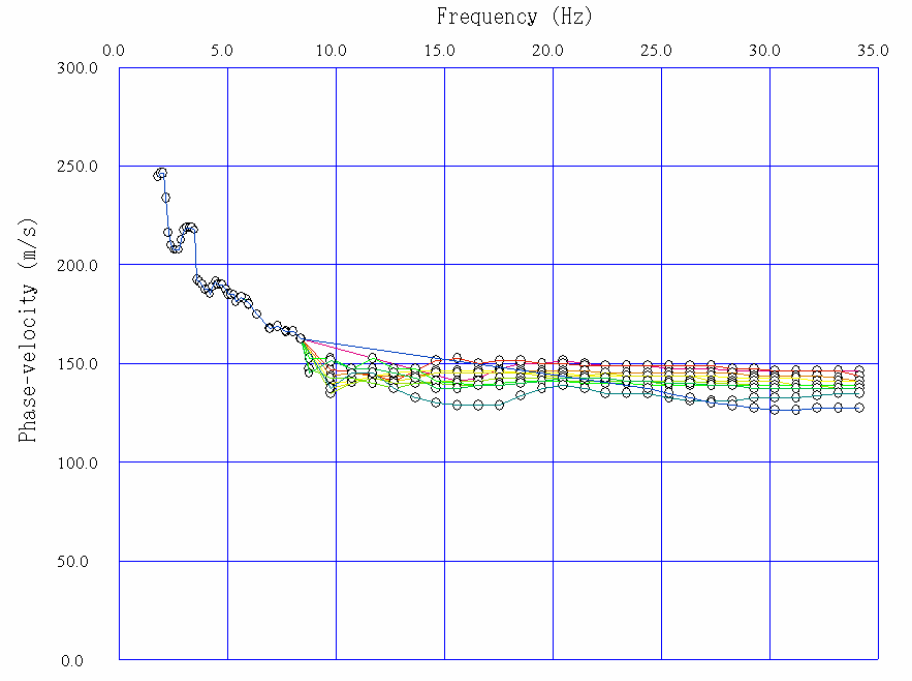

2) South site

Figure 5.4.20 Example of active method dispersion curves for east and south sites. Red to yellow curves indicate the beginning of the survey line and green to blue curves indicate the ending of the survey line.

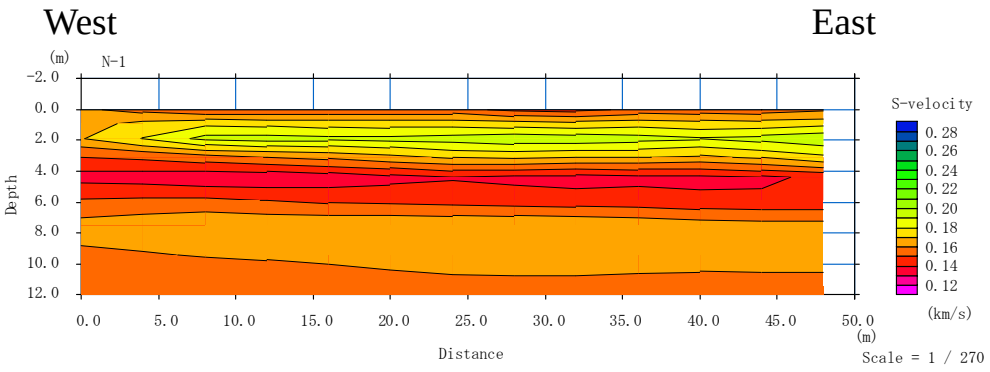

1) N-1 line.

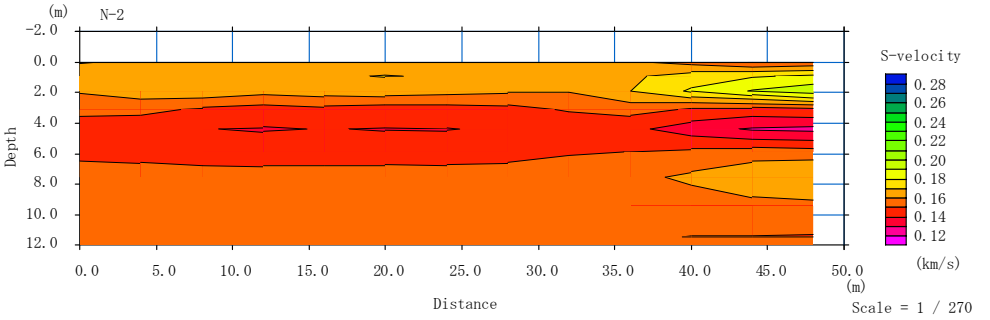

2) N-2 line.

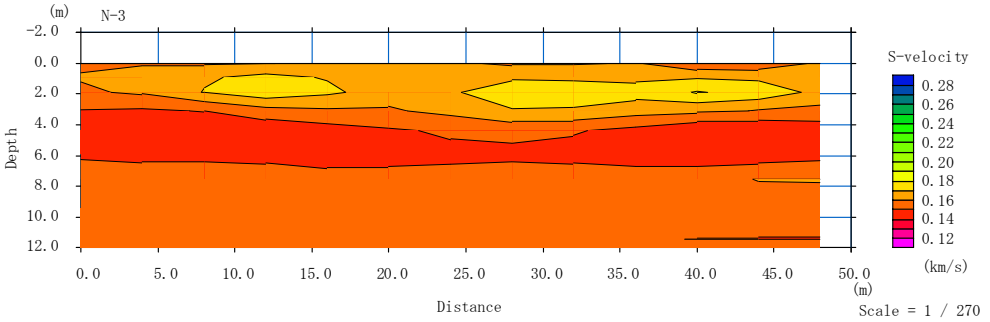

3) N-3 line.

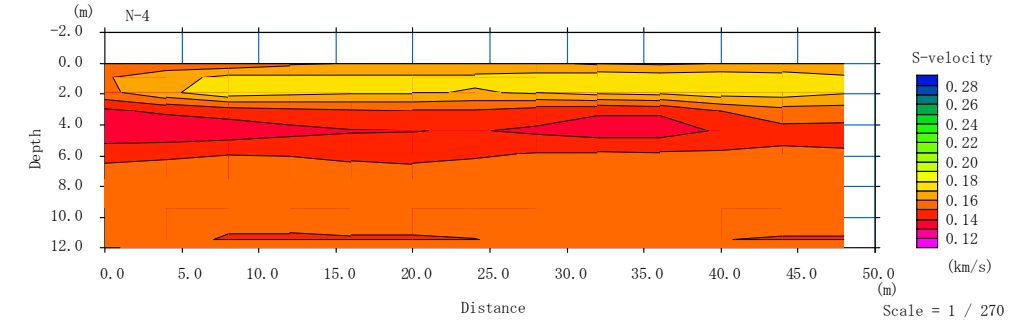

4) N-4 line.

Figure 5.4.21. Resultant S-wave velocity models for north site.

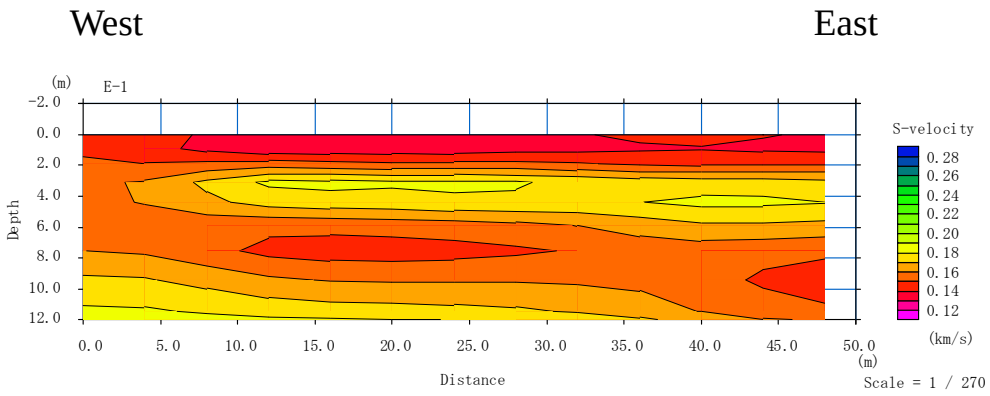

1) E-1 line.

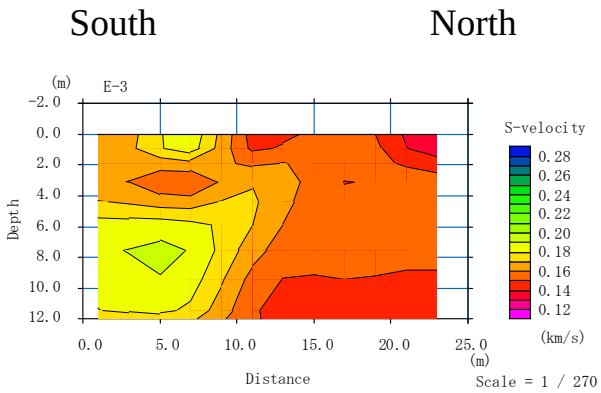

2) E-2 line.

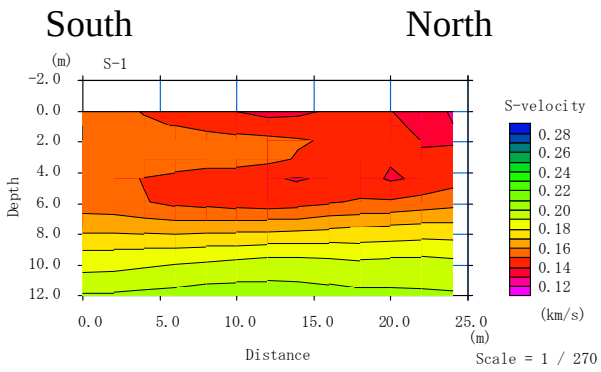

3) S-1 line.

Figure 5.4.22. Resultant S-wave velocity models for east (top and middle) and south site (bottom).

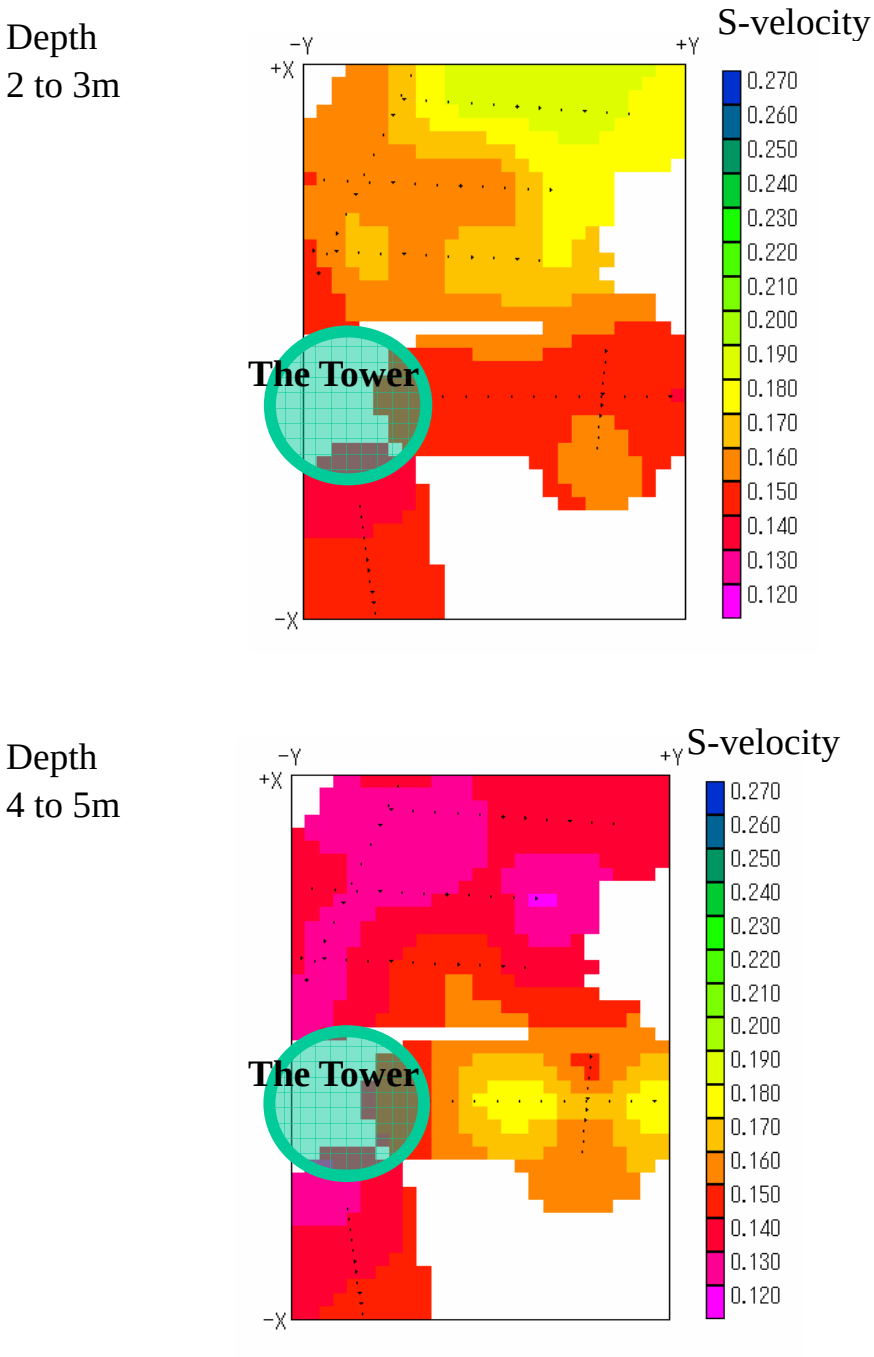

Figure 5.4.23. Plan views of interpolated S-wave velocity model around the Tower.

Depth
6 to 7m

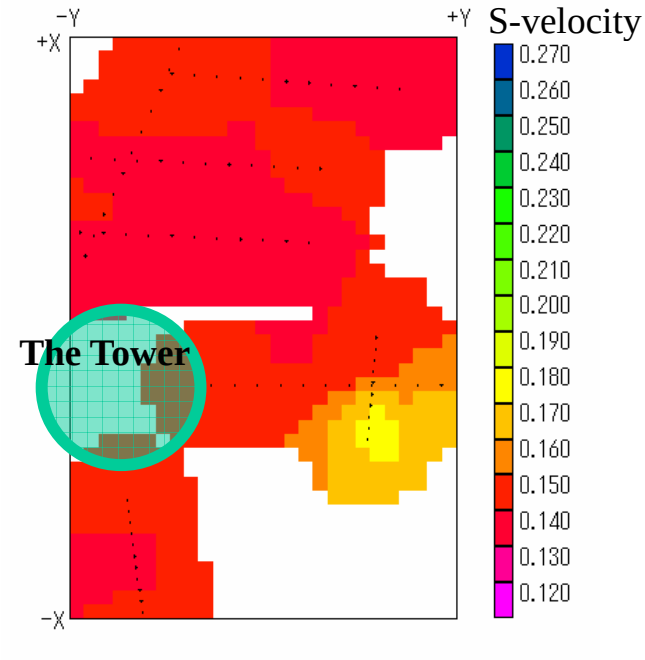

Depth
8 to 9m

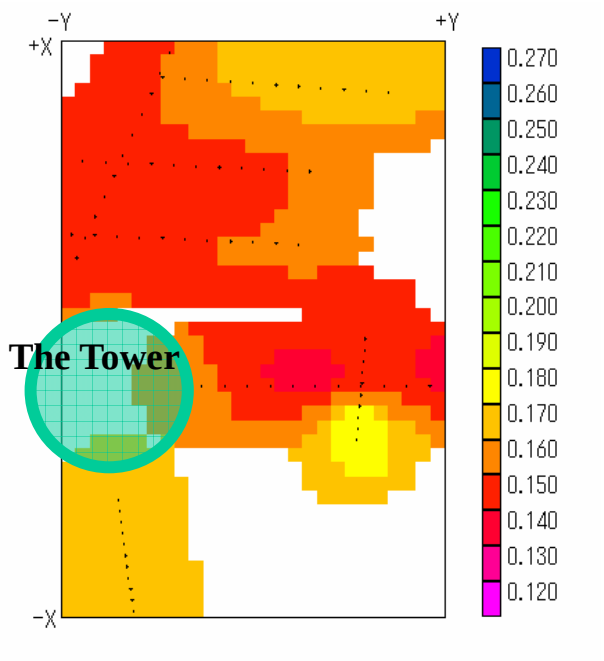

Figure 5.4.23 (continue)

Depth
10 to 11m

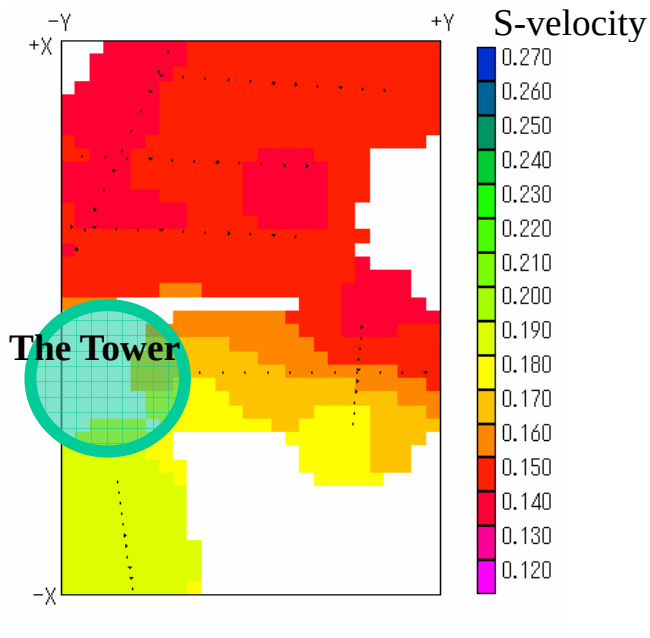

Depth
15 to 16m

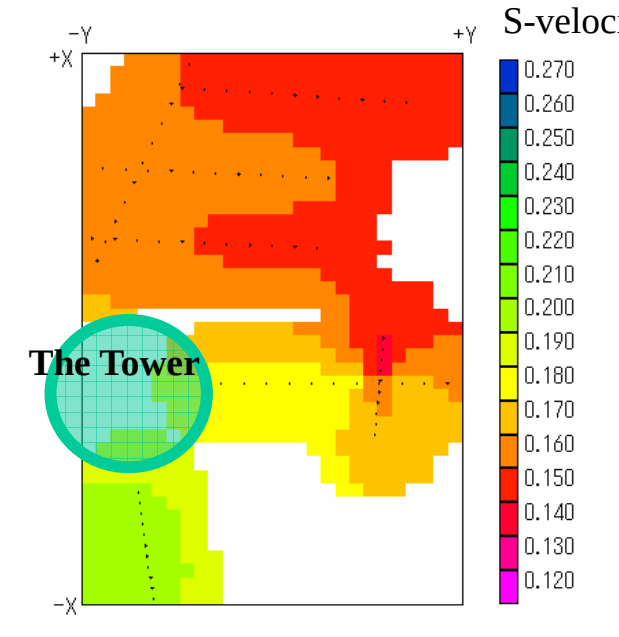

Figure 5.4.23 (continue)

Depth
20 to 21m

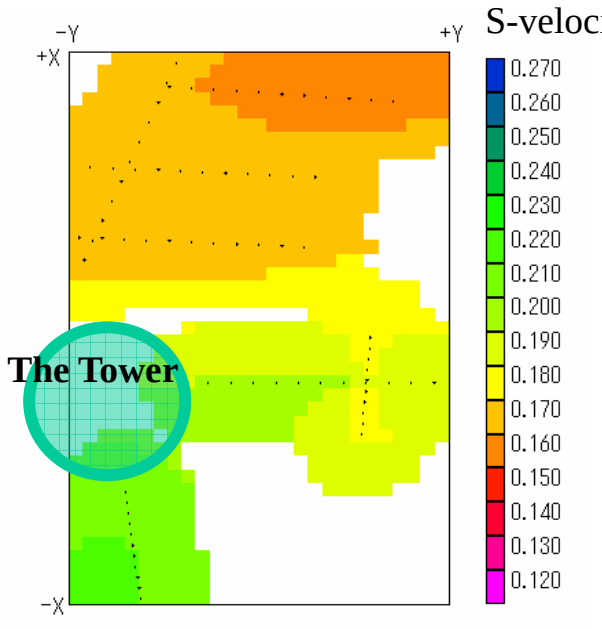

Depth
25 to 26m

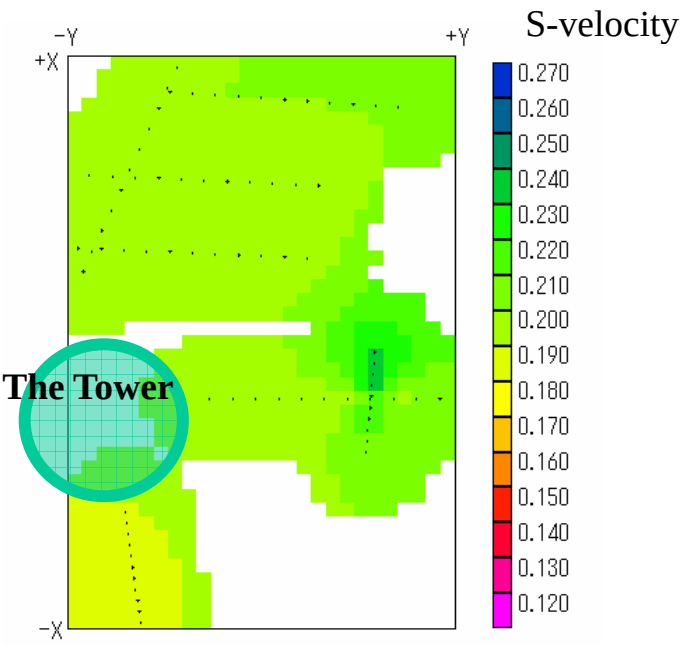

Figure 5.4.23 (continue)

5.5 Application to Liquefied Site

5.5.1 Introduction

Many geo-technical investigations, such as a standard penetrating test (SPT) and a corn penetrating test (CPT), have been used for evaluating liquefaction potential. Such methods, however, have to drill ground and it makes the investigations to be expensive and time consuming. A liquefaction potential analysis using share-wave velocity has been also proposed as a nondestructive method that can be performed form surface. The method, however, is not commonly used because of difficulty in shear-wave velocity measurement from the surface. Recently, surface-wave methods enable us to obtain shear-wave velocity structure of ground from the surface inexpensively. The liquefaction potential analysis using shear-wave velocity obtained from the surface-wave methods can be effective tools for evaluating earthquake risk in wide area without drilling. In order to evaluate the applicability for the liquefaction potential analysis using shear-wave velocity, we have applied the methods to residential area in Niigata, Japan, where liquefied by The Mid Niigata Prefecture Earthquake in 2004.

5.5.2 Liquefaction Potential Analysis in Terms of Shear-wave Velocity

Using shear-wave velocity and groundwater level, a liquefaction potential analysis in terms of overburden stress-corrected shear wave velocity (e.g. Juang et al., 2001) has been used in recent years. Outline of the analysis is summarized as follows.

Generally, liquefaction potential is evaluated as a factor of safety (Fs) in which the “resistance of soil” expressed as the cyclic resistance ratio (CRR) is divided by the “loading induced by a earthquake” expressed as cyclic stress ratio (CSR) as follows;

$$Fs = \frac{CRR}{CSR}. \tag{5.5.1}$$

The cyclic stress ratio (CSR) is generally expressed as (Seed and Idriss, 1971);

$$CSR = 0.65\left(\frac{\sigma_\upsilon}{\sigma'_\upsilon}\right)\left(\frac{a_{\max}}{g}\right)\frac{r_d}{MSF} \tag{5.5.2}$$

where σ_v is total overburden stress at the depth in question; σ'_v is initial effective overburden stress at the same depth; a_{max} is peak horizontal ground surface acceleration; g is acceleration of gravity; r_d is shear stress reduction factor to adjust for flexibility of the soil profile. The value of r_d at the depth of z can be calculated using the following equation (Liao et al., 1988; Robertson and Wride, 1998);

$$r_d = 1.0 - 0.00765z \text{ , for } z \le 9.15m \text{ .}$$

$$r_d = 1.174 - 0.0267z \text{ , for } 9.15m < z \le 23m$$

$$r_d = 0.744 - 0.008z \text{ , for } 23m < z \le 30m \tag{5.5.3}$$

MSF is the value related to the magnitude of an earthquake and can be calculated as follows;

$$MSF = \left(\frac{M_w}{7.5}\right)^n \tag{5.5.4}$$

where M_w is moment magnitude of a earthquake. The value of n is defined as -2.56 etc..

The resistance of the soil, expressed as the cyclic resistance ratio is generally established by separating liquefied cases from non-liquefied cases in actual earthquakes. Here, following empirical equation defined by Andrus et al. (1999) is used;

$$CRR = \left\{a\left(\frac{Vs_1}{100}\right)^2 + b\left(\frac{1}{c - Vs_1}\right) - \frac{1}{c}\right\} \tag{5.5.5}$$

where, *a, b, c* are curve fitting parameters (*a=0.022*、*b=2.8*、*c= 200～215m/s*). Vs_1 is overburden stress-corrected shear wave velocity and defined as;

$$Vs_1 = Vs\left(Pa/\sigma'_v\right)^{0.25} \tag{5.5.6}$$

where, *Vs* is measured shear-wave velocity (m/s), Pa=reference stress (100kPa), σ'_v= initial effective overburden stress (kPa). The parameter c in the equation (6) represents the limiting upper value of Vs_1 for liquefaction occurrence. Generally, in the SPT based simplified method, a corrected blow count (N) of 30 is assumed as the limiting upper value for liquefaction occurrence.

5.5.3 Investigation in Kariwa Village

1) Outline of the Investigation

Figure 5.5.1 shows investigation site and the epicenter of the Mid Niigata Prefecture Earthquake. The investigation site is placed in Kariwa village, Niigata Prefecture, Japan and the distance from the epicenter is about 20km. Even if the structural damage of buildings was not significant in the village, ground disaster, such as landslide and liquefaction, occurred frequently around the investigation site. The site placed on the foot of gentle slope on sandy dune. The foundation damage of houses by the liquefaction was concentrated in small area. Figure 5.5.2 shows the summary of damage and the site of investigations. Even if the geological condition of the site from A to K seems to be almost identical, foundation damage by liquefaction at the site from E to J was significant whereas site A and B had no damage. Elevation is highest at the site A and B and lowest at the site from I to K. Elevation difference between the site B and J is about 4m and it implies that the groundwater level is not constant through the site. It seems that the difference of groundwater level caused the difference of damage associated with liquefaction. Therefore, we have carried out a surface-wave method and a refraction method in order to compare the subsurface condition. A standard penetrating test (SPT), a Swedish weighted sounding test (SWS), a Swedish ram

sounding test (SRS) and a three components corn penetrating test (CPT) were also carried out in order to obtain detailed geo-technical parameters.

2) Result of Seismic Methods

Figure 5.5.3 shows waveform data (vertical velocity) obtained through seismic investigations performed at the site B and J. A 10kg sledge hammer was used as source and 4.5Hz geophones (vertical component) were used as receivers. Twenty-four geophones were deployed with 1m intervals. Whole waveforms are shown on top and first arrivals are enlarged on bottom. Large amplitude after waves in whole waveforms correspond to surface-waves. Shear-wave velocity models were obtained by a phase-velocity analysis of the surface-waves. P-wave velocity models were obtained by a traveltime analysis using first arrivals picked from same waveform data.

As shown in the Figure 5.5.3 (bottom), the apparent velocity of refracted arrivals are approximately 1500m/s and it seems to be refraction from a groundwater table. Figure 5.5.4 shows the traveltime curves for the site B and J. We can see that the traveltime curves have clear difference between two sites. A time-term linear inversion was applied to the traveltime data with the assumption of a two-layer model. Table 1 shows the average thickness of the first layer and the P-wave velocity of the second layer obtained through the refraction method. The P-wave velocity of the second layer is about 1300m/s at the site B and 1600m/s at the site J. Therefore, the second layer can be considered as a groundwater table. Groundwater levels are monitored by wells at the investigation site. Table 5.5.1 also shows groundwater level obtained through the monitoring wells.

Table 5.5.1. Result of the seismic refraction method

	Average 1st layer thickness (m)	2nd layer P-wave velocity (m/s)	Groundwater level of monitoring well (m)
Site B	2.2	1263	1.7
Site J	1.2	1578	0.4

Even if groundwater level obtained through the refraction analysis is slightly deeper compared with one obtained by monitoring wells, it can be reasonably concluded

that groundwater level obtained by the refraction method almost agrees with one of the monitoring wells. Therefore, we can say that the groundwater level that is important in the liquefaction potential analysis can be obtained by the refraction method.

A CMP cross-correlation analysis (Hayashi and Suzuki, 2004) and the multi-channel analysis of surface-waves (Park et al., 1999) were employed for the surface-wave analysis. The CMP cross-correlation analysis was employed so that horizontal heterogeneity can be obtained even if a survey line is short. Figure 5 shows the P-wave velocity and S-wave (shear wave) velocity models for the site B and J obtained through the seismic refraction analysis and the surface-wave method respectively. N-value (blow counts) obtained through the standard penetrating test (SPT) at the site J is also shown in Figure 5.5.5. Soil type of the site is fine sand down to the depth of 10m. Both the site B and J, underground structure is almost flat and result of the analysis can be summarized as follows. From the surface to the depth of 4m, N-value is 10 to 15 and shear-wave velocity is 100 to 150m/s and soil condition seems to be loose with small N-value and slow shear-wave velocity. Deeper than the depth of 4m, N-value is 18 to 36 and shear-wave velocity is 150 to 220m/s and soil condition seems to be relatively stiff. Figure 6 shows shear-wave velocity models (middle of survey line) obtained through the surface-wave method and groundwater level obtained through monitoring wells. Groundwater level is extremely shallow with 0.4m at the site J whereas it is relatively deep with 1.7m at the site B. Shear-wave velocity of the site B is relatively higher than that of the site J in the depth region shallower than 3m.

3) Liquefaction potential analysis in Kariwa Village

In the analysis, the cyclic resistance ratio (CRR) and the cyclic stress ratio (CSR) are calculated as mentioned above. It is considered that liquefaction will be occurred if the ratio of CRR and CSR (Fs) is smaller than 1. In this study, the moment magnitude (Mw) of 6.8 and the peak horizontal ground surface acceleration (a_{max}) of 150gal are used in calculation. The a_{max} is assumed by actual ground motion recorded at a strong ground motion observation station around the investigation site. As the limiting upper shear-wave velocity c, 215m/s suggested by Andrus et al., (1999) is used.

Figure 5.5.7 shows the cyclic resistance ratio (CRR) and the cyclic stress ratio

(CSR) obtained through the liquefaction potential analysis (middle of survey line) for the site B and J. Figure 5.5.8 shows the factor of safety (Fs) models calculated from the CRR and the CSR for the site B and J. At the site B, the thickness of a layer in which Fs is lower than 1 is about 2m, with the depth from 2.5m to 4.5m. At the site J, however, thickness of a layer in which Fs is lower than 1 is about 3.5m, with the depth from 1.0 m to 4.5m. The result agrees with actual damage that the site J has significant damage whereas the site B has no damage. At the site B, shear-wave velocity in the shallow depth is higher than the site-J. It seems that the shear-wave velocity becomes slow by decrease of effective stress below the water table at the site J. Therefore, we can conclude that the difference of the groundwater level mainly caused the difference of damage.

5.5.4 Investigation in Mitsuke City

In order to investigate the relationship between S-wave velocity and land condition, a surface-wave method was performed in old river channel and on old river bank. Figure 5.5.9 shows the location of investigations. Site-A is placed in the old river channel and liquefaction occurred around the site. Site-B is placed on the old river bank and liquefaction did not occurred. Figure5.5.10 shows the result of a surface-wave method at the site-A and -B. S-wave velocity at the site-B is much higher than that of site-A. Figure 5.5.11 shows the result of a liquefaction potential analysis at the site-A. Ground water level was estimated by a seismic refraction analysis applied to waveform data obtained through the surface-wave method. Liquefaction potential at the site-A is high below ground water level and it agrees with that liquefaction occurred at the site. S-wave velocity at the site-B is too high to apply the liquefaction potential analysis. Generally speaking, liquefaction potential is very low at the site where S-wave velocity is higher than 200m/s and it agrees with that liquefaction did not occurred at the site-B.

5.5.5 Investigation in Various Sites and Earthquakes

Similar comparative studies have been carried out various sites liquefied by

various earthquakes in order to evaluate the applicability of empirical equation presented by Andrus et al.(1999). Table 5.5.2 summarizes investigation sites and earthquakes in Japan.

Table 5.5.2 Investigation sites and earthquakes.

Site	Earthquake	Magnitude	Maximum acceleration at ground surface (a_{max})	Ground motion record
Mitsuku, Miigata	2004 Mid-Niigata Prefecture earthquake	6.8	300gal	No record
Niigata, Niigata	2004 Mid-Niigata Prefecture earthquake	6.8	104gal	K-NET Niigata
	1964 Miigata Earthquake	7.5	150gal	Record at Kawagishi
Yonago, Tottori	2001 West-Tottori Prefecture Earthquake	7.3	249gal	K-NET Mihoseki
Ashiya, Hyogo	1996 South-Hyogo Prefectur Earthquake	7.2	426gal	Record at reclaimed land
Kariwa,Niigata	2004 Mid-Niigata Prefecture earthquake	6.8	150gal	K-NET Kashiwazaki
	2007 Mid-Niigata-off Prefecture earthquake	6.8	667gal	K-NET Kashiwazaki
Kashiwazaki, Niigata (Hashiba and Matsunami)	2004 Mid-Niigata Prefecture earthquake	6.8	150gal	K-NET Kashiwazaki
	2007 Mid-Niigata-off Prefecture earthquake	6.8	667gal	K-NET Kashiwazaki

Figure 5.5.12 summarizes the result of comparative study. Horizontal axis indicates stress-corrected S-wave velocity at the depth of 5m in each site and vertical axis indicates cyclic stress ratio. Solid symbols indicate sites damaged by liquefaction and light symbols indicates site without damage. Solid line indicates the empirical equation proposed by Andrus et al.(1999). We can say that the most of damaged sites are placed above the line and the most of sites without damage are placed below the line. We can recognize from Figure 5.5.12 that liquefaction potential analysis in terms of S-wave velocity obtained through surface-wave methods and empirical equation proposed by Andrus et al.(1999) can be applied to general liquefaction potential

evaluation in Japan.

5.5.6 Conclusions

The surface-wave method and the seismic refraction method can be carried out from ground surface nondestructively. Shear-wave velocity that can be obtained by the surface-wave method, and groundwater level that can be obtained by the seismic refraction method, are important factor in the liquefaction potential evaluation. We have applied the seismic investigations to various liquefied site. The result of the analysis agrees with actual damage and it implies that geophysical methods enable us to evaluate the liquefaction potential from the surface nondestructively.

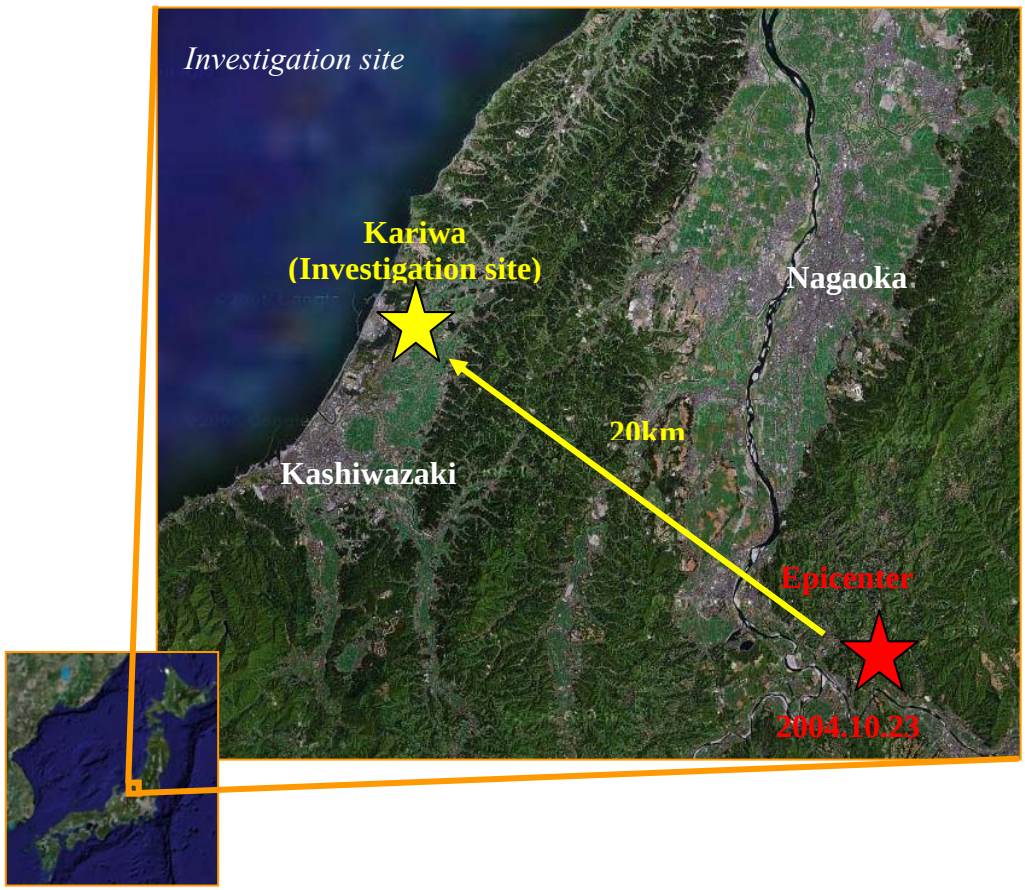

Figure 5.5.1. Investigation site and the epicenter of the Mid Niigata Prefecture Earthquake.

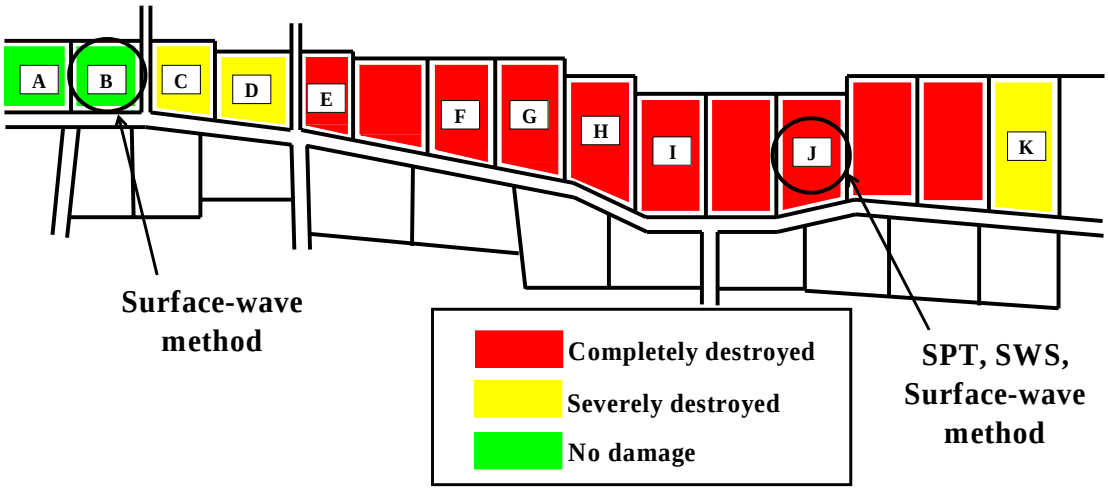

Figure 5.5.2. Summary of damage and site of investigations.

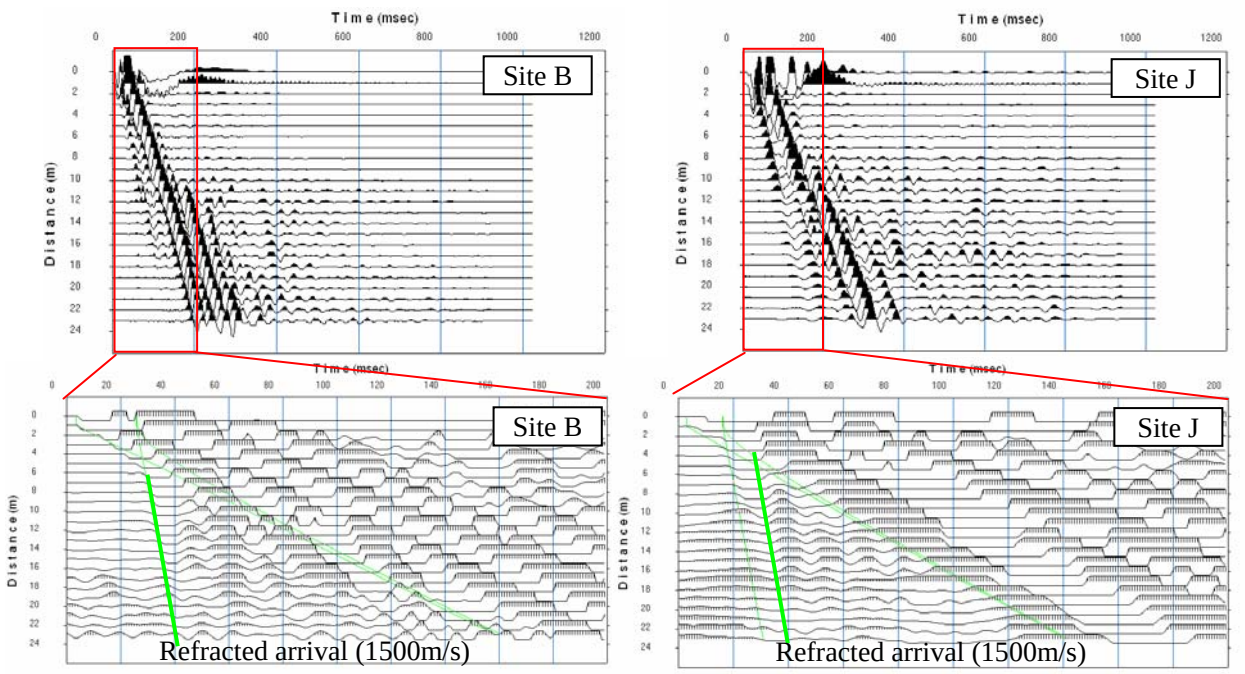

Figure 5.5.3. Waveform data obtained through seismic investigations.
(left : site B, right : site J, top : whole waveforms, bottom : first arrival)

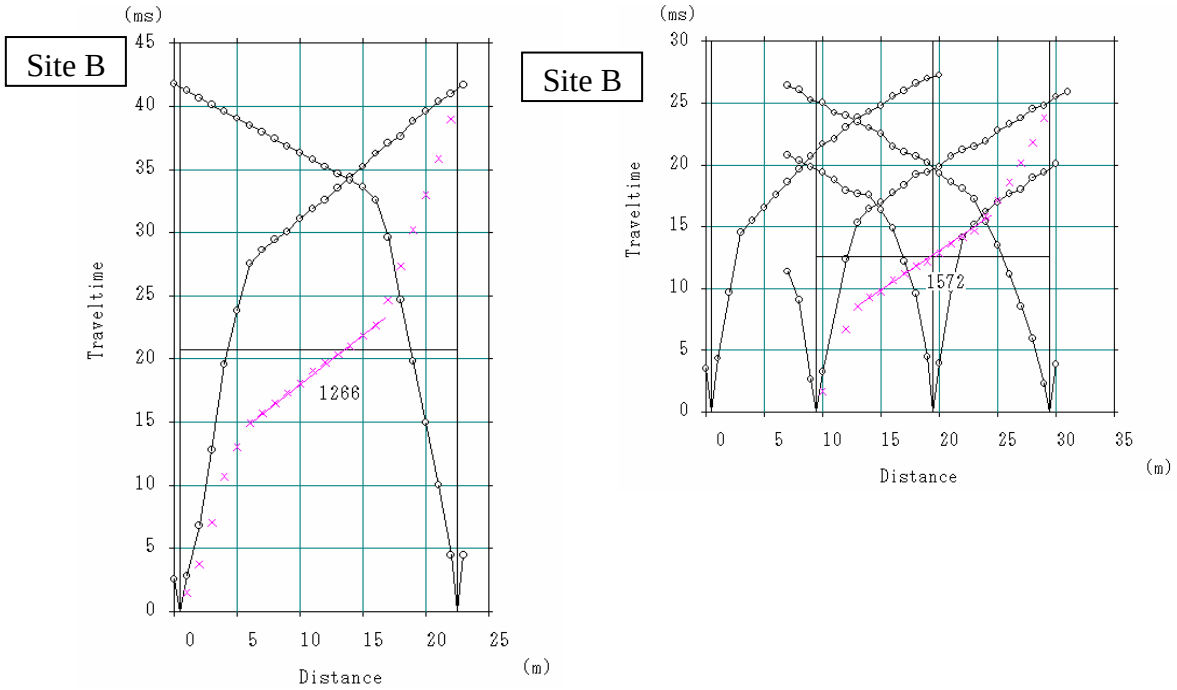

Figure 5.5.4. Traveltime curves for the site B (left) and J (right).

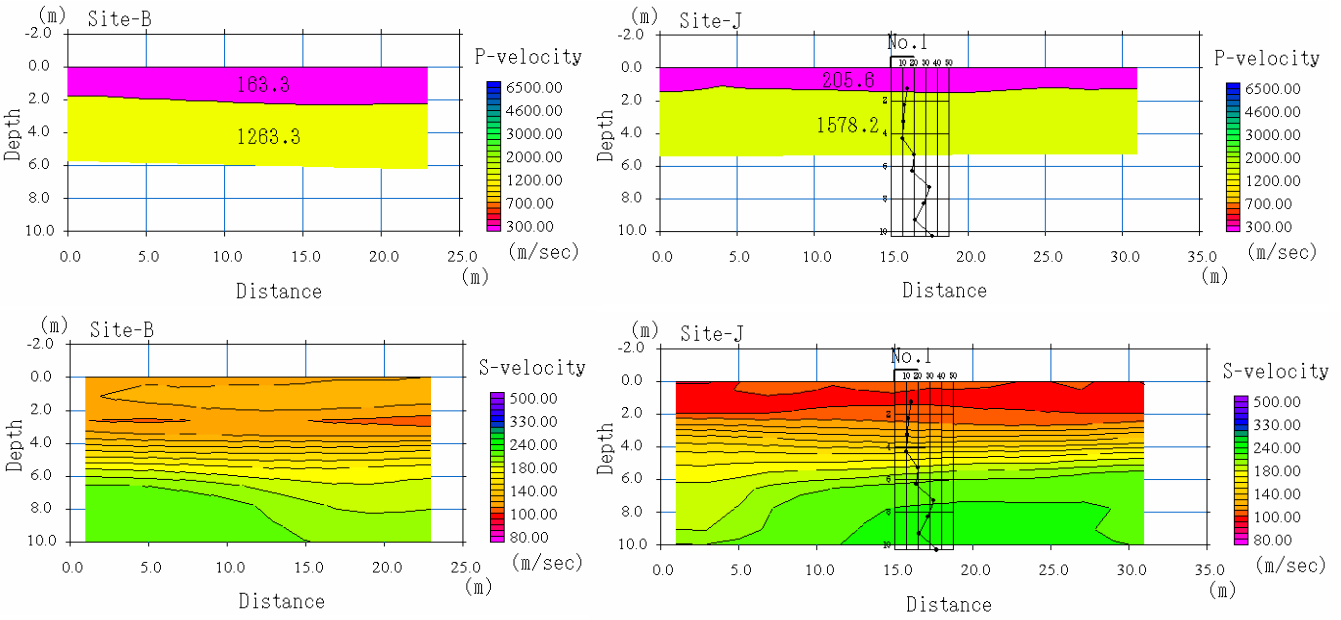

Figure 5.5.5. P-wave (top) and S-wave velocity (bottom) models for the site B (left) and J (right) obtained through the seismic refraction analysis and the surface-wave method respectively. N-value (blow counts) obtained through the standard penetrating test (SPT) at the site J is also shown.

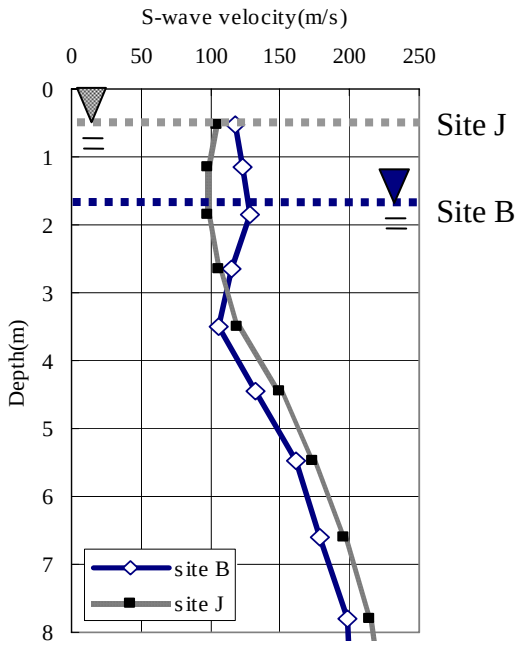

Figure 5.5.6. Shear-wave velocity models (middle of survey line) obtained through the surface-wave method and groundwater level obtained through monitoring wells.

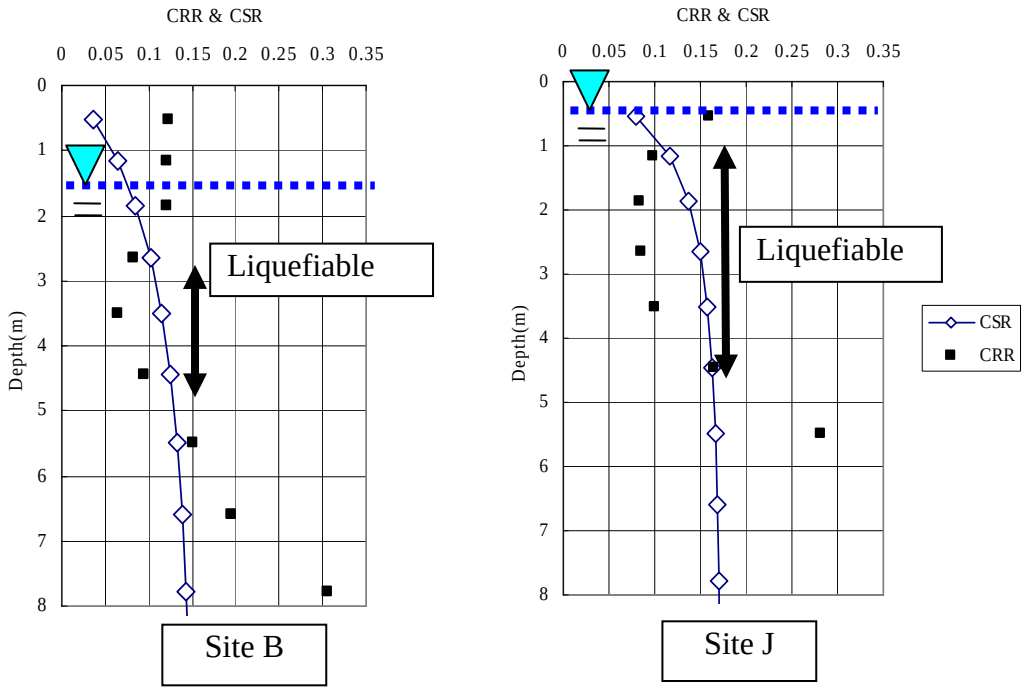

Figure 5.5.7. Cyclic resistance ratio (CRR) and cyclic stress ratio (CSR) obtained through the liquefaction potential analysis (middle of survey line) for the site B (left) and J (right).

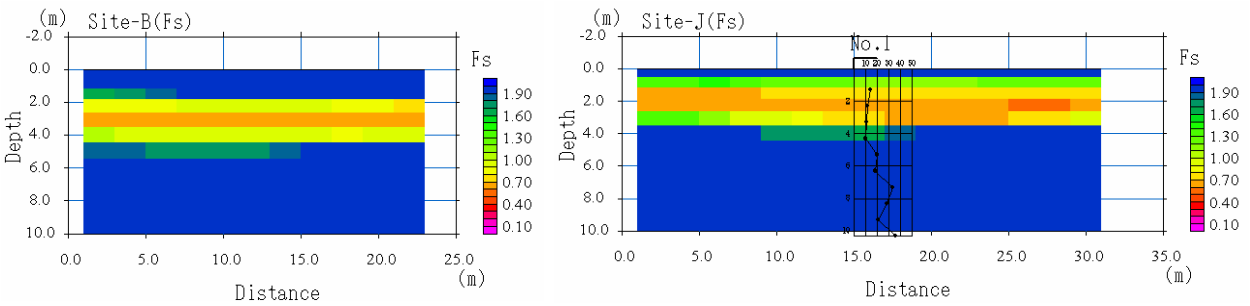

Figure 5.5.8. Factor of safety (Fs) models calculated from the CRR and the CSR for the site B (left) and J (right).

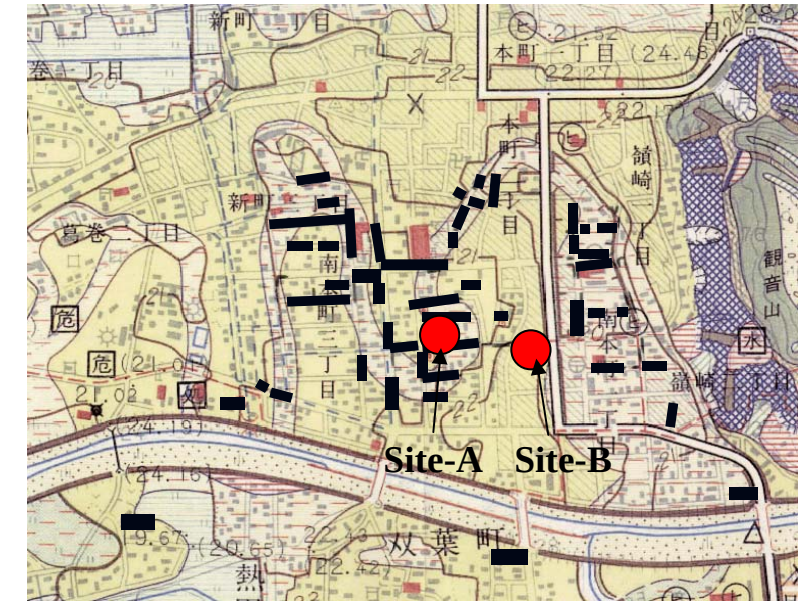

Figure 5.5.9. The Land condition map and the location of investigations in Mitsuke-shi.

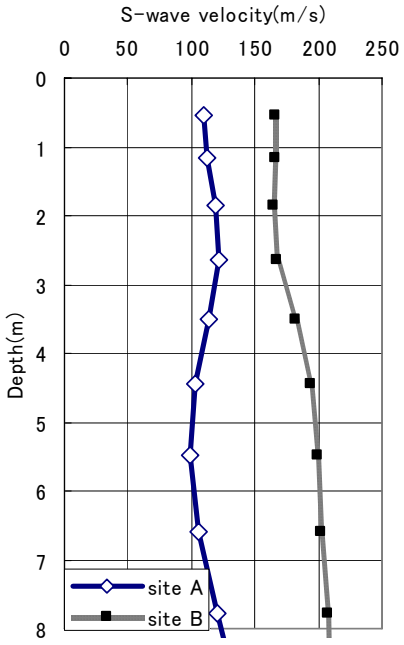

Fig.5.5.10. Result of a surface-wave method at the site A and B.

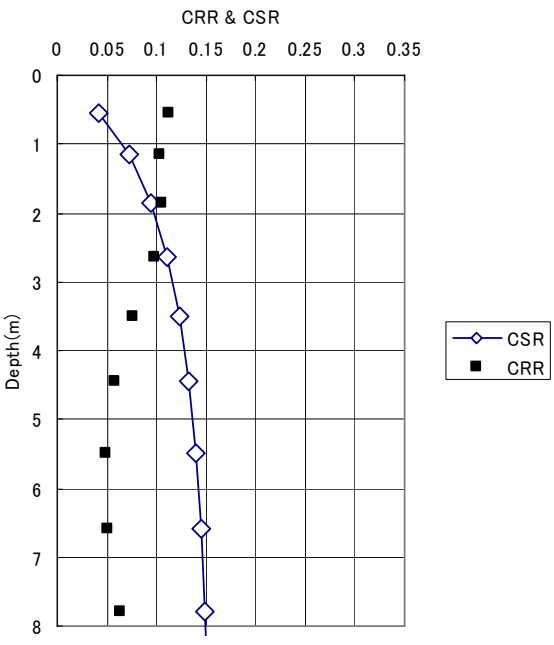

Fig.5.5.11. Result of a liquefaction potential analysis at the site-A based on S-wave velocity.

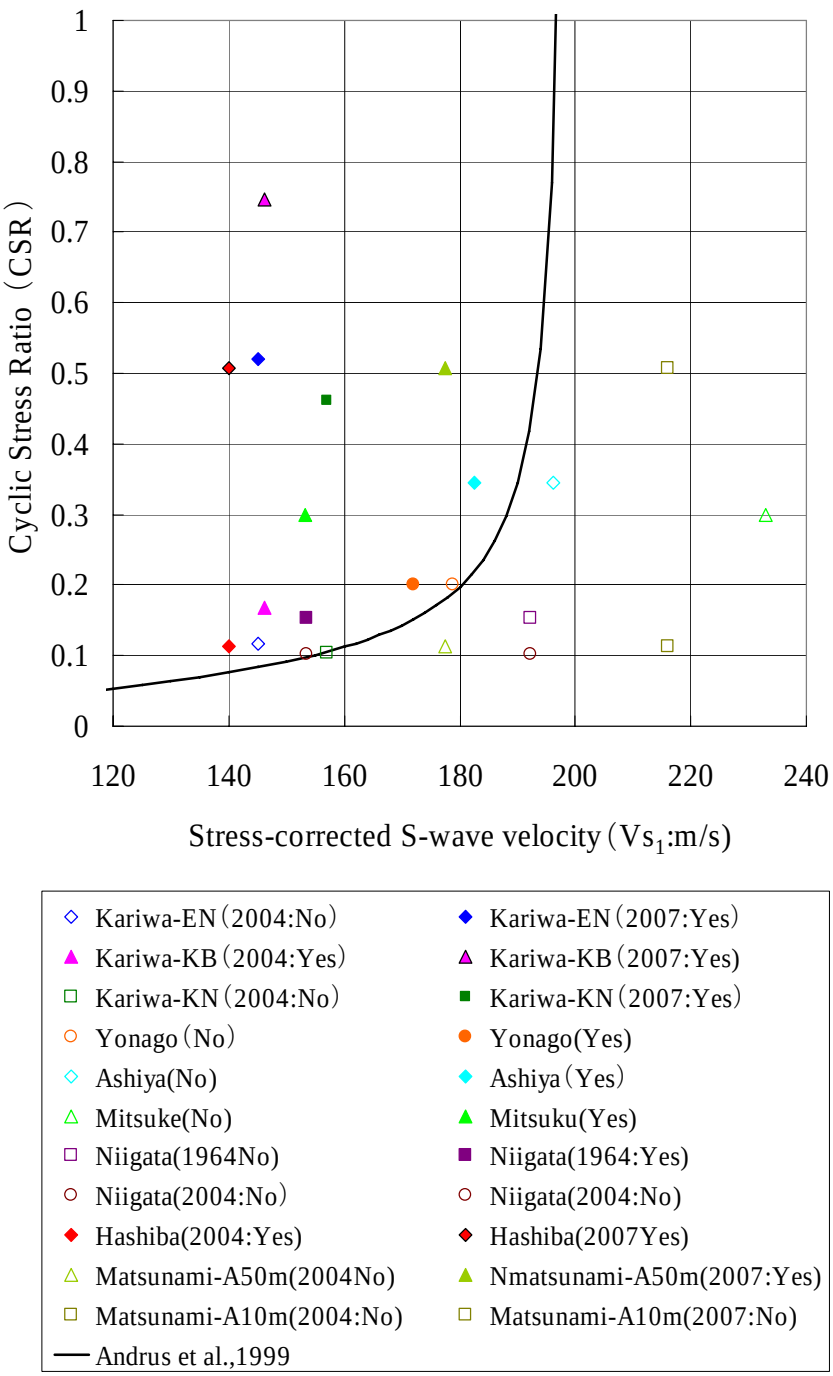

Figure 5.5.12 result of comparative study.

5.6 Application to Levee Inspections

5.6.1 Land Streamer for Surface-wave Method

In seismic reflection methods, so called land streamer, in which all geophones are connected to the belts or wires and can be towed on paved ground surface, was proposed (Van der Veen and Green, 1998; Inazaki, 1999) and has been applied to many civil engineering investigations. The surface-wave methods mainly use relatively low frequency waves compare with the reflection methods. It implies that the geophone coupling is not crucial and the land streamed can be easily used in the surface-wave method. We have developed a new land streamer for the surface-wave method and applied it to many civil engineering problems. In those investigations, we have evaluated the applicability of the land streamer to the surface-wave method.

Our land streamer mainly consists of base plates and two ropes. Figure 5.6.1 shows a land streamer for the surface-wave method. Ordinal 4.5Hz vertical geophones and spread cables are used in order to reduce additional cost associate with making the land streamer. The base plates of geophones are simply clamped with polyester ropes so that geophone interval can be changed easily. In typical surface-wave survey, 24 geophones are clamped to ropes with 1 to 2m intervals. A 10kg sledgehammer or 50kg weight drops are used as sources. The sources are placed with 2 to 4m intervals. Total weight of the land streamer including geophones and spread cables is about 40kg and one person can easily tow the land streamer.

We have performed a comparative test on the paved surface in order to evaluate the applicability of the land streamer to the surface-wave method. Surface-wave data obtained through the land streamer was compared with the data obtained through same geophones placed on the paved surface with clay pads. Data acquisition was performed on a paved road at the top of a levee in Japan. Twenty-four geophones were deployed with 1m intervals. A 10kg sledgehammer was used as a source. Figure 5.6.2 shows waveform data and its power spectrum. We can see almost same waveform data was obtained in both time and frequency domain. Figure 5.6.3 shows phase-velocity image in frequency domain and dispersion curves calculated from the waveform data

shown in Figure 5.6.2. The dispersion curves were determined from the maximum amplitude at each frequency. It is obvious that almost same phase-velocity was obtained except frequencies lower than 15Hz where phase-velocity was not clear. We can recognize from these results that the land streamer can provide surface-wave data equal to those obtained traditional geophones with clay pads on paved surface. Using the land streamer on paved surface, 500 to 800m of surface-wave data with 2m shot intervals can be obtained in a day. Data acquisition using the land streamer is two times faster than those using traditional geophones with clay pads.

5.6.2 Application to Levee Inspections

In order to evaluate the quality of levees along rivers, N-value obtained from a standard penetrating test (SPT) has been used for many years in Japan. However, SPT was performed only 200m to 1km intervals along river and continuous information can not be obtained from it. Geophysical methods, such as resistivity methods and surface-wave methods can provide continuous soil information of the levees. We have applied such geophysical methods to levee inspections and evaluated the applicability of the methods. The surface-wave method has been applied to several levees along long rivers in Japan. In this Chapter, we are going to introduce the application of the surface-wave method to a levee inspection in Kyushu Island in Japan (Okada et al., 2003).

Total survey-line length is 26km and the land-streamer could obtain surface-wave data 500 to 1000m in a day with 1m receiver intervals and 2m shot intervals. Figure 5.6.4 shows the example of surface-wave data and its phase-velocity image in frequency domain. CMPCC analysis (Hayashi and Suzuki, 2004) was applied to shot gathers and MASW analysis (Park et al., 1999) was applied to CMPCC gathers in order to obtain dispersion curves along the survey line. Figure 5.6.5 shows the example of survey result. N-value curves obtained from SPT are superimposed. We can see that the S-wave velocity models agree with SPT very well.

There were 46 boreholes along the 26km levee. From the S-wave velocity model obtained through the surface-wave method and N-value curves obtained through

SPT performed at boreholes, average S-wave velocity and average N-value of levee body are evaluated. Average height of the levee is about 5m and S-wave velocity and N-value down to the depth of 5m were averaged. Figure 5.6.6 shows the correlation between S-wave velocity and N-value. It is clear that there is good correlation between S-wave velocity and N-value. From this correlation, we derived the relationship between S-wave velocity (Vs) and N-value (N) as following equation.

$$Vs(m/s) = 115N^{0.314} \tag{5.6.1}$$

Using this equation, we can estimate continuous N-value model of the levee from S-wave velocity model obtained from the surface-wave method. Quality of levee can be continuously evaluated using N-value converted from S-wave velocity.

Figure 5.6.1 Land streamer for a surface-wave method.

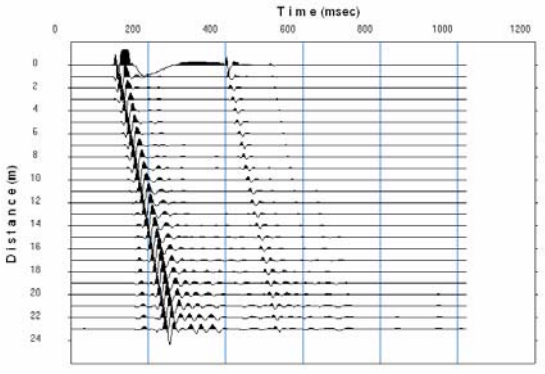

Geophones with clay pads

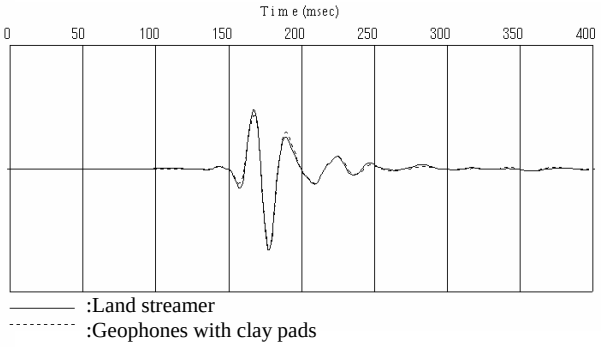

Waveform data at the distance of 10m

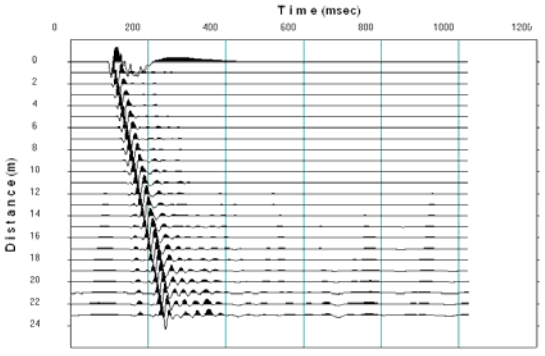

Land streamer

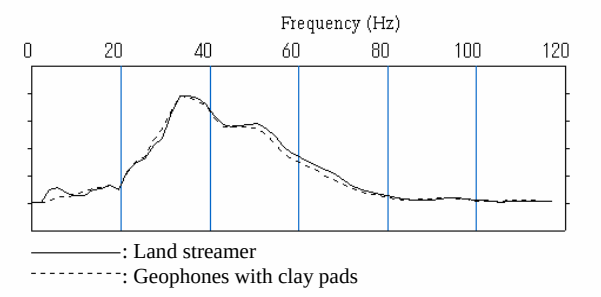

Power spectrum at the distance of 10m

Figure 5.6.2 Comparison of common shot gathers obtained on a paved road at the top of a levee.

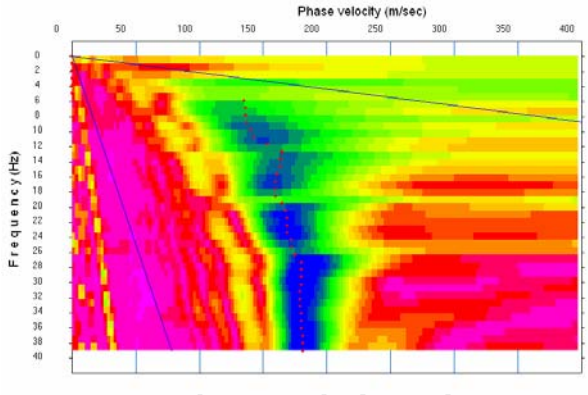

Geophones with clay pads

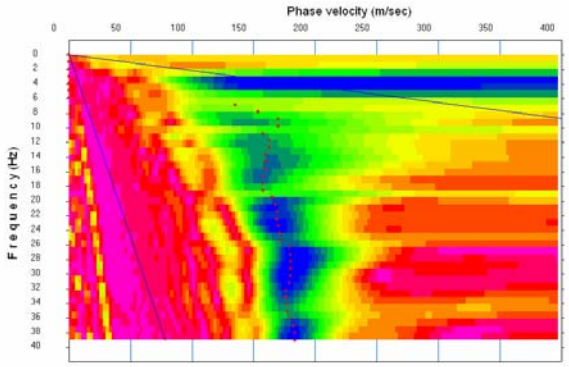

Land streamer

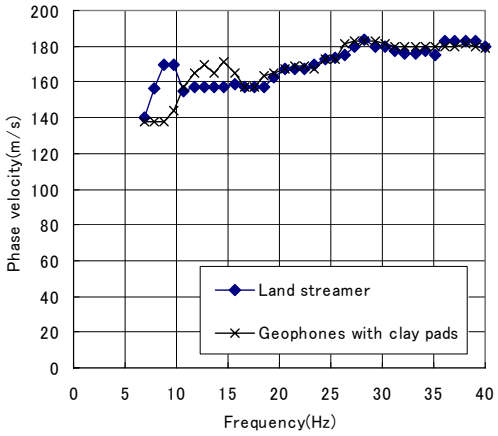

Figure 5.6.3 Comparison of phase-velocity image (left) and dispersion curves (right).

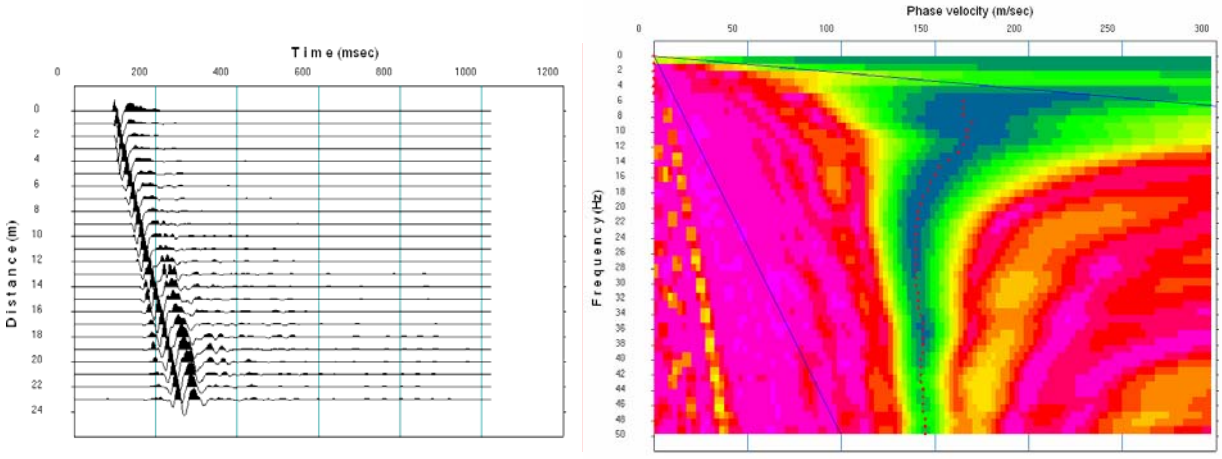

Figure 5.6.4 Example of waveform data (left) and its phase-velocity image in frequency domain (right).

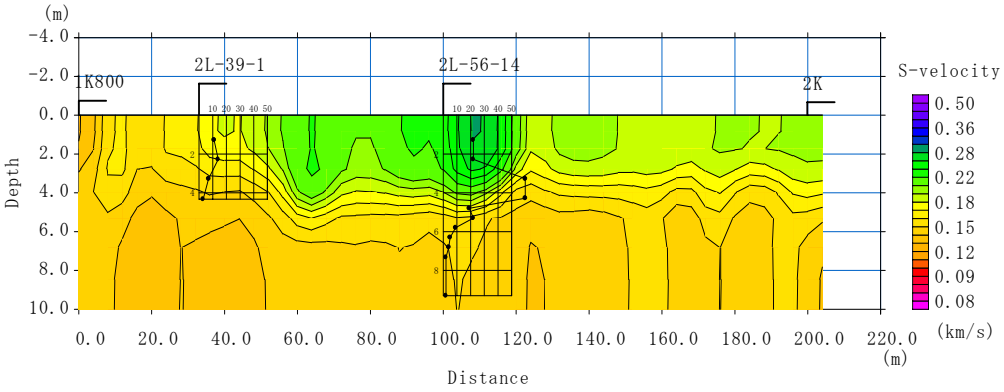

S-wave velocity model 1.8 to 2.0km from the mouth of the river.

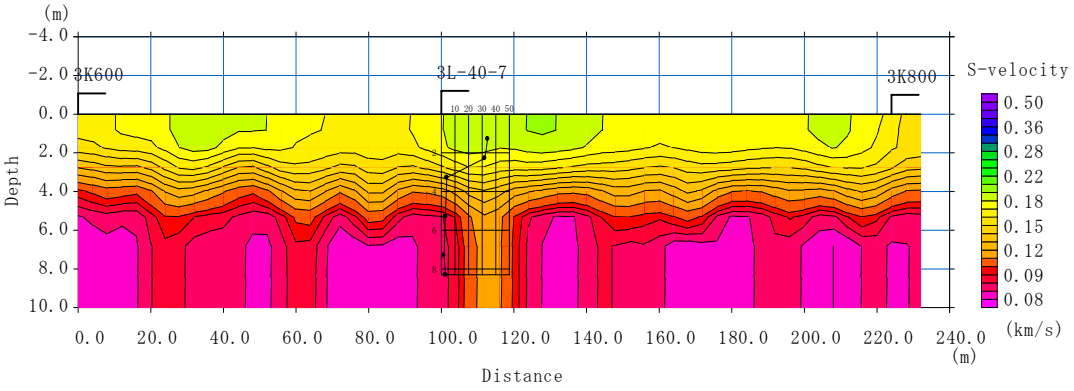

S-wave velocity model 3.6 to 3.8km from the mouth of the river.

Figure 5.6.5 Example of analysis result in levee inspection using surface-wave method.

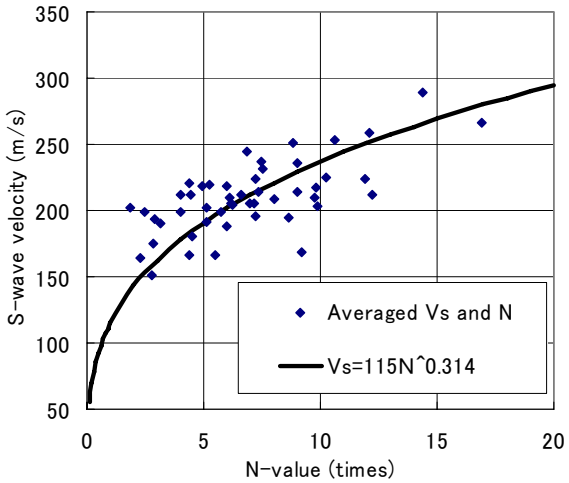

Figure 5.6.6 Correlation between S-wave velocity and N-value in levee body.

5.7 Application to Tidal Flat Investigations

In recent years, natural environmental protection of a tidal flat or their revitalization attract much interest. Over the past few years, a considerable number of studies have been made on the ecosystem and hydrological environment of tidal flat in terms of such environmental protection or revitalization. In addition to that, geo-environmental studies have been also made in order to understand the dynamics of the tidal flat in terms of soil structure (Watabe and Sassa, 2005; Sassa and Watabe, 2005). It is hoped that geophysical and geotechnical investigation technique play important rolls in such geo-environmental investigations. Geophysical and geotechnical investigation methods for tidal flat have to satisfy following issues;

1) It does not destruct natural environment.
2) It can investigate wide area in short time.
3) It can investigate not only the ground surface but also down to the depth of several meters.
4) It can be performed on the very soft ground surface soaked with seawater.

Considering those issues, we have applied the surface wave method using the land streamer to the geo-environmental investigation of tidal flat. In order to evaluate the applicability of the method, we have performed the surface-wave method at several tidal flats in Japan. In this Chapter, we are going to introduce the investigation at a sandy tidal flat as an example (Hayashi et al., 2005b).

The investigation was performed in the sandy tidal flat in Chiba prefecture, Japan. A survey line was almost perpendicular to a shoreline and length of the line was 1130m. Twenty-four geophones were clamped to a land streamer with 1m intervals and shots were placed with 2m intervals. A 10kg sledgehammer was used as a source (Figure 5.7.1). Figure 5.7.2 and 5.7.3 shows the examples of waveform data and their phase-velocity images in frequency domain. Figure 5.7.2 shows the data obtained around the mouth of the river where 50m away from a shoreline. Figure 5.7.3 shows the data obtained at offing where 800m away from the shoreline. We can see that later

arrival that mainly consists of Rayleigh waves is clear in time domain. Dispersion curves varying from 300m/s to 60m/s between 10Hz to 50Hz are also obvious in frequency domain. In both time domain and frequency domain, Figure 5.7.2 and 5.7.3 show clear difference. It implies that S-wave velocity structure laterally changes along survey line. Figure 5.7.4 shows the comparison of dispersion curves and S-wave velocity models obtained through a non-linear least square inversion. It is clear that the S-wave velocity down to the depth of 10m could be obtained and velocity structure laterally changed along the survey line significantly. The CMPCC analysis was applied to 1131 shot gathers and 282 dispersion curves. The non-linear least square inversion was applied to each dispersion curve and 1D S-wave velocity models were continuously calculated. Resultant 1D S-wave velocity models were shown as a pseudo 2D S-wave velocity image in Figure 5.7.5. A detailed S-wave velocity structure was obtained along the survey line. We can recognize from the result that the surface-wave method provides the detailed S-wave velocity structure of tidal flat even if difficult surface conditions.

Figure 5.7.1. Surface-wave data acquisition using land streamer in tidal flat.

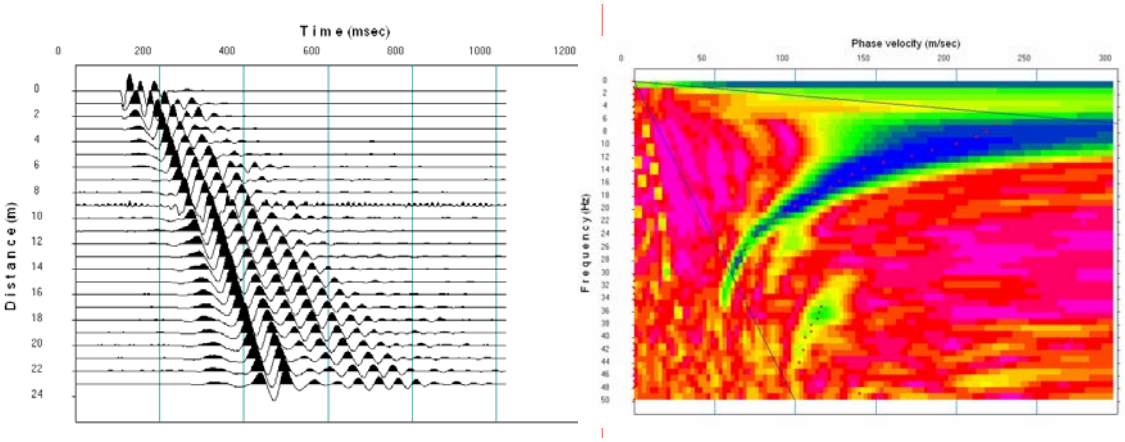

Figure 5.7.2. Example of waveform data (left) and its phase-velocity image (right) obtained around the mouth of the river where 50m away from a shoreline.

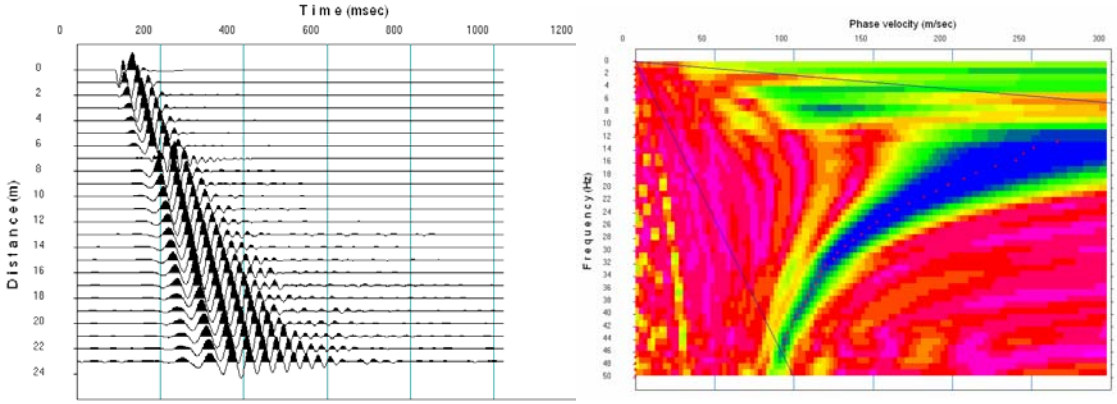

Figure 5.7.3. Example of waveform data (left) and its phase-velocity image (right) obtained at offing where 800m away from a shoreline.

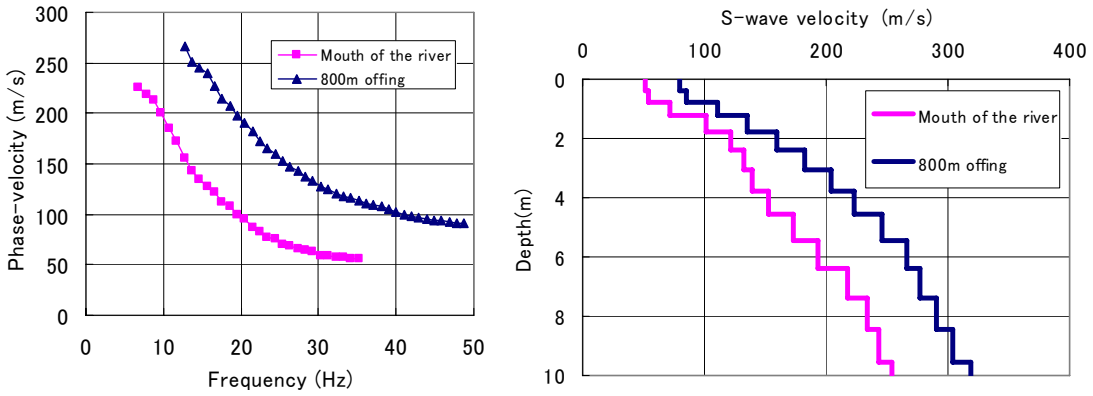

Figure 5.7.4. Comparison of dispersion curves (left) and S-wave velocity models obtained through a non-linear least square method (right).

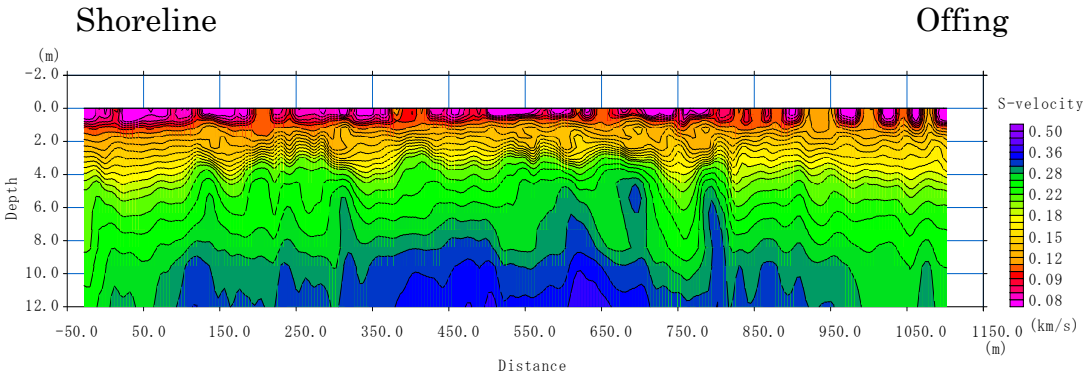

Figure 5.7.5. S-wave velocity model obtained from the surface-wave method (From Watebe et al., 2005).

5.8 Application to Buried Channel Delineation

A passive surface wave method has been applied to delineate buried channels in urban area of Japan (Hayashi et al., 2007). S-wave velocity structure down to 100m is very important in the local site effect of strong ground motion caused by earthquake. Especially, the buried channels filled with alluvial deposits intensify seismic waves and cause strong ground shaking. We have tried to delineate three-dimensional S-wave velocity structure down to 100m on the basis of the passive surface wave method. The test site is in Soka city, Saitama prefecture, Japan and the size of the site is about 6 by 4 km rectangle. One-hundred and four passive surface wave surveys were carried out to delineate buried channels filled with alluvial deposits, which is embedded about 50m beneath surface of this area. Array size is about 50 to 100m and triangular or L shaped arrays with 10 or 11 receivers were deployed. A spatial auto correlation (SPAC) method was applied to the approximately ten minutes vertical component of micro-tremors data. Phase velocity curves were calculated in the frequency range of between 2 and 10 Hz. Fundamental mode of phase-velocity curves are clearly obtained in all observation points. A one dimensional inversion using a non-linear least square method has been applied to the phase-velocity curves and one-dimensional S-wave velocity structures were obtained. The resultant one-dimensional structures were interpolated into a three-dimensional structure. We succeeded to map the shape of buried channel and the depths of the channel agree very well with the borehole data.

5.8.1 Introduction

After the 1995 Hanshin earthquake, Japanese seismology has been greatly developed by a considerable number of studies. It enables us to predict the strong ground motion by future earthquakes with high accuracy. The surface ground motion of natural earthquakes is generally represented as the convolution of three characters, such as 1) source characteristics, 2) propagation path effects and 3) local site effects.
Over the last decade, a large number of studies have been made on the source

characteristics, such as active fault characteristics and rupture processes. Active fault survey has revealed the activity and cycle of each fault. Geophysical exploration methods, such as seismic reflection, and fault trenching have played important roll in such progress. Observed strong ground motion data revealed the rupture process of large earthquakes. A nation-wide network of strong motion seismometers, which is called K-NET and KiK-net has provided valuable observation data to researchers.
The understanding of propagation path effects has also progressed in the last decade. It has been established that the effect of two- or three- dimensional S-wave velocity structure has large effect on the earthquake damage. Three-dimensional P- and S-wave velocity structure of sedimentary basin has been constructed and it has made possible three-dimensional simulation of strong ground motions. The geophysical exploration methods and the network of strong motion seismometers have also played important roll in such progress.

All these things make it clear that the new observation method, such as the geophysical exploration methods and the nation-wide network of seismometers, cause the progress in the source characteristics and the propagation path effects.

However, only few attempts have so far been made at new observation methods for evaluating the local site effects in the last decades. A great deal of effort has been made on the collection of existing borehole data in the local site effects evaluation. What seems to be lacking, however, is the development of new non-destructive observation method for near-surface velocity structures. For example, almost existing borehole data has only blow count (N-value) and no S-wave velocity that is the most important for the local site effects. Considering that the understanding of the source characteristics and the propagation path effects has progressed with new observation data, the understanding of local site effects can also progress with the new observation data in near-surface region. Therefore, we have started the development of new exploration method which can be used for estimating S-wave velocity structures down to the depth of 100m from the surface.

5.8.2 A Passive Surface-wave Method

We have developed a multi-channel and multi-shot surface wave (Rayleigh wave) method using active sources and applied it to engineering and environmental problems such as river banks, reclaimed lands and housing sites (Hayashi and Suzuki, 2004). The investigation depth of the surface wave method is about 10m using a sledge hammer as a source and 20m using a weight drop.

There is fairly general agreement that the S-wave velocity model down to the depth of 30m is important for evaluating the local site effect of strong ground motion. The investigation depth of the surface wave method with active sources is not enough for the local site effect evaluation. Large source power and long survey line are required for increasing investigation depth in the surface wave method. However, the large source power and long survey line decrease convenience of the survey and increase survey cost. Therefore, we started to develop alternative method.

Okada (2003) had developed a large scale passive surface wave method, so called a micro-tremors array measurements, using long period micro-tremors. The penetration depth of the method is from 100m to several kilometers. We have employed the Okada's method and applied it to shallower problems, such as geo-technical, environmental and earthquake engineering. Our depth of interests is from several ten meters to 100m. Henceforth, we use the term "passive surface wave method" to refer to the micro-tremors array measurements for shallower surveys. Unlike the active surface wave methods, the passive method does not need any sources and needs two-dimensional arrays, such as triangles, circles or crosses. Because the sources of the micro-tremors are distributed randomly in space, the micro-tremors do not have any specific propagation directions. Therefore, two dimensional arrays are required for calculating the phase-velocity of micro-tremors.

5.8.3 Outline of Test Site

The test site is in Soka city, Saitama prefecture, Japan. The size of the site is about 6 by 4km rectangle. The site is placed in the Nakagawa Lowland area and topography is almost flat. AIST (National Institute of Advanced Industrial Science and Technology) has collected existing boring data in the site and approximate

geological condition has been already known (Nakanishi et al., 2007). A suspension PS-logging has been carried out in a borehole (GS-SK1) in the test site as well.

Figure 5.8.1 shows the location of boreholes and the depth of alluvium estimated from the borehole data. The test site consists of buried channels and buried terraces. The depth (thickness of alluvium) of channels is about 50m and one of terraces is about 15m. Figure 5.8.1 shows that the Soka Park, placed at the center of the test site, is on the buried terrace. It is clear that a deep buried channel exists in south-east side of the Soka Park. However, the boundary of the channel and the terrace winds unnaturally in south of the park. In east side and north side of the park, the boundary cannot be determined due to the lack of borehole data.

The main purpose of the passive surface wave method is the delineation of buried channels and terraces. Data acquisition was carried out at 104 points in the test site. Figure 5.8.2 shows the location of data acquisition points.

5.8.4 Data Acquisition and Analysis

Geophones that have the natural frequency of 2 Hz are used as receivers and an OYO McSEIS-SXW is used for data acquisition. Triangular arrays are used at 4 points and L-shaped arrays are used at 100 points. L-shape arrays were deployed along road crossings. The triangular arrays consist of 10 receivers and the L-shaped arrays consist of 11 receivers. All receivers are connected to the seismograph through a spread cable. The size of array is 40 to 80m. Figure 5.8.3 shows the receiver arrays used in the passive surface wave method. Sampling time is 2msec and data length is about 10 minutes. It takes about one hour for the data acquisition for one point.

In the phase velocity analysis, SPAC (spatial autocorrelation) method (Okada, 2003) is employed. Okada (2003) shows spatial autocorrelation function $\rho(\omega, r)$ is expressed by Bessel function.

$$\rho(\omega, r) = J_0(\omega r / c(\omega)) \tag{5.8.1}$$

Where, r is the distance between receivers, ω is the frequency, $c(\omega)$ is phase

velocity of micro-tremors, J_0 is the first kind of Bessel function. The phase velocity can be obtained at each frequency using equation (5.8.1). The detail of the spatial autocorrelation (SPAC) method is explained in the Chapter 2. In this survey, phase velocity curves were calculated in the frequency range between 2 and 10 Hz. Figure 5.8.4 shows the phase velocity versus frequency. The residual between the Spatial Autocorrelation function and the Bessel function is plotted in the figure as difference of color. We can see that the fundamental mode of phase velocity curve is clearly obtained. Phase velocity curves can be obtained clearly in all observation points as shown in Figure 5.8.4. A one-dimensional inversion using a non-linear least square method has been applied to the phase velocity curves and one-dimensional S-wave velocity structures down to the depth of 100m were obtained. In the inversion, we used the following relationship between P-wave velocity and S-wave velocity (Kitsunezaki et. al., 1990):

$$Vp = 1.29 + 1.11Vs \tag{5.8.2}$$

where, Vs is S-velocity (km/s), Vp is P-wave velocity (km/s). In order to assume density from S-wave velocity, we refer to the relationship of Ludwig et al. (1970):

$$\rho = 1.2475 + 0.399Vp - 0.026Vp^2 \tag{5.8.3}$$

where, ρ is density (g/cm3). The resultant one-dimensional structures were interpolated into a three-dimensional structure.

5.8.5 Survey Results

Figure 5.8.5 shows the typical phase velocity curves on buried terrace and in buried channel. It is obvious that the phase velocity curves on terrace and in channel have large difference. It implies that the S-wave velocity structures have also large difference between terrace and channel. Figure 5.8.6 shows all 104 dispersion curves obtained through the passive surface-wave methods.

A non-linear least square inversion was applied to each dispersion curve and one-dimensional S-wave velocity models were estimated. Figure 5.8.7 shows the typical S-wave velocity models on buried terrace and in buried channel. Figure 5.8.8 shows the comparison of suspension PS-logging and the passive wave method at the borehole. Although a high velocity layer placed in the depth between 15 and 20m is not clear, the velocity structure obtained through the passive surface wave method agrees with PS-logging very well.

The bottom of alluvial layer is defined at the depth of 50m in the borehole shown in Figure 5.8.8. S-wave velocity from the passive surface wave method at the depth of 50m is about 250m/s. Therefore, we assumed the S-wave velocity of 250m/s is the boundary of alluvium and diluvium. Figure 5.8.9 shows the depth of the S-wave velocity of 250m/s in the three dimensional S-wave velocity model obtained through the passive surface wave method. The map shown in Figure 5.8.9 can be considered as the depth of alluvium bottom obtained through the survey. We can say that the bottom of alluvium obtained through the survey (Figure 5.8.9) agrees with that of borehole data (Figure 5.8.1). From the Figure 5.8.9, it seems reasonable suppose that the boundary of terrace and channel in south side of the Soka Park is straight. The slope of boundary in east and north side of the park is relatively smooth compare with the boundary in south-east side of the park.

5.8.6 Conclusions

We have carried out the passive surface wave method at 104 points in the 6 by 4km rectangle test site in a suburb of Tokyo. The resultant three-dimensional velocity structure clearly shows the shape of buried channels and agrees with the existing borehole data very well. Considering that the demand for the investigation of local site effect is increasing, the passive surface wave method presented here can play important role much more in such situation.

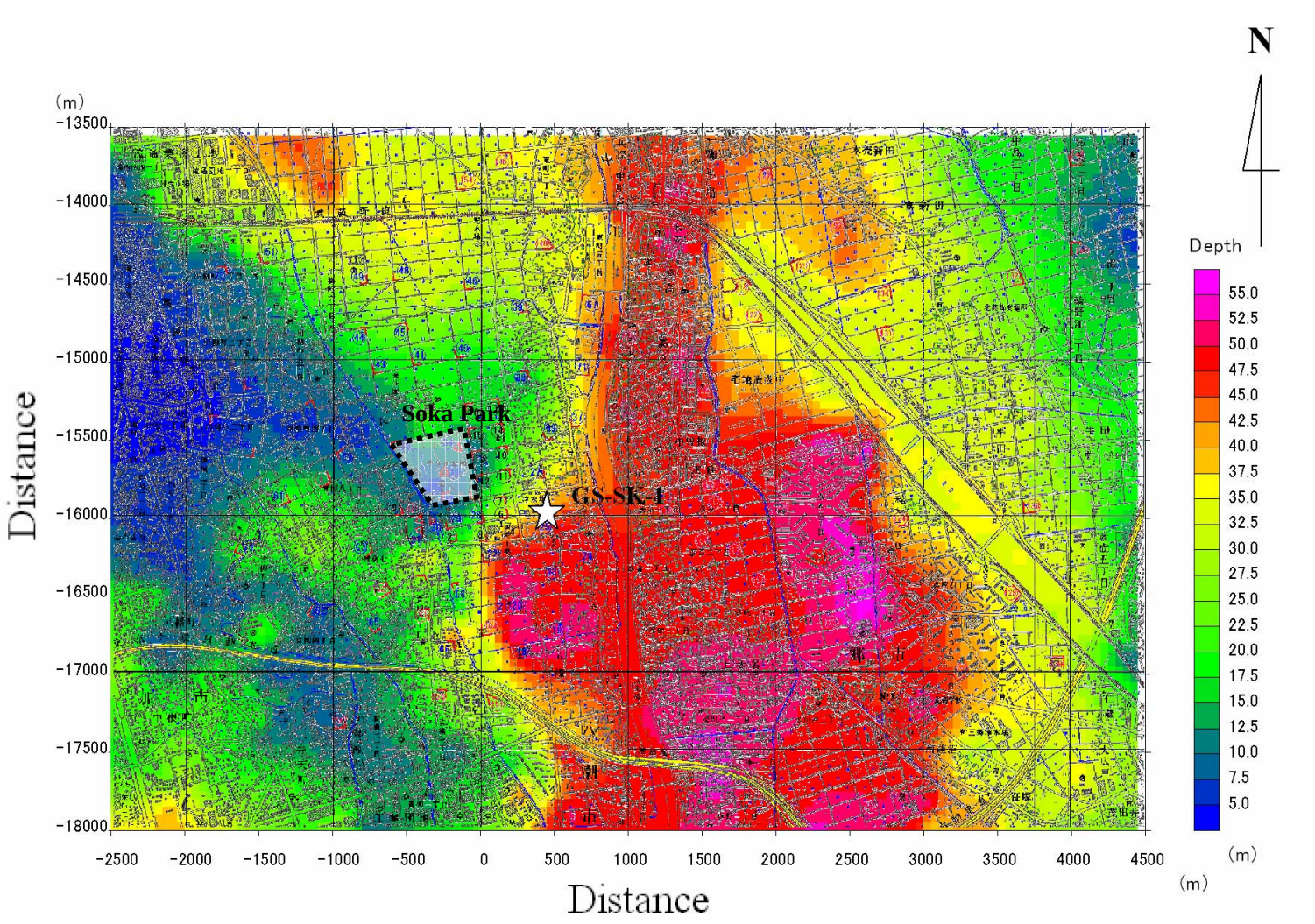

Figure 5.8.1. Location of existing boreholes (white circles) estimated depth of alluvium.

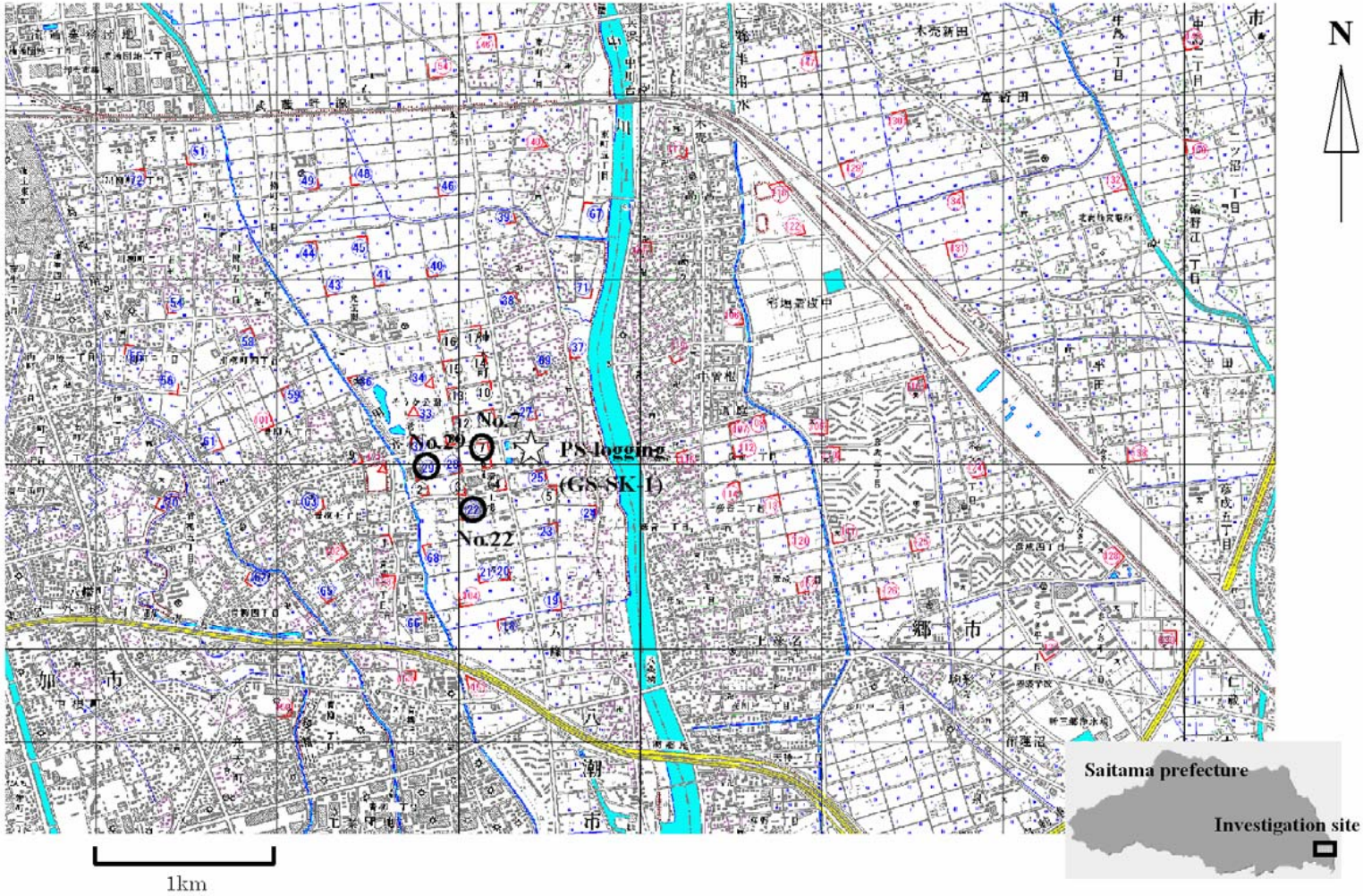

Figure 5.8.2. Data acquisition points. Array geometry is shown as red line at each point.

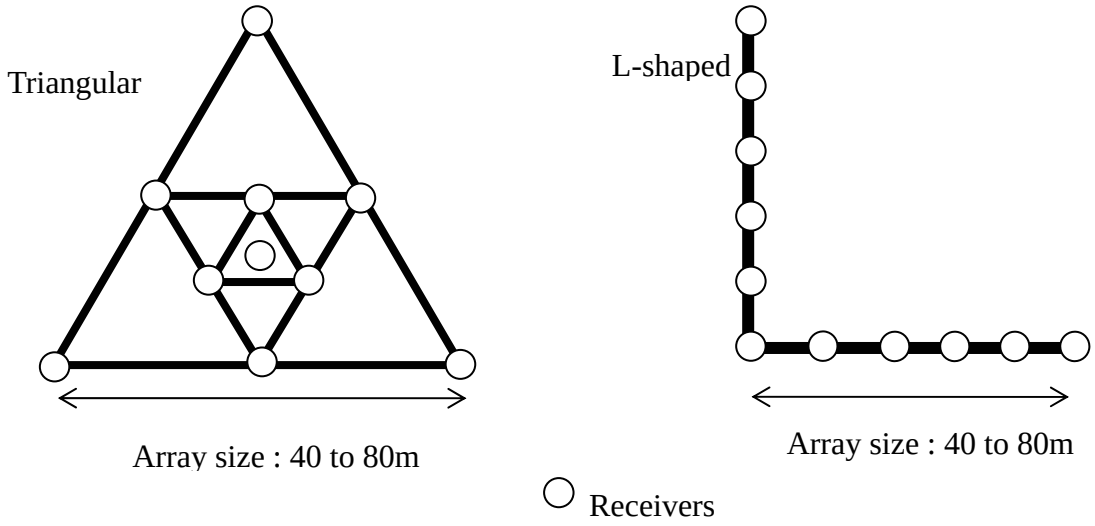

Figure 5.8.3. Receiver arrays used in the passive method.

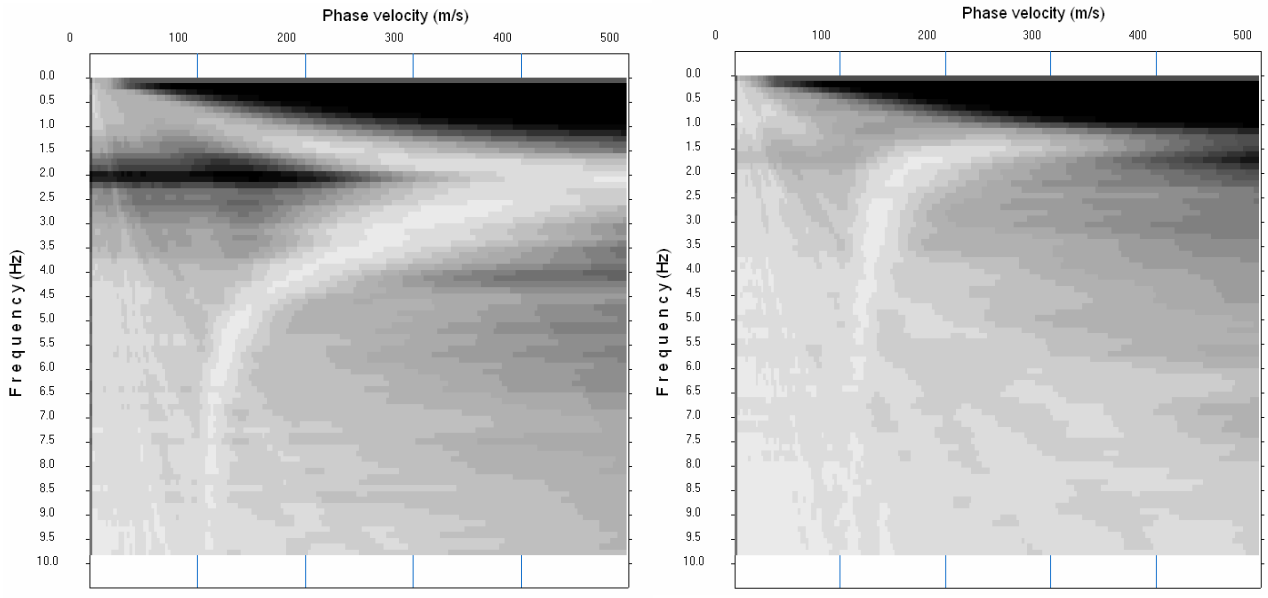

No.29 No.22

Figure 5.8.4. Example of phase velocity versus frequency.

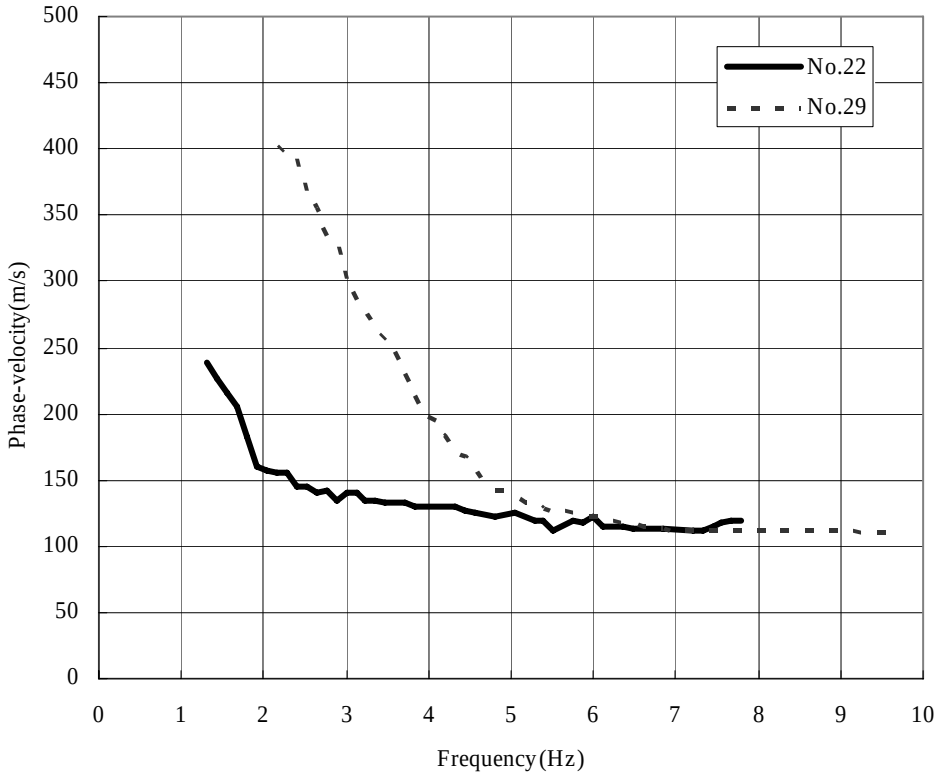

Figure 5.8.5. Phase velocity curves on terrace (No.29) and in channel (no.22).

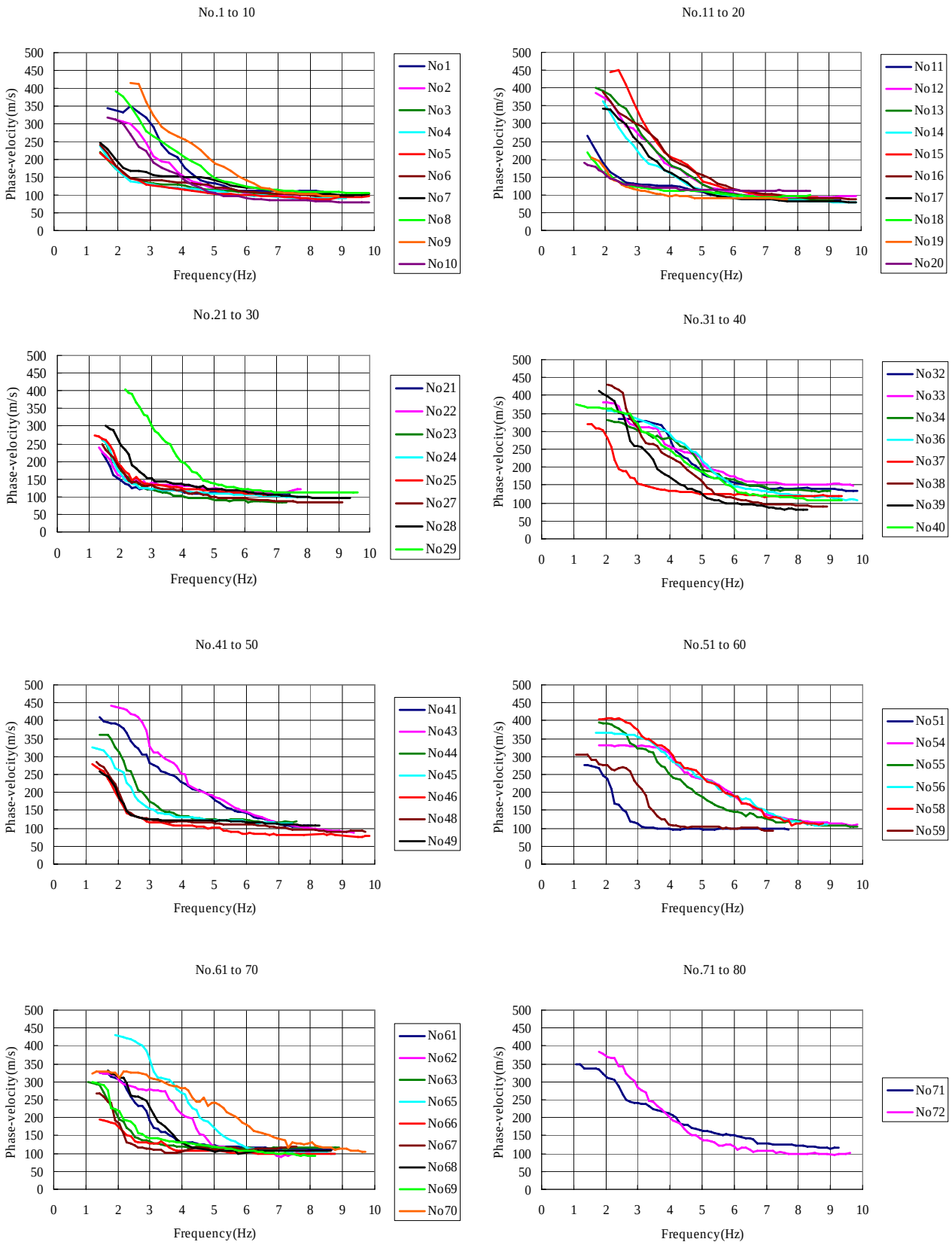

Figure 5.8.6 Dispersion curves for all 104 measurements points.

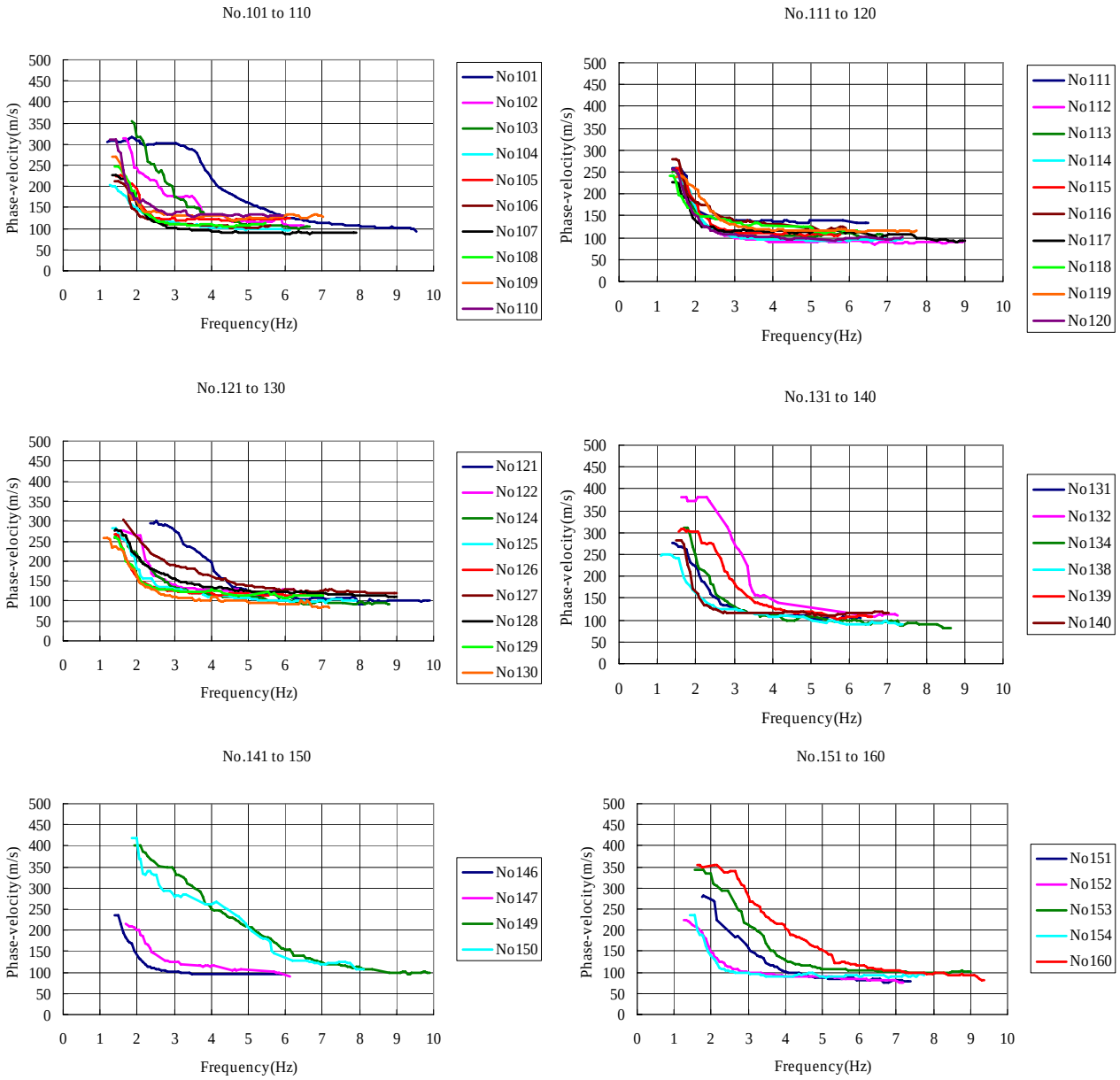

Figure 5.8.6. Continued.

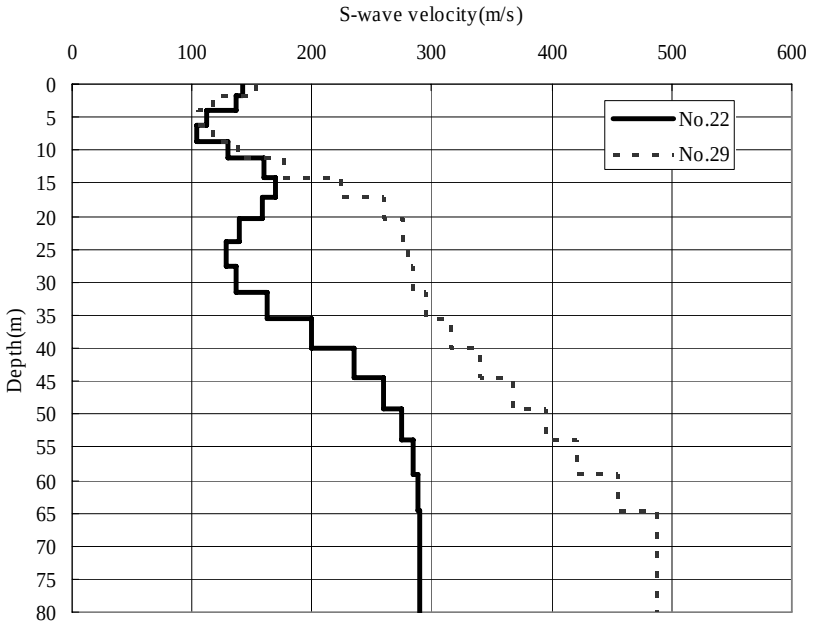

Figure 5.8.7. S-wave velocity models on terrace (No.29) and in channel (no.22).

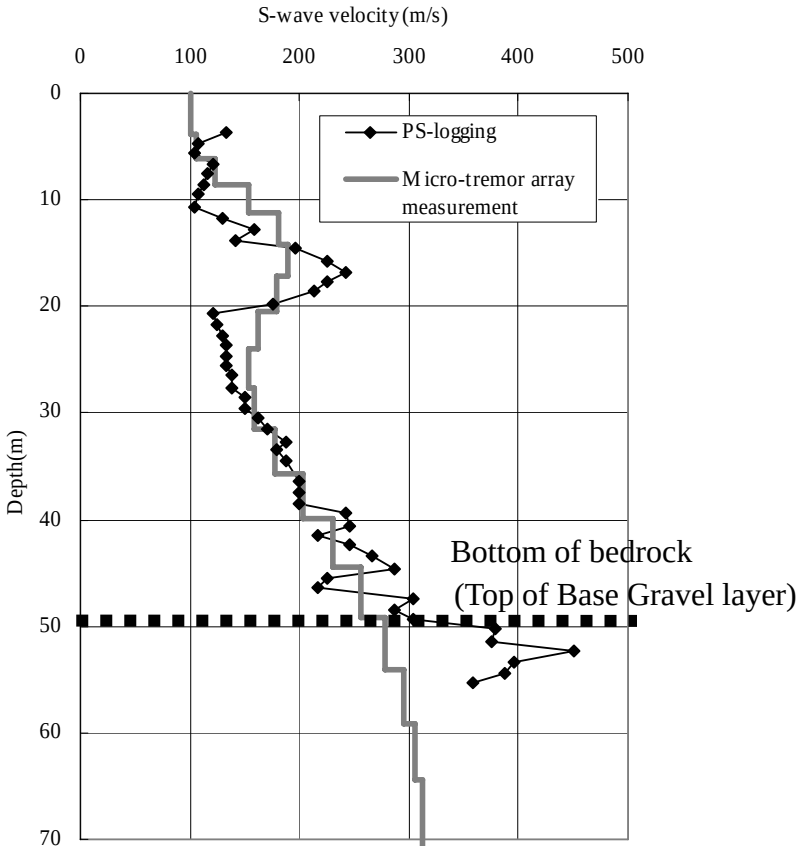

Figure 5.8.8. Comparison of suspension PS-logging and the passive wave method around the borehole.

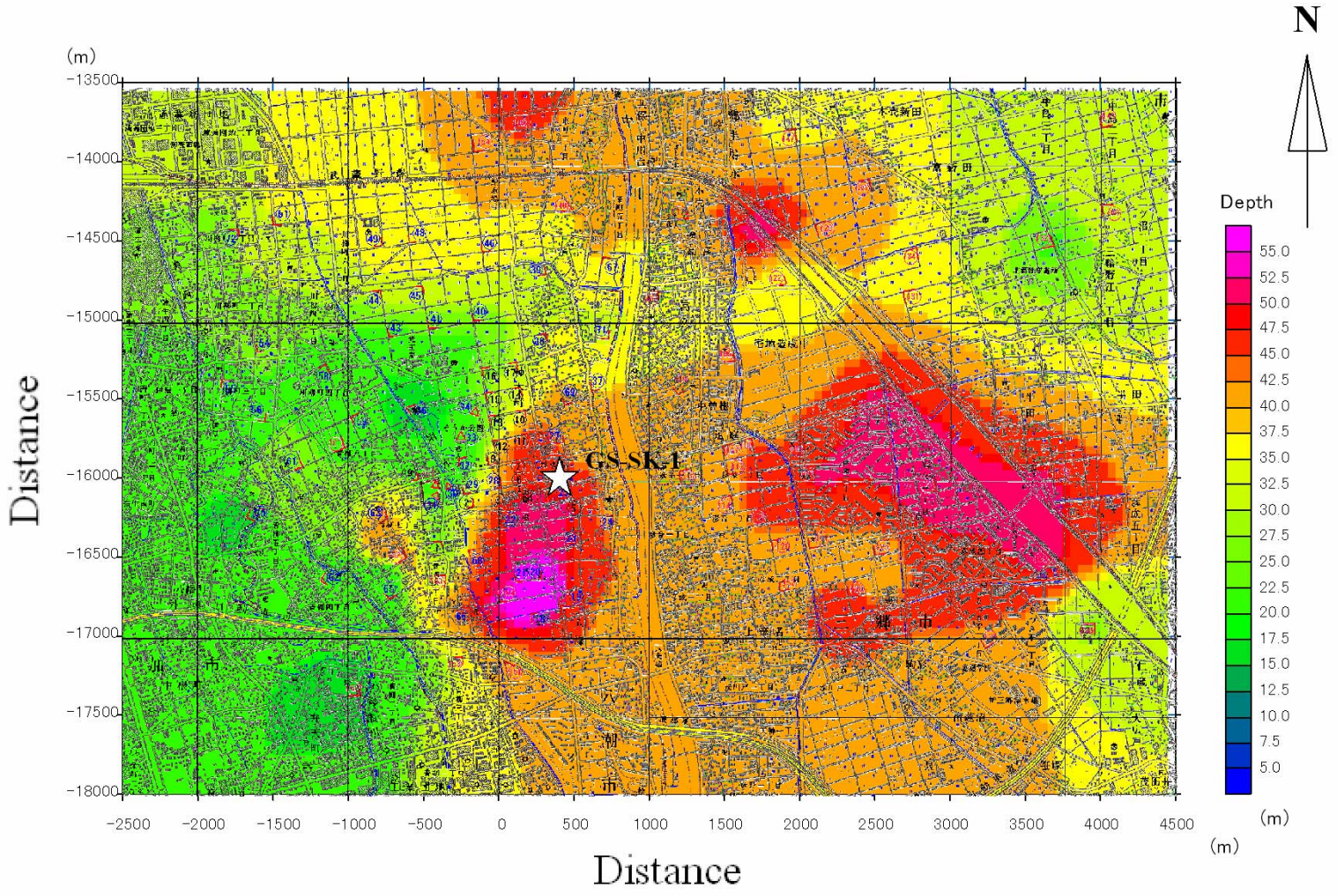

Figure 5.8.9. Depth of alluvium bottom obtained through the survey.

5.9 Summary

We started the development of active and passive surface-wave methods in the year 2000, and have applied the methods to more than 100 sites in actual civil engineering investigations as shown in this chapter. Most of such investigations include other in-situ geo-technical tests, such as drilling, cone penetrating test, and Swedish weighted soundings. We have compared the result of the surface-wave method with such in-situ tests and arrived at the conclusions that the surface-wave methods provide S-wave velocity model at the most of the case. Although the resolution and accuracy of the surface-wave methods are limited, rapid and non-destructive data acquisition is very efficient in civil engineering investigations.

References

Andrus, R. D., Stokoe, K. H., and Chung, R. M., 1999, Draft guidelines for evaluating liquefaction resistance using shear-wave velocity measurements and simplified procedure, NISTIR6277, National Institute of Standards and Technology, Gaithersburg, Md.

Banerjee, B. and Das Gupta, S. P., 1977, Gravitational attraction of a rectangular parallelepiped, Geophysics, 42, 1053-1055.

Feng, S., Sugiyama, T., and Yamanaka, H., 2001, Multi-site inversion in array micro tremor survey, Proceedings of the 104th SEJG Conference, 35-39.

Foti, S, 2003, small-strain stiffness and damping ratio of Pisa clay from surface-wave tests, geotechnique, No.5, 455-461.

Hayashi, K. and Suzuki, H., 2003, CMP analysis of multi-channel surface wave data and its application to near-surface S-wave velocity delineation, Proceedings of the symposium on the application of geophysics to engineering and environmental problems 2003, 1348-1355.

Hayashi, K., and Suzuki, H., 2004, CMP cross-correlation analysis of multi-channel surface-wave data, Butsuri-Tansa, 57, 7- 13.

Hayashi, K., Matsuoka, T. and Hatakeyama, H., 2005a, Joint analysis of a surface-wave method and micro-gravity survey, Journal of environmental and engineering geophysics, 10, 175-184.

Hayashi, K., Watabe, Y. and Sassa, S., 2005b, Development of S-velocity measurement using surface-waves in sandy tidal flat, Proceedings of the 40th Japan national conference on geotechnical engineering, 233-234 (in Japanese).

Hayashi, K., Inazaki, T. and Suzuki, H., 2007, Buried incised channels delineation using microtremor array measurements at Soka and Misato Cities in Saitama Prefecture, Bulletin Geological Survey of Japan, 57, 309-325 (in Japanese).

Imai, T. and Tonouchi, K., 1982, Correlation of N-value with S-wave velocity and shear modulus, Proceedings of the second European symposium on penetration testing, 67-72.

Inazaki, T., 1999, Land Streamer: A New System for High-Resolution S-Wave

Shallow Reflection Surveys, Proceedings of the symposium on the application of geophysics to engineering and environmental problems ‘99, 207-216.

Nakanishi, T., Ishihara, Y., Tanabe S., Kimura, K., Hachinohe, S. and Inazaki, T., 2007, Isopach map of the latest Pleistocene-Holecene incised valley fills under the southern area of the Nakagawa Lowland, Kanto Plain, based on interpretation of borehole logs, Geologocal Survey of Japan Open File Report, 454 (in Japanese).

Juang, C. H., Chen, C. J. and Jiang, T., 2001, Probabilistic framework for liquefaction potential, Journal of geotechnical and geoenvironmental engineering. 2001, 670-678.

Kitsunezaki. C. ,N. Goto, Y. Kobayashi., T. Ikawa, M. Horike, T. Saito, T. Kurota, K. Yamane, and K. Okuzumi, 1990, Estimation of P- and S- wave velocities in Deep Soil Deposits for Evaluating Ground Vibrations in Earthquake, Sizen-saigai-kagaku,9-3,1-17 (in Japanese).

Liao, S. C. C., Veneziano, D., and Whitman, R. V., 1988, Regression models for evaluating liquefaction probability, J. Geotech. Engrg., 114, 389-411.

Ludwig, W. J., Nafe, J.E., and Drake, C.L., 1970, Seismic refraction, in the Sea vol. 4, part1, Wiley-interscience, 53-84.

Okada, H., 2003, The microtremor survey method, Society of Exploration Geophysicist, Tulsa.

Okada, S., Hayashi, K., Tomari, K., Inoue, M. and Fujino, T., 2003, Application of the surface-wave method to levee survey, Proceedings of the 38th Japan national conference on geotechnical engineering, 39-40 (in Japanese).

Park, C. B., Miller, R. D., and Xia, J., 1999, Multimodal analysis of high frequency surface waves, Proceedings of the symposium on the application of geophysics to engineering and environmental problems '99, 115-121.

Robertson, P. K., Wride, C. E., 1998, Evaluating cyclic liquefaction potential using the cone penetration test, Can. Geotech. J., 35, 442-459.

Sassa, S. and Watabe, Y., 2005, Tidal flat geo-environments toward their revitalization -Part 2: Geo-environmental dynamics of sandy flat-, Proceedings of the 40th Japan national conference on geotechnical engineering, 903-904 (in Japanese).

Seed, H. B., and Idriss, I. M., 1971, Simplified procedure for evaluating soil

liquefaction potential, J. Soil Mech. And Found. Div., ASCE, 97, 1249-1273.

Van der Veen, M. and Green, A. G., 1998, Land streamer for shallow seismic data acquisition; evaluation of gimbal-mounted geophones, Geophysics, 63, 1408-1413.

Watabe, Y. and Sassa, S., 2005, Geophysical characterization of intertidal sedimentary environments: sand, mud and sand-mud layered flats, Proceedings of International Symposium on Fluvial and Coastal Disasters, ISBN4-9902861-0-3, Paper No. 13, 1-10.

Xia, j., Miller, R. D. and Park, C. B., 1999, Configuration of near-surface shear-wave velocity by inverting surface wave, Proceedings of the symposium on the application of geophysics to engineering and environmental problems '99, 95-104.

Chapter 6

Conclusions and Future Work

6.1 Conclusions

In this dissertation, we have developed a surface-wave method in order to estimate the S-wave velocity model form the ground surface in civil engineering investigations.

In the Chapter 2, we have reviewed fundamental theory behind surface wave propagation and its analysis. Theoretical consideration and numerical examples have shown the surface-waves are understandable and sub-surface velocity model can be derived from the dispersion character of surface-waves. Dispersion curves can be obtained from both active and passive surface-wave data in terms of simple waveform transformation. Numerical examples have also shown that the amplitude of the surface-waves is relatively large in comparison with refraction and reflection waves. It indicates that the data acquisition of surface-waves is easy and implies that the surface-wave methods can be used for many geo-technical investigations as non-destructive testing.

In the Chapter 3, we have evolved the surface-wave methods so that the methods can rapidly delineate two-dimensional S-wave velocity model. We have introduced the CMPCC analysis instead of the traditional MASW in which a dispersion curve is calculated from each shot gather. Unlike the MASW, multi-channel and multi-shot surface-wave data can be processed in the CMPCC analysis. One of the notable features of the CMPCC analysis is that the method does not require any summation and average of phase differences. The reason is that the CMPCC analysis processes the multi-channel and multi-shot waveform data into the cross-correlations. The conventional SASW method determines phase-velocities from different spacing cross-correlations separately. The SASW cannot determine high-frequency phase velocities from large-spacing cross-correlations due to a spatial aliasing. Therefore, SASW uses only limited information in whole waveform data. On the contrary, MASW is better than SASW because the methods can determine phase-velocities precisely using whole waveform data. The CMPCC analysis is a further extension of MASW and enables us to determine phase-velocities from multi-shot data directly by using CMPCC gathers.

In the Chapter 4, we have applied a passive surface-wave method, so called small scale microtremor array measurements, to many sites and compared the results with the active surface-wave method and other geo-technical investigations. These results lead to the conclusion that small scale microtremor array measurements can be used for S-wave velocity delineation in civil engineering investigations. Irregular two-dimensional arrays, such as L-shaped array, provide almost same dispersion curves as one of isotropic arrays. Although an array is linear, microtremor data may provide correct dispersion curves at some of the sites. Investigation depth is almost same as the size of array. Arrays whose size of 50m and 2Hz geophones are enough for estimating S-wave velocity model down to the top of diluvium layer in most of sites. It seems that about 10 minutes of micro-tremor data is enough for 50m arrays. We have concluded the passive surface-wave method, together with the active method, enables us to estimate S-wave velocity models down to the depth of 50m non-destructively from the surface.

In the chapter 5, the examples of geotechnical investigations, in which surface-wave methods have been employed, are described. We started the development of active and passive surface-wave methods in the year 2000, and have applied the methods to more than 100 sites in civil engineering investigations as shown in the Chapter 5. Most of such investigations include other in-situ geo-technical tests, such as drilling, cone penetrating test, and Swedish weighted soundings. We have compared the result of the surface-wave method with such in-situ tests and arrived at the conclusions that the surface-wave methods provide appropriate S-wave velocity model at the most of the case. Although the resolution and accuracy of the surface-wave methods are limited, rapid and non-destructive data acquisition is very efficient in civil engineering applications.

In conclusions, the active and passive surface-wave methods enable us to estimate two-dimensional S-wave velocity models down to the depth of 50m non-destructively from the surface. Considering that the demand for non-destructive investigations for soil engineering and earthquake engineering is increasing, the surface-wave methods proposed in this dissertation can play a very important role increasingly for such investigations.

6.2 Recommendation for Future Work

Although the surface-wave methods have been greatly improved in the last decade, there are so many issues to be studied in order to develop the methods to more useful tools in civil engineering investigations. As the last of the dissertation, we are going to summarize the issues to be studied in the future.

1) Higher modes

We have considered dispersion curves to be a fundamental mode of Rayleigh wave through the study. Many studies shows that higher modes can not be neglected in complex velocity models, such as a model in which a high velocity top layer overlies on low velocity layers, or a model in which a high velocity layer is embedded in low velocity layers. For example, Hayashi and Saito (2004) shows the higher modes dominate phase-velocity curves when a high velocity top overlies on low velocity layers. It seems that the higher modes must be taken into account in both active and passive surface-wave methods. Although a large number of studies have been made on surface-wave analysis including higher modes, stable, quick and reliable inversion method has not been established yet.

2) Irregular array in passive method

In the Chapter 4, we have evaluated the applicability of irregular arrays in a passive surface-wave method and reached the empirical conclusion that the irregular two-dimensional arrays, such as L-shaped array, provide almost same dispersion curves as one of isotropic arrays. The use of irregular arrays enables us to apply the passive methods in urban area. In recent years, several theoretical studies have been made on the applicability of irregular arrays (e.g. Yokoi et al., 2006). What seems to be lacking, however, is integrated study based on both field experience and theoretical study. Over the past few years, several articles (e.g. Wapenaar, 2003) have been devoted to the study of so called “seismic interferometry” in which Green’s function can be calculated from the cross-correlation of micro-tremor data obtained at different locations. The passive surface-wave methods can be considered as the phase-velocity analysis in terms of the seismic interferometry. Linear receiver arrays are usually employed in the seismic interferometry and the use of irregular arrays in the passive surface-wave methods may be understood in terms of the seismic interferometry.

3) The use of S-wave velocity as engineering parameters

As mentioned in the Chapter 1, a boring and standard penetrating test (SPT) is most widely adopted as geo-technical test in soil engineering. Most of the engineering parameters, such as cohesion (c), internal friction angle (ϕ) or confined compressive strength (qu) can be evaluated from blow counts (N-value) obtained through the SPT using the industrial standard in Japan. Soil mechanic and dynamic analysis, such as slope stability analysis or liquefaction potential analysis, can be done by engineering parameters obtained from the blow counts. Such analyses are authorized by public organizations, such as the Ministry of Land, Infrastructure and Transportation. On the contrary, S-wave velocity is only used for calculating seismic amplification of sites. S-wave velocity has not been widely used because expensive boring and PS-logging are required to obtain S-wave velocity of unconsolidated soil ground. In order to apply the S-wave velocity obtained through the surface-wave methods to soil engineering analysis, we have to establish the relationship between S-wave velocity and the engineering parameters. It is also important that the analyses or design works based on the S-wave velocity are authorized by public organizations.

References

Hayashi, K. and Saito, M., 2004, The dispersion curve of P-SV wave propagation with a high velocity top layer and its analysis, Proceedings of the 110th SEGJ Conference, 39-42, (in Japanese).

Wapenaar, C.P.A., 2003, Synthesis of an inhomogeneous medium from its acoustic transmission response, Geophysics, 68, 1756-1759.

Yokoi, T., Hayashi, K. and Aoike, K., 2006, A case study on dependence of the complex coherence function on the azimuth SPAC method of microtremor array measurement, Proceedings of the 114th SEGJ Conference, 138-141, (in Japanese).

Appendix A

Love Waves Propagating with 1D Multi-layered Medium

A.1. SH Wave

In this appendix, we are going to review calculation of Love wave dispersion curve based on the matrix method described by Saito (1979). Equation of motion in elastic medium (equation (2.2.9)) can be generally written as follows.

$$\rho \frac{\partial^2 u}{\partial t^2} = \frac{\partial \sigma_{xx}}{\partial x} + \frac{\partial \sigma_{xy}}{\partial y} + \frac{\partial \sigma_{xz}}{\partial z} \tag{A.1}$$

Above equation shows a x component of displacement (u) and other components can be written as similarly. σ_{xx}, σ_{xy} and σ_{xz} are stresses and can be written as follows using Lame constants λ and μ (equation (2.1.16)).

$$\begin{aligned} \sigma_{xx} &= \lambda\left(\frac{\partial u}{\partial x}+\frac{\partial v}{\partial y_2}+\frac{\partial w}{\partial z}\right)+2\mu\frac{\partial u}{\partial x} \\ \sigma_{xy} &= \mu\left(\frac{\partial u}{\partial y}+\frac{\partial v}{\partial x}\right) \\ \sigma_{xz} &= \mu\left(\frac{\partial u}{\partial z}+\frac{\partial w}{\partial x}\right). \end{aligned} \tag{A.2}$$

where, v and w are y and z components of displacement respectively.

Now, we assume SH type of solution that satisfies equations (A.1) and (A.2) as follows.

$$u = y_1(z)\frac{\partial Y}{k\partial y},\ \ v = -y_1(z)\frac{\partial Y}{k\partial x} \ \text{ and } \ w = 0. \tag{A.3}$$

where,

$$Y(x,y,t) = e^{i(\omega t - k_x x - k_y y)} \tag{A.4}$$

Stresses in x-y plane can be written as follows in terms of separation of variables.

$$\sigma_{xz} = y_2(z)\frac{\partial Y}{k\partial y},\ \ \sigma_{yz} = -y_2(z)\frac{\partial Y}{k\partial x} \ \text{ and } \ \sigma_{zz} = 0. \tag{A.5}$$

Substituting (A.3) into (A.2) yields,

$$\sigma_{xz} = \mu\left(\frac{\partial u}{\partial z}+\frac{\partial w}{\partial x}\right) = \mu\frac{dy_1}{dz}\frac{\partial Y}{k\partial y} \tag{A.6}$$

Comparing (A.6) with (A.5) indicates,

$$y_2 = \mu \frac{dy_1}{dz} . \qquad \text{(A.7)}$$

Writing σ_{xx} and σ_{xy} using y_1 and substituting them into the equation of motion (A.1) gives,

$$-\rho\omega^2 y_1 = -k^2 \mu y_1 + \frac{dy_2}{dz} . \qquad \text{(A.8)}$$

The equations (A.7) and (A.8) are basic equation for SH wave. These equations can be rewritten as,

$$\frac{dy_1}{dz} = \frac{1}{\mu} y_2 , \quad \frac{dy_2}{dz} = \mu \left(k^2 - \frac{\omega^2}{\beta^2} \right) y_1 \qquad \text{(A.9)}$$

where, β is S-wave velocity as follows,

$$\beta = \sqrt{\frac{\mu}{\rho}} . \qquad \text{(A.10)}$$

The equations (A.9) are simultaneous equations for y_1 and y_2.

A.2. Solution in Homogeneous Layers and Layer Matrix

Solution for equations (A.7) can be obtained easily in layered medium, in which each layer has constant density ($\rho=\rho_m$) and S-wave velocity ($\beta=\beta_m$) in the layer of index m, as follows.

$$y_1(z) = A_m e^{\nu_{\beta m}(z - z_{m+1})} + B_m e^{-\nu_{\beta m}(z - z_{m+1})}$$

$$y_2(z) = \mu_m \nu_{\beta m} \left(A_m e^{\nu_{\beta m}(z - z_{m+1})} + B_m e^{-\nu_{\beta m}(z - z_{m+1})} \right) \qquad \text{(A.11)}$$

or,

$$y_1(z) = A_m' \cosh \nu_{\beta m}(z - z_{m+1}) + B_m' \sinh \nu_{\beta m}(z - z_{m+1})$$

$$y_2(z) = \mu_m \nu_{\beta m} \left[A_m' \sinh \nu_{\beta m}(z - z_{m+1}) + B_m \cosh \nu_{\beta m}(z - z_{m+1}) \right] \qquad \text{(A.12)}$$

where,

$$\nu_{\beta m}^2 = k^2 - \left(\frac{\omega}{\beta_m}\right)^2 \tag{A.13}$$

Substituting $z=z_{m+1}$ into the equation (A.12) gives the solution on the boundary of (m+1) as follows,

$$y_1^{m+1} = A_m', \qquad y_2^{m+1} = \mu_m \nu_{\beta m} B_m'. \tag{A.14}$$

Substituting these A_m' and B_m' into the equations (A.12) gives us,

$$y_1(z) = y_1^{m+1} \cosh\nu_{\beta m}(z - z_{m+1}) + y_2^{m+1} \frac{1}{\mu_m \nu_{\beta m}} \sinh\nu_{\beta m}(z - z_{m+1})$$

$$y_2(z) = y_1^{m+1} \mu_m \nu_{\beta m} \sinh\nu_{\beta m}(z - z_{m+1}) + y_2^{m+!} \frac{1}{\mu_m \nu_{\beta m}} \cosh\nu_{\beta m}(z - z_{m+1}) \tag{A.15}$$

Now, we calculate solution only on the layer boundary and put $d_m=z_m-z_{m+1}$ as thickness of m's layer. The equation (A.15) can be written as a matrix form,

$$\begin{bmatrix} y_1^m \\ y_2^m \end{bmatrix} = \begin{bmatrix} \cosh\nu_{\beta m} d_m & \dfrac{\sinh\nu_{\beta m} d_m}{\mu_m \nu \beta_m} \\ \mu_m \nu_{\beta m} \sinh\nu_{\beta m} d_m & \cosh\nu_{\beta m} d_m \end{bmatrix} \begin{bmatrix} y_1^{m+1} \\ y_2^{m+1} \end{bmatrix} \tag{A.16}$$

or we can use matrix notation as follows,

$$\mathbf{y}^m = \mathbf{B}_m(\mathbf{d}_m)\mathbf{y}^{m+1}, \qquad m=n-1, n-2 \ldots\ldots \tag{A.17}$$

The matrix L_m (d_m) is so called a layer matrix for layer m. The matrix is essentialy equal to the matrix so called "Haskell" layer matrix. Advantage of the matrix (A.16) is that the elements of the matrix is always real. We can calculate solution on layer boundary using the layer matrix iteratively from the initial condition Y^n.

A.3 Dispersion Curve of Love Wave

The dispersion curve of Love waves can be calculated by integrating the equation (A.7) upward with incident of SH type plane waves in bottom layer as shown in Figure A.1. Initial condition in the layer boundary n is,

$$\mathbf{y}^n = \begin{pmatrix} 1 \\ \mu_n \nu_{\beta n} \end{pmatrix} \tag{A.18}$$

where $\mu_n \nu_{\beta n}$ must be larger than 0 so that y_1 and y_2 go to 0 where z goes to infinite. This condition implies that phase-velocity of Love wave must be slower that S-wave velocity of bottom layer (β_n). At the free surface, y_2 must be 0 so that stress goes to 0. Therefore, characteristic equations for Love wave can be written as follows.

$$F_L(c,\omega) = y_2^0 = 0,$$

or

$$F_L(c,\omega) = \frac{y_2^0}{y_1^0} = 0 \tag{A.19}$$

where c is phase velocity. Actual calculation procedure of a dispersion curve using equation (A.19) is described with simple source code example in Appendix C.

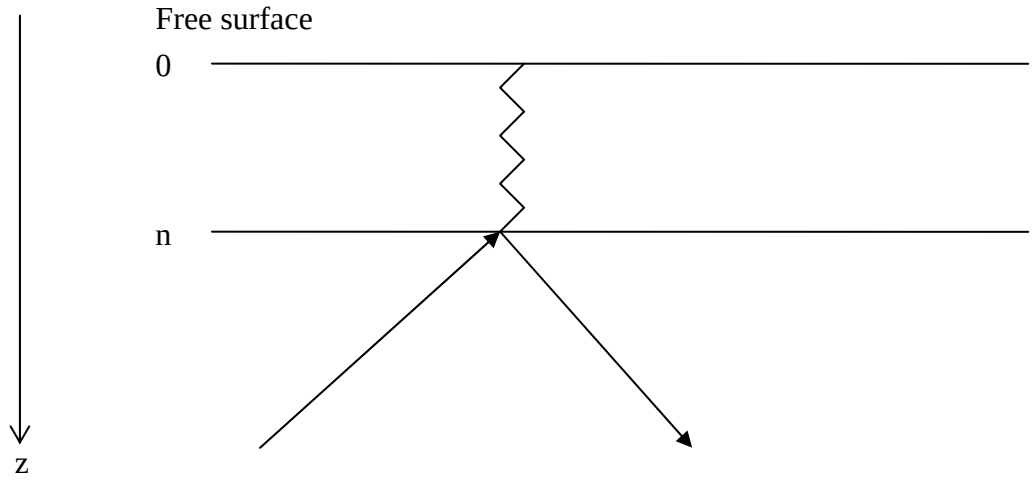

Figure A.1. Incident of plane SH wave.

References

Saito, M., 1979, Computation of reflectivity and surface wave dispersion curves for layered media 1. Sound wave and and SH wave, Butsuri-tanko, 32, 15-26, (in Japanese) .

Appendix B

Rayleigh Waves Propagating with 1D Multi-layered Medium

B.1 P-SV Wave

In this appendix, we are going to review calculation of Rayleigh wave dispersion curve based on the method described by Saito and Kabasawa (1993). Let us take *x* and *y* axis in horizontal plane and *z* axis in vertical direction with upward in Cartesian coordinate system. Figure B.1 shows coordinate system used in this appendix. Density and elastic constants are only function of *z*.

Now, we write displacement components (u_x, u_y, u_z) of P-SV wave as follows in this model for the sake of convenience.

$$u_x = y_1(z;k,\omega)Y_k(x,y)e^{-i\omega t}$$

$$u_y = y_3(z;k,\omega)\frac{1}{k}\frac{\partial Y_k}{\partial x}e^{-i\omega t}$$

$$u_z = y_3(z;k,\omega)\frac{1}{k}\frac{\partial Y_k}{\partial y}e^{-i\omega t} \qquad \text{(B.1)}$$

where, k is wave number for horizontal direction, ω is angular frequency and $Y_k(x,y)$ is solution of Helmhortz equation as follows.

$$\left(\frac{\partial^2}{\partial x_2}+\frac{\partial^2}{\partial y_2}+k^2\right)Y(x,y)=0 \qquad \text{(B.2)}$$

The solution of $Y_k(x,y)$ can be written as follows in Cartesian coordinate system.

$$Y(x,y)=e^{i(k_x x-k_y y)} \qquad \text{(B.3)}$$

We are going to omit arguments of y_1 and y_2, such as z, k, ω, and time term $exp(-i\omega t)$ in followindg description s .

Let us define $y_2(z)$ and $y_4(z)$ from equation (B.1) using Lame constants $\lambda(z)$ and $\mu(z)$.

$$\omega c y_2 = (\lambda+2\mu)\frac{dy_1}{dz}-k\lambda y_3, \quad \omega c y_4 = \mu\frac{dy_3}{dz}+k\lambda y_1 \qquad \text{(B.4)}$$

Stress components in horizontal plane can be written as,

$$\sigma_{zz} = \omega c y_2(z) Y_k(x,y)$$

$$\sigma_{zx} = \omega c y_4(z)\frac{1}{k}\frac{\partial Y_k}{\partial x}$$

$$\sigma_{yz} = \omega c y_4(z)\frac{1}{k}\frac{\partial Y_k}{\partial y} \tag{B.5}$$

where, c is phase-velocity in horizontal direction.

$$c = \frac{\omega}{k} \tag{B.6}$$

Substituting equations (B.1) and (B.5) into equation of motion yields following set of equations.

$$\frac{dy_1}{d_z} = \frac{kc^2}{\lambda+2\mu}y_2 + \frac{k\lambda}{\lambda+2\mu}y_3$$

$$\frac{dy_2}{d_z} = -k\rho y_1 + k y_4$$

$$\frac{dy_3}{d_z} = -k y_1 + \frac{kc^2}{\mu}y_4$$

$$\frac{dy_4}{d_z} = \frac{k\lambda}{\lambda+2\mu}y_2 + k\left\{-\rho + \frac{1}{c^2}\left[(\lambda+2\mu) - \frac{\lambda^2}{\lambda+2\mu}\right]\right\}y_3 \tag{B.7}$$

where, $\rho(z)$ indicates density.

B.2 Solution in Homogeneous Layers and Layer Matrix

Solution for equations (B.7) can be obtained easily in layered medium, in which each layer has constant density ($\rho=\rho_m$), P-wave velocity ($\alpha=\alpha_m$) and S-wave velocity ($\beta=\beta_m$) in the layer of index m. General solution for equations (B.7) is,

$$y_1 = r_\alpha\left(Ae^{\nu_\alpha z} + Ce^{-\nu_\alpha z}\right) + \left(Be^{\nu_\beta z} + De^{-\nu_\beta z}\right)$$

$$y_2 = \rho\left[(\gamma-1)\left(Ae^{\nu_\alpha z} - Ce^{-\nu_\alpha z}\right) + \gamma r_\beta\left(Be^{\nu_\beta z} - De^{-\nu_\beta z}\right)\right]$$

$$y_3 = \left(Ae^{\nu_\alpha z} - Ce^{-\nu_\alpha z}\right) + r_\beta\left(Be^{\nu_\beta z} - De^{-\nu_\beta z}\right)$$

$$y_4 = \rho\left[\gamma r_\alpha \left(Ae^{\nu_\alpha z} - Ce^{-\nu_\alpha z}\right) + (\gamma - 1)\left(Be^{\nu_\beta z} - De^{-\nu_\beta z}\right)\right] \tag{B.8}$$

where, *A, B, C, D* are constants obtained from baundary condition and other values are defined as follows;

$$r_\alpha^2 = 1 - \left(\frac{c}{\alpha}\right)^2,\ r_\beta^2 = 1 - \left(\frac{c}{\beta}\right)^2,\ \gamma = 2\left(\frac{\beta}{c}\right)^2,\ \nu_\alpha = kr_\alpha,\ \nu_\beta = kr_\beta \tag{B.9}$$

where, α is P-wave velocity and β is S-wave velocity.
Let us define a vector,

$$\mathbf{y}(z) = \begin{pmatrix} y_1(z) \\ y_2(z) \\ y_3(z) \\ y_4(z) \end{pmatrix} \tag{B.10}$$

then, equation (B.8) can be written as,

$$\mathbf{y}(z) = \mathbf{D}(z)\begin{pmatrix} A+C \\ A-C \\ B+D \\ B-D \end{pmatrix} \tag{B.11}$$

Matrix **D***(z)* is 4 by 4 matrix and cabe obtained from equation (B.8) by rewritiing exponential functions as hyperbolic functions. Substituting *z=0* into above equation yields,

$$\begin{pmatrix} A+C \\ A-C \\ B+D \\ B-D \end{pmatrix} = \mathbf{D}^{-1}(0)\mathbf{y}(0) \tag{B.12}$$

Above equation calculates constants from displacements and stresses at z=0. **D***(0)* can be written as follows from equation (B.8).

$$\mathbf{D}(0) = \begin{pmatrix} r_a & 0 & 1 & 0 \\ 0 & \rho(\gamma - 1) & 0 & \rho\gamma r_\beta \\ 0 & 1 & 0 & r\beta \\ \rho\gamma r_\alpha & 0 & \rho(\gamma - 1) & 0 \end{pmatrix} \tag{B.13}$$

Inverse of **D***(0)* can be obtained easily as,

$$\mathbf{D}^{-1}(0)=\begin{pmatrix} -(\gamma-1)/r_a & 0 & 0 & 1/\rho r_\alpha \\ 0 & -1/\rho & \gamma & 0 \\ \gamma & 0 & 0 & -1/\rho \\ 0 & 1/\rho r_\beta & -(\gamma-1)/r_\beta & 0 \end{pmatrix} \tag{B.14}$$

Substituting equatuion (B.14) into equation (B.12) expresses constants using **y***(0)*. Substituing the **y***(0)* into equation (B.11) yields,

$$\mathbf{y}(z)=\mathbf{D}(z)\mathbf{D}^{-1}(0)\mathbf{y}(0)=\mathbf{P}(z)\mathbf{y}(0). \tag{B.15}$$

Origin of z coordinate in above is arbitrary and it can be generally written as,

$$\mathbf{y}(z+h)=\mathbf{P}(h)\mathbf{y}(z). \tag{B.16}$$

In a multi-layered model as shown in Figure B.1, above equation obtaines displacements and strresses at the top of a layer from that of bottom of the layer. Therefore, displacements and strresses at the top and bottom of a layer can be expressed as,

$$\mathbf{y}_n=\mathbf{P}_n(h_n)\mathbf{y}_{n-1},\ \ \mathbf{y}_n=\mathbf{y}(z_n) \tag{B.17}$$

where, h_n is thickness of n_{th} layer $\mathbf{P}_n(h_n)$ is a layer matrix calculated from elastic moduli for n_{th} layer. Displacements and stresses at free surface ($\mathbf{y}_N$) can be calculated from arbitral initial condition ($\mathbf{y}_0$) using equation (B.17) and layer matrix $\mathbf{P}_n(h_n)$ for each layer.

The layer matrix $\mathbf{P}_n(h_n)$ can be summalized as follows:

$$P_{11}=C_\alpha-\gamma(C_\alpha-C_\beta),\ \ P_{12}=\frac{1}{\rho}\left(-r_\alpha^2 S_\alpha-S_\beta\right),\ \ P_{13}=\gamma r_\alpha^2 S_\alpha-(\gamma-1)S_\beta,$$

$$P_{14}=\frac{1}{\rho}(C_\alpha-C_\beta),\ \ P_{21}=\rho\left[-(\gamma-1)^2 S_\alpha+\gamma^2 r_\beta^2 S_\beta\right],\ \ P_{23}=\rho\gamma(\gamma-1)(C_\alpha-C_\beta),$$

$$P_{24}=(\gamma-1)S_\alpha-\gamma r_\beta^2 S_\beta,\ \ P_{33}=C_\beta+\gamma(C_\alpha-C_\beta),\ \ P_{34}=\frac{1}{\rho}\left(S_\alpha-r_\beta^2 S_\beta\right),$$

$$P_{43}=\rho\left[\gamma^2 r_\alpha^2 S_\alpha-(\gamma-1)^2 S_\beta\right],\ \ P_{22}=P_{11},\ \ P_{31}=-P_{24},\ \ P_{32}=-P_{14},\ \ P_{41}=-P_{23},\ \ P_{42}=-P_{13},$$

$P_{44}=P_{33}$. (B.18)

where,

$$C_\alpha = \cosh\nu_\alpha h,\ \ S_\alpha = \frac{\sinh\nu_\alpha h}{r_\alpha}, C_\beta = \cosh\nu_\beta h,\ \ S_\beta = \frac{\sinh\nu_\beta h}{r_\beta},$$

$$C_\alpha - C_\beta = 2\left(\sinh^2\frac{\nu_\alpha h}{2} - \sinh^2\frac{\nu_\beta h}{2}\right) \tag{B.19}$$

B.3 Dispersion Curve of Rayleigh Wave

Using equation (B.17), we can calculate differential equations (B.8) as initial value problem with both upoward and dowaneard. In the calculation of surface-waves in which amplitude increases with upwared direction, calculating from bottom to free sutrface with upward direction is much accurate. Inisial condition can be obtained as follows.

Let us assume $z < z_0=0$ is homogeneous halfspace, solution at the z can be experessed as follows from equation (B.8),

$$y_1 = Ar_\alpha e^{\nu_\alpha z} + Br_\alpha e^{\nu_\beta z}$$

$$y_2 = A\rho(\gamma - 1)e^{\nu_\alpha z} + B\gamma r_\beta e^{\nu_\beta z}$$

$$y_3 = Ae^{\nu_\alpha z} + Br_\beta e^{\nu_\beta z}$$

$$y_4 = A\rho\gamma r_\alpha e^{\nu_\alpha z} + B\rho(\gamma - 1)e^{\nu_\beta z} \tag{B.20}$$

where, A and B are constants in homogeneous half space and ρ and γ are values in homogeneous half space. In order to avoid solution diverges at zgoes to negative infinite, following condition must be considerd.

$$\mathrm{Re}(\nu_\alpha) > 0,\ \ \mathrm{Re}(\nu_\beta) > 0 \tag{B.21}$$

In order to obtaine solution, we use linear conbination because differential equations are linear. At first, we calculate a solution $\mathbf{y}^{(A)}(z)$ in which A=1 and B=0, and a solution $\mathbf{y}^{(B)}(z)$ in which A=0 and B=1. Next, we apply following equation.

$$\mathbf{y}(z) = Ay^{(A)}(z) + y^{(B)}(z) \tag{B.22}$$

Initial condition for both equation can be expressed as,

$$\mathbf{y}^{(A)}(0)=\begin{pmatrix} r_\alpha \\ \rho(\gamma-1) \\ 1 \\ \rho\gamma r_\alpha \end{pmatrix},\quad \mathbf{y}^{(B)}(0)=\begin{pmatrix} 1 \\ \rho\gamma r_\beta \\ r_\beta \\ \rho(\gamma-1) \end{pmatrix} \qquad (k>0) \qquad \text{(B.23)}$$

Boundary condition at free surface is,

$$\sigma_{zz}(z_N)=0,\ \ \sigma_{zx}(z_N)=\sigma_{yz}(z_N)=0\ . \qquad \text{(B.24)}$$

This condition can be written using equation (B.22) as follows:

$$y_2=Ay_2^{(A)}(z_N)+By_2^{(B)}(z_N)=0$$

$$y_4=Ay_4^{(A)}(z_N)+By_4^{(B)}(z_N)=0 \qquad \text{(B.25)}$$

In order to satisfy above equation, following condition can be satisfied.

$$F_R(k,\omega)=y_2^{(A)}(z_N)y_4^{(B)}(z_N)-y_2^{(B)}(z_N)y_4^{(A)}(z_N)=0 \qquad \text{(B.26)}$$

This is the characteristic equation for Rayleigh waves. Actual calculation procedure of a dispersion curve using equation (B.26) is same as Love wave.

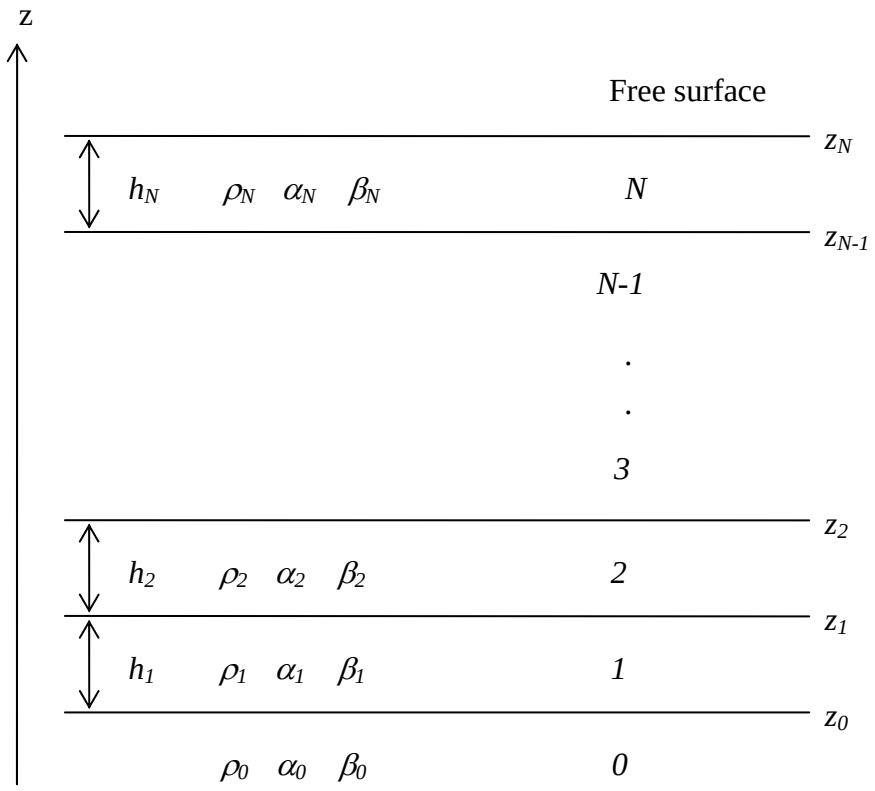

Figure B.1. Coordinate system and layered model.

References

Saito, M. and Kabasawa, H., 1993, Computation of reflectivity and surface wave dispersion curves for layered media 2. Rayleigh wave calculations, Butsuri-tansa, 46, 283-298, (in Japanese).

Appendix C

Calculation Procedure of a Dispersion Curve

C.1. Calculation Procedure

This Appendix describes actual calculation procedure of dispersion curve. For the moment, let us take a fundamental mode of Love wave dispersion curve as example. Characteristic equation of Love wave can be written as follows (equation (A.19)).

$$F_L(c,\omega) = y_2^0 = 0 \tag{C.1}$$

In order to calculate a dispersion curve, we generally fix angular frequency ω and search phase-velocity c that makes characteristic equation (2.3.11) as zero. Outline of calculation can be summarized as follows. This procedure calculates a dispersion curve for a multi layer model.

```
// Frequency loop
for (i=0;i<Number of frequencies ;i++)
{
        // Setup angular frequency ω.

        // Phase velocity loop
        for (j=0;j<Number of phase velocities ;j++)
        {
                // Setup phase-velocity c.
                // Setup initial condition for given ω and c.
                        at bottom layer using equation (A.18).

                for (k=0;k<Number of layers ;k++)
                {
                        // Calculate variables y1(z) and y2(z) from bottom to top layer
                                using layer matrix (A.16).
                }
                // Check if FL(c,w) is 0.
        }
}
```

Simple source code example and calculated result are shown in following sections. For the sake of simplicity, this source code example calculates characteristic equation $F_L(c,w)$ only 1m/s intervals and a dispersion curve is not accurate. Source code used in this dissertation applies Newton's method for determining the zero of characteristic

equation in order to calculate a much accurate dispersion curve.

C.2. Source Code Example

```
void SHMultiLayer(int nLayer,float *Beta,float *Rho,float *Thickness)
{
	// nLayer	: Number of layers
	// Beta		: S-wave velocity for each layer (vector)
	// Rho		: Density vector for each layer (vector)
	// Thickness	: Thickness for each layer (vector)

	int i,j,k;
	float c;			// Phase velocity
	float freq;			// Frequency
	float w;			// Angular frequency
	float w2;
	float fcw,fcw0;
	float nb0;
	float nb1;
	float fk;
	float y1,y2;
	float y1b,y2b;
	float b0,b02;
	float b1,b12;
	float d0;
	float r0;
	float m0;
	int nc;
	float root;
	float BetaMin=Beta[0];
	float pi2 = 1.;
	pi2 = atan(pi2)*8.;

	float *mu=new float [nLayer];

	FILE *fp,*fp2,*fp3;

	for (i=0;i<nLayer;i++)
	{
		mu[i]=Beta[i]*Beta[i]*Rho[i];
	}

	fp=fopen("sh.dat","w");

	for (i=1;i<nLayer;i++)
	{
		BetaMin=min(BetaMin,Beta[i]);
	}

	nc=int(Beta[nLayer-1]-BetaMin);

	if (nc <= 0)
	{
		exit(0);
	}

	for (i=0;i<200;i++)		// Frequency loop
	{
		freq=float(i+1)/2.;		// Calculate frequency range from 0.5 to 100Hz

		fprintf(fp,"%d %f ",i,freq);

		w=freq*pi2;
		w2=w*w;

		for (j=0;j<nc-1;j++)		// Phase velocity loop
		{
			c=float(j+1)+BetaMin;

			fk=w/c;
```

```
                        // initial condition
                        b1=Beta[nLayer-1];
                        b12=b1*b1;
                        nb1=sqrt(fk*fk-w2/b12);  // Always real (c < Beta[nLayer-1])

                        y1b=1.;                                 // Initial condition
                        y2b=mu[nLayer-1]*nb1;  // Initial condition

                        for (k=0;k<nLayer-1;k++)                // Layer loop
                        {
                                b0=Beta[nLayer-2-k];
                                b02=b0*b0;
                                d0=Thickness[nLayer-2-k];
                                r0=Rho[nLayer-2-k];
                                m0=mu[nLayer-2-k];

                                root=fk*fk-w2/b02;      //

                                if (root >= 0.)                 // real
                                {
                                        nb0=sqrt(root);                 // top layer : real

                                        y1=y1b*cosh(nb0*d0)+y2b/m0/nb0*sinh(nb0*d0);
                                        y2=y1b*m0*nb0*sinh(nb0*d0)+y2b*cosh(nb0*d0);

                                }
                                else            // imaginary
                                {
                                        nb0=sqrt(-root);                // top layer : imaginary

                                        y1=y1b*cos(nb0*d0)+y2b/m0/nb0*sin(nb0*d0);
                                        y2=-y1b*m0*nb0*sin(nb0*d0)+y2b*cos(nb0*d0);
                                                // First term must be negative

                                }
                                y1b=y1;
                                y2b=y2;
                        }
                        fcw=y2;

                        if (j > 0)
                        {
                                if (fcw*fcw0 < 0.)
                                {
                                        fprintf(fp," %f ",c);
                                }
                        }
                        fcw0=fcw;
                }
                fprintf(fp,"¥n");
        }
        fclose(fp);

        delete [] mu;
}
```

C.3. Example of Calculated Result

Calculated result using the source code shown in the Chapter C.2 for a following S-wave velocity model (Table C.1) is shown in Table C.2 and Figure C.1.

Table C.1 S-wave velocity model used in calculation

Layer No.	S-wave velocity(m/s)	Density(kg/m3)	Thickness(m)
1	500	1895.5	10
2	1000	2055.8	30
3	2000	2328.4	-

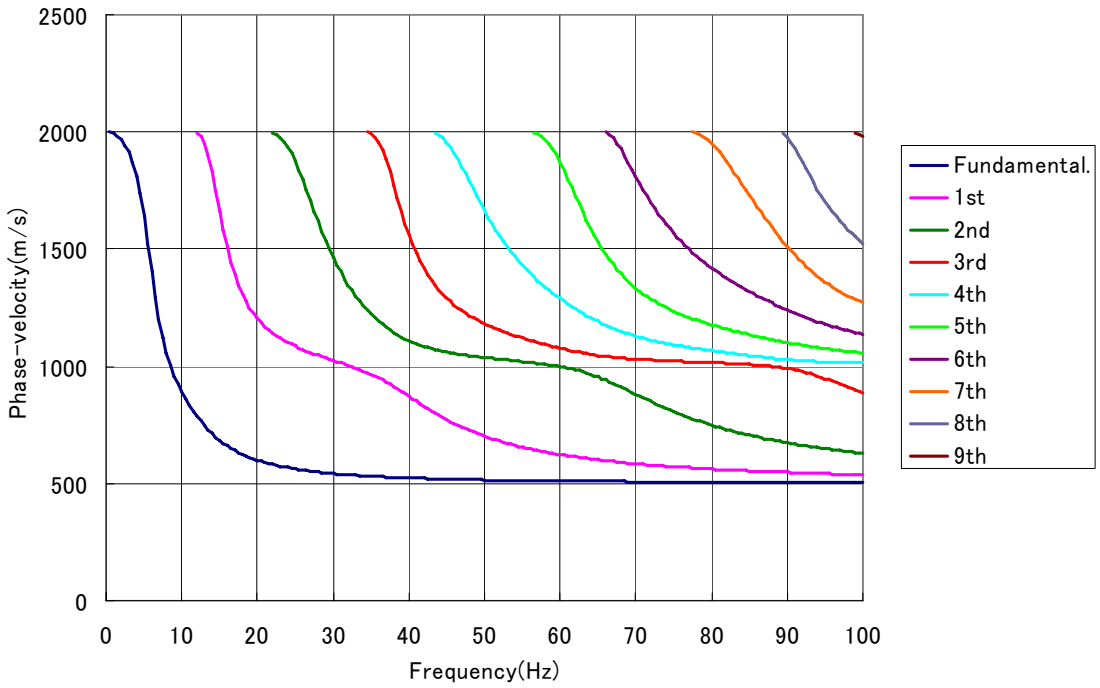

Figure C.1 Calculated result using the source code shown in the Chapter C.2

Table C.2 Calculated result using the source code shown in the Chapter C.2 (1).

Frequency(Hz)	Fund.	1st	2nd	3rd	4th	5th	6th	7th	8th	9th
0.5	1999									
1	1993									
1.5	1983									
2	1967									
2.5	1945									
3	1914									
3.5	1872									
4	1814									
4.5	1737									
5	1639									
5.5	1524									
6	1404									
6.5	1293									
7	1199									
7.5	1121									
8	1058									
8.5	1005									
9	961									
9.5	923									
10	890									
10.5	860									
11	833									
11.5	808									
12	786	1996								
12.5	765	1980								
13	746	1949								
13.5	728	1901								
14	712	1833								
14.5	698	1751								
15	684	1663								
15.5	672	1580								
16	661	1506								
16.5	650	1443								
17	641	1390								
17.5	632	1346								
18	625	1309								
18.5	618	1277								
19	611	1249								
19.5	605	1226								
20	599	1205								
20.5	594	1187								
21	590	1170								
21.5	585	1156								
22	581	1143	1995							
22.5	577	1131	1986							
23	574	1121	1973							
23.5	571	1111	1956							
24	568	1102	1934							
24.5	565	1094	1907							
25	562	1086	1875							

Table C.2 Continued (2).

Frequency(Hz)	Fund.	1st	2nd	3rd	4th	5th	6th	7th	8th	9th
25.5	559	1078	1838							
26	557	1072	1797							
26.5	555	1065	1753							
27	553	1059	1708							
27.5	551	1053	1663							
28	549	1047	1619							
28.5	547	1042	1577							
29	546	1036	1537							
29.5	544	1031	1500							
30	543	1026	1465							
30.5	541	1020	1433							
31	540	1015	1402							
31.5	539	1010	1374							
32	537	1004	1348							
32.5	536	998	1324							
33	535	993	1301							
33.5	534	987	1280							
34	533	980	1260							
34.5	532	973	1241	1999						
35	531	966	1224	1992						
35.5	530	959	1208	1978						
36	529	951	1193	1955						
36.5	529	942	1179	1922						
37	528	934	1167	1880						
37.5	527	924	1155	1829						
38	526	915	1144	1773						
38.5	526	905	1134	1717						
39	525	894	1125	1661						
39.5	525	884	1116	1610						
40	524	873	1109	1563						
40.5	523	862	1102	1521						
41	523	851	1096	1483						
41.5	522	841	1090	1449						
42	522	830	1085	1419						
42.5	521	820	1080	1392						
43	521	810	1076	1368						
43.5	520	800	1071	1346	1997					
44	520	791	1068	1326	1989					
44.5	519	781	1064	1308	1975					
45	519	773	1061	1292	1958					
45.5	519	764	1058	1277	1936					
46	518	756	1055	1263	1911					
46.5	518	748	1052	1250	1883					
47	517	741	1050	1239	1853					
47.5	517	733	1048	1228	1821					
48	517	726	1045	1217	1789					
48.5	516	720	1043	1208	1757					
49	516	714	1041	1199	1725					
49.5	516	707	1039	1190	1694					
50	515	702	1037	1182	1664					

Table C.2 Continued (3).

Frequency(Hz)	Fund.	1st	2nd	3rd	4th	5th	6th	7th	8th	9th
50.5	515	696	1035	1175	1635					
51	515	691	1034	1168	1608					
51.5	515	686	1032	1161	1582					
52	514	681	1030	1154	1557					
52.5	514	676	1028	1148	1534					
53	514	671	1027	1142	1511					
53.5	514	667	1025	1137	1490					
54	513	663	1023	1131	1470					
54.5	513	659	1022	1126	1451					
55	513	655	1020	1121	1433					
55.5	513	651	1018	1116	1416					
56	512	648	1017	1111	1399					
56.5	512	644	1015	1106	1383	1998				
57	512	641	1013	1101	1368	1992				
57.5	512	638	1011	1097	1354	1982				
58	512	635	1009	1093	1340	1967				
58.5	511	632	1007	1089	1327	1949				
59	511	629	1004	1084	1314	1926				
59.5	511	626	1002	1080	1301	1900				
60	511	623	999	1077	1290	1869				
60.5	511	621	996	1073	1278	1836				
61	511	618	993	1069	1267	1801				
61.5	510	616	989	1066	1256	1765				
62	510	614	985	1063	1246	1728				
62.5	510	611	981	1060	1236	1692				
63	510	609	977	1057	1226	1657				
63.5	510	607	972	1054	1217	1623				
64	510	605	966	1051	1208	1591				
64.5	510	603	961	1049	1200	1560				
65	509	601	955	1046	1192	1531				
65.5	509	599	948	1044	1184	1504				
66	509	597	942	1042	1176	1479	1999			
66.5	509	595	935	1041	1169	1456	1989			
67	509	594	927	1039	1162	1434	1973			
67.5	509	592	920	1037	1156	1414	1952			
68	509	590	912	1036	1150	1395	1926			
68.5	509	589	905	1034	1144	1378	1899			
69	508	587	897	1033	1139	1362	1869			
69.5	508	586	889	1032	1134	1347	1839			
70	508	584	881	1031	1129	1333	1809			
70.5	508	583	873	1030	1124	1320	1780			
71	508	582	865	1029	1120	1308	1752			
71.5	508	580	857	1028	1116	1297	1724			
72	508	579	850	1027	1112	1287	1698			
72.5	508	578	842	1026	1108	1277	1674			
73	508	576	835	1025	1104	1268	1650			
73.5	507	575	828	1024	1101	1259	1628			
74	507	574	821	1024	1098	1251	1607			
74.5	507	573	814	1023	1095	1243	1587			
75	507	572	807	1022	1092	1236	1568			

Table C.2 Continued (4).

Frequency(Hz)	Fund.	1st	2nd	3rd	4th	5th	6th	7th	8th	9th
75.5	507	571	801	1021	1089	1229	1550			
76	507	570	794	1021	1086	1222	1533			
76.5	507	569	788	1020	1083	1215	1516			
77	507	568	782	1019	1081	1209	1500			
77.5	507	567	776	1019	1078	1203	1486	1999		
78	507	566	770	1018	1076	1198	1471	1995		
78.5	507	565	765	1018	1074	1192	1458	1988		
79	507	564	760	1017	1071	1187	1444	1978		
79.5	506	563	754	1016	1069	1182	1432	1966		
80	506	562	749	1016	1067	1177	1420	1951		
80.5	506	561	744	1015	1065	1172	1408	1935		
81	506	560	740	1014	1063	1168	1397	1916		
81.5	506	559	735	1014	1060	1163	1386	1895		
82	506	559	731	1013	1058	1159	1375	1874		
82.5	506	558	726	1012	1056	1155	1365	1851		
83	506	557	722	1012	1054	1151	1355	1827		
83.5	506	556	718	1011	1052	1147	1346	1803		
84	506	555	714	1010	1050	1143	1336	1779		
84.5	506	555	710	1009	1048	1139	1327	1754		
85	506	554	706	1008	1046	1135	1318	1730		
85.5	506	553	703	1007	1044	1131	1310	1706		
86	506	553	699	1006	1042	1128	1301	1683		
86.5	506	552	696	1005	1041	1124	1293	1659		
87	505	551	692	1004	1039	1121	1285	1637		
87.5	505	551	689	1002	1037	1117	1277	1614		
88	505	550	686	1000	1035	1114	1270	1593		
88.5	505	549	683	998	1033	1111	1262	1572		
89	505	549	680	996	1032	1107	1255	1551		
89.5	505	548	677	994	1030	1104	1248	1532	1992	
90	505	548	674	991	1029	1101	1241	1512	1976	
90.5	505	547	671	988	1027	1098	1234	1494	1955	
91	505	546	669	985	1026	1095	1227	1476	1930	
91.5	505	546	666	981	1025	1093	1221	1459	1901	
92	505	545	663	977	1024	1090	1214	1443	1872	
92.5	505	545	661	973	1023	1087	1208	1427	1841	
93	505	544	659	968	1022	1085	1202	1412	1812	
93.5	505	544	656	964	1021	1082	1196	1398	1783	
94	505	543	654	958	1020	1080	1190	1385	1755	
94.5	505	543	652	953	1020	1078	1185	1372	1729	
95	505	542	649	948	1019	1075	1180	1360	1704	
95.5	505	542	647	942	1018	1073	1175	1349	1681	
96	505	541	645	936	1018	1071	1170	1338	1659	
96.5	505	541	643	930	1017	1069	1165	1328	1639	
97	505	540	641	924	1017	1068	1160	1318	1619	
97.5	504	540	639	917	1016	1066	1156	1309	1601	
98	504	540	637	911	1016	1064	1152	1300	1584	
98.5	504	539	635	905	1016	1063	1148	1292	1567	
99	504	539	633	898	1015	1061	1144	1284	1552	1997
99.5	504	538	632	892	1015	1059	1140	1277	1537	1991
100	504	538	630	886	1015	1058	1137	1270	1523	1982